



HAL
open science

Mini Squeezers Towards Integrated Systems

Alexandre Brioussel

► **To cite this version:**

Alexandre Brioussel. Mini Squeezers Towards Integrated Systems. Quantum Physics [quant-ph]. Université Pierre et Marie Curie, 2016. English. NNT: . tel-01353795

HAL Id: tel-01353795

<https://theses.hal.science/tel-01353795>

Submitted on 17 Aug 2016

HAL is a multi-disciplinary open access archive for the deposit and dissemination of scientific research documents, whether they are published or not. The documents may come from teaching and research institutions in France or abroad, or from public or private research centers.

L'archive ouverte pluridisciplinaire **HAL**, est destinée au dépôt et à la diffusion de documents scientifiques de niveau recherche, publiés ou non, émanant des établissements d'enseignement et de recherche français ou étrangers, des laboratoires publics ou privés.

A thesis submitted for the degree of Doctor of
Philosophy in Physics

Mini Squeezers Towards Integrated Systems

Alexandre Brioussel

Defended the 13th of May 2016

Australian National University

&

Université Pierre et Marie Curie



Australian
National
University



Supervisors:

Prof. Claude FABRE

Prof. Nicolas TREPS

Prof. Ping Koy LAM

Dr. Thomas SYMUL

Referees:

Prof. Ulrik Lund ANDERSEN

Dr. Hidehiro YONEZAWA

Examiners:

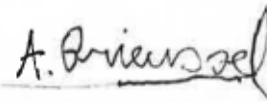
Dr. Michel LEFEBVRE

Prof. Agnes MAITRE (Jury president)

Declaration

This thesis is an account of research undertaken between October 2011 and January 2016 at The Department of Quantum Science, Research School of Physics, Faculty of Science, The Australian National University, Canberra, Australia and the Laboratoire Kastler Brossel, Paris, France.

Except where acknowledged in the customary manner, the material presented in this thesis is, to the best of my knowledge, original and has not been submitted in whole or part for a degree in any university.



Alexandre Briussel
January, 2016

Acknowledgments

First I wish to thank my official supervisors which were of great help during this thesis. Ping Koy Lam, Thomas Symul in Australia and Claude Fabre and Nicolas Treps in France, but Also my non official supervisors Jiri Janousek and Ben Buchler who were always here to answer my questions and to help me in the lab.

I want to thank my lab team in Australia who struggled with me with the SqOPO, Shen Yong, Geoff Campbell and my house-mate Giovanni Guccione. I thank all my lab co-workers in Australia hoping not to forget anyone. Sara Hosseini, Jiao Geng, Syed M Assad, Helen Chrzanowski, Seiji Armstrong, Sophie Zhao Jie, Oliver Thearle, Jin Yang, Melanie Mraz and Mark Bradshaw, and the people I didn't necessarily worked with, but with who I shared meals, played cards or that I just met in the corridor and had a chat Pierre Vernaz-Gris, Harry Slatyer, Mahdi Hosseini, Daniel Higginbottom, Julien Bernu, Jesse Everett, Jian Su, Boris Hage, Jessica Eastman, Shasha Ma, Young-Wook Cho, Ben Sparkes and André Carvalho from the group and Michael Stefszky, Georgia Mansell, John Debs with his 3D printer, Nick Robin and Kyle Hardman that I always met late in the week-end and John Close who taught me how to play guitar. In France I also want to thank my lab coworkers Hanna Lejeannic, Guillaume Labroille, Olivier Morin, Kun Huang, and Julien Laurat. And the people in my group Pu Jian, Jean-François Morizur, Valérian Thiel, Clément Jacquard, Valentin A. Averchenko, Roman Schmeissner, Jonathan Roslund, Vanessa Chille, Cai Yin, Guilia Ferrini, Zheng Zhan and also Simon François, Baptiste Gouraud, Dominik Maxein, Leander Hohmann, Sébastien Garcia, Konstantin Ott, Claire Lebouteiller and Jacob Reichel.

I also want to thank all the people from the administration, the people from the mechanical workshop and the people from the electrical workshop in France and in Australia who helped me a lot during this PhD, especially Gaël Coupin, Arnaud Leclercq, Brigitte Delamour and Jean-Pierre Okpizs, and all the people that didn't necessarily contributed directly to this thesis, but who supported me in France and in Australia. And finally a special thanks for April Sprague and Rhonda Sprague for correcting all my spelling mistakes and my awful English in this thesis, thanks everybody.

Abstract

Squeezed states of light are quantum states that can be used in numerous protocols for quantum computation and quantum communication. Their generation in laboratories has been investigated before, but they still lack compactness and practicality to easily integrate them into larger experiments.

This thesis considers two experiments: one conducted in France, the miniOPO; and one conducted in Australia, the SquOPO. Both are new designs of compact sources of squeezed states of light towards an integrated system.

The miniOPO is a linear cavity of 5mm length between the end of a fiber and a curved mirror with a PPKTP crystal of 1mm inside it. The squeezing generated in this cavity is coupled into the fiber to be able to be brought to a measurement device (homodyne) or to a larger experiment. The cavity is resonant for the squeezed light and the pump light, and locked in frequency using self-locking effects due to absorption of the pump in the crystal. The double resonance is achieved by changing the temperature of the crystal.

Two different fibers have been tested in this experiment, a standard single-mode fiber and a photonic large core single-mode fiber.

The squeezing obtained is still quite low ($0.5dB$ with the standard fiber and $0.9dB$ for the photonic fiber) but a number of ameliorations are investigated to increase these levels in the future.

The SqOPO is a monolithic square cavity made in a Lithium Niobate crystal using four total internal reflections on the four faces of the square to define an optical mode for the squeezed mode and the pump mode. The light is coupled in the resonator using frustrated internal reflection with prisms. The distance between the prisms and the resonator defined the coupling of the light, which allows us to control the finesse of the light in the resonator and by using birefringent prisms it is possible to tune independently the two frequencies in the resonator to achieve an optimal regime. The frequency of the light is locked using absorption of the pump light in the resonator to achieve self-locking, and double resonance is controlled by tuning the temperature of the crystal.

We demonstrated $2.6dB$ of vacuum squeezing with this system. Once again, the amount of squeezing is low, but ameliorations that could be implemented in the future are discussed.

Publication:

A. Briussel, Y. Shen, G. Campbell, G. Guccione, J. Janousek, B. Hage, B. C. Buchler, N. Treps, C. Fabre, F. Z. Fang, X. Y. Li, T. Symul, and P. K. Lam, "Squeezed light from a diamond-turned monolithic cavity," *Opt. Express* 24, 4042-4056 (2016)

Contents

Acknowledgments	5
Abstract	7
I. Theoretical Background	1
1. Introduction	5
1.1. The Maxwell Equations and the Wave Equations	5
1.2. Energy Considerations	6
1.3. Fourier Transforms	6
1.4. Dielectric Medium and the Wave Equation	8
1.4.1. Properties of Susceptibilities	8
2. Light Propagation	11
2.1. Linear Homogeneous Isotropic (LHI) Behavior	11
2.1.1. Gaussian Propagation Solution	12
2.1.2. High Order Propagation Mode Solutions	13
2.1.3. Astigmatism	14
2.1.4. ABCD Matrix	14
2.2. Linear Anisotropic Medium	15
2.2.1. Ordinary Beam	18
2.2.2. Extraordinary Beam	19
2.2.3. Dispersion Angle	19
2.3. Non Linear Medium	20
2.3.1. Propagation Equation	20
2.3.2. Second Harmonic Generation	22
2.3.3. Degenerate Parametric Amplification	24
3. Interface Conditions	25
3.1. Field Interface Conditions	25
3.1.1. Normal Fields	25
3.1.2. Tangential Fields	26
3.1.3. Poynting Vector	26
3.2. Fresnel Equations	26
3.2.1. TE Polarization or S-Polarization	28
3.2.2. TM Polarization or P-Polarization	29

4. Cavity	33
4.1. Beam Splitter Conventions	34
4.2. Cavity Transmission	34
4.3. Stability	37
4.4. Non Linear Cavity	39
5. Quantum Optics	43
5.1. Quantization of the Field	43
5.2. Quadratures and Homodyne Measurements	46
5.2.1. Quadratures	46
5.2.2. Optics Components	46
5.2.3. Homodyne	47
5.3. Different Light States and Wigner Function	49
5.3.1. Fock States	50
5.3.2. Coherent States	51
5.3.3. Squeezed States	52
5.4. Squeezing Creation and Interaction with Environment	53
5.4.1. Single pass squeezing generation in a non-linear crystal	53
5.4.2. Squeezing Interaction in a Lossy Channel	55
5.4.3. Squeezing generation in a non linear crystal in a cavity	55
II. Fibered Mini OPO	61
6. Introduction	63
6.1. Introduction	63
6.2. Squeezing Generation	63
6.3. Toward an all-fibered squeezer	64
7. Experimental Method	67
7.1. The OPO Cavity, Description of the Experiment	67
7.1.1. Coupling Mirror	68
7.1.2. Crystal and Crystal Mount	71
7.1.3. Fiber and Fiber Mount	73
7.1.4. Base	75
7.2. Other experimental consideration	75
7.2.1. Laser Source	75
7.2.2. Fibered Elements	76
7.2.3. Crystal Temperature Control	80
7.2.4. High Voltages Amplifiers:	81
7.2.5. Homodyne Detectors	81
7.2.6. Optical Suspension Table	83
7.3. Alignment of the Cavity	83
7.3.1. Schematic of the Set Up	83

7.3.2.	Crystal Alignment with White Light Interferometry	84
7.3.3.	Temperature Tuning	87
7.3.4.	Homodyne Alignment:	87
7.3.5.	Curved Mirror:	89
7.3.6.	Alignment of the Green and Red:	90
7.4.	System Limitations	91
7.4.1.	Curvature Matching	91
7.4.2.	Asphericity of the phase surfaces	92
7.4.3.	Grey Tracking and Damaging:	95
7.5.	Locking the System	96
7.5.1.	PDH locking	96
7.5.2.	Self Locking	97
7.5.3.	Locking with a Micro-Controller	100
8.	Results	103
8.1.	Second Harmonic Generation and Amplification De-Amplification . .	103
8.2.	Squeezing	104
9.	Conclusion	109
III.	Square Monolithic Resonator	115
10.	Introduction:	117
11.	Resonator Coupling	119
11.1.	Evanescant Prism Coupling	119
11.1.1.	S-Polarization	122
11.1.2.	P-Polarization	124
11.2.	Resonator	126
11.3.	Phase Control	130
11.4.	TEM Modes	132
11.5.	ABCD Matrix Considerations and Stability of the resonator	132
12.	Experimental Methods	135
12.1.	Creation of Resonators	135
12.1.1.	Polishing	135
12.2.	Prisms	136
12.3.	Mechanical System	137
12.4.	High Voltage	141
12.5.	Alignment	141
12.5.1.	How to Align Prisms and Resonators	141
12.5.2.	How to Align the Beam with Contra-Propagating Beams . . .	143
12.5.3.	Temperature Tuning of the Crystal	145

12.5.4. Homodyne Alignment	145
12.5.5. Prism Switching and alignment for Squeezing	146
12.6. Lock and Self Locking	147
13. Results	151
13.1. Non Linearity	151
13.1.1. SHG and De-amplification	151
13.1.2. Squeezing	151
13.1.3. Conclusion	154
A. Fourier Transform of the Polarisation Field versus the Susceptibility	161
B. Index calculation for the green calcite coupler in p-polarization	165

Part I.
Theoretical Background

Overview of the Thesis

During the last 50 years, we have witnessed the huge development of information technology around the world, to the point where almost everyone now has a computer in their home and an Internet-connected Smartphone in their pocket. One of the key points that allowed this sudden development was the progress of the transistors.

Quantum computation and quantum communication are the future of our information technology and like the transistor, the source of quantum states used in these technologies will be the key point for their development. Amongst the different media for these states, light is fast, easy to transport and has good interaction with matter. The two simpler candidates for quantum states of light are single photons and squeezed states. A lot of work has been done in the production of single photons, this thesis emphasizes the production of squeezing states.

This Ph.D. was a collaboration between the Laboratoire Kastler Brossel in Paris and the Australian National University in Canberra to investigate two new compact designs to potentially operate as sources of squeezing of light for larger experiments. The first one, the miniOPO, has been developed in Paris. It is a linear cavity between the end of a fiber and a curved mirror containing a non linear crystal of PPKTP. The advantage of this system is the fact that the squeezed light is directly injected in the fiber allowing easy transfer and potential processing to be done directly in the fiber. This system will be presented in the second part of the thesis. The second system considered, the SqOPO, has been developed in Canberra. It is a square piece of crystal of Lithium Niobate acting as a ring cavity with four total internal reflections on the four faces of the square. The coupling with this system is made with frustrated total internal reflection with two prisms brought into the evanescent field of the resonator. This system will be described in the third part.

But because these two systems applied a few advanced concepts of optics, this first part will provide the reader with an introduction to the necessary concepts to understand this thesis. We will start by introducing the notion of general wave propagation, and then apply it to isotropic linear material, to anisotropic material, and to non linear materials. Then we will consider interface behavior and cavities concepts. And finally we will consider the notions of quantum states with squeezed states (Figure 0.1).

Writing Conventions: In this thesis I will be using normal characters for scalar fields like ρ the charge density or q the charge. I will use bold characters for vector

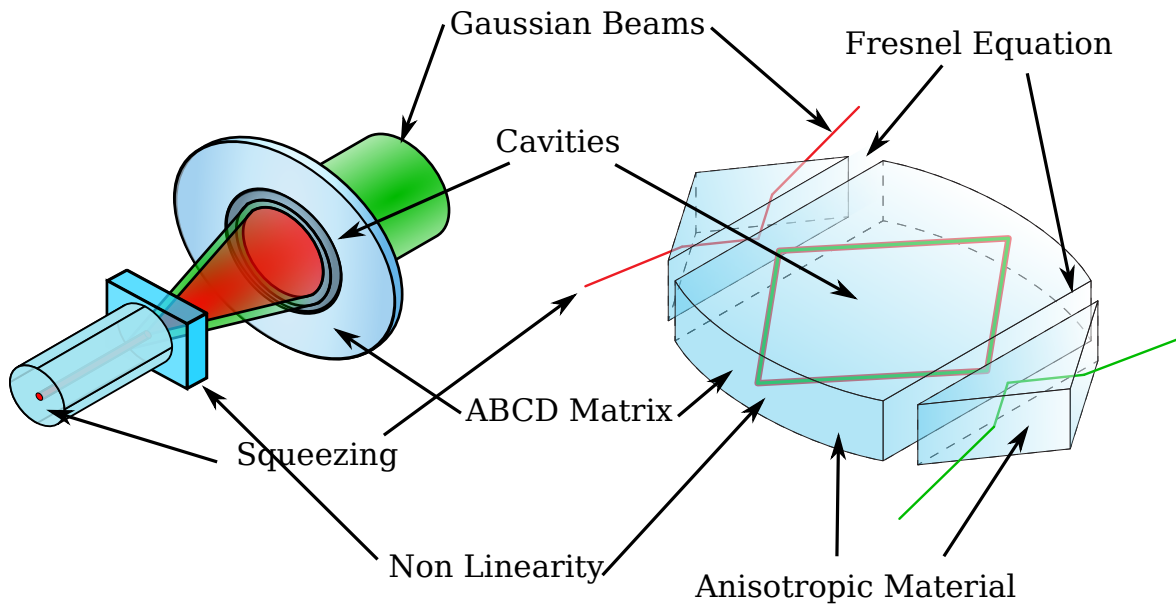


Figure 0.1.: Schematics of the two systems used in this thesis and all the concepts used for each one that will be presented in this introduction.

fields like \mathbf{E} the electric field and \mathbf{B} the magnetic field, I will use bold characters with an over-line for tensors like $\bar{\epsilon}$ the permittivity tensor, and I will use a hat for operators like the creation operator \hat{a}^\dagger .

I will be using Einstein's convention of summing terms with repeated indices, I will use the Kronecker tensor δ_{ij} and I will call the two lights used in this thesis: 1064nm light red light or sub-harmonic for the light at the wavelength of 1064nm; and 532nm light, green light or pump for the light at the wavelength of 532nm.

1. Introduction

1.1. The Maxwell Equations and the Wave Equations

We start this thesis by enunciating the four Maxwell equations [13]. These describe, the behavior of the electric field, \mathbf{E} ; the magnetic field, \mathbf{B} ; the electric displacement field, $\mathbf{D} = \epsilon_0 \mathbf{E} + \mathbf{P}$; and the magnetizing field, $\mathbf{H} = \frac{1}{\mu_0} \mathbf{B}$. Here, \mathbf{P} is the polarization field due to fixed charges of the material, and ϵ_0 and μ_0 are, respectively, the permittivity and the permeability of free space. The equations are:

$$\begin{array}{ll} \text{Maxwell-Gauss} & \text{Maxwell-Faraday} \\ \nabla \cdot \mathbf{D} = \rho_f, & \nabla \times \mathbf{E} = -\frac{\partial \mathbf{B}}{\partial t}, \\ \text{Maxwell-Thomson} & \text{Maxwell-Ampère} \\ \nabla \cdot \mathbf{B} = 0, & \nabla \times \mathbf{H} = \mathbf{j}_f + \frac{\partial \mathbf{D}}{\partial t}, \end{array} \quad (1.1)$$

where \mathbf{j}_f is the free current density, and ρ_f is the free charge density.

By applying the Curl to the Maxwell-Faraday equation and using the Maxwell-Ampère equation to eliminate the magnetic field in the assumption that there is no free current, i.e. $\mathbf{j}_f = 0$, we obtain the wave equation:

$$\nabla \times (\nabla \times \mathbf{E}) = -\frac{\partial (\nabla \times \mathbf{B})}{\partial t} = -\frac{1}{c^2} \frac{\partial^2 \mathbf{E}}{\partial t^2} - \mu_0 \frac{\partial^2 \mathbf{P}}{\partial t^2}, \quad (1.2)$$

where $c = \frac{1}{\sqrt{\epsilon_0 \mu_0}}$ is the speed of light in the vacuum.

By using the expression $\nabla \times (\nabla \times \mathbf{E}) = \nabla(\nabla \cdot \mathbf{E}) - \Delta \mathbf{E}$, we obtain an other form of the wave equation:

$$\nabla(\nabla \cdot \mathbf{E}) - \Delta \mathbf{E} = -\frac{1}{c^2} \frac{\partial^2 \mathbf{E}}{\partial t^2} - \mu_0 \frac{\partial^2 \mathbf{P}}{\partial t^2}, \quad (1.3)$$

where Δ , the Laplace operator, is given by $(\Delta \mathbf{A})_i = \nabla \cdot (\nabla A_i)$.

1.2. Energy Considerations

Consider some free charges $\{q_{f,i}\}$ moving at speed $\{\mathbf{v}_i\}$ in an electromagnetic field $\{\mathbf{E}, \mathbf{B}\}$ in matter. The charges experience a force $\mathbf{f}_i = q_i(\mathbf{E} + \mathbf{v}_i \wedge \mathbf{B})$, which corresponds to a power $P = q_i \mathbf{v}_i \cdot \mathbf{E}$. The density of electric power on the free charges is given by:

$$\mathcal{P} = \mathbf{j}_f \cdot \mathbf{E}$$

It is the energy held by the free charges in the field.

By using the Maxwell-Ampère equation, the property: $\nabla \cdot (\mathbf{E} \times \mathbf{B}) = \mathbf{B} \cdot (\nabla \times \mathbf{E}) - \mathbf{E} \cdot (\nabla \times \mathbf{B})$ and Maxwell-Faraday we obtain the Poynting Theorem [16] describing the electromagnetic energy conservation:

$$\frac{\partial u}{\partial t} + \text{div}(\mathbf{\Pi}) = -\mathbf{j}_f \cdot \mathbf{E}$$

Where $\mathbf{\Pi} = \mathbf{E} \times \mathbf{H}$ is the Poynting vector and $u = \frac{1}{2}(\mathbf{E} \cdot \mathbf{D} + \mathbf{B} \cdot \mathbf{H})$ is the electromagnetic energy density.

The change in electromagnetic energy is equal to a flux described by the Poynting vector and a source term given by the energy held by the free charges.

1.3. Fourier Transforms

The Maxwell equations are a bit complicated to use directly, but a good simplification of them can be achieved by using Fourier transforms. It allows us to solve the field equations in the Fourier domain and come back to the field in the time domain with an inverse transformation. For a field $\mathbf{E}(\mathbf{r}, t)$, and its Fourier transform in time $\mathbf{E}(\mathbf{r}, \omega)$, the two field vectors are related by

$$\mathbf{E}(\mathbf{r}, \omega) = \frac{1}{\pi} \int_{-\infty}^{+\infty} \mathbf{E}(\mathbf{r}, t) \exp(i\omega t) dt \quad \text{and} \quad \mathbf{E}(\mathbf{r}, t) = \frac{1}{2} \int_{-\infty}^{+\infty} \mathbf{E}(\mathbf{r}, \omega) \exp(-i\omega t) d\omega . \quad (1.4)$$

In this thesis, the field $\mathbf{E}(\mathbf{r}, t)$ is a real field, so $\mathbf{E}(\mathbf{r}, \omega)$ satisfies the property $\mathbf{E}(\mathbf{r}, \omega) = \mathbf{E}^*(\mathbf{r}, -\omega)$. Thanks to this it is possible to restrain ourselves to positive frequency values and take the real part of the complex field:

$$\mathbf{E}(\mathbf{r}, t) = \Re \left\{ \int_0^{\infty} \mathbf{E}(\mathbf{r}, \omega) \exp(-i\omega t) d\omega \right\} . \quad (1.5)$$

It is also possible to extend the Fourier transform to the spatial coordinate by using the wave vector space \mathbf{k} :

$$\mathbf{E}(\mathbf{k}, \omega) = \frac{1}{(2\pi)^3} \int \mathbf{E}(\mathbf{r}, \omega) \exp(-i\mathbf{k}\cdot\mathbf{r}) d\mathbf{r} \quad \text{and} \quad \mathbf{E}(\mathbf{r}, \omega) = \int \mathbf{E}(\mathbf{k}, \omega) \exp(i\mathbf{k}\cdot\mathbf{r}) d\mathbf{k} . \quad (1.6)$$

The sign convention is inverted for space and time to make the field with one single positive frequency ω and one single wave vector \mathbf{k} propagate in the direction of \mathbf{k} . We call this particular solution a plane wave.

The real field in function of the complete Fourier transform in space and time is given by

$$\boxed{\mathbf{E}(\mathbf{r}, t) = \Re \left\{ \int_0^\infty \int_{\mathbb{R}^3} \mathbf{E}(\mathbf{k}, \omega) \exp(-i\omega t) \exp(i\mathbf{k}\cdot\mathbf{r}) d\mathbf{k} d\omega \right\}} \quad (1.7)$$

where $\mathbf{E}(\mathbf{k}, \omega)$ is the Fourier transform of the field in space and time. It can be seen as a superposition of waves with a particular distribution $\mathbf{E}(\mathbf{k}, \omega)$. Because of the linearity of the Maxwell equations, it is possible to only consider propagations of single waves and to add them weighted by the distribution $\mathbf{E}(\mathbf{k}, \omega)$ to obtain the propagation of the real field. (Eq. 1.7). We can consider the field of a wave to be

$$\mathbf{E}(\mathbf{r}, t) = \boldsymbol{\mathcal{E}}_0 \exp(-i\omega t) \exp(i\mathbf{k}\cdot\mathbf{r}) + c.c \quad (1.8)$$

with $\boldsymbol{\mathcal{E}}_0$ the amplitude vector of the wave. In this regime, the Maxwell equations become:

$$\begin{array}{ll} \text{Maxwell-Gauss} & \text{Maxwell-Faraday} \\ \mathbf{k} \cdot \mathbf{D} = \rho_f & \mathbf{k} \times \mathbf{E} = i\omega \mathbf{B} \\ \text{Maxwell-Thomson} & \text{Maxwell-Ampère} \\ \mathbf{k} \cdot \mathbf{B} = 0 & \mathbf{k} \times \mathbf{H} = \mathbf{j}_f - i\omega \mathbf{D} \end{array} , \quad (1.9)$$

and the wave equation (Eq. 1.3) becomes

$$-(\mathbf{k} \cdot \mathbf{E})\mathbf{k} = \left(\frac{\omega^2}{c^2} - k^2 \right) \mathbf{E} + \mu_0 \omega^2 \mathbf{P}. \quad (1.10)$$

1.4. Dielectric Medium and the Wave Equation

In a dielectric material, without any electric field for a sufficient period of time, the polarization of the material, \mathbf{P} , will be equal to zero. The polarization field $\mathbf{P}(\mathbf{r}, t)$ is a function of the electric field \mathbf{E} , but the response is not necessarily instantaneous; rather, it will depend on every component of $\mathbf{E}(\mathbf{r}, t')$ at every value of the time, $t' < t$. The Taylor series expansion of the polarization will be given by:

$$\begin{aligned}
 P_i(t) = & \quad \varepsilon_0 \int \chi_{ij}^1(t - \tau) E_j(\tau) d\tau \\
 & + \varepsilon_0 \iint \chi_{ijk}^2(t - \tau_1, t - \tau_2) E_j(\tau_1) E_k(\tau_2) d\tau_1 d\tau_2 \\
 & + \dots \\
 & + \varepsilon_0 \iiint \chi_{ij_1 \dots j_N}^N(t - \tau_1, \dots, t - \tau_N) E_{j_1}(\tau_1) \dots E_{j_N}(\tau_N) d\tau_1 d\tau_2 \dots d\tau_N \\
 & + \dots
 \end{aligned}
 ,$$

with $\chi_{ij_1 \dots j_N}^N$ representing the susceptibility of order N , a tensor of order $N + 1$ with each coefficient a function of $N + 1$ variables corresponding to the dependence in time of each electric component in the decomposition. For the purpose of this thesis, we will restrain ourselves to the two first terms of the decomposition, $\chi_{ij}^1(t_1)$ and $\chi_{ijk}^2(t_1, t_2)$.

In the Fourier domain, we obtain:

$$P_i(\omega) = \varepsilon_0 \chi_{ij}^1(\omega) E_j(\omega) + \varepsilon_0 \int \chi_{ijk}^2(\omega', \omega - \omega') E_j(\omega') E_k(\omega - \omega') d\omega'. \quad (1.11)$$

The demonstration of this calculation is given in Appendix A.

1.4.1. Properties of Susceptibilities

The susceptibility coefficients have to satisfy some symmetry conditions that constrain their values. First, the polarization vector and the field vectors are real vectors, meaning that the quantities $\chi_{ij}^N(t_1, \dots, t_N)$ also have to be real. The Fourier transforms of the first two orders must satisfy

$$\begin{aligned}
 \chi_{ij}^1(\omega) &= \chi_{ij}^1(-\omega)^*, \\
 \chi_{ijk}^2(\omega_1, \omega_2) &= \chi_{ijk}^2(-\omega_1, -\omega_2)^*.
 \end{aligned}$$

A second property of the second order susceptibility is obtained from intrinsic symmetry. It corresponds to the fact that it doesn't matter which field is the first and which one is the second in Eq. 1.11, it gives:

$$\chi_{ijk}^2(\omega_1, \omega_2) = \chi_{ikj}^2(\omega_2, \omega_1).$$

This particularity of the notation can cause some confusion. If the two frequencies considered are equal, we will get $P(2\omega) = \chi_{ijk}^2(\omega, \omega)E^2(\omega)$, but if the frequencies are not equal, we will obtain $P(\omega_1 + \omega_2) = 2\chi_{ijk}^2(\omega_1, \omega_2)E(\omega_1)E(\omega_2)$. The factor two comes from the possibility of writing $E(\omega_1)E(\omega_2)$ as $E(\omega_2)E(\omega_1)$ in equation (Eq. 1.11).

If the material is considered lossless (which we will suppose for the rest of this calculation) then the first and second order coefficients of the susceptibility need to be real:

$$\chi_{ij}^1(\omega) = \chi_{ij}^1(\omega)^* \quad \chi_{ijk}^2(\omega_1, \omega_2) = \chi_{ijk}^2(\omega_1, \omega_2)^* .$$

There also exist two other symmetry conditions due to the fact that the material is considered to be lossless. It implies that the first order susceptibility is a symmetric tensor,

$$\chi_{ij}^1(\omega) = \chi_{ji}^1(\omega),$$

and that we can permute the frequencies and the coefficients of the second order susceptibility:

$$\chi_{ijk}^2(\omega_1, \omega_2) = \chi_{jik}^2(\omega_1 + \omega_2, -\omega_2) = \chi_{kij}^2(\omega_1 + \omega_2, -\omega_1). \quad (1.12)$$

A demonstration of this is presented in Appendix A. A more complete analysis of the properties of the susceptibility can be found in [4]

2. Light Propagation

2.1. Linear Homogeneous Isotropic (LHI) Behavior

To give the basics of wave propagation, we will first consider the LHI model. This means that we consider a susceptibility which is constant in the medium and given only by the first order in the applied electric field ($\chi^{(N)} = 0$ for $N \geq 2$). Moreover, we suppose the response of the material to be the same in each direction. This means that $\chi^{(1)}$ is a scalar.

$$P_i(\omega) = \varepsilon_0 \chi(\omega) E_i(\omega). \quad (2.1)$$

Maxwell-Gauss equation implies that $\nabla \cdot \mathbf{E} = 0$ in Eq. 1.3, so by expressing the refractive index of the material as $n = \sqrt{1 + \chi}$ we get the LHI wave propagation equation:

$$\Delta \mathbf{E} = \frac{n^2}{c^2} \frac{\partial^2 \mathbf{E}}{\partial t^2}. \quad (2.2)$$

Applying this equation to a single plane wave of frequency ω and wave vector \mathbf{k} , one obtains the expression:

$$k^2 = n^2 \frac{\omega^2}{c^2}$$

Moreover, we have $\nabla \cdot \mathbf{E} = \mathbf{k} \cdot \mathbf{E} = 0$, implying that the vector \mathbf{E} is orthogonal to the vector \mathbf{k} . It is possible to define two vectors $\boldsymbol{\epsilon}_1(\mathbf{k})$ and $\boldsymbol{\epsilon}_2(\mathbf{k})$ orthogonal to \mathbf{k} as a basis for the direction of the electric field.

To characterize the usual coherent beams in free space, we will suppose the light propagating along \mathbf{e}_z , and we will suppose the electric field to be a plane wave with an amplitude slowly varying with the position:

$$\mathbf{E}(x, y, z, t) = \sum_{i=(1,2)} \mathcal{E}_i(x, y, z) e^{ikz - i\omega t} \boldsymbol{\epsilon}_i$$

By using the propagation equation Eq. 2.2 and by supposing $\left| \frac{\partial^2 \mathcal{E}_i}{\partial z^2} \right| \ll \left| k \frac{\partial \mathcal{E}_i}{\partial z} \right|$, which means that the variation of \mathcal{E}_i in z is negligible within the scale of a wavelength, we obtain the paraxial Helmholtz propagation equation for \mathcal{E}_i :

$$\frac{\partial^2 \mathcal{E}_i}{\partial x^2} + \frac{\partial^2 \mathcal{E}_i}{\partial y^2} + 2ik \frac{\partial \mathcal{E}_i}{\partial z} = 0 \quad (2.3)$$

By transforming the x and y coordinates of \mathcal{E}_i to the Fourier domain, we get:

$$-(k_x^2 + k_y^2) \mathcal{E}_i(k_x, k_y, z) + 2ik \frac{\partial \mathcal{E}_i(k_x, k_y, z)}{\partial z} = 0$$

We obtain a solution in the shape:

$$\mathcal{E}_i(k_x, k_y, z) = \mathcal{E}_i(k_x, k_y, 0) e^{-i \frac{k_x^2 + k_y^2}{2k} z} \quad (2.4)$$

More details about propagation solutions for light can be found in [2].

2.1.1. Gaussian Propagation Solution

If we start in the plane at $z = 0$ with a field of Gaussian distribution $\mathcal{E}_i(x, y, 0) = \sqrt{\frac{2}{\pi}} \frac{\mathcal{E}_0}{w_0} e^{-\frac{x^2 + y^2}{w_0^2}}$ where w_0^2 is the variance of this distribution, and \mathcal{E}_0 , the amplitude of this distribution ($\int |\mathcal{E}_i(x, y, 0)|^2 dx dy = |\mathcal{E}_0|^2$).

The Fourier distribution of this function is $\mathcal{E}_i(k_x, k_y, 0) = \sqrt{2\pi} w_0 \mathcal{E}_0 e^{-\frac{k_x^2 + k_y^2}{4} w_0^2}$. Using Eq. 2.4 and using the inverse Fourier transform we obtain the expression of the Gaussian beam field:

$$\mathcal{E}_i(x, y, z) = \frac{k \mathcal{E}_0}{\sqrt{2\pi}} \frac{w_0}{iq(z)} e^{ik \frac{x^2 + y^2}{2q(z)}}$$

with $q(z) = z - iz_R$ and $z_R = \frac{kw_0^2}{2}$ the Rayleigh's range.

This Gaussian beam has a waist size in z given by

$$w(z) = w_0 \sqrt{1 + \left(\frac{z}{z_R} \right)^2}$$

The curvature radius of the beam is given by

$$R(z) = z + \frac{z_R^2}{z},$$

and the phase shift that the beam is experienced in function of z is:

$$\psi(z) = \arctan\left(\frac{z}{z_R}\right).$$

The coefficient q can be expressed in function of the waist and the curvature by:

$$\frac{1}{q(z)} = \frac{1}{R(z)} + i \frac{2}{kw^2}. \quad (2.5)$$

2.1.2. High Order Propagation Mode Solutions

In the same way it is possible to propagate a beam given by a Gaussian beam weighted by Hermite polynomials:

$$\mathcal{E}_{i,nm}(x, y, 0) = \mathcal{E}_0 \frac{\sqrt{2^{1-n-m}}}{w_0 \sqrt{\pi m! n!}} H_n\left(\frac{x\sqrt{2}}{w_0}\right) H_m\left(\frac{y\sqrt{2}}{w_0}\right) e^{-\frac{x^2+y^2}{w_0^2}}$$

with H_n the Hermite polynomial given by: $H_n(\xi) = (-1)^n e^{\xi^2} \frac{d^n}{d\xi^n} e^{-\xi^2}$.

Fields having this expression can be seen to be orthogonal: $\int \mathcal{E}_{i,nm}(x, y, 0) \mathcal{E}_{i,kl}(x, y, 0) dx dy = |\mathcal{E}_0|^2 \delta_{nk} \delta_{ml}$. Adding the propagation in the z direction, the field mode reads

$$\mathcal{E}_{i,nm}(x, y, z) = \mathcal{E}_0 \frac{\sqrt{2^{1-n-m}}}{w(z) \sqrt{\pi m! n!}} H_n\left(\frac{x\sqrt{2}}{w(z)}\right) H_m\left(\frac{y\sqrt{2}}{w(z)}\right) e^{ik \frac{(x^2+y^2)}{2q(z)} - i\psi_{nm}(z) + ikz} \quad (2.6)$$

with a generalized phase shift $\psi_{nm}(z) = (1 + n + m) \arctan\left(\frac{z}{z_R}\right)$.

The family of functions $\left\{ u_{nm}(x, y, z) = \frac{\mathcal{E}_{i,nm}(x, y, z)}{\mathcal{E}_0} \right\}_{nm}$ constitutes an orthonormal basis of solution of Eq. 2.3 ($\int |u_{nm}|^2 dx dy = 1$ and $\int |u_{nm} u_{kl}| dx dy = \delta_{nk} \delta_{ml}$). That means that by considering $\{u_{nm}\}$ we can reconstruct any solution of the system.

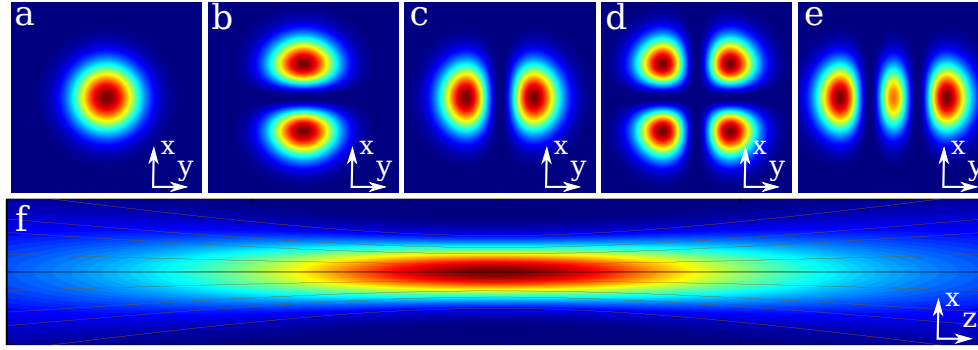


Figure 2.1.: (a) to (e) are transverse Hermitian mode intensities (from left to right TEM00, TEM10, TEM01, TEM11 and TEM02). f) is the intensity projection of a Gaussian beam in a plane containing the propagation axis.

2.1.3. Astigmatism

In the development of Gaussian beams and higher-order modes we supposed a distribution identical in the directions \mathbf{e}_x and \mathbf{e}_y . But it wasn't necessary, it is possible to separate the problem in the direction x and y , The electric field becomes

$$\mathcal{E}_i(x, y, z) = \mathcal{E}_0 u_n^{(x)}(x, z) \cdot u_m^{(y)}(y, z)$$

with $u_n^{(i)}$ such that $\int_{-\infty}^{\infty} u_n^{(i)}(\xi, z) u_m^{(i)*}(\xi, z) d\xi = \delta_{nm}$ given by:

$$u_n^{(i)}(\xi, z) = \frac{H_n\left(\frac{\sqrt{2}\xi}{w_i(z)}\right) e^{\frac{ik\xi^2}{2q_i(z)}}}{\sqrt{w_i(z)} \sqrt{\frac{\pi}{2}} 2^n n!}$$

This decomposition has the same generality than Eq. 2.6, but because it allows to consider modes with different waist size and positions in the direction x and y , it can be more convenient to use in a cavity with non spherical mirrors .

2.1.4. ABCD Matrix

The ABCD matrix method is a convenient way to propagate the light through an optical system based on a ray tracing matrices. The beams of light before and after this system are characterized by two parameters: the distance from the optical axis (x_i and x_o); and the angle relative to this axis (θ_i and θ_o). The optical system is considered as a two dimensional matrix $M = \begin{pmatrix} A & B \\ C & D \end{pmatrix}$ corresponding to the transformation of the two parameters (Figure 2.2).

$$\begin{pmatrix} x_o \\ \theta_o \end{pmatrix} = \begin{pmatrix} A & B \\ C & D \end{pmatrix} \begin{pmatrix} x_i \\ \theta_i \end{pmatrix}$$

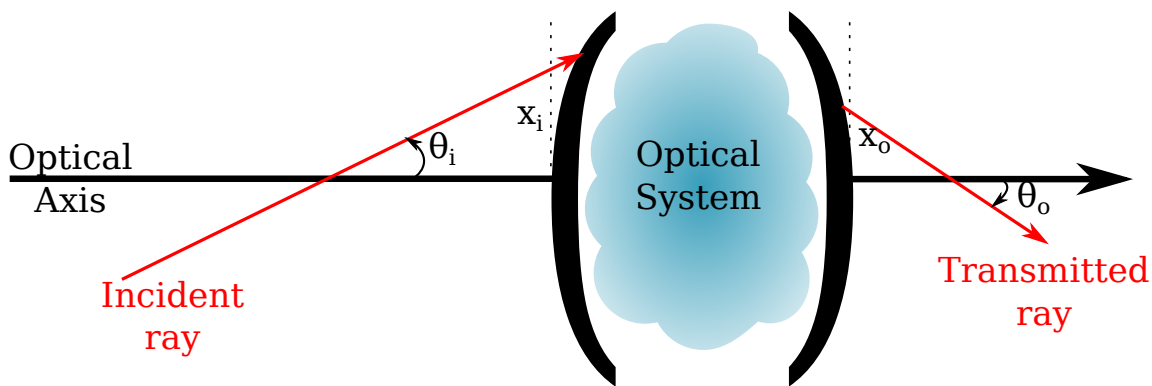


Figure 2.2.: An optical system is analyzed by the transfer matrix between the distance from the optical axis and the angle with the optical axis at the entry of the system (x_i, θ_i) and the same parameters at the output of the system (x_o, θ_o) .

M has to satisfy $\text{Det}(M) = \frac{n_1}{n_2}$ with n_1 and n_2 the indices of the medium before and after the considered optical system.

The ABCD matrices are interesting because they can also be used for propagation of a Gaussian mode, where instead of the pair of parameters (x, θ) , the complex parameter $q(z)$ (Eq. 2.5) is used:

$$q_o = \frac{Aq_i + B}{Cq_i + D}. \quad (2.7)$$

ABCD matrices of several sub-systems $T_1 \dots T_n$ crossed by the beam can be combined together so that they can be considered as a single, bigger system.

$$T_{total} = T_n * \dots * T_1.$$

Table 2.1 presents some of the most common matrices used in this thesis.

As we will see in the section on resonators (section 4.3), in order to have a beam resonating in a cavity, it needs to be identical to itself after a full round trip. Therefore, the ABCD matrix of a round trip applied to the q parameter of a mode needs to give the same value q . More details will be given in the section on cavities (section 4.3). The reader can access more detail on Gaussian beams and ABCD matrices in references [15] and [9].

2.2. Linear Anisotropic Medium

In this part, we will consider a linear material, which means: $\chi^{(2)} = 0$, but this time we will allow the linear susceptibility $\chi_{ij}^{(1)}$ to be a tensor (we will forget the

Matrix	Elements
$\begin{pmatrix} 1 & d \\ 0 & 1 \end{pmatrix}$	Propagation in a medium for a distance d .
$\begin{pmatrix} 1 & 0 \\ -2/R_e & 1 \end{pmatrix}$	Reflection at a curved mirror with an angle θ with the normal.
$\begin{pmatrix} g(\alpha) & 0 \\ 0 & \frac{n_1}{n_2} \frac{1}{g(\alpha)} \end{pmatrix}$	Refraction at a flat surface between two indices n_1 and n_2 with an angle α with the normal.

Table 2.1.: ABCD matrices used in this thesis. $R_e = R \cos(\theta)$ in the tangential plane (horizontal direction), $R_e = R / \cos(\theta)$ in the sagittal plane (vertical direction). For the refraction, $g(\alpha) = \sqrt{\frac{1 - \left(\frac{n_1}{n_2} \sin(\alpha)\right)^2}{\cos^2(\alpha)}}$ where α is the angle between the beam and the normal to the surface.

superscript in the following). The polarization in this birefringent material can be expressed as::

$$P_i(\omega) = \varepsilon_0 \chi_{ij}(\omega) E_j(\omega)$$

We usually use the relative permittivity: $\epsilon_{ij} = \delta_{ij} + \chi_{ij}(\omega)$, to describe the relation between the electric displacement and the electric field $\mathbf{D} = \varepsilon_0 \boldsymbol{\epsilon} \mathbf{E}$.

The susceptibility is symmetric, so the permeability is also symmetric. There exists a basis where the matrix ϵ_{ij} is diagonal.

$$\boldsymbol{\epsilon} = \begin{pmatrix} \varepsilon_x & 0 & 0 \\ 0 & \varepsilon_y & 0 \\ 0 & 0 & \varepsilon_z \end{pmatrix}$$

Where ε_i , $i \in \{x, y, z\}$ are the eigenvalues of $\boldsymbol{\epsilon}$. By analogy with the isotropic case, we get three refractive indices $n_i = \sqrt{\varepsilon_i}$. If all three of the values are equal $n_x = n_y = n_z$, it corresponds to the isotropic case; if only two of them are equal, the material is called uniaxial; and if the all of them are different, it is a biaxial material. In the case of this thesis we will always consider uniaxial birefringence ($n_x = n_e$ and $n_y = n_z = n_o$).

The Maxwell-Gauss $\nabla \cdot \mathbf{D} = 0$ and Maxwell-Thomson $\nabla \cdot \mathbf{H} = 0$ equations imply that the two fields \mathbf{D} and \mathbf{H} are orthogonal to the wave vector \mathbf{k} .

$$\mathbf{k} \cdot \mathbf{D} = 0 \quad \mathbf{k} \cdot \mathbf{H} = 0$$

Note that in this case: $\nabla \cdot \mathbf{E} \neq 0$, the electric field is not necessarily perpendicular to the wave vector.

By returning to the propagation equation Eq. 1.10, and by using the expression of the polarization in function of the electric field \mathbf{E} and the relative permittivity ϵ , we obtain:

$$\mathbf{E}k^2 - (\mathbf{k} \cdot \mathbf{E})\mathbf{k} - \frac{\omega^2}{c^2}\epsilon\mathbf{E} = 0 \quad (2.8)$$

One way to deduce the anisotropic Fresnel equation from there is to rewrite Eq. 2.8 for the three components of the electric field as a function of the components of the wave vector in the basis where ϵ_{ij} is diagonal. The propagation equation reduces to a matrix equation: $A(k, \omega)E = 0$ with A given by:

$$A(k, \omega) = \begin{pmatrix} \frac{\omega^2}{c^2}n_x^2 - k_y^2 - k_z^2 & k_x k_y & k_x k_z \\ k_y k_x & \frac{\omega^2}{c^2}n_y^2 - k_x^2 - k_z^2 & k_y k_z \\ k_z k_x & k_z k_y & \frac{\omega^2}{c^2}n_z^2 - k_x^2 - k_y^2 \end{pmatrix}. \quad (2.9)$$

For a non-trivial solution for the electric field to exist, the determinant of this matrix needs to be zero, $\text{Det}(A) = 0$. In this way, after a bit of calculation, we can obtain the Fresnel anisotropic equation. Another more elegant way to obtain the Fresnel anisotropic equation is to write the electric field E_i in the basis where ϵ_{ij} is diagonal as a function of $\mathbf{k} \cdot \mathbf{E}$:

$$E_i = \frac{(\mathbf{k} \cdot \mathbf{E})k_i}{k^2 - \frac{\omega^2}{c^2}n_i^2} \quad (2.10)$$

Multiplying the left and right sides of Eq. 2.10 by k_i and summing up in terms of i , we get:

$$(\mathbf{k} \cdot \mathbf{E}) = \sum_i \frac{(\mathbf{k} \cdot \mathbf{E})k_i^2}{k^2 - \frac{\omega^2}{c^2}n_i^2} \quad (2.11)$$

By simplifying by $\mathbf{k} \cdot \mathbf{E}$ and since $\{k_i\}$ verify $1 = \frac{1}{k^2} \sum_i k_i^2$, we get the Fresnel equation:

$$\boxed{\frac{n_x^2 k_x^2}{\left(\frac{k}{k_0}\right)^2 - n_x^2} + \frac{n_y^2 k_y^2}{\left(\frac{k}{k_0}\right)^2 - n_y^2} + \frac{n_z^2 k_z^2}{\left(\frac{k}{k_0}\right)^2 - n_z^2} = 0}, \quad (2.12)$$

with $k_0 = \frac{\omega}{c}$.

If we put these three terms in the same denominator and restrict ourselves to an uniaxial material: $n_x = n_e$ and $n_y = n_z = n_o$, we obtain

$$n_e^2 k_x^2 \left(\left(\frac{k}{k_0} \right)^2 - n_o^2 \right) \left(\left(\frac{k}{k_0} \right)^2 - n_o^2 \right) + n_o^2 (k_y^2 + k_z^2) \left(\left(\frac{k}{k_0} \right)^2 - n_e^2 \right) \left(\left(\frac{k}{k_0} \right)^2 - n_o^2 \right) = 0. \quad (2.13)$$

Eq. 2.13 has two solutions for \mathbf{k} , the first one is given by $k^2 = n_o^2 k_0^2$, with no constrain yet on the direction. It is the ordinary beam wave vector.

The second one is obtained by simplifying Eq. 2.13 by $\left(\left(\frac{k}{k_0} \right)^2 - n_o^2 \right)$ and by noticing that the coefficient in $\left(\frac{k}{k_0} \right)^2$ in the new equation is $n_o^2 (k_y^2 + k_z^2 + k_x^2) = n_o^2 k^2$. we obtain:

$$\frac{k_x^2}{n_o^2} + \frac{k_y^2 + k_z^2}{n_e^2} = k_0^2 \quad (2.14)$$

which is the equation obeyed by the extraordinary beam wave vector.

If the wave vector is real and its components satisfy: $k_x = nk_0 \cos(\theta)$ and k_y and k_z such that: $k_y^2 + k_z^2 = nk_0 \sin(\theta)$ with n the index that this field experiences and θ the angle between the wave vector and the extraordinary axis of the crystal, Eq. 2.14 become the regular expression from text books giving n in function of θ :

$$\frac{\cos^2(\theta)}{n_o^2} + \frac{\sin^2(\theta)}{n_e^2} = \frac{1}{n^2}$$

2.2.1. Ordinary Beam

In direction \mathbf{e}_j where $j \in \{x, y\}$ such as $k^2 - \frac{\omega^2}{c^2} n_j^2 \neq 0$ we derive from Eq. 2.10 that:

$$(\mathbf{k} \cdot \mathbf{E}) = 0$$

The ordinary beam is orthogonal to the wave vector $\mathbf{E}_o \perp \mathbf{k}$. Similarly, supposing that $n \neq n_o$, so $k^2 - \frac{\omega^2}{c^2} n_o^2 \neq 0$, Eq. 2.10 in direction e_x also shows that $E_x = 0$, so the ordinary polarization is also perpendicular to the extraordinary axis $\mathbf{E}_o \perp \mathbf{e}_x$. We obtain

$$\mathbf{E}_o \sim \begin{pmatrix} 0 \\ k_z \\ -k_y \end{pmatrix}.$$

We have also $\mathbf{D}_o = \varepsilon_0 n_o^2 \mathbf{E}_o$, and the Poynting vector $\mathbf{\Pi} = \mathbf{E} \times \mathbf{H}$ parallel to the wave vector: $\mathbf{\Pi} \parallel \mathbf{k}$.

2.2.2. Extraordinary Beam

The electric displacement is perpendicular to the wave vector $\mathbf{D}_e \cdot \mathbf{k} = \mathbf{D}_o \cdot \mathbf{k} = 0$, and the extraordinary beam and the ordinary beam are orthogonal polarizations: $\mathbf{D}_e \cdot \mathbf{D}_o = 0$. Since the Fresnel equation Eq. 2.12 can be interpreted as a scalar product of the wave vector \mathbf{k} and a vector $\mathbf{d} = \frac{n_e^2 k_x}{\left(\frac{k}{k_0}\right)^2 - n_e^2} \mathbf{e}_x + \frac{n_o^2 k_y}{\left(\frac{k}{k_0}\right)^2 - n_o^2} \mathbf{e}_y + \frac{n_o^2 k_z}{\left(\frac{k}{k_0}\right)^2 - n_o^2} \mathbf{e}_z$, $\mathbf{d} \cdot \mathbf{k} = 0$, and we can notice that $\mathbf{d} \perp \mathbf{D}_o$, we obtain that \mathbf{D}_e is parallel to \mathbf{d} :

$$\mathbf{D}_e \sim \begin{pmatrix} \frac{n_e^2 k_x}{\left(\frac{k}{k_0}\right)^2 - n_e^2} \\ \frac{n_o^2 k_y}{\left(\frac{k}{k_0}\right)^2 - n_o^2} \\ \frac{n_o^2 k_z}{\left(\frac{k}{k_0}\right)^2 - n_o^2} \end{pmatrix}.$$

Knowing that $\mathbf{E} = \frac{\varepsilon^{-1}}{\varepsilon_0} \mathbf{D}$, we get:

$$\mathbf{E}_e \sim \frac{1}{\varepsilon_0} \begin{pmatrix} \frac{k_x}{\left(\frac{k}{k_0}\right)^2 - n_e^2} \\ \frac{k_y}{\left(\frac{k}{k_0}\right)^2 - n_o^2} \\ \frac{k_z}{\left(\frac{k}{k_0}\right)^2 - n_o^2} \end{pmatrix}.$$

2.2.3. Dispersion Angle

It can be useful to know the angle between the electric field \mathbf{E} and the displacement field \mathbf{D} . This angle is also the angle between the Poynting vector and the wave vector:

$$\tan(\alpha) = \frac{|\mathbf{E}_e \times \mathbf{D}_e|}{\mathbf{E}_e \cdot \mathbf{D}_e} = \frac{(n_o^2 - n_e^2) \sqrt{k_y^2 + k_z^2}}{n_e^2 + n_o^2 \left(\frac{k_y^2 + k_z^2}{k_x^2}\right) k_x}$$

More details can be find in [17] and [18], and a good useful summary in [78].

2.3. Non Linear Medium

2.3.1. Propagation Equation

In this section, we will consider nonlinear material $\chi^2 \neq 0$, but for the sake of simplicity, we will consider the linear susceptibility to be a scalar $\chi_{ij}^1 = \chi^1 \delta_{ij}$ to avoid the problems of birefringence. In practice, it will not be true, but as long as we consider only polarizations of the beams in the axis of the crystal, it is good enough to consider the index of this specific polarization direction and to momentarily pretend the case to be isotropic. We return to the wave equation of propagation from the introduction:

$$\nabla(\nabla \cdot \mathbf{E}(\mathbf{r}, t)) - \Delta \mathbf{E}(\mathbf{r}, t) = -\frac{1}{c^2} \frac{\partial^2 \mathbf{E}(\mathbf{r}, t)}{\partial t^2} - \mu_0 \frac{\partial^2 \mathbf{P}(\mathbf{r}, t)}{\partial t^2}, \quad (2.15)$$

In most literatures, the first term is neglected. It is equivalent to neglect the contribution of the non-orthogonal field to the wave vector which is usually very small. Taking the Fourier Transform in time of Eq. 2.15 and decomposing the polarization into linear and non linear terms: $\mathbf{P} = \mathbf{P}^{(1)} + \mathbf{P}^{(2)}$, we obtain:

$$\Delta \mathbf{E}(\mathbf{r}, \omega) = -\frac{\omega^2}{c^2} \mathbf{E}(\mathbf{r}, \omega) - \mu_0 \omega^2 (\mathbf{P}^{(1)}(\mathbf{r}, \omega) + \mathbf{P}^{(2)}(\mathbf{r}, \omega)),$$

We can get rid of the linear term of the polarization by considering the linear permittivity of the material $\epsilon = n^2$. We can project the equation on a basis orthogonal to the direction of the field \mathbf{E} considered and use the non linear susceptibility. We can simplify the non linear polarization in Eq. 1.11 by considering only three frequencies ω_1 , ω_2 and $\omega_3 = \omega_1 + \omega_2$, and only one polarization at each frequency. We need only to consider the component of the second order susceptibility which links these three frequencies together. We will express this as d_{eff} . The non linear polarization is given by:

$$P^{(2)}(\omega) = \epsilon_0 d_{eff} E(\omega_1) E(\omega_2) \quad (2.16)$$

The propagation equation Eq. 1.3 becomes:

$$\Delta E(\mathbf{r}, \omega_i) = -\frac{\omega_i^2}{c^2} n(\omega_i) E(\mathbf{r}, \omega_i) - \mu_0 \omega_i^2 P^{(2)}(\mathbf{r}, \omega_i).$$

In the same way as in linear optics Eq. 2.1, we consider the propagation of the beam mostly in the direction \mathbf{e}_z , and the field to have the shape:

$$E(\omega_i, x, y, z) = \mathcal{E}(\omega_i, x, y, z) e^{ik_i z}$$

Where $\mathcal{E}(\omega_i, x, y, z)$ is the slowly varying amplitude. It means $k_i^2 = \frac{\omega_i^2}{c^2}n(\omega_i)$.

The paraxial approximation, $\left| \frac{\partial^2 \mathcal{E}}{\partial z^2} \right| \ll \left| k \frac{\partial \mathcal{E}}{\partial z} \right|$, gives the paraxial non linear equation:

$$\Delta_{\perp} \mathcal{E}(\omega_i, \mathbf{r}_{\perp}, z) + 2ik_i \frac{\partial \mathcal{E}(\omega_i, \mathbf{r}_{\perp}, z)}{\partial z} = -\omega_i^2 \mu_0 P^{(2)}(\omega_i, \mathbf{r}_{\perp}, z) e^{-ik_i z} \quad (2.17)$$

Where $\Delta_{\perp} = \frac{\partial^2}{\partial x^2} + \frac{\partial^2}{\partial y^2}$. and $\mathbf{r}_{\perp} = x\mathbf{e}_x + y\mathbf{e}_y$.

To obtain a general solution, we can use the solutions of the paraxial Helmholtz equation : $\Delta_{\perp} u_{nm}^i(\mathbf{r}_{\perp}, z) + 2ik_i \frac{\partial u_{nm}^i(\mathbf{r}_{\perp}, z)}{\partial z} = 0$ where $u_{nm}^i(\mathbf{r}_{\perp}, z)$ forms a set of orthonormal basis by satisfying: $\iint dx dy u_{nm}^{i*}(\mathbf{r}_{\perp}, z) u_{pl}^i(\mathbf{r}_{\perp}, z) = \delta_{np} \delta_{ml}$, and use the decomposition of the electric field in this basis:

$$\mathcal{E}(\omega_i, \mathbf{r}_{\perp}, z) = \sum_{lm} A_{lm}^i(z) u_{lm}^i(\mathbf{r}_{\perp}, z)$$

where $A_{lm}^i(z)$ is the amplitude of the electric field on the mode (l, m) .

However, for the purposes of this thesis, we will restrain ourselves to Gaussian beams with a waist in $z = 0$, so

$$u^i(\mathbf{r}_{\perp}, z) = u_{00}^i(\mathbf{r}_{\perp}, z) = \sqrt{\frac{k_i z_{R_i}}{\pi}} * \frac{i}{q(z)} \exp\left(i \left[\frac{k_i r^2}{2q(z)} \right]\right),$$

where $q(z) = z - iz_{R_i}$ and z_{R_i} is the Rayleigh length of the beam.

The electric field is given by:

$$\mathcal{E}(\omega_i, \mathbf{r}_{\perp}, z) = A^i(z) u^i(\mathbf{r}_{\perp}, z)$$

The paraxial equation Eq. 2.17 becomes:

$$\frac{\partial A^i(z)}{\partial z} = i \frac{\omega_i^2 \mu_0}{2k_i} \iint dx dy u^{i*}(\mathbf{r}_{\perp}, z) P^{(2)}(r, z, \omega_i) e^{-ik_i z}. \quad (2.18)$$

By substituting the non linear polarization term in Eq. 2.18 for Eq. 2.16, and by considering $\omega_1 = \omega_2 = \omega$, we get a system of two coupling equations for A^{ω} , the field at frequency ω , and $A^{2\omega}$, the field at the frequency 2ω .

$$\begin{cases} \frac{\partial A^{\omega}(z)}{\partial z} &= i \frac{\omega}{2n_{\omega} c} d_{eff} \Lambda(z) A^{2\omega}(z) A^{\omega*}(z) e^{-i\Delta k z} \\ \frac{\partial A^{2\omega}(z)}{\partial z} &= i \frac{\omega}{n_{2\omega} c} d_{eff} \Lambda(z)^* A^{\omega}(z) A^{\omega*}(z) e^{i\Delta k z} \end{cases} \quad (2.19)$$

where $\Lambda(z) = \iint dx dy u^{2\omega}(\mathbf{r}, z) u^\omega(\mathbf{r}, z)^* u^\omega(\mathbf{r}, z)^*$, $\Delta k = 2k_\omega - k_{2\omega}$; n_ω and $n_{2\omega}$ the refractive indices of beams at frequencies ω and 2ω .

We have $n_\omega \approx n_{2\omega} = n$ which makes $k_{2\omega} \approx 2k_\omega$. We also consider the Rayleigh length of the beam at frequencies 2ω and ω to be equal. We denote it z_R . (In practice, we consider only doubly resonant OPOs, so the Rayleigh lengths are defined by the cavities.)

The calculation of the integral in Λ gives:

$$\Lambda(z) = \frac{-1}{w_{0\omega} \sqrt{\pi}} \frac{z_R}{Z_R - iz}.$$

More detail can be find in [5].

2.3.2. Second Harmonic Generation

Second harmonic generation (SHG) is the process of starting with a beam of frequency ω (the pump) and generating another beam of frequency 2ω . We assume we will start with no light at 2ω and we will solve the equations Eq. 2.19.

It is interesting to observe first what is the evolution of the SHG with Δk . The optimization of this parameter corresponds to the phase matching conditions. In practice it is always very important to maximize this parameter to achieve the maximum of non linearity. For plane waves, phase matching conditions correspond to $\Delta k = 0$. It can be achieved by tilting the crystal compared to the beam, changing the temperature of the crystal, or applying a voltage on the crystal. It corresponds to matching the index of refraction of both frequencies: $\Delta k = 2\frac{\omega}{c}(n_{2\omega} - n_\omega) = 0$. Tilting the beam has an inconvenience, in that it adds walk off, which degrades the non linearity, and moreover it is not allowed by the two experimental setups utilized in this thesis, so we will not consider it here.

For a plane wave $z_r = \infty$, we can neglect the z evolution of $\Lambda(z)$. We will also suppose the crystal (from $z = -\frac{l}{2}$ to $z = \frac{l}{2}$) small enough to consider the power of the pump constant $A_\omega(z) = A_\omega(0)$. We use Eq. 2.19 to obtain the SHG field at the end of the crystal ($z = \frac{l}{2}$):

$$A^{2\omega}\left(\frac{l}{2}\right) = i \frac{\omega}{n_{2\omega} c} d_{eff} \Lambda(0)^* |A^\omega|^2 l \text{sinc}\left(\frac{\Delta k l}{2}\right)$$

The power of the light beam is given by: $P = \frac{n\epsilon_0 |A|^2}{2}$:

$$P^{2\omega}\left(\frac{l}{2}\right) = (P^\omega)^2 \frac{2\omega^2 \mu_0}{n^3} d_{eff}^2 |\Lambda(0)|^2 l^2 \text{sinc}^2\left(\frac{\Delta k l}{2}\right)$$

with P^ω the pump power. We have considered here that $n = n_{2\omega} = n_\omega$. A typical plot can be seen in Figure 2.3.

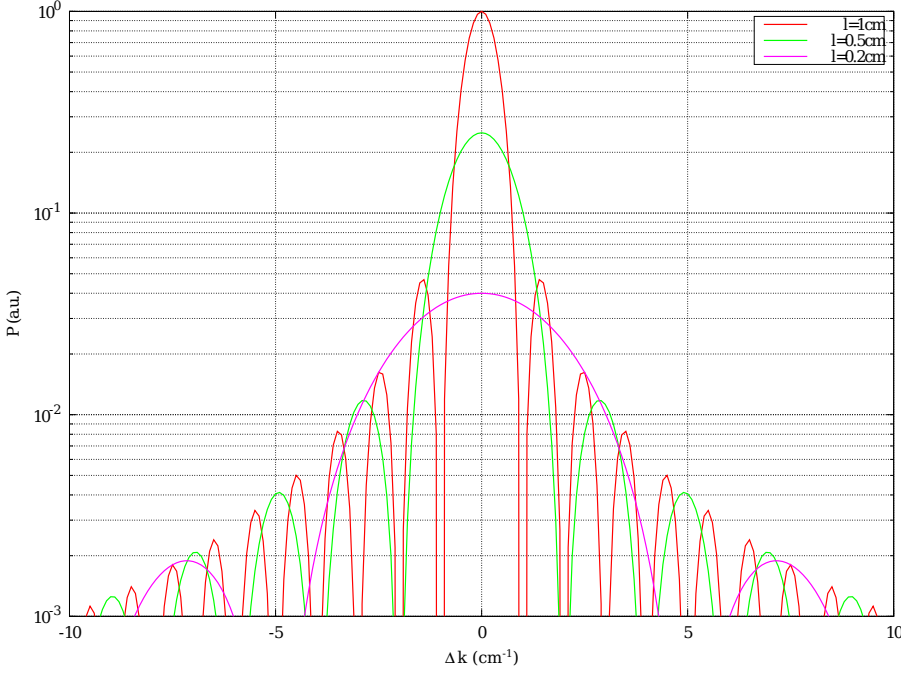


Figure 2.3.: A typical sinc plot of SHG power vs Δk for different lengths of crystal.

When the light is focused in the crystal, it is not possible to neglect the evolution of $\Lambda(z)$ anymore, and the phase conditions change in the crystal. For all lengths of crystal there is an optimal Rayleigh length for the light to maximize the non linearity. The optimization is made in the general case by Boyd and Kleinman [36]

.

For a pump field with a Rayleigh length z_R focused in the middle of the crystal, supposing that the amplitude of the pump is large enough to be considered as constant in the crystal $A^\omega(z) = A^\omega(0)$ and that there is no light at frequency 2ω entering in the crystal (in $z = -\frac{l}{2}$) we can use Eq. 2.19 to obtain the second harmonic power at the end of the crystal ($z = \frac{l}{2}$):

$$A^{2\omega}\left(\frac{l}{2}\right) = \frac{-i\omega^3/2 d_{eff} |A^\omega|^2 \sqrt{l}}{2\sqrt{n\pi}c^{3/2}} H\left(\frac{l}{2z_R}, \Delta k z_R\right)$$

with $H(\xi, \sigma) = \frac{1}{\sqrt{\xi}} \int_{-\xi}^{\xi} \frac{e^{i\sigma\zeta}}{1-i\zeta} d\zeta$. We have considered $n = n_{2\omega} = n_\omega$. The optimization of $H(\xi, \sigma)$ can be found for $\xi = \frac{l}{2z_R} = 2.84$, and $\sigma = z_R \Delta k = 0.57$ with a value of $H = 2.07$. It is interesting to see that the phase matching is no longer $\Delta k = 0$, but because $z_R \gg \lambda$, with λ the wavelength of the light, the hypothesis $n_{2\omega} = n_\omega$ is still valid.

In power, we obtain:

$$P^{2\omega}\left(\frac{l}{2}\right) = \left(P^{2\omega}\right)^2 \frac{\omega^3 \mu_0 d_{eff}^2 l}{2n^2 c \pi} H^2\left(\frac{l}{2z_R}, \Delta k z_R\right)$$

2.3.3. Degenerate Parametric Amplification

Degenerate parametric amplification is the inverse process of SHG. We consider a beam with frequency 2ω (the pump) with a high power that we can consider to be constant across the entire crystal $A^{2\omega}(z) = A^{2\omega}(0)$. To apply the above equation, it is necessary to have a seed A^ω (the signal) at the input of the crystal, otherwise there is no amplification. In practice, the quantum fluctuation of the vacuum is able to work as a seed and to be amplified by this process. Obviously, the same arguments as for SHG can be applied to the optimal focusing of the beam in the crystal, but for the sake of simplifying the expression, we will consider only the case where $z \ll z_R$, which makes $\Lambda(z)$ a constant equal to $\Lambda = \frac{-1}{w_{0\omega}\sqrt{\pi}}$, and where $\Delta k = 0$. The second equation of Eq. 2.19 gives:

$$\frac{\partial A^\omega(z)}{\partial z} = -\frac{ie^{i\phi^{2\omega}}}{z_c} A^{\omega*}(z)$$

with $\frac{1}{z_c} = \frac{\omega d_{eff}}{2n_\omega c w_{0\omega} \sqrt{\pi}} |A^{2\omega}| = \frac{\omega d_{eff}}{c w_{0\omega} n_\omega^{3/2} \sqrt{2\varepsilon_0 \pi}} \sqrt{P^{2\omega}}$ and $\phi^{2\omega}$ such that $A^{2\omega} = |A^{2\omega}| e^{i\phi^{2\omega}}$.

By deriving a second time we obtain:

$$\frac{d^2 A_\omega}{dz^2} = \frac{1}{z_c^2} A_\omega$$

which has the solutions:

$$A_\omega = A_\omega(z=0) e^{i\frac{\pi/2 - \Delta\phi}{2}} \left(\cos\left(\frac{\pi/2 - \Delta\phi}{2}\right) e^{(-\frac{z}{z_c})} + i \sin\left(\frac{\pi/2 - \Delta\phi}{2}\right) e^{(\frac{z}{z_c})} \right) \quad (2.20)$$

with $\Delta\phi = 2\phi^\omega - \phi^{2\omega}$ and ϕ^ω such that $A^\omega(z=0) = |A^\omega(z=0)| e^{i\phi^\omega}$.

If the pump and the signal at the input of the crystal have a difference of phase $\Delta\phi = -\frac{\pi}{2}$, the signal will experience amplification, so the power of the light at ω will increase in the crystal. If the phase difference is $\Delta\phi = \frac{\pi}{2}$, the signal will be de-amplified, and the power will decrease.

More details can be find in [4].

3. Interface Conditions

All the previous calculations in this thesis supposed that the medium in which the light is propagating is always the same. In practice, however, the fields will have to travel between air and different crystals or glass, which are the different prisms and the resonator. It is important to know how the fields will behave at the interfaces.

3.1. Field Interface Conditions

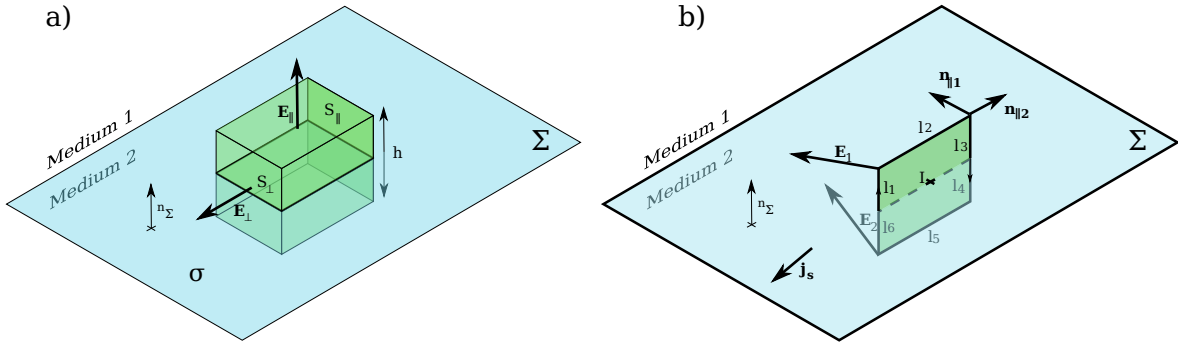


Figure 3.1.: a) The normal field interface conditions are obtained by considering the flux of the fields through an infinitely small box containing the surface Σ with a surface charge σ . b) The tangential field interface conditions are obtained by considering the circulation of the fields in a rectangle crossing the surface Σ with a surface current j_s , and by making the square infinitely small.

3.1.1. Normal Fields

We consider a surface Σ between two media with a surface charge σ . By using the Ostrogradsky theorem on a box Figure 3.1.a containing the surface, and the value of the divergence of a field, and by making the length h and the surface of the box $S_{||}$ go to zero, we obtain the surface conditions for the normal part of this field:

$$\begin{cases} (\mathbf{E}_1 - \mathbf{E}_2) \cdot \mathbf{n}_\Sigma = \varepsilon_0 \sigma \\ (\mathbf{D}_1 - \mathbf{D}_2) \cdot \mathbf{n}_\Sigma = \sigma_f \\ (\mathbf{B}_1 - \mathbf{B}_2) \cdot \mathbf{n}_\Sigma = 0 \end{cases}$$

with σ_f the free surface charge and \mathbf{n}_Σ the normal vector of the surface.

3.1.2. Tangential Fields

In the same way, through using the Stokes theorem on a rectangle crossing the surface Figure 3.1.b , by making all the lengths $l_{1 \rightarrow 6}$ equal and approaching 0 and by using the expression of the **Curl** of a field, we obtain the surface conditions for the tangential part of this field:

$$\begin{cases} (\mathbf{E}_1 - \mathbf{E}_2) \times \mathbf{n}_\Sigma & = & 0 \\ (\mathbf{H}_1 - \mathbf{H}_2) \nu \mathbf{n}_\Sigma & = & \mathbf{j}_{S,\text{free}} \times \mathbf{n}_\Sigma \\ (\mathbf{B}_1 - \mathbf{B}_2) \times \mathbf{n}_\Sigma & = & \mu_0 \mathbf{j}_{S,\text{free}} \times \mathbf{n}_\Sigma \end{cases}$$

3.1.3. Poynting Vector

We use the interface conditions that we just obtained to see how the Poynting vector $\mathbf{\Pi}$ behaves at the interface. With the \mathbf{X}_\parallel the component of a vector \mathbf{X} parallel to the surface, and \mathbf{X}_\perp the tangential component, we can write:

$$\mathbf{\Pi} = \mathbf{E} \times \mathbf{H} = (\mathbf{E}_\parallel + \mathbf{E}_\perp) \times (\mathbf{H}_\parallel + \mathbf{H}_\perp) = \underbrace{\mathbf{E}_\parallel \times \mathbf{H}_\parallel}_{\mathbf{\Pi}_\perp} + \underbrace{\mathbf{E}_\parallel \nu \mathbf{H}_\perp + \mathbf{E}_\perp \times \mathbf{H}_\parallel}_{\mathbf{\Pi}_\parallel}.$$

\mathbf{E}_\parallel is conserved at the interface and \mathbf{H}_\parallel is conserved if the free charges at the interface are zero, which we will always assume to be true in this thesis. So we obtain:

$$\boxed{(\mathbf{\Pi}_1 - \mathbf{\Pi}_2) \times \mathbf{n}_\Sigma = 0}$$

3.2. Fresnel Equations

We consider the interface between two dielectric materials 1 and 2 to be isotropic, or anisotropic but with the principal axis (\mathbf{c}_1 and \mathbf{c}_2) limited to being along one of the axes ($\mathbf{e}_x, \mathbf{e}_y, \mathbf{e}_z$). We suppose an incident field \mathbf{E}_i to be coming from the left and splitting at the interface between a reflected beam \mathbf{E}_r and a transmitted beam \mathbf{E}_t . The different fields are given by:

$$\mathbf{E}_m(\mathbf{r}, t) = \mathbf{E}_{m0} \exp[i\mathbf{k}_m \cdot \mathbf{r} - i\omega t]$$

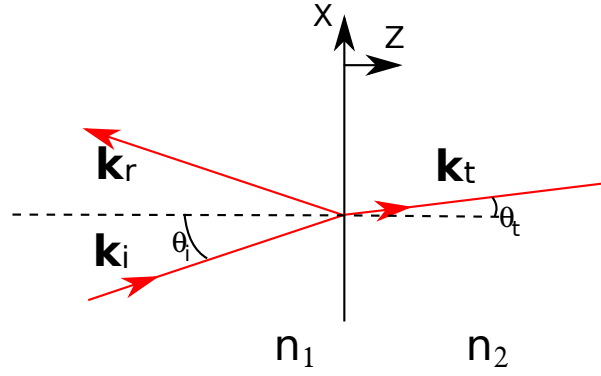


Figure 3.2.: Incident, reflected and transmitted wave vectors k_i , k_r and k_t at the interface between two materials of index n_1 and n_2 .

Where $m = (i, r, t)$. We suppose the propagation of the incident beam to be in the plane $(\mathbf{e}_x, \mathbf{e}_z)$, which means that we have $\mathbf{k}_i \in (\mathbf{e}_x, \mathbf{e}_z)$.

The tangential part of the electric field \mathbf{E}_{\parallel} is conserved at the interface:

$$\mathbf{E}_{i\parallel} + \mathbf{E}_{r\parallel} = \mathbf{E}_{t\parallel}$$

We get for all time t and all points \mathbf{r} on the surface:

$$\mathbf{E}_{i0\parallel} \exp[i\mathbf{k}_i \cdot \mathbf{r} - i\omega_i t] + \mathbf{E}_{r0\parallel} \exp[i\mathbf{k}_r \cdot \mathbf{r} - i\omega_r t] = \mathbf{E}_{t0\parallel} \exp[i\mathbf{k}_t \cdot \mathbf{r} - i\omega_t t]$$

This means that the frequencies of each field are the same $\omega_i = \omega_r = \omega_t$ and that we have equality in the tangential wave vectors $\mathbf{k}_{i\parallel} = \mathbf{k}_{r\parallel} = \mathbf{k}_{t\parallel}$, corresponding to the first law of Snell-Descartes. We suppose that the incident beam is given by:

$$\mathbf{k}_i = \begin{pmatrix} k_{ix} \\ 0 \\ k_{iz} \end{pmatrix}.$$

Knowing that each wave vector verifies: $\|\mathbf{k}_m\| = n_m \frac{\omega}{c}$, with n_m the index experienced by the light in the medium m at this particular polarization, we obtain:

$$\mathbf{k}_r = \begin{pmatrix} k_{ix} \\ 0 \\ -k_{iz} \end{pmatrix} \quad \mathbf{k}_t = \begin{pmatrix} k_{ix} \\ 0 \\ \left[\left(n_2 \frac{\omega}{c} \right)^2 - (k_{ix})^2 \right]^{1/2} \end{pmatrix}.$$

If the incident beam is real, we consider θ_i such that $k_{ix} = n_1 \sin(\theta_i)$ and $k_{iz} = n_1 \cos(\theta_i)$, and if we have the two indices respecting: $\frac{n_1}{n_2} \sin(\theta_i) \leq 1$. We obtain the second Snell-Descartes law:

$$n_1 \sin(\theta_i) = n_2 \sin(\theta_t)$$

with θ_t such that $k_{tx} = n_2 \sin(\theta_t)$ and $k_{tz} = n_2 \cos(\theta_t)$.

If the crystal on the left is isotropic Figure 3.2, we consider the s-polarization with the electric field along \mathbf{e}_y and the p-polarization with the electric field in the plane $(\mathbf{e}_x, \mathbf{e}_z)$ perpendicular to \mathbf{k} . If the crystal is anisotropic with the extraordinary axis \mathbf{c}_1 along \mathbf{e}_y , the problem is the same. The ordinary beam polarization \mathbf{E}_o is perpendicular to the extraordinary axis \mathbf{c}_1 and the wave vector \mathbf{k} , so it is in the plane $(\mathbf{e}_x, \mathbf{e}_z)$ (p-polarization case), and the extraordinary polarization \mathbf{E}_e is along \mathbf{e}_y (s-polarization case) because \mathbf{k} is orthogonal to the extraordinary axis \mathbf{c}_1 (subsection 2.2.3). If the crystal is anisotropic with the extraordinary axis \mathbf{c}_1 along \mathbf{e}_x or \mathbf{e}_z , the ordinary polarization \mathbf{E}_o is perpendicular to the extraordinary axis and \mathbf{k} , so \mathbf{E}_o is along \mathbf{e}_y (s-polarization case), and the extraordinary polarization \mathbf{E}_e is perpendicular to the ordinary polarization, so \mathbf{E}_e is in the plane $(\mathbf{e}_x, \mathbf{e}_z)$ (but $\mathbf{E}_e \perp \mathbf{k}$ is no longer necessarily true).

The same reasoning used on the crystal on the right shows that the s-polarization and p-polarization are good common bases for the problem.

From now on, in calculations, we will omit $\exp(-i\omega t)$ for simplicity.

3.2.1. TE Polarization or S-Polarization

The incident electric field \mathbf{E}_i is supposed to be polarized in the \mathbf{e}_y axis. The three electric fields' expressions are:

$$\begin{cases} \mathbf{E}_i &= E_0 \mathbf{e}_y \exp[i(k_{ix}x + ik_{iz}z)] \\ \mathbf{E}_r &= r_s E_0 \mathbf{e}_y \exp[i(k_{ix}x - ik_{iz}z)] \\ \mathbf{E}_t &= t_s E_0 \mathbf{e}_y \exp[i(k_{ix}x + ik_{tz}z)] \end{cases}, \quad (3.1)$$

with r_s and t_s the reflection and transmission factors.

The continuity of E_{\parallel} gives a first equation:

$$E_0 + r_s E_0 = t_s E_0. \quad (3.2)$$

Maxwell-Faraday equation: $\nabla \times \mathbf{E} = i\omega \mathbf{B}$ gives in the x direction: $\frac{\partial E_y}{\partial z} = -i\omega B_x$. The continuity of B_{\perp} gives the continuity of $\frac{\partial E_y}{\partial z}$, which gives the second equation:

$$k_{iz} E_0 - r_s k_{iz} E_0 = k_{tz} t_s E_0. \quad (3.3)$$

We have two equations with two variables:

$$\begin{cases} 1 + r_s &= t_s \\ k_{iz}(1 - r_s) &= k_{tz}t_s \end{cases} ,$$

These equations can easily be solved and give:

$$\begin{cases} r_s &= \frac{k_{iz} - k_{tz}}{k_{tz} + k_{iz}} \\ t_s &= \frac{2k_{iz}}{k_{tz} + k_{iz}} \end{cases} .$$

If k_{iz} and k_{tz} are real, we can rewrite these coefficients:

$$\begin{cases} r_s &= \frac{n_1 \cos(\theta_i) - n_2 \cos(\theta_t)}{n_2 \cos(\theta_t) + n_1 \cos(\theta_i)} \\ t_s &= \frac{2n_1 \cos(\theta_i)}{n_2 \cos(\theta_t) + n_1 \cos(\theta_i)} \end{cases} .$$

The interesting values to measure are the reflectance $R = \frac{|\Pi_{r\perp}|}{|\Pi_{i\perp}|}$ and transmittance of the system $T = \frac{|\Pi_{t\perp}|}{|\Pi_{i\perp}|}$, with $\Pi_{i\perp}, \Pi_{r\perp}$ and $\Pi_{t\perp}$ the normal components of the incident, the reflected, and the transmitted Poynting vectors $\mathbf{\Pi}_{\perp} = \mathbf{E}_{\parallel} \times \mathbf{H}_{\parallel}$. By using the Maxwell-Faraday equation $\nabla \times \mathbf{E} = -\frac{\partial \mathbf{B}}{\partial t}$ we can calculate the parallel magnetizing field $H_x = -\frac{k_z}{\omega\mu_0} E_y$ and $H_y = 0$.

$$\begin{cases} R &= \frac{|\mathbf{E}_{r\parallel} \times \mathbf{H}_{r\parallel}|}{|\mathbf{E}_{i\parallel} \times \mathbf{H}_{i\parallel}|} = r_s^2 \\ T &= \frac{|\mathbf{E}_{t\parallel} \times \mathbf{H}_{t\parallel}|}{|\mathbf{E}_{i\parallel} \times \mathbf{H}_{i\parallel}|} = t_s^2 \frac{k_{tz}}{k_{iz}} \end{cases} .$$

They represent the reflection and transmission of the energy through the surface. The conservation of energy implies $R + T = 1$.

3.2.2. TM Polarization or P-Polarization

We suppose here that the electric fields \mathbf{E} are in the plane $(\mathbf{e}_x, \mathbf{e}_z)$. For the calculation, we will consider the field \mathbf{H} which is only in the direction \mathbf{e}_y . We will define the same coefficient, but for the \mathbf{H} field instead:

$$\begin{cases} \mathbf{H}_i &= H_0 \mathbf{e}_y \exp[i(k_{ix}x + ik_{iz}z)] \\ \mathbf{H}_r &= r_H H_0 \mathbf{e}_y \exp[i(k_{ix}x - ik_{iz}z)] \\ \mathbf{H}_t &= t_H H_0 \mathbf{e}_y \exp[i(k_{ix}x + ik_{tz}z)] \end{cases}$$

with r_H and t_H the reflection and transmission factors.

There is no free charge at the surface which gives the continuity of \mathbf{H}_{\parallel} :

$$H_0 + r_B H_0 = t_B H_0.$$

For the second equation, we use the Maxwell-Ampère equation: $\nabla \times \mathbf{H} = i\omega \mathbf{D} = i\bar{\epsilon}\omega \mathbf{E}$. If one of the media at least is anisotropic, $\bar{\epsilon}$ is a tensor, but by hypothesis,

it is diagonal. $\bar{\epsilon} = \begin{pmatrix} n_x^2 & 0 & 0 \\ 0 & n_y^2 & 0 \\ 0 & 0 & n_z^2 \end{pmatrix}$. By projecting the equation in the direction \mathbf{e}_x ,

we obtain: $\frac{1}{n_x^2} \frac{\partial H_y}{\partial z} = i\omega \epsilon_0 E_x$. The continuity of E_x implies the continuity of $\frac{1}{n_x^2} \frac{\partial H_y}{\partial z}$. We obtain:

$$\frac{k_{iz}}{n_{x1}^2} H_0 - r_B \frac{k_{iz}}{n_{x1}^2} H_0 = \frac{k_{tz}}{n_{x2}^2} t_B H_0.$$

The two equations of the problem become:

$$\begin{cases} 1 + r_B & = & t_B \\ \frac{k_{iz}}{n_{x1}^2} (1 - r_B) & = & \frac{k_{tz}}{n_{x2}^2} t_B \end{cases}$$

which are easily solved thus:

$$\begin{cases} r_B & = & \frac{n_{x2}^2 k_{iz} - n_{x1}^2 k_{tz}}{n_{x1}^2 k_{tz} + n_{x2}^2 k_{iz}} \\ t_B & = & \frac{2n_{x2}^2 k_{iz}}{n_{x1}^2 k_{tz} + n_{x2}^2 k_{iz}} \end{cases}.$$

If k_{iz} and k_{tz} are real, we can rewrite these coefficients:

$$\begin{cases} r_B & = & \frac{n_2^2 n_1 \cos(\theta_i) - n_1^2 n_2 \cos(\theta_t)}{n_1^2 n_2 \cos(\theta_i) + n_2^2 n_1 \cos(\theta_t)} & = & \frac{n_2 \cos(\theta_i) - n_1 \cos(\theta_t)}{n_1 \cos(\theta_i) + n_2 \cos(\theta_t)} \\ t_B & = & \frac{2n_2^2 n_1 \cos(\theta_i)}{n_1^2 n_2 \cos(\theta_i) + n_2^2 n_1 \cos(\theta_t)} & = & \frac{2n_2 \cos(\theta_i)}{n_1 \cos(\theta_i) + n_2 \cos(\theta_t)} \end{cases}.$$

The Maxwell-Ampère equation allows us to calculate the two coefficients for E_x and E_z : $\frac{1}{n_x^2} \frac{\partial H_y}{\partial z} = i\omega \epsilon_0 E_x$ and $\frac{1}{n_z^2} \frac{\partial H_y}{\partial x} = -i\omega \epsilon_0 E_z$

$$\begin{cases} \mathbf{E}_i & = & \frac{1}{\omega \epsilon_0} \left(\frac{k_{iz}}{n_{x1}^2} \mathbf{e}_x - \mathbf{e}_z \frac{k_{ix}}{n_{z1}^2} \right) H_0 \exp[i(k_{ix}x + ik_{iz}z)] \\ \mathbf{E}_r & = & \frac{-1}{\omega \epsilon_0} \left(\frac{k_{iz}}{n_{x1}^2} \mathbf{e}_x + \mathbf{e}_z \frac{k_{ix}}{n_{z1}^2} \right) r_B H_0 \exp[i(k_{ix}x - ik_{iz}z)] \\ \mathbf{E}_t & = & \frac{1}{\omega \epsilon_0} \left(\frac{k_{tz}}{n_{x2}^2} \mathbf{e}_x - \mathbf{e}_z \frac{k_{ix}}{n_{z2}^2} \right) t_B H_0 \exp[i(k_{ix}x + ik_{tz}z)] \end{cases}$$

$$E_{0i} = \frac{H_0}{\omega \varepsilon_0} \sqrt{\left(\frac{k_{iz}}{n_{x1}^2}\right)^2 + \left(\frac{k_{ix}}{n_{z1}^2}\right)^2}$$

If $n_{x1} = n_{z1}$, we get $E_{0i} = \frac{H_0}{n_x \varepsilon_0 c}$

So we get:

$$\begin{cases} r_p = r_B \\ t_P = t_B \frac{\sqrt{\left(\frac{k_{tz}}{n_{x2}^2}\right)^2 + \left(\frac{k_{ix}}{n_{z2}^2}\right)^2}}{\sqrt{\left(\frac{k_{iz}}{n_{x1}^2}\right)^2 + \left(\frac{k_{ix}}{n_{z1}^2}\right)^2}} \end{cases} .$$

If $n_{x1} = n_{z1}$, and $n_{x2} = n_{z2}$ we get $t_P = t_B \frac{n_{z2}}{n_{x2}}$

The coefficients in energy become:

$$\begin{cases} R = \frac{|\mathbf{E}_{r\parallel} \times \mathbf{H}_{r\parallel}|}{|\mathbf{E}_{i\parallel} \times \mathbf{H}_{i\parallel}|} = r_p^2 \\ T = \frac{|\mathbf{E}_{t\parallel} \times \mathbf{H}_{t\parallel}|}{|\mathbf{E}_{i\parallel} \times \mathbf{H}_{i\parallel}|} = t_p t_B \frac{k_{tz} n_{x1}^2}{k_{iz} n_{x2}^2} \end{cases} .$$

If $n_{x1} = n_{z1}$, and $n_{x2} = n_{z2}$ we get $T_P = t_B^2 \frac{k_{tz} n_{x1}}{k_{iz} n_{x2}}$.

The more simple example of the interface between two isotropic materials can be found in [11] and [6].

4. Cavity

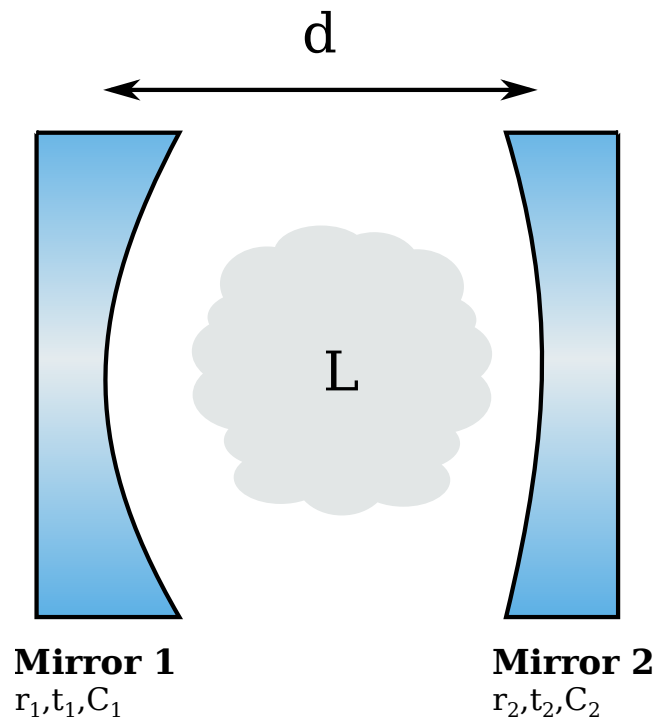


Figure 4.1.: Fabry Perot cavity with two mirrors of reflectivity r_1 and r_2 , transmissivity t_1 and t_2 and curvature radius C_1 and C_2 , with intra-cavity loss L .

Cavities can be used for defining a mode spatially and temporally, like with a mode cleaner, or they can be used to increase and build power (the power inside the cavity being equal to the finesse of the cavity multiplied by the input power). By putting a crystal, or anything interacting with a mode of the cavity, inside it, the interaction increases. For example, putting a material with positive gain in a cavity is the principle of making a laser.

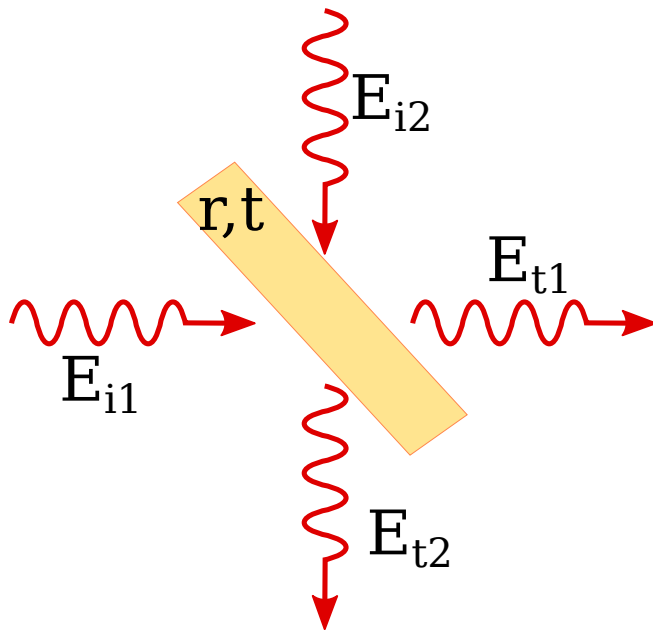


Figure 4.2.: The beam splitter mixes the two input fields. We obtain $E_{t1} = tE_{i1} + rE_{i2}$ and $E_{t2} = -rE_{i1} + tE_{i2}$.

4.1. Beam Splitter Conventions

There are several conventions for beam splitters' transmission and beam splitters' reflection. We will suppose the transmitted and reflected beam to be given by:

$$\begin{cases} E_{t1} &= tE_{i1} + rE_{i2} \\ E_{t2} &= -rE_{i1} + tE_{i2} \end{cases}$$

With this convention, the parameters r and t are real parameters. And the reflectance and transmittance of the beam splitters are given by:

$$\begin{cases} R &= r^2 \\ T &= t^2 \end{cases}$$

4.2. Cavity Transmission

We consider a Fabry Perot cavity with two coupling mirrors with reflectance and transmittance coefficients r_1, t_1 and r_2, t_2 respectively. We suppose the cavity to have absorption losses, which means that the power in the cavity decays as $e^{-\alpha l}$ with l the distance considered and α the linear attenuation coefficient (Figure 4.1). We shine a beam $E_i = E_0 e^{ikx - i\omega t}$ to the left of the cavity (mirror 1). We want to find the transmitted beam E_t going out of (mirror 2) and the reflected beam E_r from (mirror 1). We can obtain them by adding the contributions of all the possible

paths that the light can take before exiting the resonator through one of the mirrors. For the transmitted beam:

$$E_t = E_i \left(t_1 t_2 e^{ikd-\alpha d} \sum_{N=0}^{\infty} (r_1 r_2 e^{2ikd-2\alpha d})^N \right),$$

$$E_t = E_i \left(\frac{t_1 t_2 e^{ikd-\alpha d}}{1 - r_1 r_2 e^{2ikd-2\alpha d}} \right).$$

The intensity of the beam is given by:

$$I_t = |E_t|^2 = I_i \left(\frac{T_1 T_2 e^{-2\alpha d}}{(1 - r_1 e^{-2\alpha d} r_2)^2 + 4r_1 r_2 e^{-2\alpha d} \sin^2(kd)} \right)$$

with $I_i = |E_i|^2$ the intensity of the incident beam, and $T_1 = t_1^2$ and $T_2 = t_2^2$. We use \mathcal{F} the coefficient of finesse given by: $\mathcal{F} = \frac{4r_1 r_2 e^{-2\alpha d}}{(1 - r_1 r_2 e^{-2\alpha d})^2}$. We obtain:

$$I_t = |E_t|^2 = \frac{\mathcal{F} I_i}{4r_1 r_2} \left(\frac{T_1 T_2}{1 + \mathcal{F} \sin^2(kd)} \right).$$

In the same way we can obtain the expression of the reflection beam:

$$E_r = E_i \left(\frac{r_1 - (1 - L_m) r_2 e^{2ikd-2\alpha d}}{1 - r_1 r_2 e^{2ikd-2\alpha d}} \right)$$

Where L_{m1} is the absorption in the first mirror satisfying: $r_1^2 + t_1^2 = 1 - L_{m1}$.

The intensity of the reflected beam is given by:

$$I_r = I_i \left(\frac{(r_1 - (1 - L_m) r_2 e^{-2\alpha d})^2 + 4(1 - L_m) r_1 r_2 e^{-2\alpha d} \sin^2(kd)}{(1 - r_1 r_2 e^{-2\alpha d})^2 + 4r_1 r_2 e^{-2\alpha d} \sin^2(kd)} \right)$$

$$I_r = \mathcal{F} I_i \left(\frac{\left(\frac{r_1 - (1 - L_m) r_2 e^{-2\alpha d}}{4r_1 r_2 e^{-2\alpha d}} \right)^2 + (1 - L_m) \sin^2(kd)}{1 + \mathcal{F} \sin^2(kd)} \right)$$

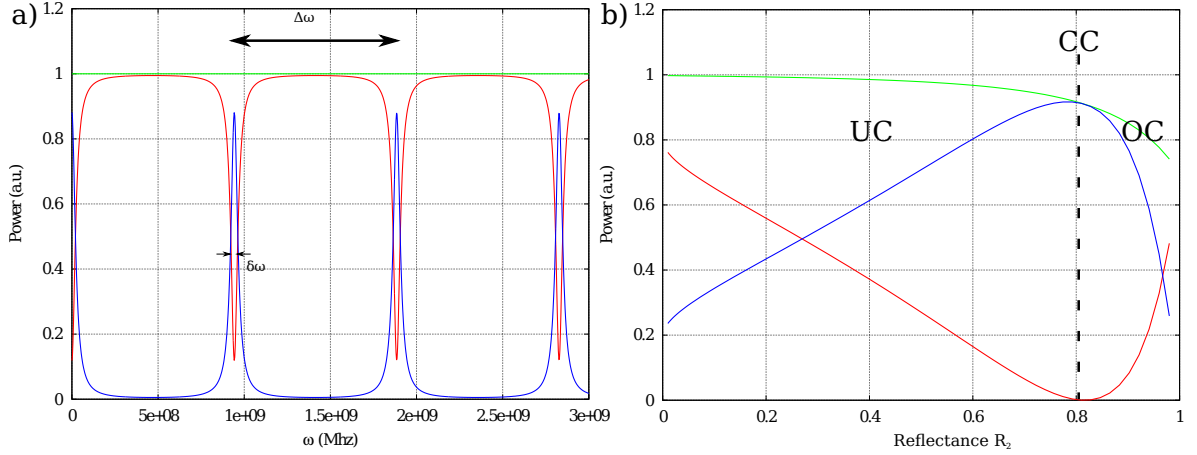


Figure 4.3.: a) Power in reflection (red line) and in transmission (blue line) vs frequency of incident light. We supposed no losses in the mirror, which makes the sum of the transmitted power and the reflected power (green line) one (1). The mirror reflectivity coefficients are $r_1 = 0.9$ and $r_2 = 0.95$. b) is the power in reflection (red line) and transmission (blue line) at resonance in function of the reflectance R_2 of the second mirror for the reflectance of the first mirror fixed at $R_1 = 0.8$. We supposed $L = 2\%$ of loss per round trip in the cavity. When $R_1 = R_2(1 - L)$, the total reflectivity is minimized, and this is called critical coupling (CC). When $R_1 > R_2(1 - L)$ it is in an under coupling (UC) regime, and when $R_1 < R_2(1 - L)$ it is an over coupling (OC) regime. For both plots, we normalized the powers by the power of the incident beam.

In the case $\alpha = 0$ and $L_{m1} = 0$, we can verify $I_r + I_t = I_i$. The transmission and reflection intensities in function of the frequency and in function of the reflection of one mirror at resonance is shown Figure 4.3.

An important parameter in the characterization of a cavity is the finesse F (not to be confused with the finesse coefficient \mathcal{F}). The finesse F of a cavity is more or less the number of round trips that a photon will make in the cavity before either exiting or being absorbed. The power in the cavity at resonance is the incident power multiplied by the finesse. The finesse F of the cavity is given by:

$$F = \frac{\Delta\omega}{\delta\omega} = \frac{\pi}{2 \arcsin\left(\frac{1}{\sqrt{\mathcal{F}}}\right)}$$

with \mathcal{F} the finesse coefficient. When $r_1 r_2 e^{-2\alpha d} > 0.5$ we can generally approximate the expression by:

$$F \approx \frac{\pi\sqrt{\mathcal{F}}}{2} \approx \frac{\pi\sqrt{r_1 r_2} e^{-\alpha d}}{1 - r_1 r_2 e^{-2\alpha d}}$$

Or even if the absorption is negligible and $r_1 r_2 \approx 1$:

$$F \approx \frac{\pi\sqrt{\mathcal{F}}}{2} \approx \frac{\pi}{L_T}$$

with $L_T = 1 - r_1 r_2 e^{-2\alpha d}$ which can be seen as the losses of a round trip in the cavity. More details can be found in [1].

4.3. Stability

To be able to resonate within the cavity, the light shape after one round trip must remain unchanged. If not, the phase surface will not be the same and the cavity will not be able to build the power inside. To analyze the wavefront deformation in the cavity we can use ABCD matrices.

To be a stable cavity, the transformation matrix $M = \begin{pmatrix} A & B \\ C & D \end{pmatrix}$ of one complete round trip in the cavity has to transform the Gaussian coefficient q of the beam in the resonator to itself: $\frac{Aq+B}{Cq+D} = q$. We obtain an equation of the second order in q which need to have complex solutions:

$$Cq^2 + (D - A)q - B = 0.$$

The solutions of this equations are complex if Δ given by $\Delta = (D - A)^2 + 4BC$ is negative.

$$\Delta = D^2 + A^2 - 2AD + 4BC$$

The determinant of the matrix M is one because we start and end with the same index material: $\text{Det}(M) = AD - BC = 1$ so we obtain:

$$\Delta = (A + D)^2 - 4$$

The stability condition in the cavity $\Delta \leq 0$ corresponds to:

$$0 < \frac{\text{Tr}(M) + 2}{4} < 1.$$

It is also possible to calculate the coefficient q at the position where we calculated M :

$$q = \frac{-(D - A) \pm i\sqrt{4 - (\text{Tr}(M))^2}}{2C}$$

The two values correspond to the two directions of propagation (\mathbf{e}_z and $-\mathbf{e}_z$) in the cavity.

The waist size of the beam is given by:

$$w_0^2 = \frac{|\Im(q)|\lambda}{\pi} = \frac{\lambda}{\pi} \frac{\sqrt{1 - (\frac{\text{Tr}(M)}{2})^2}}{|C|}$$

For the linear cavity in Figure 4.1 with C_1 and C_2 the curvature radius of the two mirrors, the matrix M is given by :

$$M = \begin{pmatrix} 1 & 0 \\ -\frac{2}{C_1} & 1 \end{pmatrix} * \begin{pmatrix} 1 & d \\ 0 & 1 \end{pmatrix} * \begin{pmatrix} 1 & 0 \\ -\frac{2}{C_2} & 1 \end{pmatrix} * \begin{pmatrix} 1 & d \\ 0 & 1 \end{pmatrix}$$

$$M = \begin{pmatrix} 1 - \frac{2d}{C_2} & 2d - \frac{2d^2}{C_2} \\ -\frac{2}{C_1} - \frac{2}{C_2} + \frac{4d}{C_1 C_2} & \left(1 - \frac{2d}{C_1}\right) \left(1 - \frac{2d}{C_2}\right) - \frac{2d}{C_1} \end{pmatrix}$$

The stability condition corresponds to:

$$0 < g_1 g_2 < 1,$$

with $g_1 = 1 - \frac{d}{C_1}$ and $g_2 = 1 - \frac{d}{C_2}$. It is possible to visualize the stability conditions on a diagram like in Figure 4.4.

The waist of the beam in the cavity is given by:

$$W_0 = \sqrt{\frac{\lambda d}{\pi} \frac{\sqrt{g_1 g_2 (1 - g_1 g_2)}}{g_1 + g_2 - 2g_1 g_2}}$$

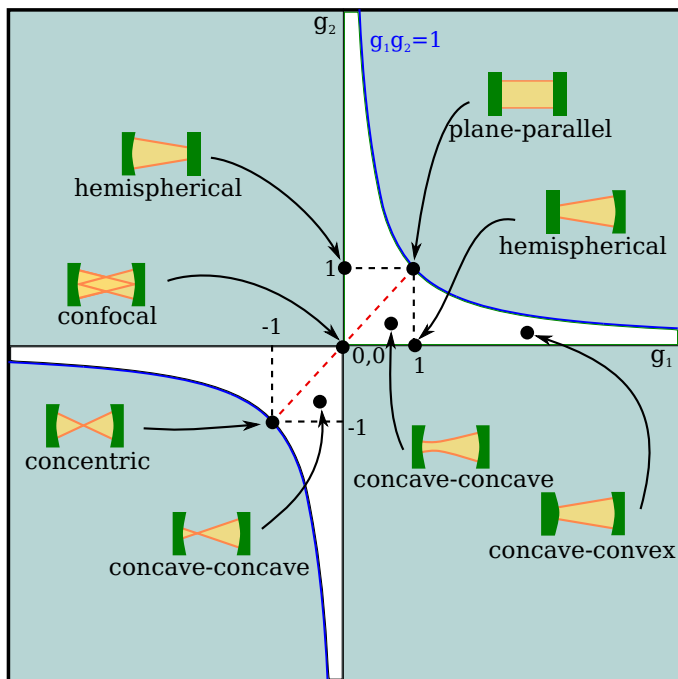


Figure 4.4.: In white, the stability domains in function of g_1 and g_2 .

4.4. Non Linear Cavity

We consider a non linear crystal with an index n in a cavity like in Figure 4.5. We suppose some light at frequency 2ω in the cavity, which causes some non linear gain (see chapter on parametric amplification subsection 2.3.3) to generate some light at the frequency ω in the crystal. We suppose the light at frequency ω at point A to be given by: $E_0 e^{-i\omega t - ikz}$ with E_0 real. (The imaginary part would be de-amplified until it reaches zero after a few round trips in the cavity, so we can consider the field to be real there). We simplify the calculation considering the crystal to be touching mirror 2. Using the equation Eq. 2.20 twice, and multiplying by the reflectivity of mirror 2, we get the field in point C . Supposing that there is no light at frequency ω coming from outside, then a simple propagation of the field to the point A gives the equation:

$$E_0 = E_0 e^{2\gamma l} r_1 r_2 e^{2k(d+nl)} \quad (4.1)$$

with $\gamma = \frac{1}{z_c} = \frac{\omega \mu_0^{3/2} d_{eff}}{\sqrt{2\pi n_\omega^{3/2}} \omega_0^\omega} \sqrt{P^{2\omega}}$, from the chapter on parametric amplification: subsection 2.3.3.

By taking the amplitude of this equation, we get the condition for a light seed at frequency ω to build up in the cavity:

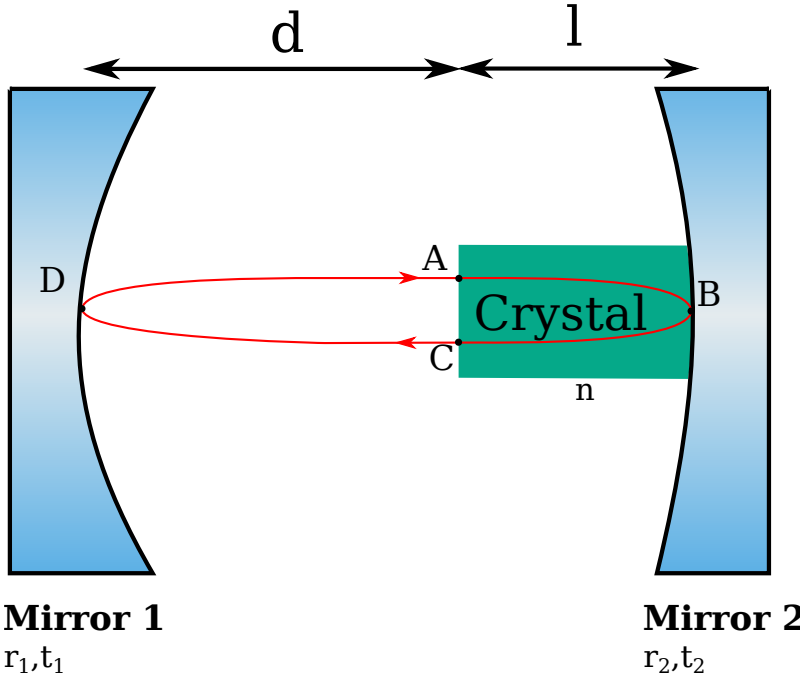


Figure 4.5.: Fabry Perot cavity with two mirrors of reflectivity r_1 and r_2 , and transmittivity t_1 and t_2 with a non linear crystal of length l and index n . To be stable in the cavity, the field in the point A at a time t and the field after a round trip need to be equal.

$$\gamma > \frac{1}{2l} \ln \left(\frac{1}{r_1 r_2} \right)$$

which gives the condition for the power of the pump $P^{2\omega} > P_{thr}^{2\omega}$ with the threshold power given by:

$$P_{thr}^{2\omega} = \frac{\pi n_\omega^3 (w_0^{2\omega})^2}{\omega^2 \mu_0^3 d_{eff}^2 l^2} \ln^2 \left(\frac{1}{r_1 r_2} \right)$$

with $w_0^{2\omega}$ the waist of the pump.

If the power of the pump is higher than the threshold power $P_{thr}^{2\omega}$ some light will be generated at the frequency ω . Above the threshold, the losses will just increase or the gain saturate, avoiding divergence of the power.

It is also possible to include in Eq. 4.1 absorption losses in the crystal $L = 1 - e^{-\alpha l}$ and losses at the coupling interfaces t_{c1} and t_{c2} , considering that the light still exits the crystal and enters at the two interfaces. The equation becomes:

$$E_0 = E_0 e^{2\gamma l} e^{-2\alpha l} t_{c1}^2 t_{c2}^2 r_1 r_2 e^{2k(d+nl)}. \quad (4.2)$$

The threshold becomes:

$$P_{thr}^{2\omega} = \frac{\pi n_{\omega}^3 (w_0^{2\omega})^2}{\omega^2 \mu_0^3 d_{eff}^2 l^2} \ln^2 \left(\frac{1}{r_1 r_2 e^{-2\alpha l} t_{c1}^2 t_{c2}^2} \right)$$

More details can be found in [1].

5. Quantum Optics

Classical non linear optics allows us to understand a lot of phenomena pertaining to laser beams in crystals, but to explain squeezing or above-threshold behavior, it is necessary to go beyond. The development of parametric generation in a classical regime showed that spontaneous parametric generation does not happen. That is, it is necessary to send a seed at frequency ω in the cavity in order to obtain generation of light. Experimentally, however, it is in fact not necessary. With a non linear crystal in a cavity with no seed, and with a pump at frequency 2ω , when the power of the pump reaches the threshold, some light at frequency ω will be generated. Moreover, when the power is lower than the threshold where nothing should happen in classical physics, squeezed states of light are generated.

5.1. Quantization of the Field

We consider an electric field \mathbf{E} constrained in a box of volume $V = L^3$ in the vacuum. We consider \mathbf{E} given by:

$$\mathbf{E}(\mathbf{r}, t) = \frac{1}{L^3} \iiint \mathbf{A}(\mathbf{k}, t) \exp(i\mathbf{k} \cdot \mathbf{r}) + \mathbf{A}^*(\mathbf{k}, t) \exp(-i\mathbf{k} \cdot \mathbf{r}) d\mathbf{k}$$

The field \mathbf{E} is null outside of the volume V , so the integrals become a sum of wave functions:

$$\mathbf{E}(\mathbf{r}, t) = \sum_l (A(\mathbf{k}_l, t) \exp(i\mathbf{k}_l \cdot \mathbf{r}) \boldsymbol{\epsilon}_1 + A^*(\mathbf{k}_l, t) \exp(-i\mathbf{k}_l \cdot \mathbf{r}) \boldsymbol{\epsilon}_1^*) \quad (5.1)$$

with l corresponding to the parameters $l = (n_x, n_y, n_z, s)$ with (n_x, n_y, n_z) three integers and $s \in (1, 2)$. The wave vectors are given by:

$$k_{l,x} = n_x \frac{2\pi}{L} \quad ; \quad k_{l,y} = n_y \frac{2\pi}{L} \quad ; \quad k_{l,z} = n_z \frac{2\pi}{L}.$$

and $\boldsymbol{\epsilon}_1$ and $\boldsymbol{\epsilon}_2$ two vectors orthogonal to each other and to the vector \mathbf{k}_l . (Complex $\boldsymbol{\epsilon}_1$ and $\boldsymbol{\epsilon}_2$ will describe circular polarizations).

The magnetic field can also be described by:

$$\mathbf{B}(\mathbf{r}, t) = - \sum_l \left(A(\mathbf{k}_l, t) \exp(i\mathbf{k}_l \cdot \mathbf{r}) \frac{\mathbf{k}_l}{\omega_l} \times \boldsymbol{\epsilon}_l + A^*(\mathbf{k}_l, t) \exp(-i\mathbf{k}_l \cdot \mathbf{r}) \frac{\mathbf{k}_l}{\omega_l} \times \boldsymbol{\epsilon}_l^* \right).$$

By applying the propagation equation Eq. 2.2 in the vacuum to the electric field Eq. 5.1, we obtain an equation for A_l :

$$\frac{d^2 A_l}{dt^2} = -\omega_l^2 A_l$$

The solution of this equation $A_l(t) = A_{l0} e^{i\omega_l t}$ allows us to rewrite the equation as:

$$i \frac{dA_l}{dt} = \omega_l A_l. \quad (5.2)$$

We can calculate the energy of the field in function of A_l :

$$H_R = \epsilon_0 \int d_r^3 \left(\mathbf{E}^2(\mathbf{r}, t) + c^2 \mathbf{B}^2(\mathbf{r}, t) \right) = 2\epsilon_0 L^3 \sum_l |A_l|^2 = 2\epsilon_0 L^3 \sum_l \left(A_{lq}^2 + A_{lp}^2 \right)$$

with $A_{lq}(t)$ and $A_{lp}(t)$ the real part and imaginary part of $A_l(t)$. With Eq. 5.2 we can write the evolution equations in the Hamiltonian Jacobi form:

$$\begin{aligned} \frac{d}{dt} A_{lq} &= \omega_l A_{lp} &= \frac{\omega_l}{4\epsilon_0 L^3} \frac{\partial H_R}{\partial A_{lp}} \\ \frac{d}{dt} A_{lp} &= -\omega_l A_{lq} &= -\frac{\omega_l}{4\epsilon_0 L^3} \frac{\partial H_R}{\partial A_{lq}} \end{aligned} \quad (5.3)$$

For some variables $(q_i(t), p_i(t))$ with an energy given by a Hamiltonian H , $(q_i(t), p_i(t))$ are conjugate variables when:

$$\frac{d}{dt} q_i = \frac{\partial H}{\partial p_i} \quad \frac{d}{dt} p_i = -\frac{\partial H}{\partial q_i} .$$

The usual way to quantize this system is to consider $(q_i(t), p_i(t))$ as operators respecting:

$$[q_i, p_j] = i\hbar \delta_{ij}$$

Eq. 5.3 allows a quantization of the fields by setting:

$$\hat{q}_i \leftrightarrow 2\sqrt{\frac{\epsilon_0 L^3}{\omega_l}} \hat{A}_{lq} \quad \hat{p}_i \leftrightarrow 2\sqrt{\frac{\epsilon_0 L^3}{\omega_l}} \hat{A}_{lp}$$

We generally join the two Hermitian operators \hat{A}_{lq} and \hat{A}_{lp} with a normalized non Hermitian operator \hat{a}_l :

$$\hat{a}_l = \sqrt{\frac{2\varepsilon_0 L^3}{\omega_l \hbar}} (\hat{A}_{lq} + i\hat{A}_{lp})$$

which satisfies:

$$[\hat{a}_l, \hat{a}_{l'}^\dagger] = \delta_{ll'} \quad (5.4)$$

\hat{a}_l is called the annihilation operator and \hat{a}_l^\dagger the creation operator. In the Schrödinger representation, the field operators expressed with the annihilation and creation operators are:

$$\begin{aligned} \hat{\mathbf{E}}(\mathbf{r}) &= \sum_l \sqrt{\frac{\hbar\omega_l}{2\varepsilon_0 L^3}} a_l \boldsymbol{\epsilon}_l e^{i\mathbf{k}_l \cdot \mathbf{r}} + cc \\ \hat{\mathbf{B}}(\mathbf{r}) &= - \sum_l \sqrt{\frac{\hbar\omega_l}{2\varepsilon_0 L^3}} \hat{a}_l \frac{\mathbf{k}_l}{\omega_l} \times \boldsymbol{\epsilon}_l e^{i\mathbf{k}_l \cdot \mathbf{r}} + cc \\ \hat{H}(\mathbf{r}) &= \sum_l \hbar\omega_l \left(\hat{N} + \frac{1}{2} \right) \end{aligned}$$

with $\hat{N} = \hat{a}_l^\dagger \hat{a}_l$ as the operator number of photons.

In the Heisenberg representation, the time dependence is in the operators and the state vector is replaced by the state of the initial condition of the experiment:

$$i\hbar \frac{d\hat{a}_{H,l}(t)}{dt} = [\hat{a}_{H,l}(t), \hat{H}_R] = \hbar\omega_l \hat{a}_{H,l}(t)$$

$$\hat{a}_{H,l}(t) = \hat{a}_l e^{-i\omega_l t}$$

$$\hat{\mathbf{E}}_H(\mathbf{r}, t) = \sum_l \sqrt{\frac{\hbar\omega_l}{2\varepsilon_0 L^3}} \hat{a}_l \boldsymbol{\epsilon}_l e^{i\mathbf{k}_l \cdot \mathbf{r} - i\omega_l t} + cc$$

$$\hat{\mathbf{B}}_H(\mathbf{r}, t) = - \sum_l \sqrt{\frac{\hbar\omega_l}{2\varepsilon_0 L^3}} \hat{a}_l \frac{\mathbf{k}_l}{\omega_l} \times \boldsymbol{\epsilon}_l e^{i\mathbf{k}_l \cdot \mathbf{r} - i\omega_l t} + cc.$$

In the following sections we will always use the Heisenberg representation, but we will omit the index H .

More details about the quantification of the field can be find in [8].

5.2. Quadratures and Homodyne Measurements

5.2.1. Quadratures

The operators \hat{a} and \hat{a}^\dagger are not Hermitian operators, so they do not correspond to any measurable quantities. It is some times useful to define two new operators $X_1 = \hat{a} + \hat{a}^\dagger$ and $X_2 = \frac{\hat{a} - \hat{a}^\dagger}{i}$ called quadratures, which are twice the real part (amplitude quadrature) and imaginary part (phase quadrature) of the operator \hat{a} . These operators are Hermitian and can be measured with a homodyne detector. In function of the quadratures, the electric field operator, expressed in Heisenberg representation, becomes:

$$\hat{\mathbf{E}}(\mathbf{r}, t) = \sum_l \mathcal{E}_{l0} (X_1(t) \cos(\mathbf{k}_l \cdot \mathbf{r}) + X_2(t) \sin(\mathbf{k}_l \cdot \mathbf{r})) \boldsymbol{\epsilon}_l$$

with $\mathcal{E}_{l0} = \sqrt{\frac{\hbar\omega_l}{2\varepsilon_0 L^3}}$. We consider here $\boldsymbol{\epsilon}_l$ with real components to simplify the expression.

It is also possible to define a quadrature with rotation θ :

$$X_\theta = X_1 \cos(\theta) + X_2 \sin(\theta) = \hat{a}^\dagger e^{i\theta} + \hat{a} e^{-i\theta}$$

The property on the commutator between \hat{a} and \hat{a}^\dagger (Eq. 5.4) gives the expression:

$$[X_\theta, X_{\theta+\frac{\pi}{2}}] = 2i.$$

For any states, the two observables X_θ and $X_{\theta+\frac{\pi}{2}}$ will satisfy a Heisenberg inequality.

$$\Delta X_\theta \Delta X_{\theta+\frac{\pi}{2}} \geq 1$$

More details can be found in [1].

5.2.2. Optics Components

Most components in optics can have an input-output characterization [8] with regards to operators, making the quantum interpretation of an experiment very easy. We start with an ensemble of input states and vacuum states and propagate them, mix them together and detect them by transforming the inputs operators.

5.2.2.1. Photo-detectors

A photo-detector is a system converting photons on its surface to current that can be analyzed with an oscilloscope or any other electric systems. A photo-detector measures a current i proportional to the power of the field P , which is proportional to the number of photons:

$$\hat{i} \sim \hat{X}_\theta^2 + \hat{X}_{\theta+\frac{\pi}{2}}^2 = \hat{a}_l^\dagger \hat{a}_l$$

$$i \sim \langle \psi_0 | \hat{a}_l^\dagger \hat{a}_l | \psi_0 \rangle$$

with $|\psi_0\rangle$ the initial state of the incident light.

5.2.2.2. Free Propagation

The free space propagation is the most simple transformation that can be applied to our system. It corresponds to adding a phase to the annihilation operator.

$$\hat{a}^{out} = e^{i\phi} \hat{a}^{in}$$

For the propagation in free space from (\mathbf{r}_1, t_1) to (\mathbf{r}_2, t_2) , the phase ϕ is given by:
 $\phi = \mathbf{k}_1 \cdot (\mathbf{r}_1 - \mathbf{r}_2) - \omega_l(t_1 - t_2)$

5.2.2.3. Beam Splitter

The beam splitter is a very important component allowing us to combine and mix beams together. The two output ports of the beam splitter will correspond to the sum and difference of what enters in the two inputs weighted by the coefficients r and t .

$$\begin{aligned} \hat{a}^{out1} &= r\hat{a}^{in1} + t\hat{a}^{in2} & \hat{X}^{out1} &= r\hat{X}^{in1} + t\hat{X}^{in2} \\ \hat{a}^{out2} &= t\hat{a}^{in1} - r\hat{a}^{in2} & \hat{X}^{out2} &= t\hat{X}^{in1} - r\hat{X}^{in2} \end{aligned} \quad .$$

5.2.3. Homodyne

Consider a setup in which we mix two beams in a beam splitter: a signal beam (S) that needs to be characterized, and a strong beam, called the Local Oscillator (LO).

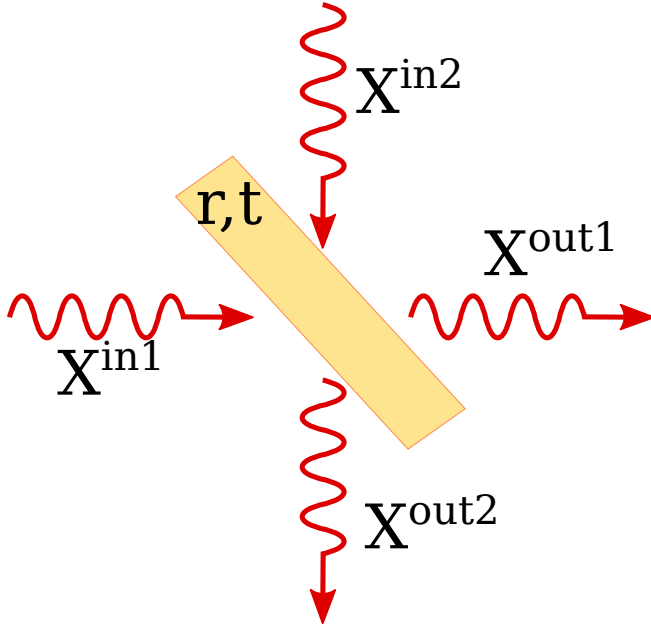


Figure 5.1.: The beam splitter mixes the two input quadratures. We obtain $\hat{X}^{out1} = r\hat{X}^{in1} + t\hat{X}^{in2}$ and $\hat{X}^{out2} = t\hat{X}^{in1} - r\hat{X}^{in2}$, where r is the reflection coefficient and t is the transmission coefficient.

By measuring the two output ports with photo-detectors, and by taking the difference between the two electrical signals, it is possible to measure the quadrature of the signal X_θ in a particular angle θ . We call this system a homodyne measurement. Figure 5.2.

We suppose the LO in the mode of the signal strong enough such that we can treat it classically, $\hat{a}_{LO}(t) \sim \alpha_{LO}$ with α_{LO} a complex number corresponding to the complex amplitude of the beam. We also suppose that the frequency of the LO and the signal are the same.

The two currents for the detectors a and b (Figure 5.2) are given by:

$$\begin{aligned} \hat{i}_a \sim \hat{a}_a^\dagger \hat{a}_a &= (r\hat{a}_s^\dagger + t\alpha_{LO}^*)(r\hat{a}_s + t\alpha_{LO}) \\ &= (r^2\hat{N}_s + t^2N_{LO}) + rt(\alpha_{LO}\hat{a}_s^\dagger + \alpha_{LO}^*\hat{a}_s) \end{aligned}$$

$$\begin{aligned} \hat{i}_b \sim \hat{a}_b^\dagger \hat{a}_b &= (t\hat{a}_s^\dagger - r\alpha_{LO}^*)(t\hat{a}_s - r\alpha_{LO}) \\ &= (t^2\hat{N}_s + r^2N_{LO}) - rt(\alpha_{LO}\hat{a}_s^\dagger + \alpha_{LO}^*\hat{a}_s) \end{aligned}$$

with \hat{N}_s the operator number of photons, N_{LO} the number of photons of the LO.

Supposing the coefficients of proportionality between the current and the number of photons for the two detectors are the same,

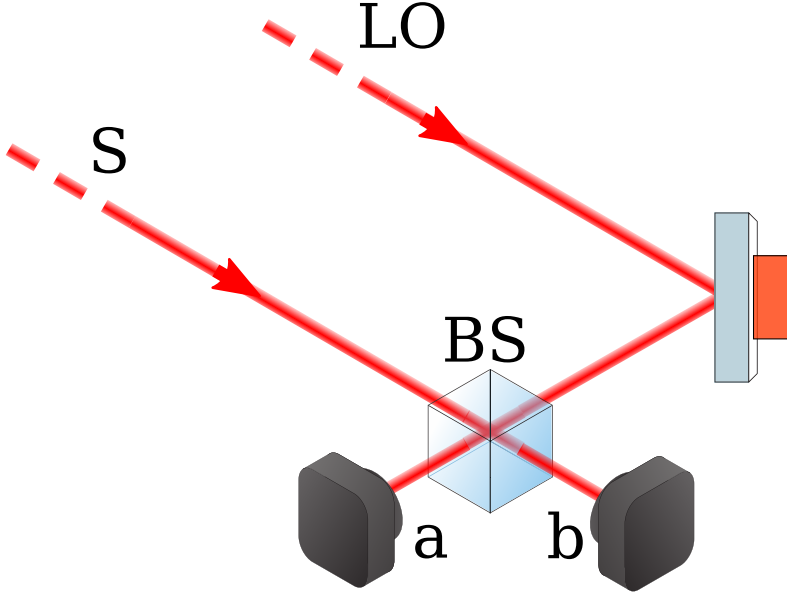


Figure 5.2.: A signal beam (S) is mixed with a bright beam, the Local Oscillator (LO) in a balanced beam splitter. The output lights are collected with two detectors. The difference of the two electric signals are proportional to the quadrature of the signal. By changing the phase of the LO, we can choose the direction of the quadrature to measure.

$$\hat{i}_a - \hat{i}_b \sim (t^2 - r^2) (-\hat{N}_s + N_{LO}) + 2rt (\alpha_{LO} \hat{a}_s^\dagger + \alpha_{LO}^* \hat{a}_s)$$

For a balanced detection, $r = t$. By defining φ such as $\alpha_{LO} = |\alpha_{LO}| e^{i\varphi}$:

$$\hat{i}_a - \hat{i}_b \sim 2rt |\alpha_{LO}| (e^{i\varphi} \hat{a}_s^\dagger + e^{-i\varphi} \hat{a}_s)$$

$$\hat{i}_a - \hat{i}_b \sim 2rt |\alpha_{LO}| \hat{X}_\varphi$$

Hence, by measuring the two currents and by taking the difference between them, it is possible to measure the observable X_φ . By changing the phase of the LO, we can control the angle of the measurement. And by measuring the variance of the difference of current, we can measure ΔX_φ .

5.3. Different Light States and Wigner Function

In this thesis we use three different states of light: the Fock states; the coherent states; and the squeezed states. One way to characterize them is by using the

Wigner Function. In classical mechanics, it is possible to define a probability for the state to be in any point of a phase diagram. But in quantum mechanics, the Heisenberg uncertainty makes the notion of defined points in the phase diagram not anymore correct. It is not possible to define at the same time the two quadratures X_1 and X_2 . However, it is still possible to define a quasi-density of probability, which is the Wigner function. It is defined by:

$$W(X_1, X_2) = \frac{1}{2\pi} \int_{-\infty}^{\infty} dq \langle X_1 - q | \rho | X_1 + q \rangle e^{iX_2 q}$$

with ρ the density matrix of the state and $|X_1 + q\rangle$ the eigenstate of the observable \hat{X}_1 with the eigenvalue $X_1 + q$.

The probability distribution of the system measured in one quadrature is the integral of the Wigner function in the conjugate quadrature $P(X_1) = \int W(X_1, X_2) dX_2$. The difference with the classical equivalent is that the Wigner function can be negative, which corresponds to the possibility to have interference in quantum mechanics.

For any operator \hat{O} symmetric in \hat{X}_1 and \hat{X}_2 , it is possible to obtain the expectation value with the Wigner function:

$$\langle \psi | \hat{O} | \psi \rangle = \int_{-\infty}^{\infty} \int_{-\infty}^{\infty} dx_1 dx_2 W(x_1, x_2) O(x_1, x_2)$$

5.3.1. Fock States

The Fock states $|n\rangle$ are states defined by a specific number n of photons. They are the eigenvectors of the operators \hat{N} and \hat{H} . The creation operator applied to a Fock state increases the number of photons by one, and the annihilation operator decreases the number of photons by one:

$$a^\dagger |n\rangle = \sqrt{n+1} |n+1\rangle \quad a |n\rangle = \sqrt{n} |n-1\rangle$$

The state with zero photons $|0\rangle$ is the vacuum state. It is the state that we will consider coming from the empty port of a beam splitter. All the other states $|n\rangle$ can be derived from the vacuum state by applying the creation operator n times:

$$|n\rangle = \frac{\hat{a}^{\dagger n}}{\sqrt{n!}} |0\rangle$$

By using the density matrix of the Fock state $\rho = |n\rangle\langle n|$ we can calculate the Wigner function (Figure 5.3)

$$W_n(X_1, X_2) = \frac{(-1)^n}{2\pi} e^{-\frac{(X_1^2 + X_2^2)}{2}} L_n(X_1^2 + X_2^2)$$

with $L_n(q)$ the Laguerre polynomials given by: $L_n(q) = \frac{e^q}{n!} \frac{d^n}{dq^n} (e^{-q} q^n)$.

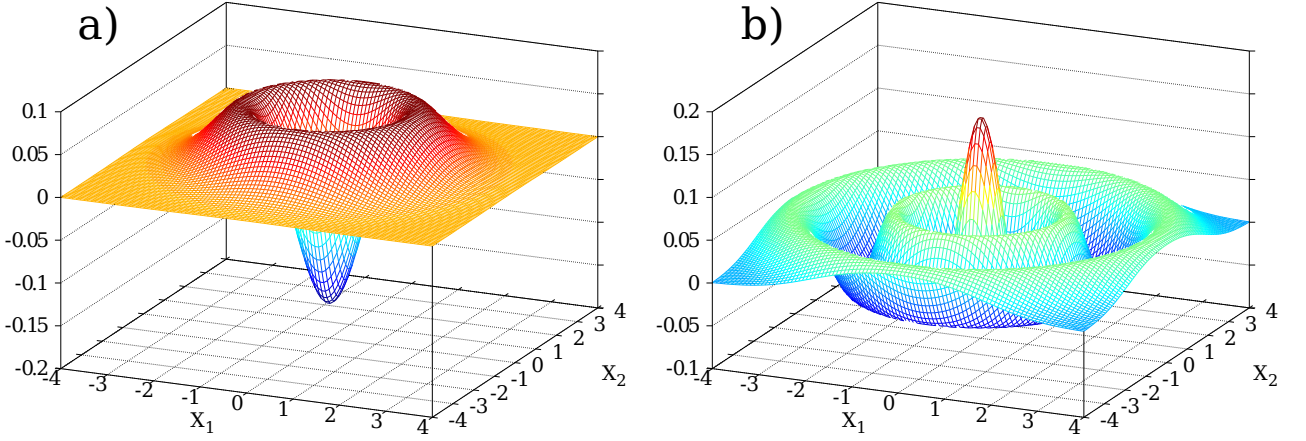


Figure 5.3.: Wigner function of (a) a one-photon Fock state and (b) a four-photon Fock state.

5.3.2. Coherent States

The coherent state $|\alpha\rangle$ (with $\alpha \in \mathbb{C}$) is the eigenvector of the annihilation operator \hat{a} with eigenvalue α . It corresponds to a good approximation of the mode coming out of a laser:

$$|\alpha\rangle = e^{-\frac{|\alpha|^2}{2}} \sum_{n=0}^{\infty} \frac{\hat{a}^n}{\sqrt{n!}} |n\rangle.$$

It can be considered as the displacement operator $\hat{D} = e^{\alpha\hat{a}^\dagger - \alpha^*\hat{a}}$ applied to the vacuum state:

$$|\alpha\rangle = \hat{D}|0\rangle.$$

This state has the same uncertainty in X_1 and X_2 and minimizes the Heisenberg inequality:

$$\begin{aligned} \Delta X_1 &= \langle \alpha | (\hat{X}_1 - \langle X_1 \rangle)^2 | \alpha \rangle = 1 \\ \Delta X_2 &= \langle \alpha | (\hat{X}_2 - \langle X_2 \rangle)^2 | \alpha \rangle = 1 \end{aligned}$$

with $\langle X_1 \rangle = \langle \alpha | \hat{X}_1 | \alpha \rangle = \alpha + \alpha^*$ and $\langle X_2 \rangle = \langle \alpha | \hat{X}_2 | \alpha \rangle = \frac{\alpha - \alpha^*}{i}$.

The photon distribution of the coherent state respects a Poisson distribution:

$$\Delta n = |\alpha|^2 \quad \langle n \rangle = |\alpha|^2 .$$

The Wigner function associated with this state is given by using the density matrix $\rho = |\alpha\rangle\langle\alpha|$:

$$W_\alpha(X_1, X_2) = \frac{1}{2\pi} e^{-\frac{(\hat{X}_1 - \langle X_1 \rangle)^2}{2} - \frac{(\hat{X}_2 - \langle X_2 \rangle)^2}{2}}$$

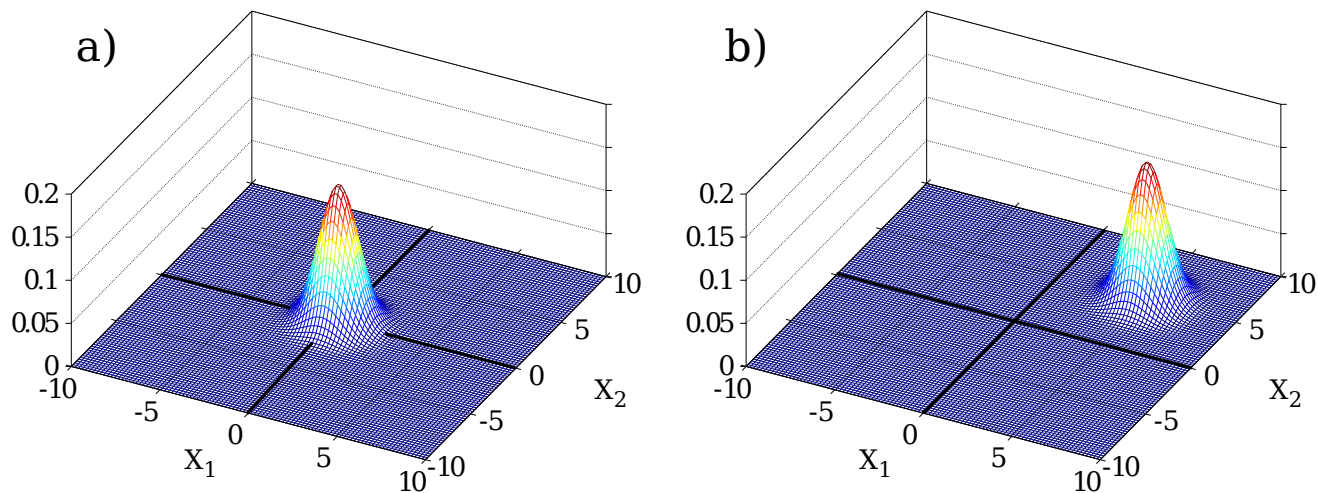


Figure 5.4.: Wigner function of (a) a vacuum state and (b) a coherent state.

5.3.3. Squeezed States

A squeezed state is a state similar to a coherent state, but with the uncertainty in one quadrature “squeezed” below one. The squeezed state $|s\rangle$ (with $s \in \mathbb{C}$) is defined by the operator \hat{S} applied to a coherent state:

$$|s\rangle = \hat{S}\hat{D}|0\rangle$$

with $\hat{S} = e^{s^* \hat{a}^2 - s \hat{a}^{\dagger 2}}$ and s a complex number given by $s = |s|e^{i\phi}$. If the operator \hat{S} is directly applied to the vacuum state, we obtain a vacuum squeezed state. The uncertainty relation for this state becomes:

$$\Delta X_\phi = e^{-|s|} \quad \Delta X_{\phi+\pi/2} = e^{|s|}$$

The Wigner function of the squeezed vacuum state is given by using the density matrix $\rho = \hat{S}|0\rangle\langle 0|\hat{S}^\dagger$ for $\phi = 0$ we obtain:

$$W_s(X_1, X_2) = \frac{1}{2\pi} e^{-\frac{(\hat{X}_0)^2}{2V_s} - \frac{(\hat{X}_{\pi/2})^2}{2V_s^{-1}}}$$

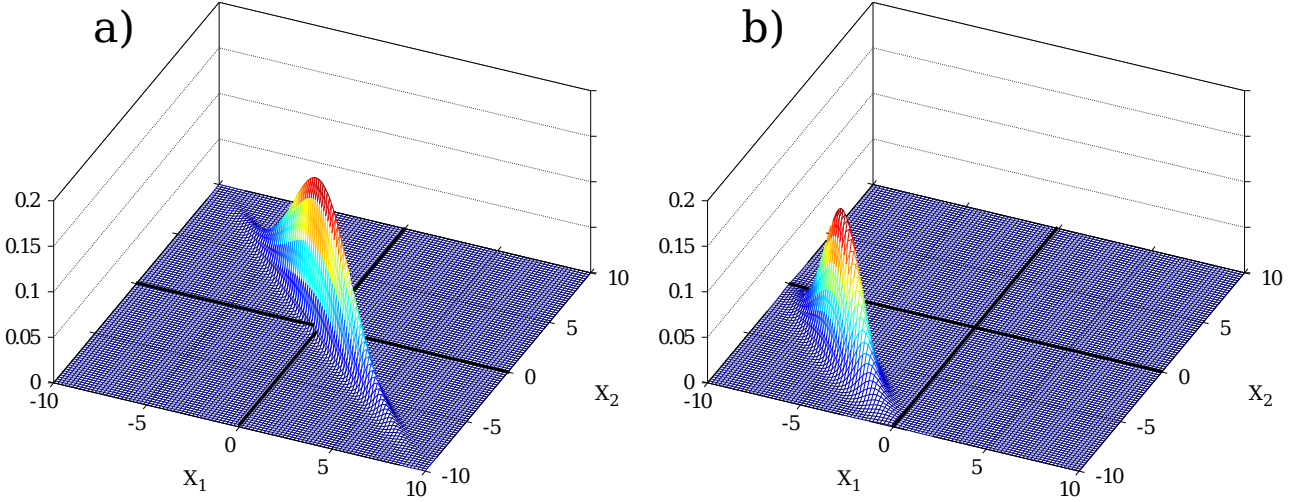


Figure 5.5.: Wigner function of (a) the squeezing of a vacuum state and (b) the squeezing of a coherent state.

with $V_s = (\Delta X_0)^2$ the squeezed variance.

More information about Wigner functions of usual states in optics can be find in [12].

5.4. Squeezing Creation and Interaction with Environment

5.4.1. Single pass squeezing generation in a non-linear crystal

One way to create squeezing state of light is to use non linear crystals. Classically the energy of interaction between the field and matter is given by **D.E.** In a non linear crystal, it can be seen in Appendix A that the energy of interaction due to the non linear polarization is given by:

$$U_{p2} = \frac{\varepsilon_0}{2} E^*(2\omega) * 2\chi^{(2)}(\omega, \omega) E(\omega)^2 + cc$$

with $E(2\omega)$ and $E(\omega)$ the fields at frequency 2ω and ω , and $2\chi^{(2)}(\omega, \omega)$ the effective non linear susceptibility of the material at frequency ω . The Hamiltonian corresponding to this classical energy is given by:

$$\hat{H} = g\hat{a}_{2\omega}^\dagger \hat{a}_\omega^{\dagger 2} + g^* \hat{a}_{2\omega} \hat{a}_\omega^2$$

with $\hat{a}_{2\omega}$ and \hat{a}_ω the annihilation operators for the light at frequencies 2ω and ω , and g a constant proportional to $\chi^{(2)}(\omega, \omega)$ real (we consider the lossless case $g = g^*$).

The two terms of the Hamiltonian correspond to the annihilation of two photons at the frequency ω and the creation of one photon at frequency 2ω , or the annihilation of one photon at 2ω and the creation of two photons at frequency ω .

Typically, the light at frequency 2ω is the pump, with a high power hence, it can be considered classically. The Hamiltonian becomes:

$$\hat{H} = g\alpha_{2\omega}^* \hat{a}_\omega^{\dagger 2} + g\alpha_{2\omega} \hat{a}_\omega^2$$

with $\alpha_{2\omega}$ the amplitude of the field of the pump.

Starting with a vacuum state in the cavity for the frequency ω , the interaction with this Hamiltonian can be expressed by the time evolution operator:

$$\hat{S} = e^{\frac{i\hat{H}t}{\hbar}} = e^{\frac{i}{\hbar}g(\alpha_{2\omega}^* \hat{a}_\omega^{\dagger 2} + \alpha_{2\omega} \hat{a}_\omega^2)t}$$

which is the squeezing operator, with $t = \frac{L}{c}$, L the length of the medium and c the speed of light. The strength of the squeezing is defined by the power of the light at 2ω , and the direction of squeezing by the phase.

The evolution equation of the operator \hat{a}_ω can be obtain from the Hamiltonian: $i\hbar \frac{\partial \hat{a}_\omega}{\partial t} = [\hat{H}, \hat{a}_\omega]$, we obtain:

$$i\hbar \frac{\partial \hat{a}_\omega}{\partial t} = -2g\alpha_{2\omega}^* \hat{a}_\omega^\dagger$$

The solution of this equation is given by:

$$\hat{a}_\omega(t) = \hat{a}_\omega(0) \cosh\left(\frac{2g|\alpha_{2\omega}|}{\hbar}t\right) + \hat{a}_\omega^\dagger(0)e^{i\left(\frac{\pi}{2} - \Phi(\alpha_{2\omega})\right)} \sinh\left(\frac{2g|\alpha_{2\omega}|}{\hbar}t\right) \quad (5.5)$$

where $\Phi(\alpha_{2\omega})$ is the phase of the field $\alpha_{2\omega}$. By choosing a phase of the pump such as: $\frac{\pi}{2} - \Phi(\alpha_{2\omega}) = 0$, and by coming back to the quadratures, we obtain the squeezing and anti-squeezing factors due to a time of interaction τ with the crystal:

$$\begin{aligned} X_{out} &= e^{\frac{2g|\alpha_{2\omega}|}{\hbar}\tau} X_{in} \\ Y_{out} &= e^{-\frac{2g|\alpha_{2\omega}|}{\hbar}\tau} Y_{in} \end{aligned}$$

where $\tau = nlc$ with n the index of the crystal, l the length of the crystal and c the speed of light.

5.4.2. Squeezing Interaction in a Lossy Channel

The squeezed state as defined in the previous section subsection 5.3.3 minimizes the Heisenberg inequality $\Delta X_1 \Delta X_2 = 1$. But when losses are introduced into the system, this is no longer the case and we obtain a mixed state $\Delta X_1 \Delta X_2 > 1$. As long as $\min_\phi(\Delta X_\phi) < 1$, we still call this mixed state a squeezed state. It is possible to model losses in the system by supposing a pure squeezed state like that described in subsection 5.3.3 going into a beam splitter, mixing the state with a vacuum state and thus changing the amount of squeezing $S = \min_\phi(\Delta X_\phi)$ and anti squeezing $A = \max_\phi(\Delta X_\phi)$ that we measure (Figure 5.6).

We define \hat{X}_s and \hat{X}_a the quadratures of the pure state in the direction of squeezing and anti-squeezing, and \hat{X}'_s and \hat{X}'_a the quadratures after the beam splitter of reflectivity η :

$$\begin{aligned}\hat{X}'_s &= \sqrt{\eta}\hat{X}_s + \sqrt{1-\eta}\hat{X}_{v1} \\ \hat{X}'_a &= \sqrt{\eta}\hat{X}_a + \sqrt{1-\eta}\hat{X}_{v2}\end{aligned}$$

with \hat{X}_{v1} and \hat{X}_{v2} the two quadratures of the vacuum state coming from the beam splitter. We have:

$$\hat{X}'_s{}^2 = \left(\sqrt{\eta}\hat{X}_s + \sqrt{1-\eta}\hat{X}_v\right)^2 = \eta\hat{X}_s^2 + (1-\eta)\hat{X}_v^2 + 2\sqrt{\eta(1-\eta)}\hat{X}_s\hat{X}_v.$$

If we call $S = \langle s | (\hat{X}_s - \langle X_s \rangle)^2 | s \rangle$ and $A = 1/S = \langle s | (\hat{X}_a - \langle X_a \rangle)^2 | s \rangle$ the squeezing and anti-squeezing of the pure state that we started with, and S' and A' the squeezing and anti-squeezing obtained after the beam splitter, by supposing that there is no coupling between the squeezed state and the vacuum state from the beam splitter $\langle X_v X_s \rangle = \langle X_v \rangle \langle X_s \rangle$ and because $\langle X_v \rangle = 0$ and $\Delta X_v = 1$:

$$\begin{aligned}S' &= \eta S + (1-\eta) \\ A' &= \eta A + (1-\eta)\end{aligned}$$

Usually we measure the squeezing in dB with $S_{dB} = 10 \log_{10}(S)$ and $A_{dB} = 10 \log_{10}(A)$.

5.4.3. Squeezing generation in a non linear crystal in a cavity

We consider a non-linear crystal in a linear cavity. One of the mirror has an infinite reflectivity, the other one is characterized by its transmission T . The losses in the cavity are modeled by a beam splitter with a reflection L mixing the mode of the cavity with a vacuum mode Figure 5.7.

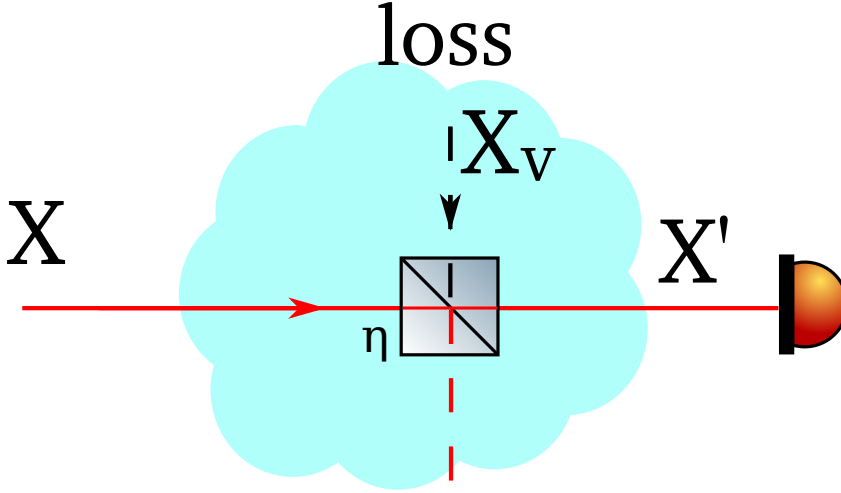


Figure 5.6.: Losses in the system can be modeled with a beam splitter of transmission coefficient η mixing the state with a vacuum state $X' = \sqrt{\eta}X + \sqrt{1-\eta}X_v$.

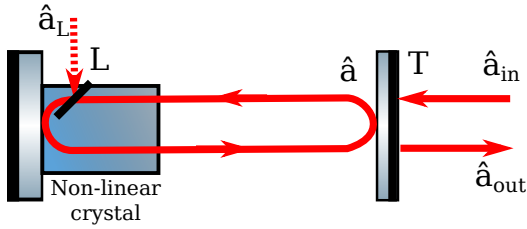


Figure 5.7.: Schematic of a non-linear crystal in a cavity. The left mirror is supposed with a reflection $R = 1$, the second mirror has a transmission T . The losses in the cavity are modeled by a beam splitter with a reflectivity L which mix the field of the cavity corresponding to an operator \hat{a} to a vacuum field corresponding to the operator \hat{a}_L . The field coming in the resonator correspond to the operator \hat{a}_{in} , and the field leaving the cavity correspond to the operator \hat{a}_{out} .

The mode in the cavity after one round trip needs to be equal to the original mode. By supposing the transmission T and the losses L low ($\sqrt{1-T} \sim 1-T/2$, $\sqrt{1-L} \sim 1-L/2$ and $(1-L/2)(1-T/2) \sim 1 - \frac{T+L}{2}$) and the size of the crystal small enough to be able to linearize Eq. 5.5, the annihilation operator at frequency ω (we will forget the index ω) in the cavity $\hat{a}(t)$ verifies:

$$\hat{a}(t + \tau_c) = \left(1 - \frac{T+L}{2}\right) \left(\hat{a}(t) + \frac{2g|\alpha_{2\omega}|}{\hbar} \tau \hat{a}^\dagger(t)\right) + \sqrt{L}\hat{a}_L + \sqrt{T}\hat{a}_{in}$$

where τ_c is the round trip time for the light in the cavity and $\tau = 2nlc$ where n is the index of the crystal, l the length of the crystal, c is the speed of light, \hat{a}_L correspond to the field coming from the losses and \hat{a}_{in} is the input field.

we develop the field $\hat{a}(t + \tau_c)$ in Taylor series, and by neglecting $\frac{T+L}{2} \frac{2g|\alpha_{2\omega}|}{\hbar} \tau \hat{a}^\dagger(t)$ we obtain:

$$\tau_c \frac{\partial \hat{a}}{\partial t} = -\frac{T+L}{2} \hat{a}(t) + \frac{2g|\alpha_{2\omega}|}{\hbar} \tau \hat{a}^\dagger(t) + \sqrt{L} \hat{a}_L + \sqrt{T} \hat{a}_{in}.$$

By getting the same equation for $\frac{\partial \hat{a}^\dagger}{\partial t}$, and by taking the sum and difference of both equations, we obtain the equations for the two quadratures in the cavity:

$$\begin{aligned} \tau_c \frac{\partial \hat{X}_1}{\partial t} &= -\frac{T+L}{2} \hat{X}_1 + \frac{2g|\alpha_{2\omega}|}{\hbar} \tau \hat{X}_1 + \sqrt{L} \hat{X}_{1L} + \sqrt{T} \hat{X}_{1in} \\ \tau_c \frac{\partial \hat{X}_2}{\partial t} &= -\frac{T+L}{2} \hat{X}_2 - \frac{2g|\alpha_{2\omega}|}{\hbar} \tau \hat{X}_2 + \sqrt{L} \hat{X}_{2L} + \sqrt{T} \hat{X}_{2in} \end{aligned} \quad (5.6)$$

where \hat{X}_{1L} , \hat{X}_{2L} are the quadratures of the field coming from the losses and \hat{X}_{1in} , \hat{X}_{2in} the quadratures of the input field. By writing $\omega_c = \frac{T+L}{2\tau_c}$ and $\epsilon = \frac{4g|\alpha_{2\omega}|}{\hbar} \frac{\tau}{T+L} = \sqrt{P_{2\omega}/P_{th}}$ where $P_{2\omega} = |\alpha_{2\omega}|^2$ is the power of the pump and $P_{th} = \left(\frac{4g}{\hbar} \frac{\tau}{T+L}\right)^2$ is the threshold power of the squeezer. We apply a Fourier transform to Eq. 5.6, we obtain:

$$\begin{aligned} \left(1 - \epsilon - i\frac{\omega}{\omega_c}\right) \hat{X}_1(\omega) &= \frac{2\sqrt{L}}{T+L} \hat{X}_{1L}(\omega) + \frac{2\sqrt{T}}{T+L} \hat{X}_{1in}(\omega) \\ \left(1 + \epsilon - i\frac{\omega}{\omega_c}\right) \hat{X}_2(\omega) &= \frac{2\sqrt{L}}{T+L} \hat{X}_{2L}(\omega) + \frac{2\sqrt{T}}{T+L} \hat{X}_{2in}(\omega) \end{aligned} \quad (5.7)$$

Outside of the cavity, the quadrature are obtained by the equation: $X_{\theta Out} = \sqrt{T} X_\theta - (1 - T/2) X_{\theta in}$ where $\theta = \{1, 2\}$. We suppose that we have a vacuum state at the input of the cavity and at the level of the losses: $\langle \hat{X}_{1L}(\omega) \hat{X}_{1L}(-\omega) \rangle = \langle \hat{X}_{1in}(\omega) \hat{X}_{1in}(-\omega) \rangle = \sigma_0^2$ and $\langle \hat{X}_{2L}(\omega) \hat{X}_{2L}(-\omega) \rangle = \langle \hat{X}_{2in}(\omega) \hat{X}_{2in}(-\omega) \rangle = \sigma_0^2$, but there is no correlation between them: $\langle \hat{X}_{1L}(\omega) \hat{X}_{1in}(-\omega) \rangle = \langle \hat{X}_{2L}(\omega) \hat{X}_{2in}(-\omega) \rangle = 0$.

The noise of the output state normalized to the noise of the vacuum: $s_1 = \langle \hat{X}_{1out}(\omega) \hat{X}_{1out}(-\omega) \rangle / \sigma_0^2$ and $s_2 = \langle \hat{X}_{2out}(\omega) \hat{X}_{2out}(-\omega) \rangle / \sigma_0^2$ are given by:

$$\begin{aligned} s_1 &= 1 + \eta \frac{4\epsilon}{(1-\epsilon)^2 + 4\left(\frac{\omega}{\omega_c}\right)^2} \\ s_2 &= 1 - \eta \frac{4\epsilon}{(1+\epsilon)^2 + 4\left(\frac{\omega}{\omega_c}\right)^2} \end{aligned} \quad .$$

Where $\eta = \frac{T}{T+L}$ is the escape efficiency. s_1 and s_2 are the squeezing and anti-squeezing expected from the cavity.

More details can be found in [1] and in Olivier Morin's Thesis [14].

Bibliography

- [1] H.A. Bachor and T.C. Ralph. *A Guide to Experiments in Quantum Optics*. Wiley, 2004.
- [2] Michael Bass, Casimer DeCusatis, Jay Enoch, Vasudevan Lakshminarayanan, Guifang Li, Carolyn Macdonald, Virendra Mahajan, and Eric Van Stryland. *Handbook of Optics, Third Edition Volume II: Design, Fabrication and Testing, Sources and Detectors, Radiometry and Photometry*. McGraw-Hill, Inc., New York, NY, USA, 3 edition, 2010.
- [3] G.D Boyd and Kleinman D. A. *Parametric Interaction of Focused Gaussian Light Beams*, volume 15. SIAM, 1968.
- [4] Robert W. Boyd. *Nonlinear Optics, Third Edition*. Academic Press, 3rd edition, 2008.
- [5] C. Fabre M.A.M. Marte H. Ritsch A. Gatti L. Lugiato C. Schwob, P.F. Cohadon. Transverse effects and mode couplings in opos. 1998.
- [6] Remi Carminati and Claude Boccara. *Optique (2eme partie) Lumiere et matiere*. 2010.
- [7] Salah Hassab Elnaby. *Optics of anisotropic media*. 2013.
- [8] Claude Fabre. Quantum optics, from one mode to many modes. Cours des Houches (2007), 2007.
- [9] Sebastien Forget. *Optique des lasers et faisceaux gaussiens*.
- [10] Baptiste Gouraud, Dominik Maxein, Adrien Nicolas, Olivier Morin, and Julien Laurat. Optical nanofibers as light-matter interfaces for quantum networks. In *CLEO: 2015*, page FTh4B.3. Optical Society of America, 2015.
- [11] D.J. Griffiths. *Introduction to Electrodynamics*. Prentice Hall, 1999.
- [12] U. Leonhardt. *Measuring the Quantum State of Light*. Cambridge Studies in Modern Optics. Cambridge University Press, 1997.
- [13] J. Clerk Maxwell. A dynamical theory of the electromagnetic field. *Philosophical Transactions of the Royal Society of London*, 155:459–512, 1865.
- [14] Olivier Morin. Non-gaussian states and measurements for quantum information. 2014.
- [15] Francesco Pampaloni and Jörg Enderlein. Gaussian, hermite-gaussian, and laguerre-gaussian beams: A primer. *arXiv preprint physics/0410021*, 2004.

- [16] J. H. Poynting. On the transfer of energy in the electromagnetic field. *Philosophical Transactions of the Royal Society of London*, 175:343–361, 1884.
- [17] M Sluijter. Ray-optics analysis of homogeneous uniaxially anisotropic media. *Work*, 11, 2006.
- [18] F. Treussart. *Cours d optique anisotrope*. 2008.

Part II.
Fibered Mini OPO

6. Introduction

6.1. Introduction

The design that I will present has been constructed in France under the supervision of Nicolas Treps and Claude Fabre. The idea underlying the project comes from the work of Jakob Reichel on micro cavities between two fibers ([53]). With a CO_2 laser, his team shot a strong beam on the end of a fiber to create a curved shape. Then they applied a high reflectivity (HR) coating on the surface, and created a cavity between two fibers.

These cavities are used for different purposes, but mostly for trapping atoms to study the interaction between the light and the atoms([56],[47],[51]).

The idea behind my project was to investigate the possibility to add a non linear crystal into a similar cavity and create squeezed states of light which would be directly coupled into the fiber.

6.2. Squeezing Generation

A squeezed coherent state is a state with the noise in one of its quadratures smaller than the noise fluctuation of the vacuum; the excess noise is transferred to the complementary quadrature (which is anti-squeezed) to respect the Heisenberg inequality. A more mathematical description of the squeezed state can be found in Part 1 (subsection 5.3.3). This non-classical state can be used for a variety of applications like quantum communication, Quantum Key Distribution (QKD) ([41], [63]), quantum computation ([48]) and metrology ([34]). By mixing two squeezed states on a 50/50 beam splitter with the correct phase, one can create the so called EPR state ([60]), a cornerstone of quantum mechanics. It is also possible to subtract a photon from a squeezed state using a beam splitter and create Schrödinger states ([58],[40]), and it can be interacted with single photons ([55]). By using the characteristic of transferring noise in another quadrature, a squeezed state can be used to increase detection sensitivity to the theoretical limit ([59]). These days, squeezed states are used to improve the sensitivity of gravitational wave detectors such as the LIGO interferometer ([34]).

The big inconveniences of such a state is its fragility, and the complexity to create it. The amount of squeezing decreases very rapidly with losses. A state with an

infinite amount of squeezing at the start, which experiences 50% of transmission losses is reduced to 3dB of squeezing. When we want to use several of these states it is generally necessary to lock a lot of cavities, and the complexity of the experiment increases very rapidly.

Squeezed states have been generated in research laboratories for around 20 years, with optimized methods reaching up to 12.7dB of squeezing below the shot noise ([45]). The common technique is to use a $\chi^{(2)}$ non linear crystal in a cavity with a pump field interacting with its sub-harmonic field resonant in the cavity. One common design is to use a bow-tie cavity ([62],[61]) which allows easy manipulation and potential replacement of the crystal. (Some linear cavities also have been used for this purpose ([54])). The common characteristic is usually the size of the system, which is generally quite large, and the fact that the coupling and the generation of squeezing is usually in free space rather than in fibers. The advantage of the system presented in this thesis is that it is a very compact system which generates squeezing directly in fibers.

6.3. Toward an all-fibered squeezer

Fibers have the advantage to simplify a lot the transport of optical states, and for single fiber areas, the technology is very mature. We can find fibered beam splitters, phase shift controls, and polarization controls with relatively low losses, but the coupling in a fiber can be sometimes problematic and therefore imply losses.

The long time project under this thesis was to develop a very compact linear squeezer between two fibers with a crystal in the middle. The mode of the output fiber and the mode of the cavity need to be perfectly matched. If this is not the case, a part of the light going out of the cavity will not go into the fiber, but will be lost which will degrade squeezing. It means that the output coupler, where the squeezing is leaving, needs to be a flat mirror and that the waist of the cavity will be at the position of this mirror. Moreover, the non linearity is bigger at the focus point. It means that the crystal needs to be placed at the waist position, where the power is the strongest. This means it needs to be ideally stuck to the output mirror. The length of the cavity is also an issue. A too-small cavity will imply a very small crystal, and the non linearity compared to the losses will be too weak to create sufficient squeezing. The ideal length of the crystal is defined by the Boyd and Kleinman coefficient [36] to maximize non linearity.

The design implied one multi-mode fiber for coupling the pump with one of its ends curved in the shape of a mirror and coated with a reflective coating to make the first coupling mirror of the cavity. The second mirror of the cavity would have been the end of a single mode fiber glued to a non linear mirror. With a sufficient coupling from the cavity to the fiber, it would be possible to have very compact fiber-based systems generating squeezed states of light ready to be used in a bigger

experiment, see Figure 6.1 ([42]). The system described in this thesis is almost the same, but rather than using a multi-mode fiber as a coupler, it uses a curved 5mm mirror (Figure 7.1). This system still couples light directly into a fiber which allows, potentially, almost plug-and-play experiments with different fibered squeezing sources.

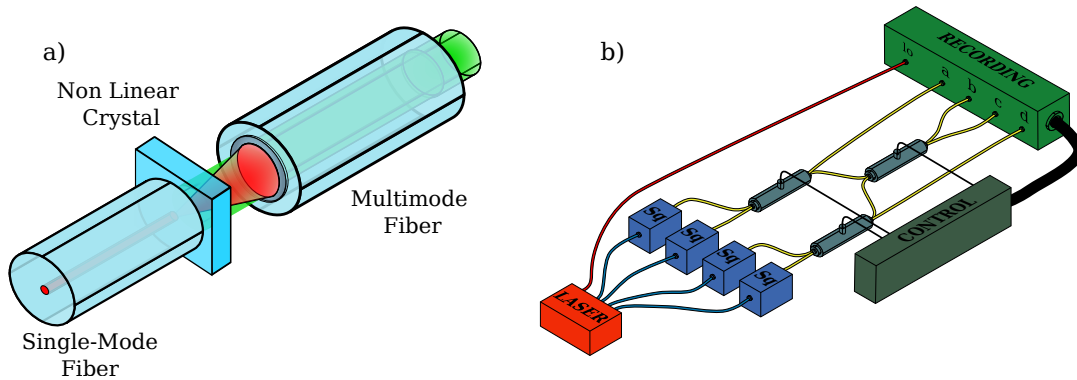


Figure 6.1.: a) is a proposal of an experiment suggested by Jakob's Reichel's team's work, going beyond the experiment presented in this thesis. It is a cavity formed between a flat mirror on a single-mode fiber and a curved mirror on a multi-mode fiber, with a non linear crystal in it. The pump (in green) is brought to the cavity by the multi-mode fiber; it generates squeezed light at the sub-harmonic (red) which is directly coupled into the single mode fiber. b) an example of protocols that could be used with four of these systems. A laser provides pump power for four squeezers identical to (a). The outputs of all squeezers are mixed on beam splitters with variable reflection coefficients and measured on four homodyne detections.

7. Experimental Method

7.1. The OPO Cavity, Description of the Experiment

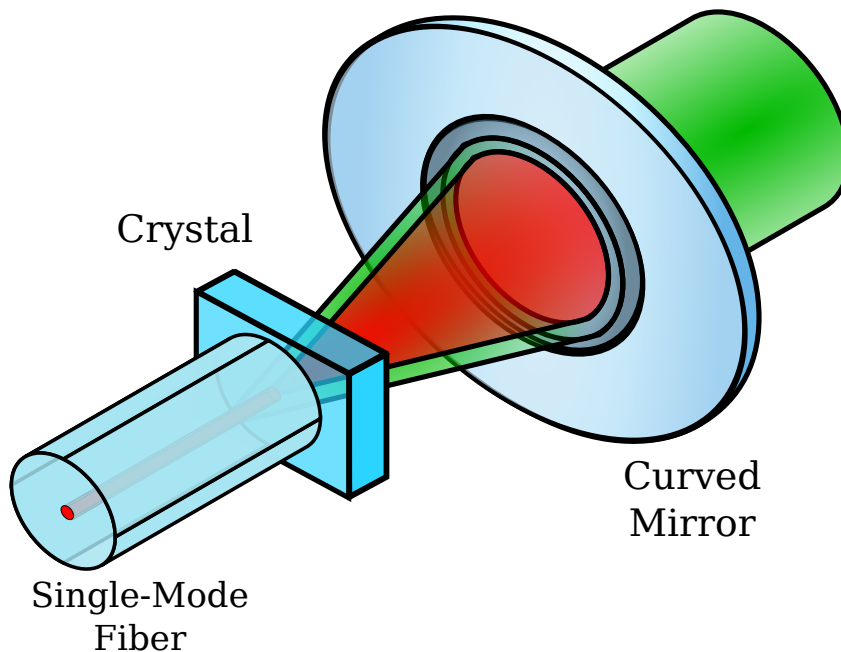


Figure 7.1.: The system proposed in this thesis is a simpler experiment than Figure 6.1. It consists of a cavity formed between a single mode fiber and a curved mirror with a non linear crystal in it. The pump (green) enters the cavity from the curved mirror, generating squeezed light (red) which is coupled in the single mode fiber.

The system that I am implementing in this thesis is a linear cavity between a curved mirror of radius of curvature of $5mm$ and an HR coated crystal with a glued fiber on the other face of the crystal to couple the output mode, see Figure 7.2. The high reflectivity coating is deposited on the crystal rather than the fiber, and we stick the fiber on it. If the fiber surface is perfectly parallel to the crystal surface and the contact is made, the result is the same as coating the fiber. The new surface behaves like another layer in a coating already composed of many other layers. As long as the distance between the crystal and the fiber doesn't change, the change of reflectivity is not really perceptible. This design allows more flexibility to switch to other fibers if needed.

The pump beam at 532nm (green) is coupled into the system through the curved mirror, see figureFigure 7.2. The crystal is HR coated for 532nm and the curved mirror is coated for a reflection $R = 95\%$ to make sure that the green light is essentially leaving the cavity by the curved mirror and not by the fiber.

The squeezed light generated in the cavity is at 1064nm (red). The reflectivity of the curved mirror is as high as possible to be sure that no squeezing will leave the cavity by this way, and the other mirror, the one between the fiber and the crystal, is of relatively low reflectivity to make all the squeezed light escape this way.

In this experiment two types of fibers are used for the output fiber carrying squeezing: a standard single mode fiber at 1064nm and a polarization-maintaining single mode photonic fiber with a mode field diameter of $15\mu\text{m}$.

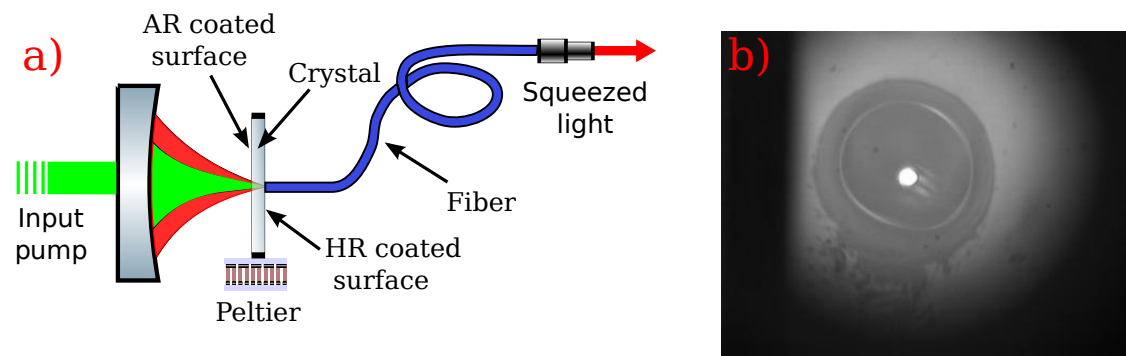


Figure 7.2.: a) The cavity is made between a curved mirror and an HR coated non linear crystal. The pump is sent to the cavity through the curved mirror, and the squeezed light generated is leaving the cavity through the fiber. A peltier element allows us to control the temperature of the system to achieve the phase matching condition. b) An image through the crystal of the fiber applied on the surface of the crystal with some liquid index spreading around it.

7.1.1. Coupling Mirror

7.1.1.1. Mirror

In order to build a compact system and to have the cavity as far from hemispherical condition as possible, the coupling mirror had to be relatively small, but cutting and coating a curved mirror on such a scale is difficult, so it becomes hard to find a manufacturer that will agree to make such a mirror. Jakob Reichel's team was able to find a company to coat mirrors much smaller (several 100th of μm of curvature) and on a much smaller system (the fiber's surface) ([19], [26]). However, it is difficult to procure them in small quantities. Ultimately, I engaged the company Altechna ([20]) to create these mirrors (Table 7.1). The mirrors are 3mm thick and have a 5mm radius of curvature with a diameter of 3mm . The back face also has a

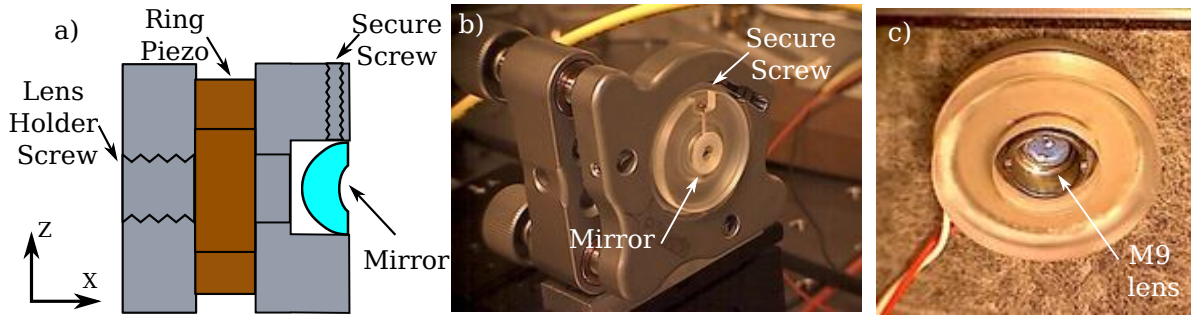


Figure 7.3.: a) Schematic of the mirror holder. A 1-inch ring with an aperture and a screw thread that allows us to mount a lens is glued to a ring piezo actuator and a smaller cylinder holding the mirror. b) An image of the mirror holder on a standard mirror mount. c) The other face of the mirror mount with a standard mounted lens fixed on it.

curvature to reduce somewhat the divergence of the beam. Without that, the beam becomes very large after the cavity, with issues of clipping of the beam on the mirror mount.

Material:	BK7
Diameter:	8 mm (+0/-0.1 mm)
Mirror diameter:	3 mm (+/-0.1 mm)
Radius of curvature:	Concave ROC1: 5 mm (spherical) Convex ROC2: 7 mm (spherical)
Surface quality:	40/20 S/D
Surface figure:	L/4@633nm Centering: <3 arcmin
Protective chamfers:	0,2 mm x 45 deg
Coatings:	S1 (ROC1): PR(R=95%+/-1.5%)@532nm + HR(R>99,5%)@1064 nm, AOI=0 deg S2 (ROC2): AR(R<0.25%)@1064nm + 532nm, AOI=0 deg
Price:	240 EUR/pc (for 5) / 180 EUR/pc (for 10)

Table 7.1.: Mirrors characteristics.

7.1.1.2. Mirror Mount

The mount for the mirror needed to be compact as well as compatible with a 1-inch mirror mount. It significantly reduces the stability of the system, but on the other hand, it allows us to change the configuration of the cavity to avoid eventual

problems of conception, and it gives two rotational degrees of freedom that could have been useful. In practice, they were not very useful, and they could have been easily replaced by a monolithic block which would allow the system to be lower and would enhance mechanical stability.

The mirror mount is placed on a positioning stage (Nanomax [67]) with a little aluminum plate to match the screws. This system is quite handy because it allows very easy modification of the whole system in case of a problem. The 3 axis positioning (0.5mm core screws + micro-metric precision screws) makes the alignment of the cavity very fast and easy. The average time to align the system is a few hours. Moreover, the long piezo in the cavity axis is very useful to have access to several Free Spectral Ranges (FSRs). But once the cavity is aligned, it is quite unlikely to be adjusted again. A good solution would be to hold the system with the Nanomax, to align it, and to use glue to fix everything in place indefinitely. Gluing cavities is a technique used by Jakob Reichel's team ([43]). With a very slow-hardening glue, we can flood the system and realign it a little bit with the Nanomax during the hardening to compensate for the expansion of the glue. The glue expands mostly at the beginning, and less and less during the process. I have not tried this technique with the system, but it is very likely that we will consider it for the next generation of miniOPO.

The mount allows the control of the three degrees of translation and the degree of rotation around the Z axis (vertical) and around the X axis (Figure 7.5 (c)). Mostly, it is only the translations that are useful. I wanted to have as many degrees of freedom as possible for the mirror. This allows us to really know which degrees of freedom are useful, and which ones can be removed later, and it makes it easier to adapt to conception mistakes.

The mirror mount is made from two cylindrical plastic parts connected by a ring piezo transducer from Noliac (NAC2125-A01 ([28])). All the parts are glued to each other using epoxy.

The part which is holding the mirror is a bit smaller than one inch so it can go through a standard mirror mount. It has a little notch so as not to have the head of the screw in the way of the mount. The notch also needs to be big enough to allow the passage of the head of a screw driver. The screw that I used was an M2 screw.

The other part is a 1 inch cylinder that fits in the mirror mount. I added to it an M9 screw thread to fit a mounted Thorlabs lens. The beam is diverging rapidly, so I wanted to be able to get a lens in the middle of the piezo ring to colimate the beam with a minimal beam waist to avoid clipping.

All the system is made of plastic and the part which is fixed to the mirror mount is a bit light, it does not make a very good counterweight for the piezo. Making this part heavier could certainly increase the piezo response of the mirror.

We have two piezos for the same directions: the ring piezo from the mirror mount is a fast piezo but with a small range (I can see just a little bit more than an FSR at

1064nm); and the Nanomax piezo in the Z axis, which has a very long range ($20\mu m$), but is very slow. To control the resonance of the system, we used the combination of both piezos.

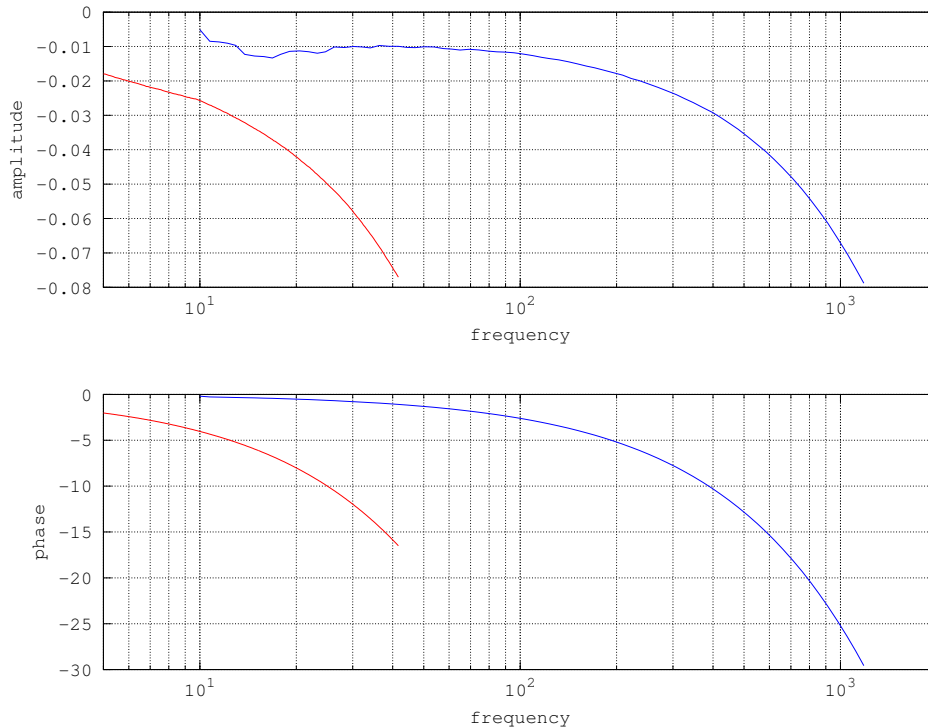


Figure 7.4.: In red, the Thorlabs Nanomax piezo frequency response; in blue, the Noliac piezo frequency response. The Thorlabs piezo has a resonant frequency at 150hz which is not visible here.

7.1.2. Crystal and Crystal Mount

Once again, the main concern for me was to make the system as small as possible to make it easy to integrate, at the same time, we still needed to allow access to the fiber holder to touch the crystal, as well as good temperature stability and good mechanical stability.

The Nanomax (Figure 7.5.c) is large in size, and constrains everything else to be quite high, so I had to make a long foot (Figure 7.5) for holding the peltier and the crystal oven (Figure 7.5.a). This setup is not, however, ideal in terms of mechanical stability. A peltier (TEC3-2.5 ([67]))(Figure 7.5.a) is sandwiched between the foot and the crystal oven, and attached with plastic screws (Figure 7.5.a) to avoid losing too much thermal energy. The horizontal extension of the crystal holder should not

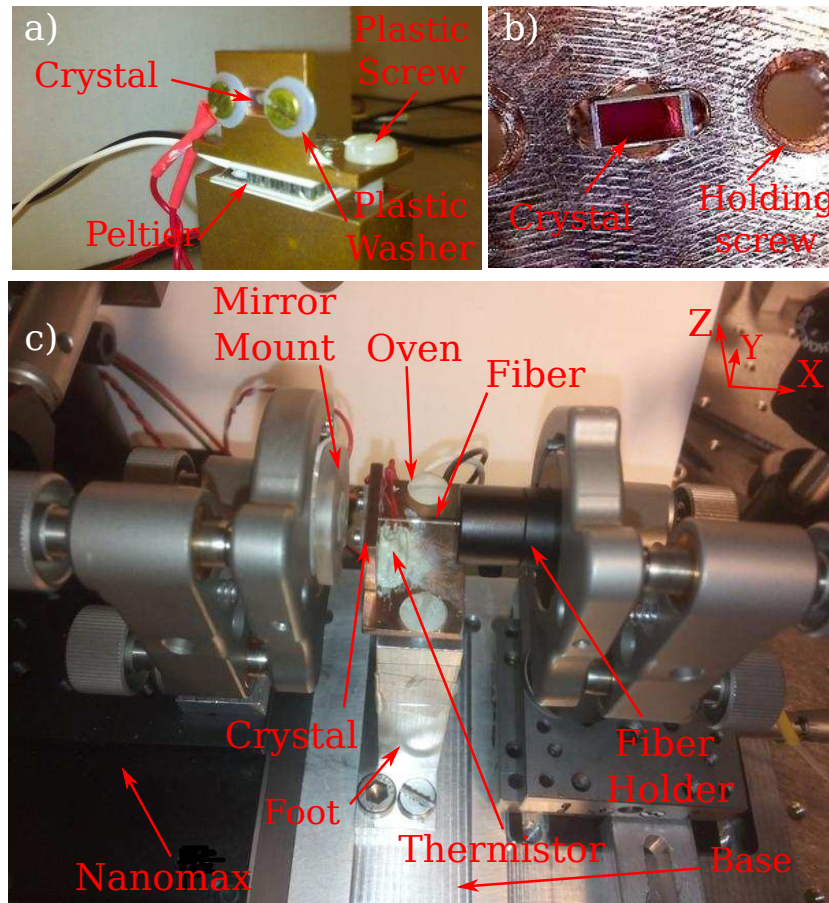


Figure 7.5.: a) Oven holding the crystal. b) Zoom of the oven hole for the crystal without the two screws and washers holding the crystal. c) An image of the whole miniOPO. On the left is the curved mirror holder on a nanomax, in the middle is the oven, and on the left is the fiber holder with the fiber touching the crystal. The fiber holder used here is the one holding the photonic crystal; the fiber holder holding the standard fiber is of a custom design (Figure 7.6).

be too large, because the fiber holder will have to go on top of it to reach the crystal with the fiber, and a too-large foot would decrease the total mechanical stability by allowing the fiber holder to oscillate with vibrations. If it is too small, it could become a bit tilted when we attach the peltier with the two plastic screws, reducing the thermal transfer and making the alignment much harder.

The crystal oven is of an L shape, made of copper and is seated on the peltier element. It allows us to have a fast thermal exchange, and to be mechanically stable. The crystal can be slid into the compartment (Figure 7.5.b) and held with the plastic washers. The compartment is adjusted vertically, but is a bit larger horizontally. This allows us to slide in the crystal more easily. Manipulating the crystal increases our likelihood of causing scratches, so to minimize risk of damage, it should not be

too hard for us to fit the crystal in the holder. The horizontal slack also allows us to adjust the crystal somewhat if we realize that we are at the edge during alignment. On the other hand, we do not want it to be too slack, because we want to be able to remove the crystal and to put it back without altering too much the angle between the crystal and the vertical axis.

On the other side of the oven, we tried to make an opening to be able to have access with the camera on the side to see the contact between the fiber and the crystal. We found that a better technique was to use the white light interferometer (Figure 7.14). The crystal is held with plastic washers (Figure 7.5.a) to make sure that it cannot move even if some compressed air is used to clean the dust from the crystal or if the fiber is touching it. Plastic screws allow us to use a bit of strength on the crystal without scratching or breaking it.

The crystal used in this project is a PPKTP crystal from Raicol ([32]) of $1 \times 1 \times 2 \text{ mm}^3$ with one face AR coated for 1064nm and 532nm, and one face with a reflecting coating $R \sim 95\%$ for 532nm and $R \sim 85\%$ for 1064nm Figure 7.5. The cavity when aligned possesses a finesse of 35 for 1064nm and 110 for 532nm.

On the crystal oven, I glued a 10KOhm thermistor (TK10K [67]) (Figure 7.5.c) using a thermal paste resin to allow us to measure the temperature of the crystal and feed it back to the peltier.

7.1.3. Fiber and Fiber Mount

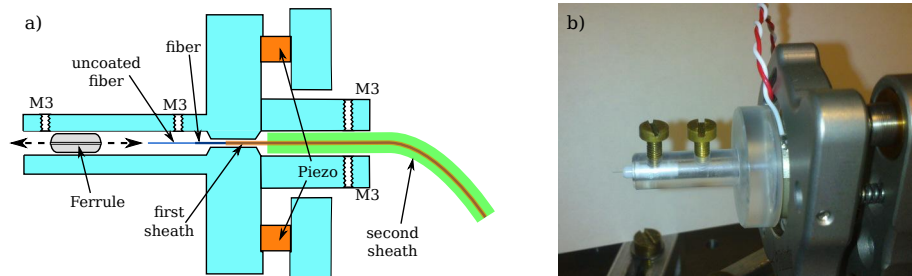


Figure 7.6.: a) A schematic of the fiber holder for the standard fiber. A groove with M3 screws can hold a ferrule in front of a groove holding the fiber sheath, allowing us to put the fiber easily in the ferrule. A piezo glued to this piece and another piece allows us to control the translation of the fiber. The small middle hole is too small for the piece to be made in one time; a very long and thin drill bit would be required. A simple solution is to make two pieces and glue them together. b) An image of the fiber holder on a mirror mount.

The cavity is directly coupled to a fiber placed against the high reflective coated surface of the crystal. The end surface of the fiber needs to be as flat as possible and perfectly parallel to the crystal surface otherwise the transmitted beam will not

be optimally coupled to the fiber and some losses will appear. (Figure 7.9) shows the effect of misalignment on the coupling.

Two types of fibers have been used in this thesis: a standard single mode fiber for 1064nm (P3-980A-FC-5 [67]) and a large mode area polarization maintaining photonic crystal fiber (LMA-PM-15 [67]). They do not have the same diameters, so different fiber mounts had to be used. For the photonic fiber, a commercial fiber holder (BFTU [67]) is fixed in a 1 inch custom ring that can be fixed into a standard mirror mount (Figure 7.5.a). The alignment is hard because the fiber is held far away from the crystal and only on one point. It usually creates a large angle with the mount which needs to be compensated for during alignment, moreover the system gets a lot of acoustic noise and may move when moving the fiber. The single mode fiber is held by a more carefully designed system (Figure 7.6) which gives a much better stability and makes the alignment easier.

The end of the fiber is made flat by using a cleaver from Nyfors ([29]). But it necessitates the removal of a few centimeters of coating sheath from the fiber, which makes it quite fragile, especially the single mode fiber which has a smaller diameter ($125\mu\text{m}$ compared to $230\mu\text{m}$ for the photonic fiber).

A ferrule is used to hold the uncoated fiber. It is difficult to put the fiber in, but the ferrule holds it very well and in a very convenient axis, simplifying the alignment. Moreover, the holder makes the placement of the fiber in the ferrule quite easy. A ferrule is slid into the front of the holder and falls where the diameter becomes thinner, see Figure 7.6. A screw hole allows us to fix the ferrule to make sure that it doesn't slide during the process. The fiber is placed in a plastic sheath ([31]) and slid at the back of the holder in the small diameter part of the holder. The fiber usually emerges exactly in front of the hole of the ferrule and slides into it. When the coated part of the fiber meets the ferrule, it can't go through and it blocks the fiber. The ferrule can be unscrewed and will slide to the end of the mount. Another screw hole allows us to fix the ferrule at the end of the holder giving a very good stability to the system. Two screws at the back of the holder gently squeeze the fiber to prevent it from moving at all. By using several sheaths of different diameters that can slide in each other (PTFE AWG 30 T and PTFE 0,9 x 2,4 mm [31]) I made sure that all the fiber is covered to protect it against bending and to also thermalize it.

The holder also contains a piezo sandwiched between two pieces of plastic. Moving this piezo can be useful during an initial alignment. But with a good illumination used in the white light interferometry system (Figure 7.14) it is very easy to see fringes without it. In a future design, the piezo will be removed and the holder shortened which will add a lot to the mechanical stability of the system.

The holder is designed in a 1 inch cylindrical shape to fit into a mirror mount. It gives two degrees of rotation allowing us to align the fiber perpendicular to the crystal. Unfortunately, the holder is quite long so moving the rotation degrees can create a big translation laterally and vertically. It is necessary to be able to compensate in those two directions. The mirror mount is attached to a regular sliding foot to

be able to adjust the height. This sliding foot is itself fixed on two micro-metric translational stages (M-UMR5.16 [65]): one to adjust the lateral mismatch, the other one to control the distance between the fiber and the crystal to get contact between them when the alignment is well done. The micro metric translation and especially the sliding fit are contributing to the instability of the system and how much acoustic noise gets coupled to the cavity. In a future design, the holder will be shorter and the mechanical alignment of every piece simpler. Hopefully, it will not be necessary anymore to compensate in those two directions allowing the mirror mount to be mounted on a rigid piece and increasing a lot the general stability.

7.1.4. Base

To decrease a bit the global acoustic coupling from the table, I installed the cavity on a big piece of aluminum to give rigidity to the whole system, see Figure 7.5. There are some very small grooves of an L shape to place the other components (Nanomax with the mirror mount, crystal holder and fiber holder). It allows us to remove the components and put them back in almost without changing alignment. It saved a lot of time and made it very easy to move the entire system.

A fine layer of material has also been removed on the other side of the mount, making the contact with the table on four very small squares. By minimizing the contact surface in this way, we decrease the acoustic coupling between the table and the system which allows a better stability. Some grooves on the side have also been added to be able to clamp it easily to the optical table.

7.2. Other experimental consideration

7.2.1. Laser Source

In this experiment, a Diablo laser from Innolight ([25]) producing light at 1064nm and 532nm have been used. This laser is using a Nd:YAG crystal pumped with a diode laser to create light at 1064nm. The crystal is coated on each side to make a monolithic cavity with a very small linewidth (around 1kHz). The light is then brought to a second cavity with a doubler crystal to generate light at 532nm. The temperature of the Nd:YAG can be changed from 20°C to 43°C which changes the refractive index of the crystal, changing the frequency of the laser to around 60Ghz. This effect is very slow and some mode hops corresponding to jumping to another FSR will appear every 12-16Ghz. Another way of changing the frequency of the laser is available by using a piezo actuator attached to the Nd:YAG crystal. By modulating its length it allows us to adjust the frequency at a rate of 2 to 4MHz/V allowing a modulation between -100V to 100V with a bandwidth of around 1Khz. The laser noise can be attenuated with a noise eater. It is an active feedback signal on the diode current to get a beam close to shot noise limit in the MHz regime.

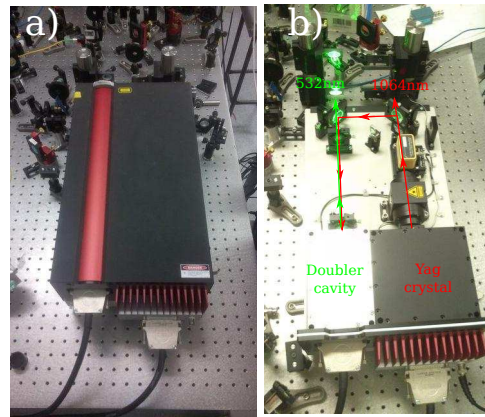


Figure 7.7.: The Diablo laser (a) providing two different light frequencies, 1064nm (red) and 532nm (green). Inside the laser (b) a YAG laser is providing some light at 1064nm which is brought to a cavity with a doubler crystal to create 532nm light.

7.2.2. Fibered Elements

Fibers are interesting because they allow easy integration and propagation of the light from one experiment to another, but they also allow a lot of direct control of the light parameters. By stressing the fiber it is possible to change the polarization of the light. So by looping the fiber in a specific way, it is possible to create $\lambda/2$ and $\lambda/4$ in the fiber path. Two fibers can be partly fused together in well-controlled condition to allow evanescent coupling between the two guided fields which makes a fiber beam splitter. An electric field can be applied on the fiber to change its refractive index and to control precisely the phase of the propagating light. Connectors which make two fibers very close in front of each other connect them with losses between 20 percent down to a few percent. And by cleaving and splicing fibers, a very good connection between two fibers of the same type can be achieved.

In this experiment, two fibers have been tested to couple the squeezing out from the cavity: a standard single mode fiber which requires a very small mode size in the cavity, and a photonic fiber which is single mode for a long range of frequencies and allows a larger mode size. I usually used a 4 or 5 meter connected fiber and cut it in the middle with a cleaver to have two usable fibers for the system. The connectors on the other part of the fiber are very useful. It is usually a FC/PC or a FC/APC. The FC/PC has a flat end face perpendicular to the fiber axis. Because the other surface on the other side is also perpendicular to the fiber axis, a parasitic cavity can appear in the fiber. But it is better when one has to connect two fibers together with a connector. The FC/APC has 8° between the normal of the end surface and the fiber axis avoiding the reflecting beam to come back into the fiber and therefore to build a cavity. Both FC/PC and FC/APC are quite reliable. The screw and the groove allows them to be removed and plugged back in an adapted female connector

on a stable post without losing too much coupling in the fiber. It allows very easy and fast modification of the system.

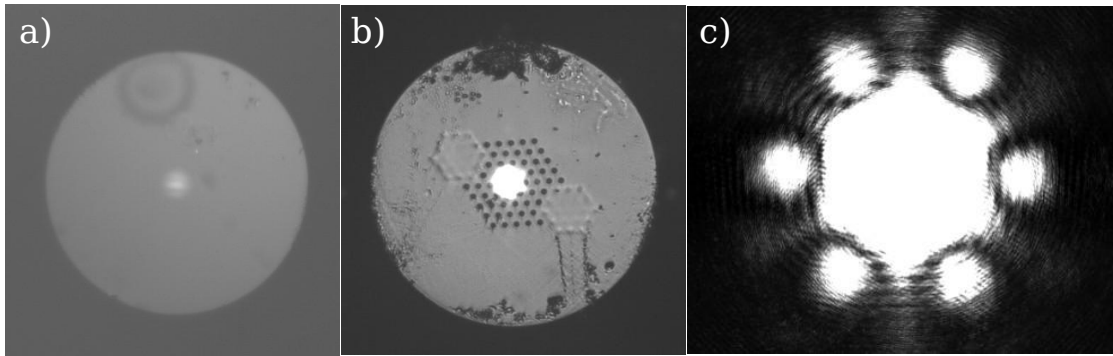


Figure 7.8.: a) Cleaved face of a standard fiber. b) Cleaved face of a photonic polarization-maintaining fiber. c) Mode coming out of the photonic fiber.

7.2.2.1. Standard Single-Mode Fiber:

Single mode fibers at 1064nm generate only around 2dB of losses per kilometer which is negligible in this experiment. Their big advantage is the fact that they are very common. They are very cheap and available with plenty of different connectors, sheaths and lengths by standard. The technology is well established so it is easy and cheap to get some compatible elements that can work with it. One can find fiber phase shifters that can change the phase of as much as 50π ([30]), fiber beam splitters (like the FC1064-50B-APC ([67])) or polarization controllers to change the polarization of the beam from any point of the block sphere to any other point (like the FPC030 ([67])). It is also possible to fuse two of these fibers with a splicer with a very small amount of losses.

The inconvenience of these fibers is the very small size of its core. For being single mode, the core of the fiber needs to be smaller than a threshold value, to forbid the propagation of higher order modes. It constrains the mode field diameter at the output of the fiber to be $6.2\mu m$. And because the fiber mode will define the mode of the cavity in our system, it will constrain the waist radius of the cavity to be of $3.1\mu m$ which is very small. It makes the cavity very close to Hemispherical conditions.

7.2.2.2. Thorlabs Endless Single Mode, Large Mode PCF Fiber:

The Photonic Crystal Fibers (PCF) are standard fibers with the core engineered with a lot of holes to propagate only one mode with a very large mode diameter at the output of the fiber (up to $25\mu m$ of mode field diameters ([67])) and 5dB/km of attenuation). It is possible to design them to be polarization maintaining, which

means they will propagate only two specific polarizations and keep them constant for the entire length of the fiber. In practice, in this experiment a $15\mu\text{m}$ mode field diameter with polarization maintaining has been used.

These fibers allow us to have a waist size much bigger in the cavity which means to be a bit further from hemispherical condition, but the technology is not as spread, so all the components like beam splitters or phase shifters do not necessarily exist, or are very expensive and they are usually sold without connectors. Furthermore, the mode in these fibers is not perfectly Gaussian and not rotation invariant. To fuse correctly two of these fibers, it is necessary to have a very good alignment which is hard to do. The fusing will collapse the holes creating an index change in the fiber potentially producing some reflection at the interface and some losses.

7.2.2.3. Cleaving Fibers:

For both fibers, the end interface which will be in contact with the crystal needs to be very well made. It needs to be very smooth to avoid scattering, and needs to be nicely perpendicular to the axis of the beam in the fiber. This surface will be joined to the surface of the cavity, so any angle difference with the axis of the fiber will end up in a difference between the mode field going out of the cavity and the mode of the fiber. If this difference is not zero, it will mean some losses in the squeezing. (Figure 7.9).

A good way to obtain a quality surface with the fiber is by cleaving it. First, with a stripping tool (T06S13 ([67])), the coating is removed from a fiber with a naked end (without connector and without protective sheath). Then a tiny scratch is made on the side of the fiber with a sharp object. And by pushing the end of the fiber (after the scratch) one makes the scratch propagate in the fiber, creating a very neat cut. There are several ways to do this: the scratch can be made with a sapphire blade (S90R ([67])). The scratch is usually huge and there is still a part of the fiber damaged on the edge after cleaving. But mostly, it is very unlikely that the initial scratch is done straight, so the fiber will end up with a massive angle between the surface and the mode axis. More generally to make a nice cut, we can use a machine that will make the scratch and pull the end of the fiber. There exist mechanical (CT-30 ([24])) and higher quality ones ([29]). For this experiment, the latter has been used. It allows us to have an angle smaller than a 0.3° for the standard single mode fibers and 0.6° for the photonic fibers. It also allows us to have a high voltage spark on the final surface to smooth it a bit more by heating it. For the photonic fiber, it collapses the holes which avoids dust going in the fiber. A good practice is to collapse them three times and turning the fiber around its axis each time to obtain a good collapsed shape. For the Photonic fiber in the experiment the holes were not collapsed at the end of the fiber touching the crystal to avoid losses, but they were on the other end.

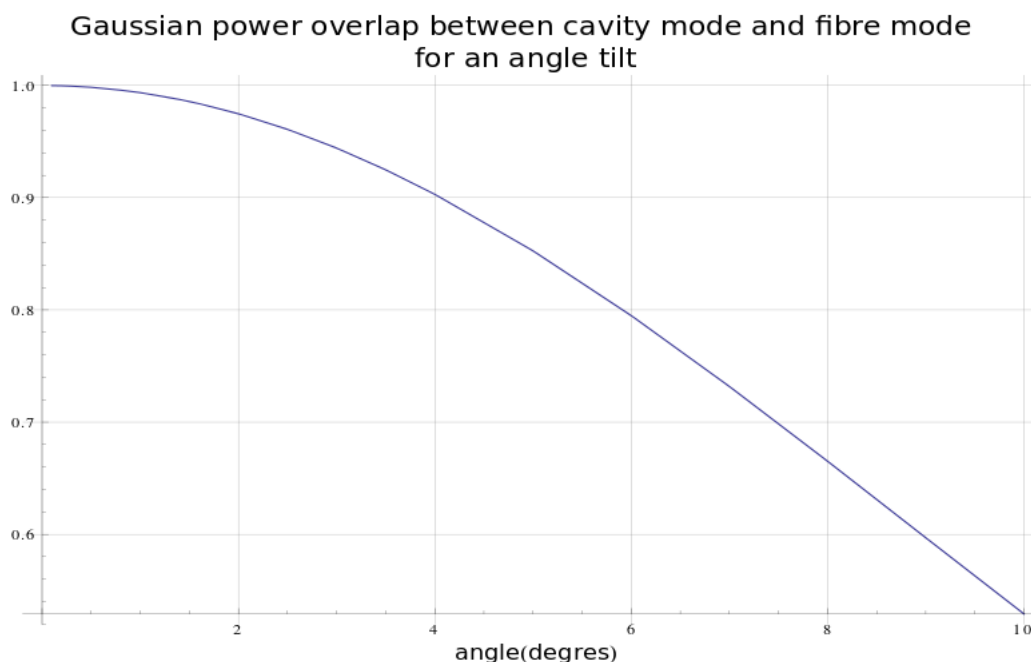


Figure 7.9.: Losses in the fiber as a function of the angle between the fiber end and the crystal.

7.2.2.4. Coupling Light into a Fiber:

Coupling light into a fiber from scratch, when no other fibers have been coupled before, can be frustrating. This process requires the position of the beam, the angle and the waist position to be very close to optimal to be able to see any light going through. When a fiber has a connector, there are commercial lens couplers to facilitate the coupling. These lenses are designed to be already very close to the optimal position for a collimated beam. It allows us to just care about the degree of freedom of positions and angles of the beam in the fiber coupler. With two mirrors it is possible to control these parameters. If a little bit of the light is already coupled in the fiber and monitored using a detector, it is possible to “walk” the beam to converge toward the maximum. It means moving out of the optimal by moving one mirror (in horizontal in one direction for example) and correct it with the other mirror. If the good direction has been chosen, the coupling increases; if not, one has to optimize the other direction. In walking the beam in this way, the optimal position of the two mirrors can be obtained. This method can be generalized with the lens’ positions. For the optimal coupling the waist position is not enough, the waist size also needs to be optimal. A good method is to start with a collimated beam (usually from the laser) using one long focal lens converging or diverging to change the size of the beam, then two identical short focal convergent lenses to collimate the beam, and a last short focal lens in front of the fiber to control the waist position (usually this one is the fiber coupler). It is possible to walk the lenses

by moving the first long focal lens for example, and correcting with the short focal lens in front of the fiber. The initial alignment of the fiber can be a bit difficult. It is much easier when some light already leaves this same fiber. One can often achieve that when the other end of the fiber has a connector and another fiber coupler is aligned somewhere else. It is possible to unscrew a fiber connector and screw another one in without moving too much the fiber coupler. It allows us to have a bit of light going out of a fiber that needs to be aligned (it still works when the fibers are not the same type, e.g. multi-mode/single-mode or different frequencies; the light is just weaker). When light comes out of the fiber, one just has to check with a good viewer card if the two contra-propagating beams are overlapping up to the laser. Usually after this process when checking for coupling, there is already a bit of light going into the fiber, and it can then be improved by walking the beam.

7.2.3. Crystal Temperature Control

The temperature control of the crystal is essential for reaching the phase matching condition and double resonance. The temperature is monitored using a thermistor TH10K ([67]) glued very close to the crystal with a thermal paste. This resistance changes its value with temperature (10 k Ω at 25° and ~5 k Ω at 40°). The temperature is controlled with a peltier (TEC3-2.5 ([67])) placed under the crystal holder, see subsection 7.1.2. This peltier is made to receive up to 6 A with ± 1.8 V. It corresponds to a lot of power that may damage electric components. It is important to design correctly the circuit to isolate the sensitive parts and to use heat sinks to dissipate heat. The power comes from a 12 V power supply, controlled with two transistors, PNP and NPN, in series (Figure 7.10). It is very important to add heat sinks on these two elements, otherwise they will burn immediately because of the power. A resistor in series with the peltier is also used to reduce the voltage to acceptable values. This resistor also gets a lot of electrical currents and will heat a lot. It is important to also add a heat sink to it. To control the heating, I used an Arduino Due ([21]). It is an inexpensive open source micro-controller with 12 analog input and 2 analog output, each one with 12 bits of resolutions. The output from the Arduino is followed by an amplifier (OP27) allowing to add an offset and a gain on the control. To measure the temperature, I used an output of the Arduino with 3.3 V connected to the thermistor, a fixed 10 k Ω resistor and the Arduino mass in a voltage divisor system to have a measurement of the temperature in tension that I can send to the input of the micro-controller directly.

The code of the Arduino is very simple: it measures the temperature, compares it with a reference, and consequently heats or cools the peltier. It is important to have pauses in the code to leave some time for the heat transfers, otherwise the temperature will oscillate. I reached a stability of around a few hundredths of a degree with this system.

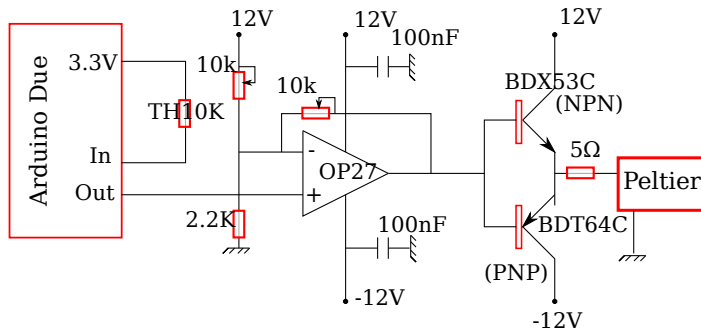


Figure 7.10.: Schematic of the temperature controller of the crystal.

7.2.4. High Voltages Amplifiers:

The two piezos controlling the position of the curved mirror are driven by two high voltage amplifiers: one is the Thorlabs MDT630B controller used to control the Nanomax positioning stage, and the second is a custom high voltage amplifier built by our electrical workshop at the LKB. The response in frequency of these HV amplifiers is given in Figure 7.11.

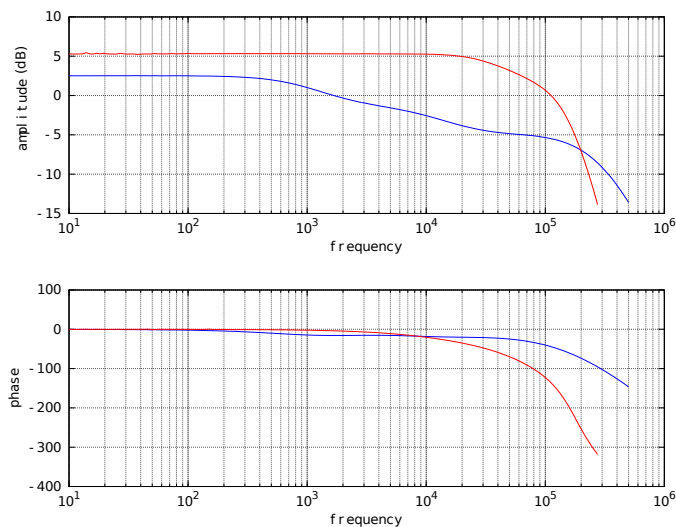


Figure 7.11.: Phase and amplitude response of the High Voltage amplifiers: (red) from Thorlabs to control the nanomax, and (blue) a custom one to control the piezo of the mirror holder.

7.2.5. Homodyne Detectors

The squeezing from the fiber is measured using homodyne detection. The light going out of the fiber from the cavity is mixed with the Local Oscillator (LO), which is coming from a similar fiber using a 50/50 Non Polarizing Beam Splitter (NPBS). The

two fibers have identical out-coupler lenses to collimate both beams in the same way and the distance between the two fibers and the NPBS are very close to match the divergence of the two arms. The LO also goes through a polarization beam splitter and a $\lambda/2$ to make sure that the polarization is linear, and to be able to control its direction. The two output beams from the NPBS are sent to two identical detectors (with two InGAs photo-diodes p/n FD500W-1064, with no window purchased from Fermionics ([23])) with identical mirrors and lenses to match the losses between both. The subtraction of the diode photocurrents is the measurement of our signal. With the signal from the cavity blocked, it is possible to measure how good is the splitting and how good is the difference. By measuring the signal from the difference of the two detectors with a spectrum analyzer, Figure 7.12, and by blocking one of the detectors we can observe the modulation of the light due to the laser (Figure 7.12 (a)). By unblocking the detector, the classical noises disappear and we observe the shot noise.

The fiber also couples light at 532nm from the cavity which will be propagating with the light at 1064nm, but as long as the mirrors used are not reflecting for 532nm, only a very small amount of green will actually hit the detectors, and InGAs is almost insensitive to 532nm, so no effect should be observed because of it.

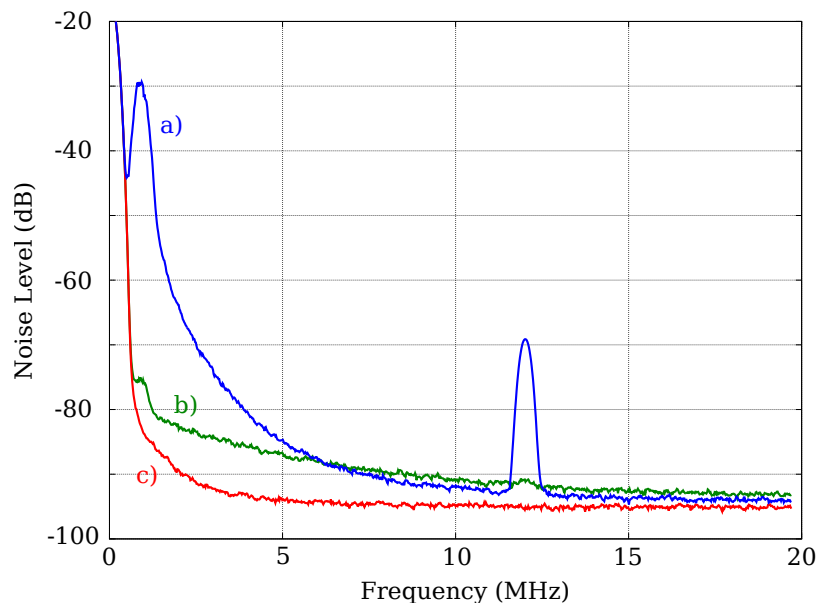


Figure 7.12.: a) Signal from the homodyne subtraction with one detector blocked and the signal fiber blocked. b) With the other detector unblocked (shot noise), the classical noise is almost completely removed. c) With both detector blocked (dark noise). The peak at 12 MHz is the modulation coming from the laser. It is completely canceled with the two detectors.

7.2.6. Optical Suspension Table

All the optics, the laser and the cavity are screwed onto our optical table. The legs of this table use active vibration isolation to limit vibration noises from the ground coupling to the experiment. Pneumatic chamber systems in the legs are connected to an air compressor to isolate low frequency vibrations.

7.3. Alignment of the Cavity

7.3.1. Schematic of the Set Up

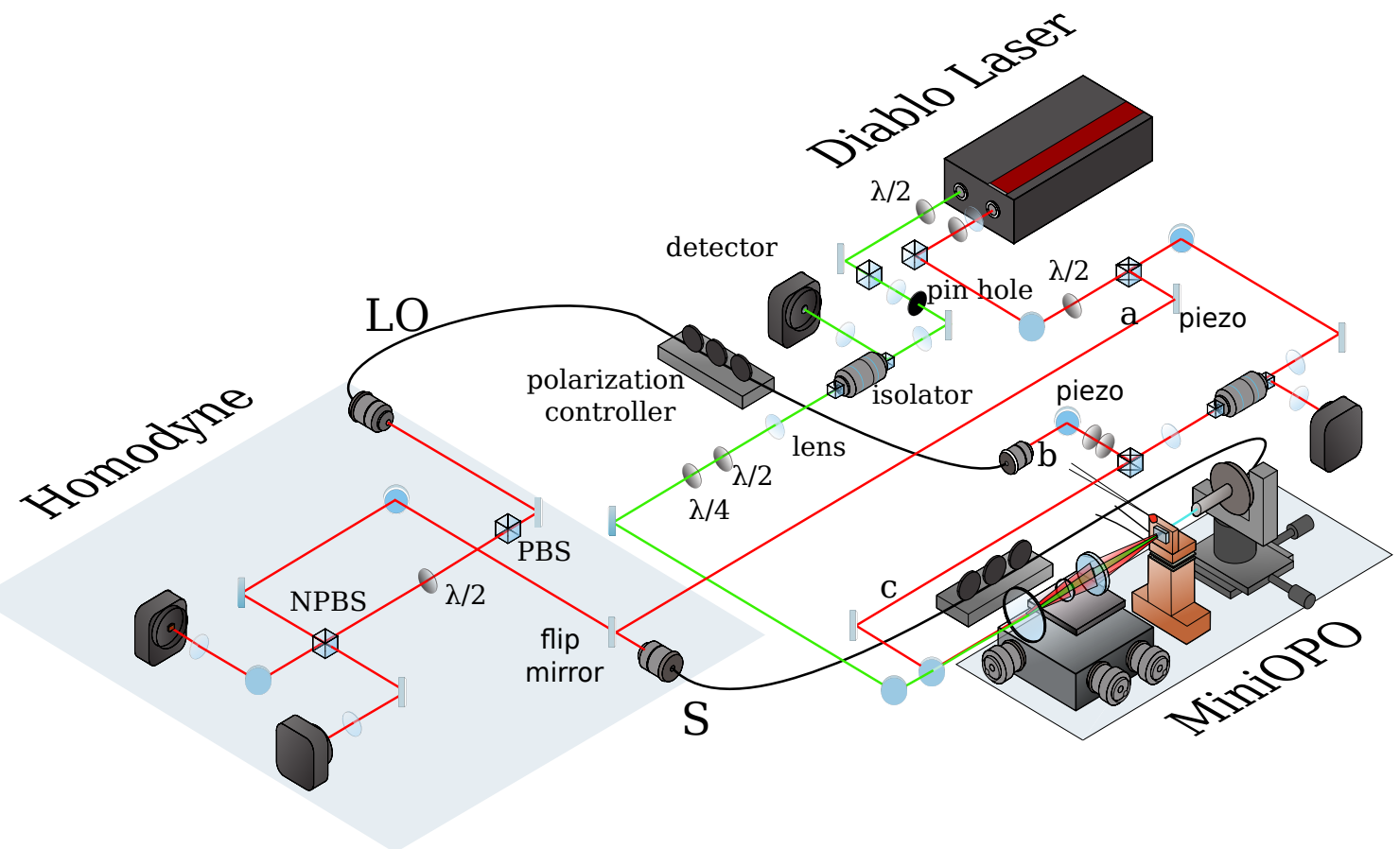


Figure 7.13.: The Diablo laser creates light at 532nm (green) and 1064nm (red). The green is sent to the cavity through an isolator and the reflection returned to the isolator is sent to a detector. The red beam is divided into three beams: (a) is used for alignment of the cavity, (b) is used for the LO and (c) is for sending a seed to the cavity. The fiber coming from the cavity S is sent to the homodyne detection to be measured.

The Diablo laser (Figure 7.13) provides the two light frequencies that will be used in this experiment, 532nm (green) and 1064nm (red). On each path, $\lambda/2$ wave plates and Polarizing Beam Splitters (PBS) are used to control the power of the beams used in the experiments. The green beam is spatially cleaned with a pin hole and sent to an isolator. The isolator provides access to the return beam, which can be sent to a detector, rather than returning to the laser. The transmitted beam goes through a $\lambda/2$ and a $\lambda/4$ waveplates for the polarization control and is sent to the cavity through a dichroic mirror. The red beam is split in two by a $\lambda/2$ waveplate followed by a PBS. One of the arms (a) in Figure 7.13 is used for alignment. A mirror on a piezo controls its phase and sends it, with a flip mirror, to the fiber coupler of the signal (S). The flip mirror stays on only during the alignment of the cavity, otherwise, it is flipped off to let the signal beam go through to the homodyne detection. The second red beam is sent to another isolator and split in two. One of the beams (b) is sent to the fiber coupler of the local oscillator with, once again, a piezo to control its phase. The other beam (c) is mixed to the green path with the dichroic mirror and sent to the cavity as a reference beam. The polarization in both fibers can be tuned with polarization controllers (FPC030 ([67])), that is, cylinders containing several loops of fiber that change the polarization by bending the fibers. They correspond to two $\lambda/2$ and one $\lambda/4$ waveplates in the middle. This configuration can transform any polarization of the Bloch sphere to any other one. I only had these polarization controllers for standard fibers. For photonic fibers, the fibers themselves are polarization maintaining and I used standard $\lambda/2$ and $\lambda/4$ waveplates to control the polarization. The two fibers are taped to the table to avoid thermal fluctuations. In the homodyne part (Figure 7.13), the LO goes through a PBS to make sure that the polarization is as good as possible and a $\lambda/2$ to control the direction of this polarization. The LO and the signals are mixed on a non polarizing 50/50 beam splitter and detected by InGaAs detectors.

7.3.2. Crystal Alignment with White Light Interferometry



Figure 7.14.: Interference pattern between the crystal face and the fiber end observed with the camera. From left to right the fiber alignment is better and better until the two faces are parallel (right).

7.3.2.1. Fiber Holders:

To align all the system one needs to start with the fibers. With standard single mode fibers, it is possible to buy a long connected fiber, cut it in the middle and cleave the bare parts. The connected parts of the fiber can then be fitted into standard coupling systems, which are relatively easy to align. With a photonic fiber, one still needs to cleave one side, but these fibers usually come without connectors, so it will be necessary to create a connector to hold the fiber at the other end and couple light in it; however, this will impair our ability to disconnect and reconnect a fiber, and still maintain a relatively good coupling.

Even with standard connectors, for fibers at the level of the homodyne, disconnecting and reconnecting the LO fiber or the signal fiber means having to realign the homodyne detections, so it is something to avoid. It is important to notice that pulling too much on these fibers close to the connectors can misalign them slightly, so it is a good idea to always tape the fibers carefully to the table after the connectors to avoid movements.

I usually start by aligning the signal fiber coupler to have some light in the cleaved fiber end with only the fiber holder placed on the base (Figure 7.5.c). In the schematic Figure 7.13 it corresponds to align the alignment beam (a) into the coupler of the fiber signal with the flip mirror up. For the standard single mode fiber, I used standard FC/APC connectors and couplers (F220APC-1064 ([67])) for the photonic fiber I used an old version of the cavity fiber holder with a 1 inch cylinder to go in a standard mount and a fine tube holding the bare fiber in a sheath with a screw. I put this holder in a translational stage (SM1Z ([67])) with a lens with a short focal to make the coupler. Then I aligned the other fiber corresponding to the LO (beam (b)) with two similar couplers.

When the signal fiber is in position in the fiber holder (Figure 7.6), it is a good idea to clean the end of it, because it could have become dirty going in the mount. I usually check the surface (Figure 7.8) with a camera attached to a microscope lens (X20) and clean the fiber with a lens tissue.

7.3.2.2. Crystal Holder and White Light Interferometry:

The crystal needs to be placed in the crystal holder with the HR face in the direction of the fiber, then the holder is placed on the foot with the peltier in the middle. The foot is then screwed to the base in front of the fiber holder along the L shape designed for it. It is possible to look on the side with a camera (in this experiment we used the DNT DigiMicro camera ([22]) which is cheap and can see the light at 1064nm, with a good resolution and which is quite reliable for this kind of camera). It is possible to get the fiber under a few millimeters to the crystal without touching it, but to get closer and to align the fiber to the crystal, a more precise system is required. I used a camera (DCC1545M ([67])) connected to a beam splitter (CM1-BP145B1([67])) and a X20 microscope lens placed behind the crystal to create a

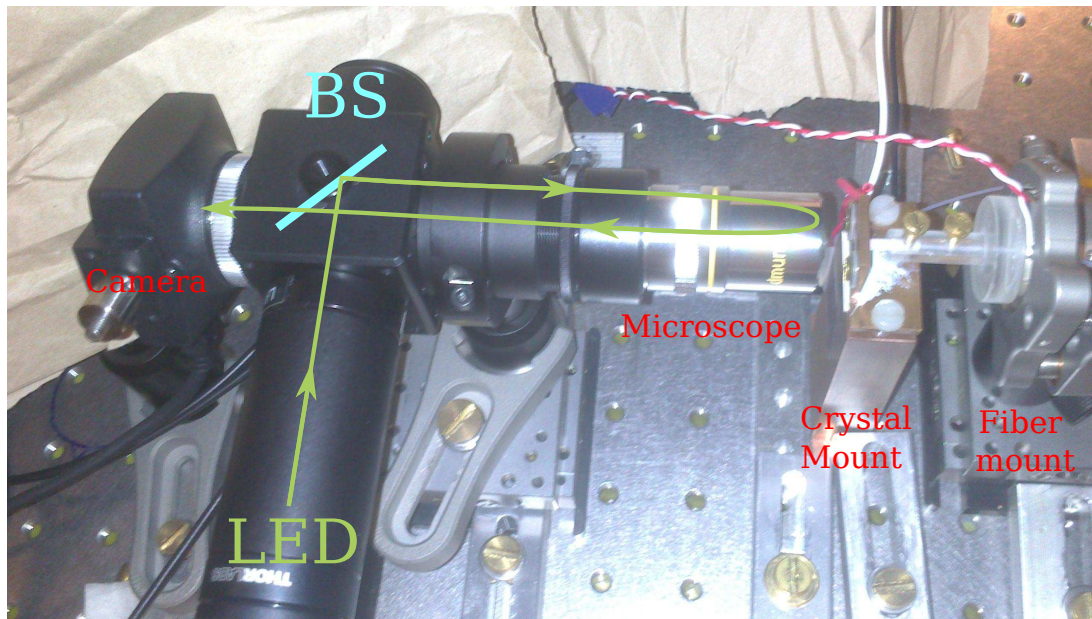


Figure 7.15.: White light interference system. The light from a red LED is collimated and sent to the crystal and the fiber end through a beam splitter. The light interferes between these two surfaces and returns to the camera. If the two surfaces are close enough, we observe interferences.

white light interferometer (Figure 7.15) to see interference patterns between the crystal and the face of the fiber. With this system, I can look at the fiber end through the crystal and measure the separation and the misalignment very precisely. The beam splitter of the interferometer is in a cage that allows other components like tubes, cameras and microscopes to be screwed to it. I used a simple red LED with a short focal lens to make the illumination, and the whole is placed on two or three translational stages to be able to move the system in all directions.

Finding the fiber with the camera is not always easy. A good trick is to use some light going in the fiber by the other end from the laser. With enough power the light is everywhere and it is easy to find the center and to focus it with the camera reducing each time the power to avoid burning the camera. When the light is perfectly in one dot, we can usually see the image of the fiber very well. The distance between the fiber and the crystal can then be reduced in moving the translational stage of the fiber holder until some interference patterns can be seen (Figure 7.14). This step is a bit dangerous at first, because it is hard to know if the interference patterns are not visible because the distance is still too far, or if the fiber and the crystal are already touching, but there is too much of an angle to see anything or the light illumination is not focused correctly leading to the damaging of the crystal. I used to use the piezo on the fiber mount moving at low frequency. The movement is visible with the camera because of the very long arm, so the contact becomes obvious, but when the lighting in the white light interferometer is set correctly, the interferences are very

visible and this step becomes useless. When the interference pattern can be seen, it is possible to know what is the angle between the surface of the end of the fiber and the crystal, and in which direction is the misalignment. Then I usually back the fiber off a little bit for safety and I adjust the mirror mount of the fiber holder to move the fiber in an orthogonal direction from the interference pattern. This movement also needs care, because moving the angle of the fiber mount generally also moves the distance between the two interfaces, and one doesn't want to scratch the crystal with the fiber. If the camera is not moved it is possible to continue to monitor the fiber and the appearance of the interference pattern. The fiber may have arrived at the end of the crystal during this procedure. If the misalignment is horizontally, it can be adjusted by the other translational stage of the fiber holder. If the misalignment is vertically, it will be necessary to back off the fiber a bit more, and move the mirror mount's height. A fiber holder less long and better care during the initial manufacturing of the holders may make these steps useless, making the need for an adjustable mount unnecessary and therefore increase the general stability of the system. When the interference pattern is flat, the fiber and the crystal are aligned.

At this point it is possible to back off completely the fiber with the translation stage and come back without changing the angle. So it is possible to back off, touch very slightly the fiber with a drop of index liquid (G608N3 ([67])) and go back to contact. It is not possible to see the pattern anymore with the index liquid, but the contact is very obvious, as the liquid spreads at the contact with the crystal. The liquid adds a little bit of stability to the system, because it is a bit elastic and a bit sticky, but it doesn't change substantially the reflection coefficient.

7.3.3. Temperature Tuning

Some red light is going through the fiber crossing the mirror. If the power is high enough, the polarization correct, and the temperature close to the functioning temperature given by the constructor, it should be possible to see some green light appearing. By collecting this light in a green detector with a dichroic, and by scanning the temperature, it is possible to find the optimal temperature of the crystal (Figure 7.16).

7.3.4. Homodyne Alignment:

In the homodyne, the fiber mount connections are not stable enough for us to be able to remove a fiber and put it back without misaligning it a bit. So when the fibers for the signal and the local oscillator (LO) are in place, they can't move anymore. It would make sense to align the homodyne after aligning completely the cavity, but it means we need to be able to lock the cavity during a long time to have a reference beam to align to the LO. Another solution is to align the homodyne before putting

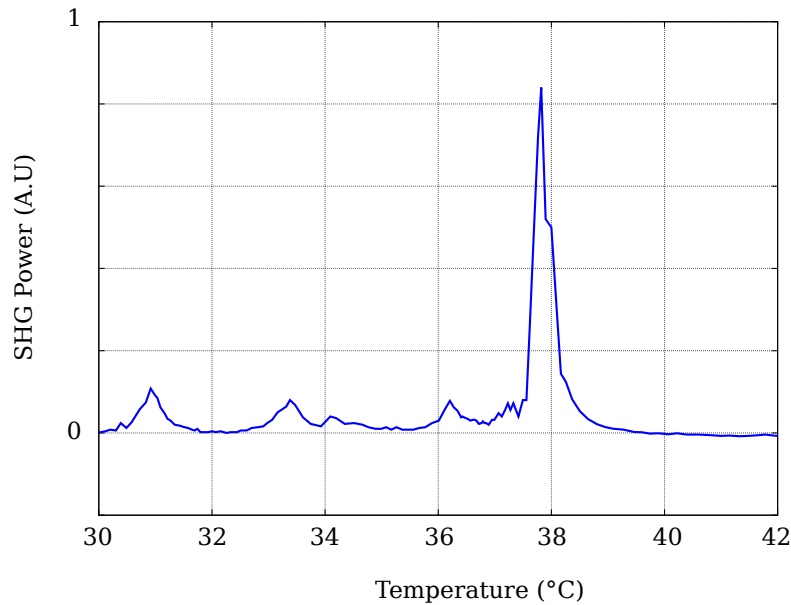


Figure 7.16.: Second harmonic generation efficiency as a function of the temperature of the crystal. The phase matching condition temperature peaks is usually more than 10°C width[38]. But the double resonance in the cavity make the peak resonance for a very narrow temperature width.

the curved mirror in the cavity. I aligned the reference beam Figure 7.13 (c) to the fiber behind the crystal. (I can have a beam going out of this fiber, and the HR coating of the crystal is not very high, so it is not much harder to align than a normal fiber.) After that, a beam goes out of the signal fiber in the homodyne, and if the LO fiber Figure 7.13 (b) is also aligned, it is possible to start to align the two beams in the homodyne (with, of course, the flip mirror down).

I usually start to align the LO without the signal. The NPBS needs to be perfectly 50/50 to make sure that the difference signal from the two detectors is zero. In practice the NPBS is not perfectly 50/50 and not perfectly polarization insensitive. It is possible to adjust the angle of the NPBS or to move the polarization direction of the LO to generally obtain a very good extinction (it assumes, of course, that the two detectors are identical, which can be verified by switching them). When the LO is equally split between the two arms, the signal can be aligned to it. A good way to do this is to modulate the phase of the LO with the piezo before the fiber (around 50hz). The piezo needs to be glued nicely in the middle of the mirror and to be close to the fiber, or the modulation may induce some amplitude modulation due to angle jitter of the beam at the coupling in the fiber. With the same power for the LO and the signal on one detector, and with good initial alignment, oscillation due to interference appears in the oscilloscope from the detector. By increasing these oscillations, the alignment and the polarization of the two beams can be optimized. When the beams are perfectly aligned, the interferences should reach zero. By

measuring the visibility: $v = \frac{V_{max} - V_{min}}{V_{max} + V_{min}}$ with V_{max} the maximum of intensity of the oscillation and V_{min} the minimum, we can measure how good is the alignment of the homodyne. The remaining misalignment will correspond to losses on the squeezing: $L = (1 - v^2)$.

In this thesis, the visibility for the standard fiber homodyne is $v = 96\%$, the visibility for the photonic fiber homodyne is 92% .

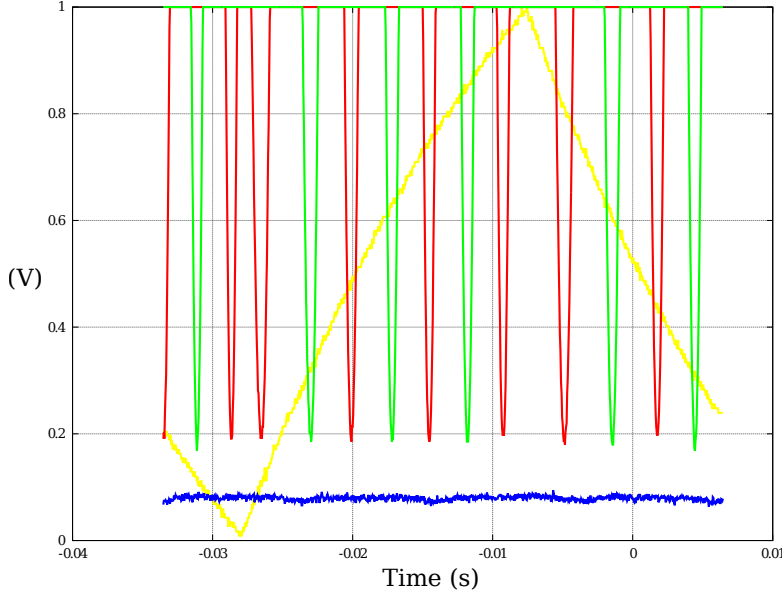


Figure 7.17.: Oscillation of the interference fringes (green and red) for both detectors of the homodyne during the scan of the phase of the LO (yellow). Blue is the signal when both detectors are blocked.

7.3.5. Curved Mirror:

At this point some light should be coupled in the fiber, it is then possible to add the curved mirror on the Nanomax. The alignment of this mirror is quite easy, by scanning the distance with the nanomax piezo, and by looking behind the mirror with the DNT camera with enough light in the fiber and the curved mirror close enough to the crystal, it is usually possible to see a tiny bit of light flashing. Usually one can see two light spots. With the translation screws of the Nanomax, it is possible to bring these spots together, and some TEM modes should appear. (the finesse for red is around 35.) With the Nanomax screw controlling the length of the cavity, it is possible to get rid of most of the high order modes. Unfortunately it is not possible to completely get rid of the higher order modes (Figure 7.18). This means that the squeezing generated in the cavity will experience losses in entering into the fiber. By measuring the area under the peaks, it is possible to have an idea of how much losses correspond to this mismatch of mode. We obtain 55% of

losses for the standard fiber and 23% for the photonic fiber. This issue is due to the very long length of the cavity for such waist sizes. The cavity is very close to hemispherical condition which could explain those losses. A curved mirror with a smaller curvature or a bigger fiber should reduce the problem in the future. At this point, when scanning slowly, it should be possible to see the transmitted light with an IR card and align a detector. If the temperature is not too far from the phase matching condition, some green light from SHG may also be visible.

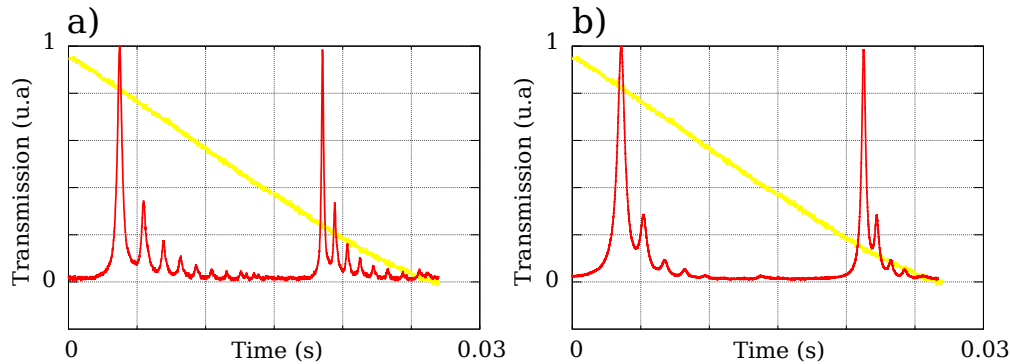


Figure 7.18.: Optimal coupling between the mode of the fiber to the TEM00 mode of the cavity for (a) the standard fiber, and (b) the photonic fiber. The light at 1064nm is coming from the fiber and measured (red) after the curved mirror during a scan of the length of the cavity (yellow). By comparing the integral under the peaks we can have an estimation of the losses due to the mismatch between the mode of the fiber and the mode of the cavity. We get 55% of losses for the standard fiber, and 23% for the photonic fiber.

7.3.6. Alignment of the Green and Red:

Now that there is a red beam going out of the cavity, it is very easy to use it to roughly align the reference beam to the cavity. Then one of the homodyne detectors can be used to maximize the coupling (with the alignment flip mirror down). The same holds for the green beam. With the right temperature (around 35°C) and the right polarization of the reference beam (with the alignment flip mirror up), the green TEM00 is visible when scanning the cavity length and can be used to roughly align the pump to the cavity (the finesse is around 110). The detector after the green isolator is used to finally maximize this alignment.

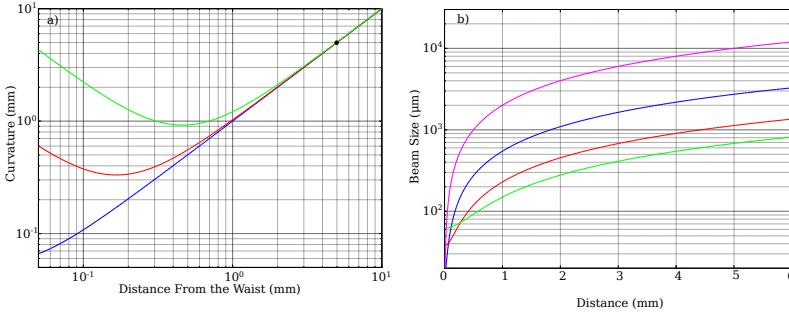


Figure 7.19.: a) Curvature of a beam from an ideal fiber as a function of the distance from the waist for: (blue) a standard fiber with $3.1\mu\text{m}$ of waist size, (red) a photonic fiber of $7.5\mu\text{m}$ of waist size (the photonic fiber used in this experiment), and (green) a photonic fiber of $12.5\mu\text{m}$ of waist size. (Such fibers exist, but haven't been used in this thesis.) The black dot corresponds to the curvature of the mirror used in this thesis (5mm). b) Size of the beam (five times the waist) in function of the distance from the waist for (blue) the standard fiber, (red) the $7.5\mu\text{m}$ photonic fiber and (green) the 12.5 photonic fiber. The purple line corresponds to the radius of a mirror with a radius of curvature equal to the distance.

7.4. System Limitations

7.4.1. Curvature Matching

To couple all the light from the cavity to the fiber, it is necessary that the mode of the fiber and the mode of the cavity be matched. It means that the waist position needs to be at the level of the fiber and the waist size of the cavity needs to be the same as the waist of the fiber. It is a very big constraint because to stay single mode, a standard fiber needs to have a very small core, which implies a very small waist size. A standard single mode fiber at 1064nm has a waist of $3.1\mu\text{m}$, and the PCF fiber that I used in this experiment has a waist of $7.5\mu\text{m}$. These waist sizes are really small and will make the cavity very close to hemispherical conditions and very sensitive to any fluctuations.

A Gaussian beam field is given by:

$$E(z, r) = E_0 \frac{w_0}{w(z)} \exp\left\{-\frac{r^2}{w^2(z)}\right\} \times \exp\left\{-i\left(kz - \tan^{-1}\left(\frac{z}{z_R}\right) + \frac{kr^2}{2R(z)}\right)\right\} \quad (7.1)$$

where $w(z) = w_0 \sqrt{1 + \left(\frac{z}{z_R}\right)^2}$, $z_R = kw_0^2/2$, z is the distance from the waist and $R(z) = z \left(1 + \left(\frac{z_R}{z}\right)^2\right)$ is the radius of curvature of the beam. Figure 7.19 (a) is showing the curvature of the beam in function of the distance exiting three different

fibers, that is, the two fibers used in this thesis, and a larger core PCF fiber that has not been tested in these experiments. We can see that the curvature is asymptotically linear. This asymptote actually corresponds to the instability position, when the equivalent length of the cavity $d = L + L_{cry}(\frac{1}{n} - 1)$ is equal to the radius of curvature of the mirror $d = R_m$, with n the index of the crystal, L the length of the cavity, L_{cry} the length of the crystal and R_m the radius of curvature of the mirror.

The Rayleigh length of the cavity is given by:

$$z_{Rc} = d\sqrt{\frac{R_m}{d} - 1}$$

If we calculate the coefficient (in power) of the projection of the Gaussian mode of the cavity (with Rayleigh length Z_{Rc}) onto the Gaussian mode exiting the fiber (with Rayleigh length Z_{Rf}), we obtain:

$$P = \frac{4z_{Rf}z_{Rc}}{(z_{Rf} + z_{Rc})^2}, \quad (7.2)$$

We can obtain the losses due to the mismatch between the mode of the fiber and the mode of the cavity as a function of the length of the cavity (Figure 7.20).

Moreover, we know that the length of the cavity has to respect $L + L_{cry}(n-1) = p\lambda/2$ with p an integer. We can notice that for the standard fiber a distance of $\lambda/2$ from the optimal position corresponds already to 12% of losses. Such a sensibility in the matching of the mode is due to the hemispherical conditions.

Those losses are too small to explain the losses observed in the mismatch between the two modes (Figure 7.18) or the losses measured on the squeezing (Figure 8.2), but It shows that the hypothesis of a spherical phase surface for the Gaussian beam can't be applied anymore.

7.4.2. Asphericity of the phase surfaces

The phase surface of the Gaussian beam is given by:

$$\varphi(z, r) = kz - \tan^{-1}\left(\frac{z}{z_R}\right) + \frac{kr^2}{2R(z)} = \text{Cst}$$

The mirror is very far from the waist, so the variation of $\tan^{-1}\left(\frac{z}{z_R}\right)$ and $R(z)$ are slow, the phase surface become $z + \frac{r^2}{2R} = \text{Cst}$ and we obtain a parabolic function.

The surface of a spherical mirror of curvature R_0 is given by:

$$z_m(r) = d_0 - R_0 + \sqrt{R_0^2 - r^2}$$

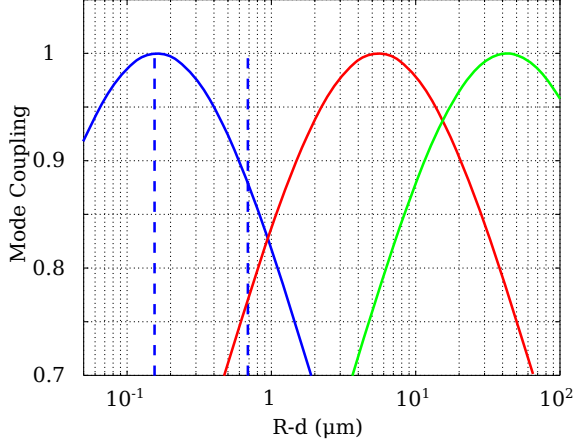


Figure 7.20.: Coupling of the mode of the cavity into the mode of the fiber as a function of the radius of the mirror (5mm) minus the equivalent length of the cavity d , for: (blue) a standard fiber with $3.1\mu m$ of waist size; (red) a photonic fiber of $7.5\mu m$ of waist size (the photonic fiber used in this experiment); and (green) a photonic fiber of $12.5\mu m$ of waist size. The blue dash lines correspond to the position of maximum coupling and a distance of half a wavelength from maximum coupling for the standard fiber.

where d_0 is the position in the z coordinate of the center of the mirror. Figure 7.21 (a) shows the difference between the phase surface at $z = 5mm$ of the Gaussian beam of waist $w_f = 3.1\mu m$ and the surface of a spherical mirror of curvature $R_m = 5mm$.

This de-phasing means that the mode of the cavity won't be Gaussian anymore, but by still considering it Gaussian anyway, and considering the projection of the mode of the light after reflection on the mirror on the initial Gaussian mode of the cavity, we obtain the coupling of higher order Laguerre Gaussian modes:

$$L = 1 - \int |E|^2 \exp(2\Delta\varphi) dx dy / \int |E|^2 dx dy$$

(Figure 7.21 (b)) with $\Delta\varphi$ the de-phasing at the mirror. The order of the Gaussian mode is zero, and only modes of the same order are resonant in the cavity in the same time, so this coupling can be considered as intra cavity losses. ([35]). By using Eq. 7.2 we get an estimation of equivalent losses due to the asphericity of the phase surface of the beam in the coupling of the cavity with the light coming from the three fibers (considered as Gaussian) as a function of the waist of the Gaussian mode in the cavity (Figure 7.22).

It is also possible that the mirror used in this experiment is not perfectly spherical and that the curvature radius changes in function of the parameter r :

$$z_{re}(r) = d_0 - R_{re}(r) + \sqrt{R_{re}^2(r) - r^2}$$

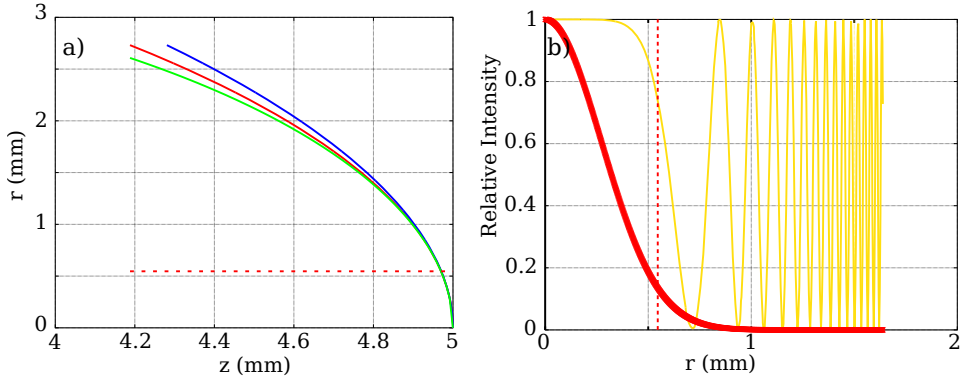


Figure 7.21.: (a) (green) Constant phase surface for a Gaussian beam of Waist $w_{f0} = 3.1\mu m$ at a distance $d = 5mm$, (red) a spherical surface of radius $R_0 = 5mm$ and (green) a surface with a radius of curvature increasing linearly ($r_{er} = 20\%$) (blue). In red dash is the radius of the beam at the mirror $w_f(z = 5mm)$. (b) (red) relative intensity of the beam on the mirror as a function of the radius of the mirror. (yellow) $\cos^2(\Delta\varphi)$ with $\Delta\varphi$ the difference of phase between the center of the point of radius r on a spherical mirror of radius of curvature $R_0 = 5mm$. The dash red line correspond to the same radius then in (a).

If we suppose a curvature radius changing linearly with r : $R_{re}(r) = R_0 + r_{er} * r$ with r_{er} the radius relative error for the mirror we can use the same principle to show how much losses in the coupling can appear due to the asphericity of the mirror. (Figure 7.22) shows the losses for different radius relative error. and (Figure 7.21 (a)) shows the surface of a mirror with a radius relative error of 20%.

The losses obtained are very large and it is possible that considering the cavity mode as a Gaussian and considering the coupling of the higher order modes is not perfectly exact. A better way would be to calculate the exact shape of the cavity mode and get the overlap with the mode of the fiber, but the orders of magnitude of the losses should be respected.

The effect of asphericity of the phase surface and the mirror shape can be reduce by changing the radius of curvature of the mirror (supposing that the radius relative error stays constant) (Figure 7.22).

Cutting mirrors with small curvature is hard for standard industry, but a good solution would be to use another fiber as the curved mirror with a spherical surface made by shooting a CO_2 laser pulse on the surface ([57]). With a multi-mode fiber it is possible to have a very large core (up to 1mm) and we can imagine a curvature of less than 1mm for the mirror making the system relatively easy to work with. Figure 7.19 (b) gives the size of the waist of the beam in function of the distance. Knowing that the index of the crystal is working in our favor in this system, we could imagine a cavity smaller than 1mm for our system. This experiment should in the future aim to this direction.

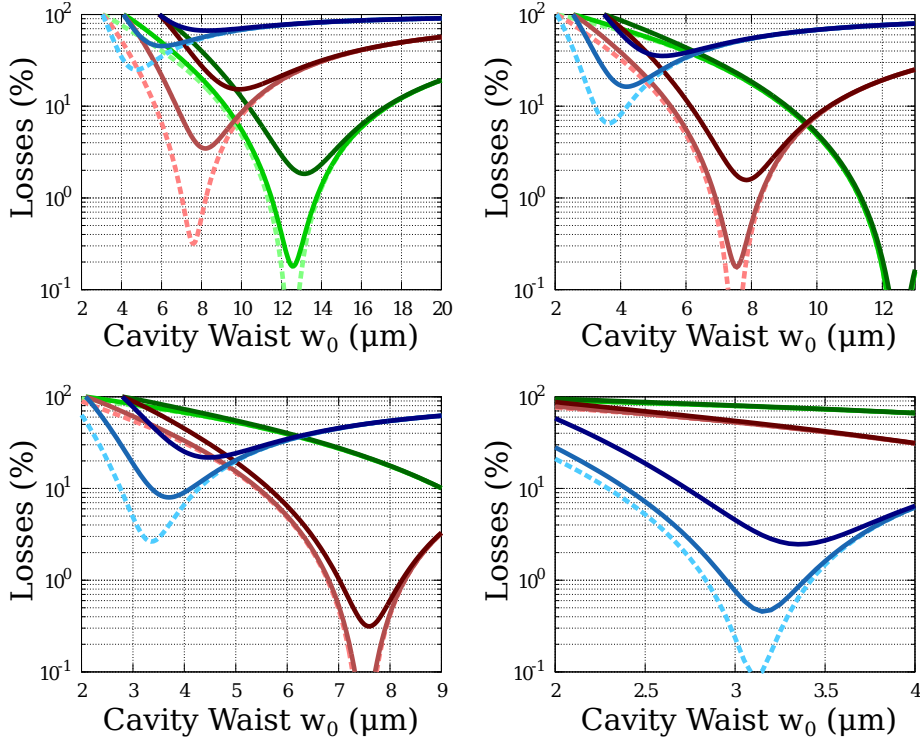


Figure 7.22.: Losses as a function of cavity waist determined by the distance of the cavity for the three fibers: (blue) standard fiber with a waist $w_f = 3.1\mu m$ (red) a PCF fiber with $w_f = 7.5\mu m$ and (green) a PCF fiber with $w_f = 12.5\mu m$. (the beam from the fibers are supposed Gaussian). For each fiber, the light colors with dash lines correspond to a spherical mirror ($r_{er} = 0$) and the increasingly dark colors correspond to a radius relative error $r_{er} = 5\%$ and $r_{er} = 20\%$. The four plots are calculating for a mirror with a radius of curvature $R_0 = 5mm$ (a), $R_0 = 1mm$ (b), $R_0 = 0.5mm$ (c), and $R_0 = 0.1mm$ (d). We considered the coupling mirror (between the fiber and the cavity) to have a reflectivity $R = 0.85$, and the spherical mirror to have a reflectivity $R = 1$.

7.4.3. Grey Tracking and Damaging:

A lot of power is sent to the crystal which can sometimes locally deteriorate the quality of the crystal and substantially increase the losses. Two phenomena can appear with a lot of power. The first is that the crystal locally burns and the damage is irreversible. The crystal cannot be used anymore at this point. Fortunately the damage is usually only done at the focused point and a displacement of a few hundreds of μm is enough to find a new good spot. The second phenomena is grey tracking ([50]) (sometimes called photo-darkening or photo-chromatic damage). It is a slight structural deformation of the crystal which usually decreases the performance of the non linearity. This damage has the advantage of being able to be cured with time and high temperature. Both types of damages can be greatly reduced by

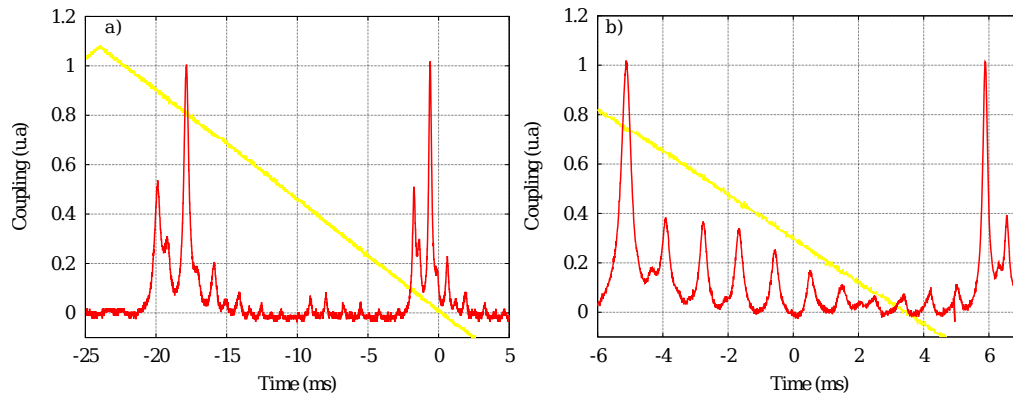


Figure 7.23.: Coupling between the mode of the fiber to the TEM00 mode of the cavity for (a) the standard fiber, and (b) the photonic fiber after too much power has been applied to the system. (To be compared to the normal behavior Figure 7.18).

working in a pulsed regime with a relatively long pulse (μs).

In our system, after using very large power for too long for taking results, by checking the coupling between the fiber and the resonator, sometimes I can see some changes in the modes compared to the normal behavior Figure 7.18 indicating some damage as shown in Figure 7.23. It would be a good idea for a future system to decrease the transmission at the face of the crystal to increase the finesse of the red light in the cavity and so decrease the threshold power for the pump.

7.5. Locking the System

7.5.1. PDH locking

In most cases an optical cavity needs feedback locking to stay in resonance or all the little fluctuations of the cavity distance due to diverse vibrations in the environment will send it out of resonance. The very small waist of the cavity and the modularity of the general design makes the whole system quite unstable and so very hard to lock. The usual locking method used for a standard cavity is PDH locking ([77]). It consists of phase modulating (usually around a few MHz) the beam going in the cavity, and demodulating the signal coming from the detector in reflection from the resonator. By using a low pass filter to remove the high frequency, we obtain an error signal proportional to the derivative of the resonance peak (Figure 7.24 (a)). Feeding back this signal to the piezo controlling the cavity length after appropriate proportional and integrating processing can set up an active feedback loop, keeping the system in resonance (Figure 7.24 (c)).

The Diablo laser provides a phase modulation of the beam at 12 MHz that can be

used for this purpose, but in practice the system is quite unstable and locking the green light by this method caused it to go out of lock all the time, especially with a lot of power. At high pump power, thermal effect starts to play an important role. The crystal will absorb a bit of light and change its temperature locally. The length and the index of the crystal are changing with the temperature, which is changing the optical length of the cavity and so changing the locking condition of the cavity. This process is non linear and can bring a lot of instabilities into the system.([37])

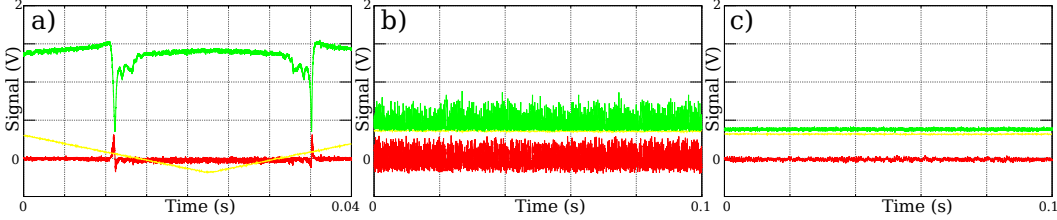


Figure 7.24.: a) Green reflection from the cavity (green) and error signal (red) during a scan of the cavity (yellow). b) and c) are the same trace without scanning with the error signal fed back to the system (PDH locking), with (b) too much feedback, and (c) optimal feedback..

7.5.2. Self Locking

Fortunately, it is also possible to use this effect to our advantage. The thermal effect can be a slow active feedback, changing the frequency of resonance to the eventual fluctuation of the frequency of the light, or the change of cavity length due to vibrations (([37], [74])).

The transmission power P in an impedance matched Fabry-Pérot cavity without absorption loss is given by:

$$\frac{P_{trans}}{P_{inc}} = \frac{1}{1 + F \sin^2(kd)}, \quad (7.3)$$

where F is the coefficient of finesse, k the wave vector, and d the optical length of the cavity. The phase kd depends on the temperature of the cavity:

$$kd = \omega(t)d_0(1 + \beta\Delta T)/c$$

with ω the frequency of the light, c the speed of light, d_0 the optical length at ambient temperature and β a coefficient accounting for index and length fluctuation with distance.

If we assume that the temperature in the crystal T has a simple first order impulse response $h(t)$ of characteristic time constant τ_0 ,

$$h(t) = \begin{cases} \frac{1}{\tau_0} \exp(-\frac{t}{\tau_0}) & \text{for } t \geq 0 \\ 0 & \text{for } t < 0 \end{cases}$$

$$\Delta T(t) = \alpha P_{trans}(t) * h(t)$$

with $f * g$ the convolution of f and g , and α a positive constant. Substituting in equation Eq.7.3 we get the transmission power P_{trans} in a Fabry Perot cavity given by:

$$\frac{P_{trans}}{P_{inc}} = \frac{1}{1 + F \sin^2 \left(\frac{\omega(t)}{c} d_0 (1 + \beta \alpha P_{trans}(t) * h(t)) \right)} \quad (7.4)$$

By considering $v = \frac{d\omega}{dt} = \text{constant}$, we can solve the equation Eq.7.4 numerically (Figure 7.25).

If we decouple the scan fluctuation and the fluctuation due to self locking, saying that these fluctuations are small compared to the wavelength, we get:

$$\frac{P_{trans}}{P_{inc}} = \frac{1}{1 + F \sin^2 \left(\frac{\omega_0 + vt}{c} d_0 + \frac{\omega_0}{c} \beta \alpha d_0 P_{trans}(t) * h(t) \right)} \quad (7.5)$$

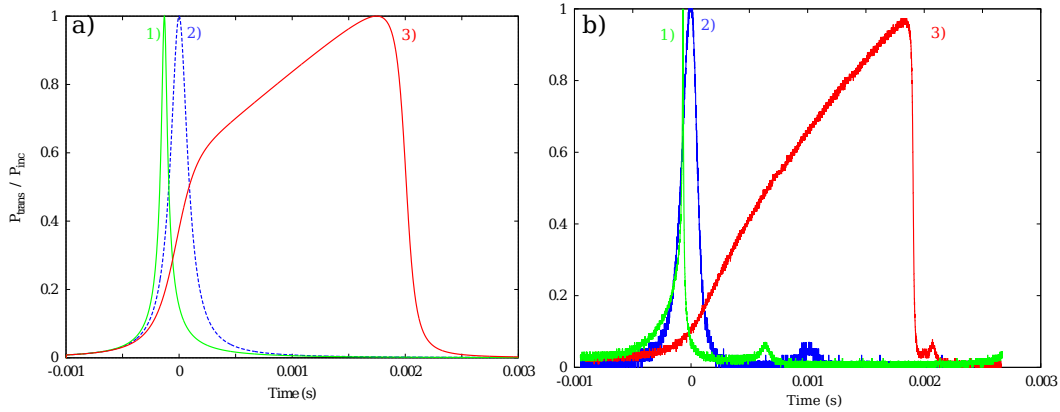


Figure 7.25.: a) $\frac{P_{trans}}{P_{inc}}$ in function of time for a finesse $F = 150$, a length of cavity $d_0 = 5.7mm$, a characteristic time $\tau = 0.002s$, an input power $P_{inc} = 10mW$ for a light at $1064nm$ and $\alpha\beta = 6 * 10^{-4}W^{-1}$. The scan speed is $3THz/s$ for (1) and $-3THz/s$ for (3). For (2) we keep the same scan speed as for (1), but we take $\alpha\beta = 0$. b) is the experimental data for scanning the cavity at the same speed but positive for 1) and negative for 2), and we reduced a lot the input power for 3) but renormalized the peak to remove thermal effects. In this experiment, the thermal effect is very fast because of the very small waist in the cavity.

When the scan is fast enough, it is possible to completely neglect dynamic thermal effect and we will observe a normal Lorentzian (Figure 7.25 (2)). Changing temperature in this condition will simply change the position of the Lorentzian by changing the length of the cavity of the index.

Now by considering dynamical thermal effect (by scanning slowly enough or increasing the power), but when the cavity is far from resonance, there is no power in the cavity, there is no absorption, so no change of temperature. Thermal effects are not doing anything. When the system is approaching resonance, for example during the scan of the frequency of the light in the cavity, when the cavity gets close to resonance, the power in the cavity increases, increasing the temperature which changes the “normal position” of the peak. If the scan speed is negative ($\frac{d\nu}{dt} < 0$) and the length and index thermal fluctuation coefficient is positive $\beta > 0$ (Figure 7.25 (3)), the change due to thermal fluctuation will go in the opposite direction to the scan, so it will correspond to a “slower scan”, which means the peak looks spread during its positive slope (blue detuning). After resonance, the power decreases and eventually the temperature will also decrease bringing back the peak to its “normal position”, but because of the delay in response of the temperature the scan still looks a bit slower in the negative slope (red detuning).

If the scan speed is positive ($\frac{d\nu}{dt} > 0$) (Figure 7.25 (1)) the thermal effects and the scan move in the same direction, corresponding to a faster scan during the positive slope (red detuning) bringing the system to resonance very quickly. The temperature doesn't have the time to increase a lot, so the negative slope (blue detuning) part of the scan looks pretty much like the case without thermal fluctuations.

Rather than moving the frequency of the light, we can move directly the length of the cavity and observe the same effect (Figure 7.25 (b)). In one direction of the scan, the peak looks bigger, and in the other direction it looks smaller, and this effect increases with the power.

Thermal absorption can be used to lock the cavity at low frequencies. If the cavity is brought almost to resonance from the direction that usually makes the peak bigger (blue detuning if $\beta > 0$ and red detuning if $\beta < 0$; we suppose here $\beta > 0$). If we stop a bit before maximum transmission to avoid reaching the other part which is unstable, it is possible to achieve self locking (Figure 7.26). The temperature of the crystal will increase creating a kind of reservoir to reduce fluctuation. If the frequency of the laser decreases for one reason or another (going from O to A in Figure 7.26), it means that the cavity goes closer to resonance, the power in the cavity increases, decreasing the frequency of resonance of the cavity (going from the curve (b) to the curve (a) in Figure 7.26 and from the point A to B). If the frequency of the light increases, it will reduce the power in the cavity decreasing the temperature, increasing the resonance frequency (going from (b) to (c) and from O to D). In this way, any fluctuation at a frequency low enough will be canceled by the cavity allowing it to stay at a power almost constant. This explanation can be transposed to length fluctuations of the cavity, the temperature fluctuation will help to cancel every fluctuation due to low frequency vibration of the mirrors and the table around the cavity. In practice this locking system can be very efficient and efficiently lock some systems that a PDH locking couldn't lock easily otherwise. More experiment data will be provided in the next chapter (section 12.6).

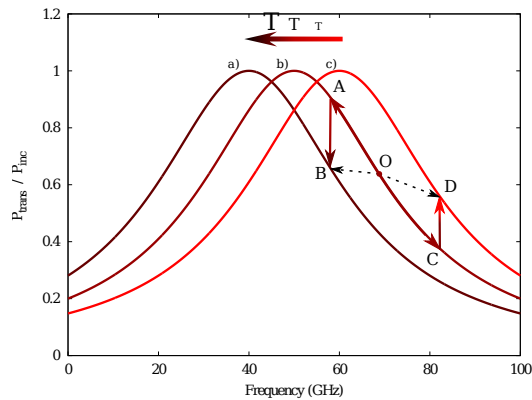


Figure 7.26.: Frequency response of the cavity for different temperatures (supposing $\beta < 0$). If the system starts in O and moves to A because the frequency decreases, the temperature in the cavity increases going from (b) to (a) and the power decreases to B. If from O, the frequency increases to D, the temperature in the cavity decreases going from (b) to (c) and the power increases to D. So if the fluctuations in frequency are not too fast, the power stays almost constant.

7.5.3. Locking with a Micro-Controller

To lock properly the cavity, I used a micro-controller (ADuC7020) from Analog Devices with five 12-bit analog to digital converter inputs and four 12-bit digital to analog converter outputs connected to Operational Amplifiers (OP27). The big advantage of this system is to be able to lock a cavity without error signals. The detector reads directly the signal from the cavity in transmission or reflection, and controls the scan. It can detect the level of the peaks to know when the system is locked or not. And then it is a simple research of maximum algorithm. The mirror controlled by the micro-controller goes in a specific direction of one increment, and the system compares the value of the signal from the detector to the previous value. If this new value is bigger, the controller continues to move the mirror in this direction; if it is smaller, it moves it in the other direction. In this way, the cavity stays locked at the top of the amplitude transmission peak, jittering around the top. It is also possible to compare the value to a reference to lock at any particular point. This technique has first been developed by Julien Laurat's team ([52]) and it allows usually a lock bandwidth around a few kilohertz. The programming of the micro-controller also allows us to add plenty of complexity features to the locking, like stopping the jitter after 90% of the maximum of the peak, pre-scanning the cavity to find the highest peak and locking only to this one, and rescanning and re-locking when the system when out of lock.

The locking system was still a bit unstable, and often pushed out of the lock by environmental noises. The best solution was to put the cavity close to locking position, and stay on the side of the peak at 50% of its maximum height helped by self-locking, let the system stabilize a bit, and slowly getting closer to resonance

until reaching 70-80% of the peak and taking measurements.

8. Results

8.1. Second Harmonic Generation and Amplification De-Amplification

To characterize the non linearity of the system without doing squeezing one can obtain Second Harmonic Generation (SHG) ([46]) in the cavity or look at amplification de-amplification of the red light in the cavity. After characterization of the losses due to coupling the red light in the fiber through the flip mirror (before mounting the curved mirror) it is possible to measure what is the non linearity of the cavity by measuring the power of green light generated as a function of the red light sent to the cavity. Locking is not necessary for this measurement, simply looking at the height of the red peak and the generated green peak on the detectors after good calibration allows us to plot the power of green as a function of the power of red (Figure 8.1).

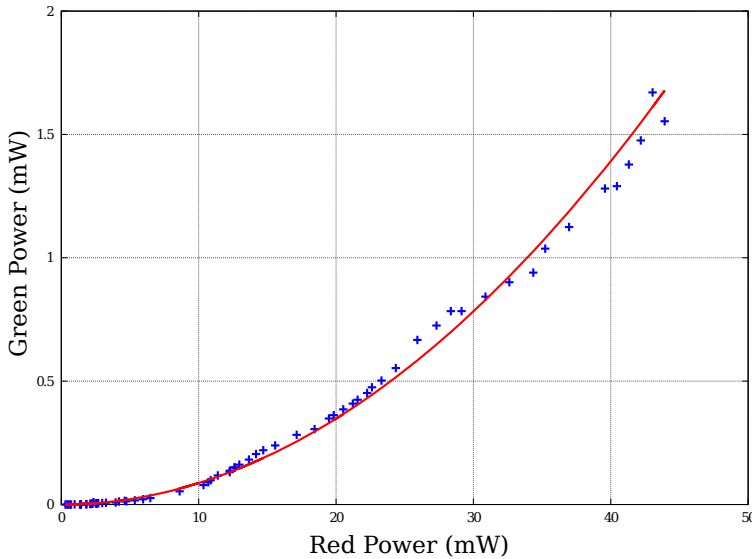


Figure 8.1.: Second harmonic generation in function of the red power sent in the cavity with the standard fiber. The red line is the fit of the curve corresponding to $P_{green} = \gamma P_{red}^2$ with $\gamma = 0.87W^{-1}$.

Amplification de-amplification can be observed by sending the pump at 532nm in the cavity and a bit of light at 1064nm, the seed. By changing the phase of the input

pump or the input seed, by sending the transmitted red light to a detector, and by tuning the temperature of the PPKTP crystal until the red peak and the green peaks are aligned, one can observe the red peak going up and down (Figure 8.2). With enough power in green, when stopping the scan, it is possible to lock the system by hand. Using self locking we can then measure the oscillations directly (Figure 8.3), but they are not as pronounced as when scanning. Maybe the crystal has been a bit damaged between the two experiments.

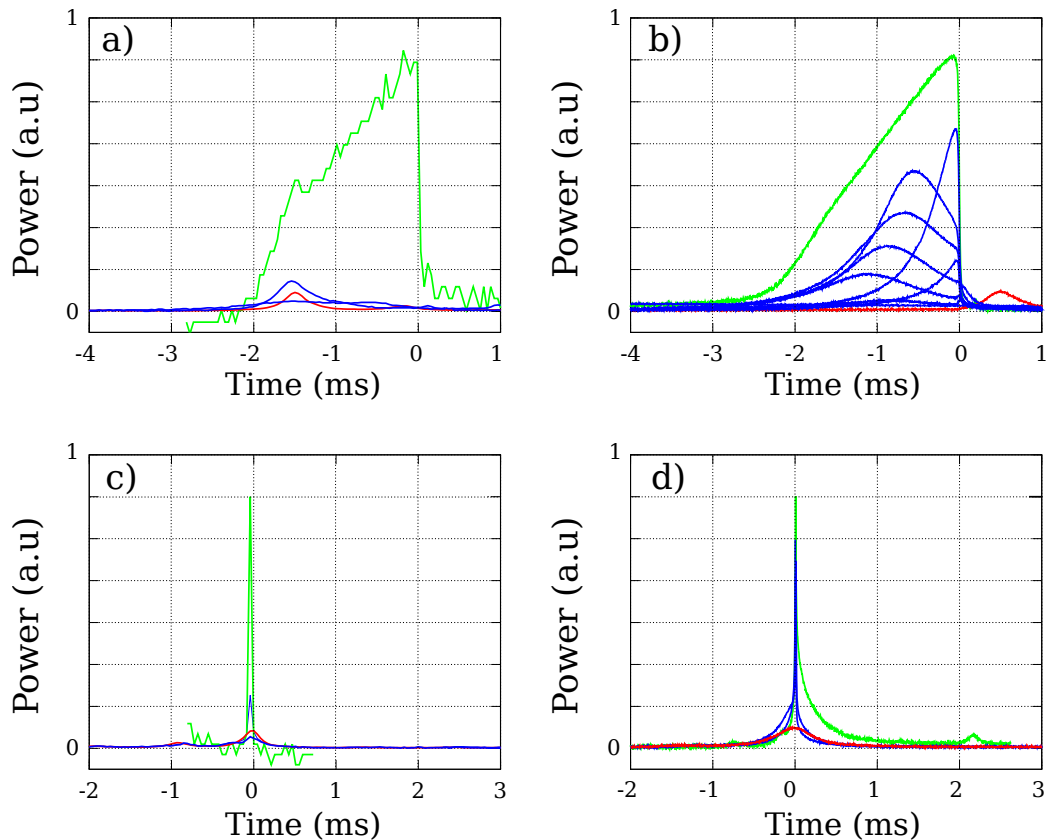


Figure 8.2.: Amplification and de-amplification for (a) and (c) the standard fiber and (b) and (d) the photonic fiber during the scan of the cavity. The scan is in the direction of self locking for (a) and (b), and in the direction of anti-self locking for (c) and (d). The green traces are the green peak, the red peaks are the red light with the pump blocked, and the blue peaks are the amplification and de-amplification of the red peak due to the pump when both frequencies are resonant.

8.2. Squeezing

To obtain squeezing, I usually start by checking the homodyne. With the signal blocked, I set the power of the LO to a bit before saturation and I turn its polariza-

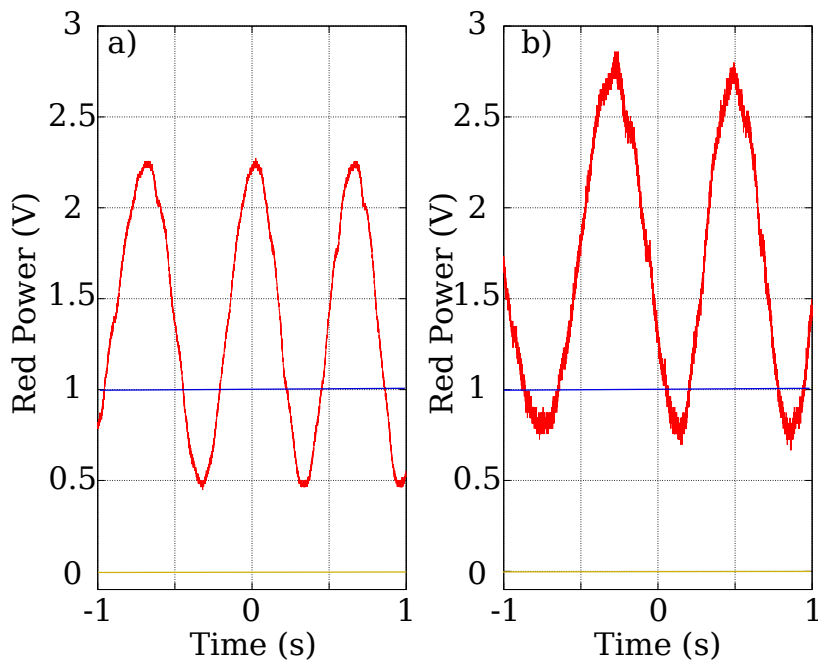


Figure 8.3.: Amplification and deamplification of the light at 1064nm for (a) the standard fiber cavity and (b) the photonic fiber cavity when the pump is turned on (red) and the seed phase is scanning, and when the pump is turned off (blue). The blue line is made by scanning the length of the cavity without the pump and getting the top of the peaks of the red light, the red lines correspond to the red power when scanning the phase of the pump and putting the cavity on resonance by changing the length of the cavity by hand (with the piezo). (Yellow) is the signal without light.

tion to make sure that the difference signal is zero in DC. The difference signal in AC is sent to the spectrum analyzer and I look at the noise around 1 MHz with a span of 0 and no gain or attenuations. The difference of noise between this situation (with the LO, but the signal blocked) called the shot noise, and the situation when both detectors are blocked (no light is going on them) called the dark noise, is around $12dB$. Then, by scanning the cavity length with the pump and a seed going to the cavity and by blocking the LO and looking at the DC of one of the homodyne detectors, I tune the temperature of the crystal to have the peaks of the green and the peaks of the red almost aligned. Usually I leave them with a little offset to have the red peak at the beginning of the ramp of the green self lock peak. Then I stop the scan and self lock the green by changing the length of the cavity from the direction allowing self locking. I can lock the system by hand and observe the data and get only one shot, or lock with the micro-controller. The lock from the micro-controller is stable enough that I can slowly change the temperature of the crystal and keep the lock, and I can choose to lock at different points of the green peak. By changing the temperature, I get double resonance by looking at the coupling of the red seed.

I usually scan the phase of the red seed, so I can see amplification de-amplification on the screen and stay at the point where they are maximal. Then I block the seed and unblock the LO. The phase of the LO is scanning at a few Hertz and I look at the noise level in the spectrum analyzer. Usually the noise will be oscillating, and if everything is set correctly and enough pump power is in the cavity, the minimum of oscillation will be lower than the shot noise (Figure 8.4). I usually take a shot noise measurement just after to be sure that nothing has drifted. It is also possible to look at the squeezing as a function of the frequency by making the span non zero in the spectrum analyzer and comparing the squeezing traces with the shot noise. The oscillation between squeezing and anti-squeezing due to the scan of the LO phase, and the frequency scan of the spectrum analyzer, are desynchronized. It gives us the squeezing and anti-squeezing as a function of frequency (Figure 8.5). Knowing that the cavity is very short ($FSR=27GHz$) and that the red cavity finesse is around 35, the bandwidth of the squeezing should be around $800MHz$, but the detector bandwidth is much smaller, and we can only detect squeezing to $40MHz$.

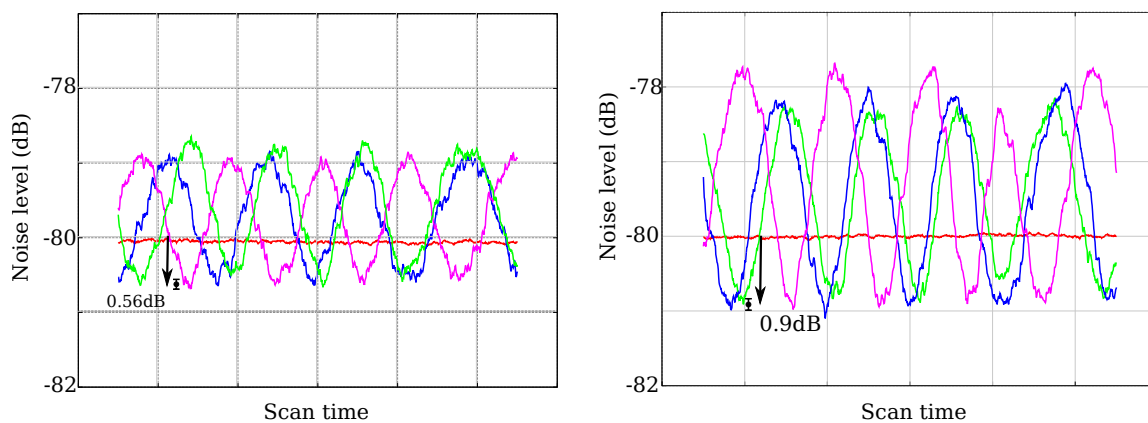


Figure 8.4.: Squeezing and anti-squeezing at $3MHz$ for (a) the standard fiber with $70mW$ of power and (b) the photonic fiber with $100mW$ of power at $3MHz$. We observe $0.56dB$ of squeezing and $1.05dB$ of anti-squeezing for the standard fiber and 0.9 of squeezing and $1.8dB$ of anti-squeezing for the photonic fiber.

We demonstrated a squeezing of $0.56 \pm 0.05dB$ ($1.05 \pm 0.05dB$ of anti-squeezing) with the standard fiber setup with 96% of visibility in the homodyne and 0.9 ± 0.05 of squeezing ($1.8 \pm 0.05dB$ of anti squeezing) with 92% of homodyne visibility for the photonic fiber set-up with a pump power around $30mW$. The detectors used in the two setups are the same with 92% of quantum efficiency each and a dark to shot noise of $8dB$. The correction from the visibility, the quantum efficiency, the shot to dark, the losses due to the different optics 2%, and the light leaving the fiber with an index around 1.5 to the air of index 1, 4% of losses gives $0.9dB$ of squeezing for the standard fiber and $1.6dB$ of squeezing for the photonic fiber.

We tested both fibers in front of a HR mirror for looking at the mismatch between the mode of the fiber and the mode after reflection after the mirror. We got $\sim 0\%$

of losses for the standard fiber (the reflected mode come back very well in the fiber) and 12% with the photonic fiber. The correction of those losses correspond to 1.7dB of squeezing for the photonic fiber. If we correct from the losses due to the coupling from the cavity to both fibers we get 2.2 dB of squeezing with the standard fiber (with 55% of losses) and 2.2dB of squeezing for the photonic fiber (with 23% of losses).

Changing the power of the pump doesn't really change the squeezing and anti-squeezing for the standard fiber, but changes the anti-squeezing considerably for the photonic fiber, increasing it up to 8dB, still with a squeezing close to 1dB (with a pump power around 100mW).

The total losses corrections, considering both squeezing and anti-squeezing, infers 3.5dB of squeezing in the cavity for the standard fiber setup and 78% of losses, and 4.4dB of squeezing for the photonic fiber with 70% of losses, for optimal power, and 14dB of squeezing with 80% of losses for high power, but with that much losses those values are just very approximate indications. By applying the model from the introduction Eq. 5.4.3 with losses $L = 1\%$ we expect 6.8dB of squeezing from the cavity.

The losses in both setups are very large, and mostly originate from the mismatch between the cavity mode and the fiber. We think that those losses are mostly due to the fact that the waist of the cavity for both fibers is extremely short for the length of the cavity. If the curvature of the mirror doesn't match perfectly the shape of a Gaussian beam coming from the fiber on all its surface, the mode of the cavity won't be Gaussian anymore. The cavity length and the waist are very small which make the phase surface not anymore circular, and if in addition, the mirror is also not perfectly circular (in the bad direction) around 70% of losses could appear. For this point, the photonic fiber should be less affected because the mode of the cavity is allowed to be larger. A better coupling between the fiber and the resonator can be achieved which explains why we obtained a bit more squeezing with it. (We measured 55% of losses due to misalignment for the standard fiber and 23% for the photonic fiber (Figure 7.18)).

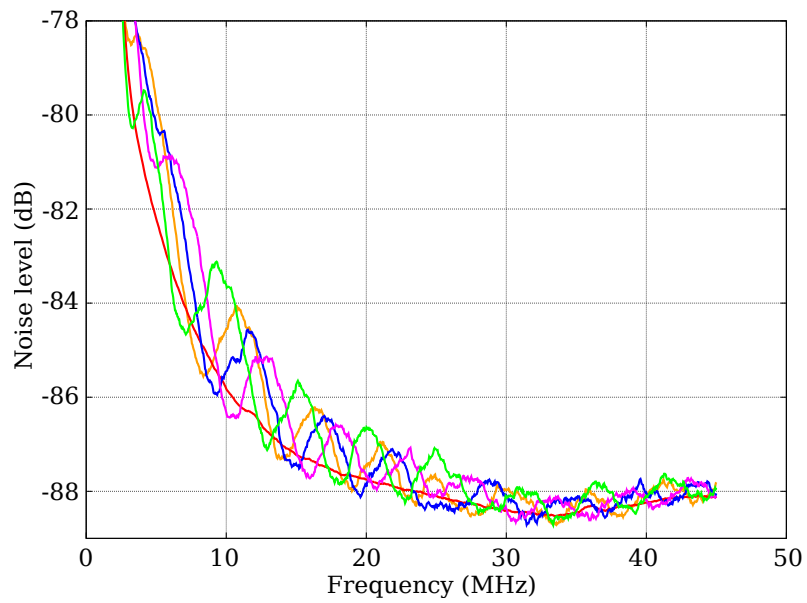


Figure 8.5.: Squeezing and anti-squeezing at different frequencies for the photonic fiber with 100mW of pump power. The measured frequency of the spectrum analyzer is scanning slowly and the phase of the LO is scanned quickly to give an idea of the squeezing and anti-squeezing at all frequencies. The red line is the shot noise.

9. Conclusion

In conclusion we demonstrated that squeezed states of light can be obtained by coupling directly a fiber to a linear OPO cavity by sticking the fiber end directly at the output of the cavity without any other optics, obtaining a squeezed state in a fiber ready to be used on any other experiment.

Moreover, the mode of the squeezed state being defined by the fiber, it is very easy and fast to obtain a good visibility in the homodyne detection in free space, or it is even possible to think about using a fiber beam splitter which would make the alignment of the homodyne no longer necessary. The implementation of a lot of complicated experiments using CV variables would be greatly simplified. Of course this convenience means that all the difficulty is transferred to the OPO. The matching between the OPO cavity and the fiber needs to be done extremely well to avoid a very high level of losses.

The system presented in this thesis is far from optimal, as reaching 0.56dB with a standard single mode fiber and 0.9dB with a photonic fiber is still much too modest to be used as a useful fiber source of squeezed states, but a lot of improvement still can be done. We demonstrated that the size of the fiber is an important parameter, that increasing the size of the fiber allowed a better coupling between the fiber and the resonator. With photonic fibers, large mode field diameters can be achieved. Single mode fibers with a waist of $12.5\mu m$ can be found easily and could be a good way to increase the coupling efficiency of our system. Another possibility would be to use a multi-mode fiber with a very large core but only a few modes (in practice a single mode fiber for a higher frequency light would work). By tapering this fiber to a smaller diameter ([49]) to reach the single mode regime on one side, it is possible to keep a very good coupling between this mode and the main Gaussian mode going out of the large core fiber. If the diameter of this fiber at the small side is the same as a standard single mode fiber, it is possible to cleave it and splice it to a standard fiber and keep all the advantage of the standard single mode fibers. Another improvement can be found in the curved mirror. A smaller curvature would decrease the constraints on the matching and also increase a lot the coupling to the fiber. A good candidate could be to use a multi-mode fiber and shoot it with a CO_2 laser on its end to create a curved surface and coat it to create a mirror (Figure 6.1 (a)). Some improvements can also be found by optimizing a bit more the coating of the crystal to match the losses of the cavity. An optimum can be found between the losses due to the crystal and the finesses of the red and the green lights in the cavity. And finally the cavity is only a few millimeters, all the mechanicals

surrounding it can be made much more compact and much more stable. If all these improvements were to be implemented, I am sure that this system should be able to reach a relatively high level of squeezing and to be used as a fiber squeezed source for larger experiments.

Bibliography

- [19] Advanced thin films. advancedthinfilms.com/.
- [20] Altechna. www.altechna.com/.
- [21] Arduino. www.arduino.cc.
- [22] Dnt digimicro. dnt.de/DigiMicro-2-0-Scale.2.html.
- [23] Fermionics. www.fermionics.com.
- [24] Fujikura. www.fujikura.co.uk.
- [25] Innolight. www.innolight.com.
- [26] Laseroptik. lo.de/.
- [27] Newport. www.newport.com/.
- [28] Noliac. www.noliac.com/.
- [29] Nyfors. nyfors.com/.
- [30] Phoenix photonics. www.phoenixphotonics.com/.
- [31] Plastimeuse. www.plastimeuse.fr/.
- [32] Raicol. raicol.com/.
- [33] Thorlabs, inc. www.thorlabs.com/.
- [34] AasiJ. and al. Enhanced sensitivity of the ligo gravitational wave detector by using squeezed states of light. *Nat Photon*, 7(8):613–619, #aug# 2013.
- [35] Charlotte Bond, Paul Fulda, Ludovico Carbone, Keiko Kokeyama, and Andreas Freise. Higher order laguerre-gauss mode degeneracy in realistic, high finesse cavities. *Phys. Rev. D*, 84:102002, Nov 2011.
- [36] G.D Boyd and Kleinman D. A. *Parametric Interaction of Focused Gaussian Light Beams*, volume 15. SIAM, 1968.
- [37] Tal Carmon, Lan Yang, and Kerry Vahala. Dynamical thermal behavior and thermal self-stability of microcavities. *Opt. Express*, 12(20):4742–4750, Oct 2004.
- [38] Y.F. Chen, Y.S. Chen, and S.W. Tsai. Diode-pumped q-switched laser with intracavity sum frequency mixing in periodically poled ktp. *Applied Physics B*, 79(2):207–210, 2004.

- [39] Jong H. Chow, Benjamin S. Sheard, David E. McClelland, Malcolm B. Gray, and Ian C. M. Littler. Photothermal effects in passive fiber bragg grating resonators. *Opt. Lett.*, 30(7):708–710, Apr 2005.
- [40] Helen Chrzanowski, Julien Bernu, Ben Sparkes, Boris Hage, Austin Lund, Tim Ralph, Ping Koy Lam, and Thomas Symul. Photon number discrimination without a photon counter and reconstructing non-gaussian states of light. In *Proceedings of the International Quantum Electronics Conference and Conference on Lasers and Electro-Optics Pacific Rim 2011*, page I763. Optical Society of America, 2011.
- [41] Helen M. Chrzanowski, Nathan Walk, AssadSyed M., Jiri Janousek, Sara Hosseini, RalphTimothy C., Thomas Symul, and Ping Koy Lam. Measurement-based noiseless linear amplification for quantum communication. *Nat Photon*, 8(4):333–338, April 2014.
- [42] Alex S. Clark, Jérémie Fulconis, John G. Rarity, William J. Wadsworth, and Jeremy L. O’Brien. All-optical-fiber polarization-based quantum logic gate. *Phys. Rev. A*, 79:030303, Mar 2009.
- [43] Yves Colombe, Tilo Steinmetz, Guilhem Dubois, Felix Linke, David Hunger, and Jakob Reichel. Strong atom-field coupling for bose-einstein condensates in an optical cavity on a chip. *Nature*, 450(7167):272–276, #nov# 2007.
- [44] R.W.P. Drever, J.L. Hall, F.V. Kowalski, J. Hough, G.M. Ford, A.J. Munley, and H. Ward. Laser phase and frequency stabilization using an optical resonator. *Applied Physics B*, 31(2):97–105, 1983.
- [45] Tobias Eberle, Sebastian Steinlechner, Jöran Bauchrowitz, Vitus Händchen, Henning Vahlbruch, Moritz Mehmet, Helge Müller-Ebhardt, and Roman Schnabel. Quantum enhancement of the zero-area sagnac interferometer topology for gravitational wave detection. *Phys. Rev. Lett.*, 104:251102, Jun 2010.
- [46] P. A. Franken, A. E. Hill, C. W. Peters, and G. Weinreich. Generation of optical harmonics. *Phys. Rev. Lett.*, 7:118–119, Aug 1961.
- [47] S. Garcia, D. Maxein, L. Hohmann, J. Reichel, and R. Long. Fiber-pigtailed optical tweezer for single-atom trapping and single-photon generation. *Applied Physics Letters*, 103(11), 2013.
- [48] Bryan T. Gard, Keith R. Motes, Jonathan P. Olson, Peter P. Rohde, and Jonathan P. Dowling. *An Introduction to Boson-Sampling*, chapter 8, pages 167–192.
- [49] Baptiste Gouraud, Dominik Maxein, Adrien Nicolas, Olivier Morin, and Julien Laurat. Optical nanofibers as light-matter interfaces for quantum networks. In *CLEO: 2015*, page FTh4B.3. Optical Society of America, 2015.
- [50] G Hétet, O Glöckl, K A Pilypas, C C Harb, B C Buchler, H-A Bachor, and P K Lam. Squeezed light for bandwidth-limited atom optics experiments at

- the rubidium d1 line. *Journal of Physics B: Atomic, Molecular and Optical Physics*, 40(1):221, 2007.
- [51] Leander Hohmann. *Using optical fibre cavities to create multi-atom entanglement by quantum Zeno dynamics*. Theses, Universite Pierre et Marie Curie UPMC Paris VI, #Feb# 2015.
- [52] K. Huang, H. Le Jeannic, J. Ruauadel, O. Morin, and J. Laurat. Microcontroller-based locking in optics experiments. *Review of Scientific Instruments*, 85(12), 2014.
- [53] David Hunger, Tilo Steinmetz, Yves Colombe, Christian Deutsch, Theodor W Hänsch, and Jakob Reichel. A fiber fabry-perot cavity with high finesse. *New Journal of Physics*, 12(6):065038, 2010.
- [54] J. Laurat, T. Coudreau, G. Keller, N. Treps, and C. Fabre. Compact source of einstein-podolsky-rosen entanglement and squeezing at very low noise frequencies. *Phys. Rev. A*, 70:042315, Oct 2004.
- [55] Olivier Morin, Kun Huang, Jianli Liu, Hanna Le Jeannic, Claude Fabre, and Julien Laurat. Remote creation of hybrid entanglement between particle-like and wave-like optical qubits. *Nat Photon*, 8(7):570–574, #jul# 2014.
- [56] Tracy E. Northup, Bernardo Casabone, Konstantin Friebe, Klemens SchÄEppert, Florian R. Ong, Moonjoo Lee, Dario Fioretto, Konstantin Ott, Sebastien Garcia, Jakob Reichel, and Rainer Blatt. An ion-cavity interface for quantum networks. *Proc. SPIE*, 9615:961506–961506–9, 2015.
- [57] K Ott, S Garcia, R Kohlhaas, K SchÄEppert, P Rosenbusch, R Long, and J Reichel. Millimeter-long fiber fabry-perot cavities. *ArXiv*, 2016.
- [58] Alexei Ourjoumtsev, Rosa Tualle-Brouiri, Julien Laurat, and Philippe Grangier. Generating optical schrödinger kittens for quantum information processing. *Science*, 312(5770):83–86, 2006.
- [59] Olivier Pinel, Julien Fade, Daniel Braun, Pu Jian, Nicolas Treps, and Claude Fabre. Ultimate sensitivity of precision measurements with intense gaussian quantum light: A multimodal approach. *Phys. Rev. A*, 85:010101, Jan 2012.
- [60] T. C. Ralph and P. K. Lam. Teleportation with bright squeezed light. *Phys. Rev. Lett.*, 81:5668–5671, Dec 1998.
- [61] M S Stefszky, C M Mow-Lowry, S S Y Chua, D A Shaddock, B C Buchler, H Vahlbruch, A Khalaidovski, R Schnabel, P K Lam, and D E McClelland. Balanced homodyne detection of optical quantum states at audio-band frequencies and below. *Classical and Quantum Gravity*, 29(14):145015, 2012.
- [62] Yuishi Takeno, Mitsuyoshi Yukawa, Hidehiro Yonezawa, and Akira Furusawa. Observation of 9 db quadrature squeezing with improvement of phase stability in homodyne measurement. *Optics Express*, 15(7):4321–4327, 2007.

- [63] Nathan Walk, Timothy C. Ralph, Thomas Symul, and Ping Koy Lam. Security of continuous-variable quantum cryptography with gaussian postselection. *Phys. Rev. A*, 87:020303, Feb 2013.

Part III.

Square Monolithic Resonator

10. Introduction:

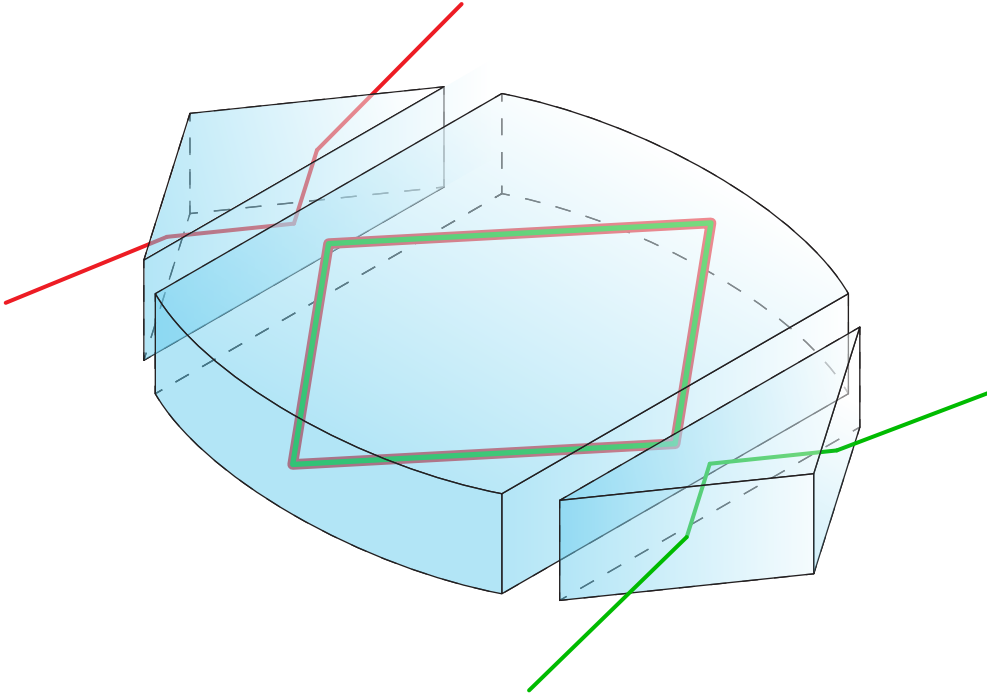


Figure 10.1.: Schematic of the resonator. An optical crystal is cut into a squared-shaped monolithic resonator that uses total internal reflection to define an optical mode. Two opposite faces are spheroidal to confine the optical mode while the remaining two faces are used to evanescently couple the circulating mode to a free-space optical mode via a prism.

The design that I will present in this part has been constructed in Australia under the main supervision of Ping Koy Lam and Thomas Symul. The idea behind this experiment is based on Whispering Gallery Mode Resonator (WGMR) systems ([97],[87],[76],[86],[81]) to try to generate squeezed light. Just before the beginning of my PHD, the group purchased a very high precision lathe ([98]) that allows a great deal of freedom in the cutting process of materials, so we tried to investigate different geometries that could fit our purpose. Rather than a cylinder shape like the WGMR, where the light is continuously guided at the surface by total internal reflection (TIR), we used a square shape (Figure 10.1) where the light is bouncing four times on the four faces of the square with TIR to form an optical mode. The precision of the lathe allows us the control of the geometry of the faces. We can add

different curvatures in the horizontal and vertical directions for each face. We used two flat surfaces to be able to bring two prisms close to the resonator to couple the light using frustrated total internal reflection and two curved surfaces to make the mode in the resonator stable.

Such TIR monolithic cavities have previously been investigated for wavelength conversion ([94],[79]) and proposed for the production of quantum light ([93]). The first successful demonstrations, however, have only recently been performed using WGMR to generate bright twin-beam squeezing ([82]) or single photon ([80]).

The goal of the project was to use a non linear material for the square resonator to create an Optical Parametric Oscillator (OPO) to generate Type I vacuum squeezing. The Square OPO (SqOPO) is made of Lithium Niobate with the extraordinary axis perpendicular to the direction of propagation. Some light at 532nm (green) polarized in the direction of the extraordinary axis is sent to the resonator by one prism and the squeezed light at 1064nm (red) polarized in the perpendicular direction is generated and coupled through the other prism.

11. Resonator Coupling

11.1. Evanescent Prism Coupling

The SqOPO is working with total internal reflection beams in the resonator crystal on the four surfaces. But pure total internal reflection doesn't allow any light to enter or exit the resonator (at least with a surface ideally smooth). So it is necessary to have a way to be able to couple the light in or out of the resonator. For this function, we use frustrated internal reflection. With a piece of crystal (usually a prism) close enough to the resonator, frustrated internal reflection can occur, which means that if the prism is placed in the evanescent part of the light coming from the resonator, and if its index allows for propagation, some light will be coupled from the resonator to the prism. In the same way, if some light is sent in the appropriate mode in the prism, it will be coupled to the resonator. The strength of the coupling depends on the distance between the prism and the resonator ([90],[95],[92]).

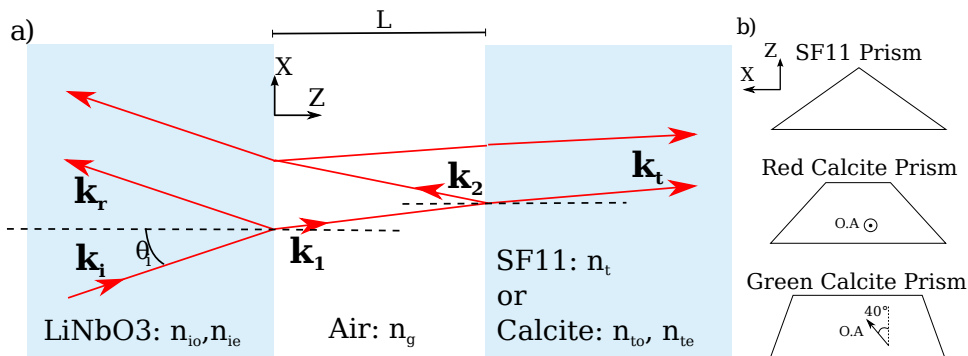


Figure 11.1.: (a) Schematic of the coupling media. On the left the resonator, in the middle the gap of air, and on the right one of the prism couplers. (b) The three different prisms that can be used as the third medium. An isotropic prism in SF11, or two anisotropic prisms in calcite with the extraordinary axis allowing us to couple only the red light, or only the green light.

We consider three different prisms that have been used in this thesis (Figure 11.1 (b)):

- A prism made of SF11 (SCHOTT) which is an isotropic material of index $n = 1.75$ for $1064nm$ and $n = 1.79$ for $532nm$. It can couple both frequencies (Figure 11.1 (b)).

- A prism made of Calcite which is a uniaxial anisotropic material with the extraordinary axis along the vertical axis. For the green the indices are: $n_e = 1.4882$ and $n_o = 1.64246$, and for the red: $n_e = 1.4796$ and $n_o = 1.6425$. We call this prism the red calcite prism because it can only couple the red light (which is polarized horizontally) (Figure 11.1 (b)).
- A second Calcite prism with the extraordinary axis in the horizontal plane with an angle of 40° with the normal of the coupling face. We call this prism the green calcite prism because it can only couple the green light (which is polarized vertically) (Figure 11.1 (b)).

For the calculation of the coupling, similarly to the calculation section 3.2, we will consider two interfaces between three media where plane waves are propagating (Figure 11.1 (a)). The first medium, on the left, is considered as a semi-infinite medium of uniaxial anisotropic material. It is the resonator material of Lithium Niobate. ($n_o = 2.2321$, for $1064nm$, $n_e = 2.2336$ for $532nm$.) The extraordinary axis is in the vertical direction, orthogonal to the wave vectors. The incident beam is propagating from the left and experiences total internal reflection in the first surface.

The second medium (Figure 11.1 (a)) is a gap of air of length L , it is an isotropic material of index $n_g = 1$. The beam is by hypothesis evanescent in this part.

The last medium, on the right, is a semi infinite material corresponding to the prism (or any other coupler material, like a fiber for example). We consider three possibilities for this calculation (Figure 11.1 (b)). The prism is either isotropic (SF11), or uniaxially anisotropic with the extraordinary axis in the vertical direction (red calcite prism), or uniaxially anisotropic with the extraordinary axis in the horizontal plan ($\mathbf{e}_x, \mathbf{e}_z$) making an angle $\theta = 40^\circ$ with the direction \mathbf{e}_z (green calcite prism). For the generality of the calculation, we will write n_{io} and n_{ie} the indexes of the first medium, n_g the index of the gap material, and n_{to} and n_{te} the indexes of the third material ((Figure 11.1 (a))).

We start with an incident plane wave of wave vector \mathbf{k}_i . By hypothesis, the field is propagating in this medium in the horizontal plane, so the components of \mathbf{k}_i are real and given by

$$\mathbf{k}_i = \begin{pmatrix} n_i k_0 \sin(\theta_i) \\ 0 \\ n_i k_0 \cos(\theta_i) \end{pmatrix},$$

where n_i is the index of refraction of the first medium (the ordinary or extraordinary index of the resonator, depending on the polarization of the incident field), $k_0 = \frac{\omega}{c}$, ω is the frequency of the light, c the speed of light in vacuum, and θ_i the angle between \mathbf{k}_i and the direction \mathbf{e}_z (Figure 11.1 (a)). (For the resonator discussed in this thesis, $\theta_i = \pi/4$, but for the purpose of generality, we conserve the variable θ_i . It allows the result to also be used for WGMR or more complex shapes.)

We call \mathbf{k}_r the wave vector of the reflected beam, \mathbf{k}_1 and \mathbf{k}_2 the wave vectors of the beams in the second medium and \mathbf{k}_t the wave vector in the last medium ((Figure 11.1 (a))), by using the conservation of k_{\parallel} (first Snell Descartes law) and the fact that $|\mathbf{k}_1| = |\mathbf{k}_2| = n_g k_0$, $|\mathbf{k}_r| = n_i k_0$ and $|\mathbf{k}_t| = n_t k_0$ we can deduce all the other wave vectors:

$$\mathbf{k}_r = \begin{pmatrix} k_{ix} \\ 0 \\ -k_{iz} \end{pmatrix} = \begin{pmatrix} n_i k_0 \sin(\theta_i) \\ 0 \\ -n_i k_0 \cos(\theta_i) \end{pmatrix} \quad \mathbf{k}_t = \begin{pmatrix} k_{ix} \\ 0 \\ k_{tz} \end{pmatrix}$$

$$\mathbf{k}_1 = \begin{pmatrix} k_{ix} \\ 0 \\ i\alpha \end{pmatrix} \quad \mathbf{k}_2 = \begin{pmatrix} k_{ix} \\ 0 \\ -i\alpha \end{pmatrix}$$

where $k_{tz} = \left((n_t k_0)^2 - (k_{ix})^2 \right)^{1/2}$ can be real or purely imaginary, with n_t being the refractive index of the last prism, and α is a real number such that $\alpha = \sqrt{(k_{ix})^2 - (n_g k_0)^2}$. We consider the three cases:

- If the third medium is the SF11, n_t is just the index of the prism.
- If the third medium is the red calcite prism, in the s-polarization case n_t is the extraordinary index of the prism $n_t = n_{te}$ and in the p-polarization case n_t is the ordinary index $n_t = n_{to}$.
- If the third medium is the green calcite prism, in the s-polarization case n_t is the ordinary index of the prism $n_t = n_{te}$ and in the p-polarization case $n_t = \left(\frac{k_{iz}^2 + k_{ix}^2}{k_0^2} \right)^{1/2}$ where the z component of the wave vector $k_{tz} = -\frac{k_{ix} n_{p1}^2}{\gamma} + n_{p1}^2 \Delta^{1/2}$ where $\Delta = \frac{k_0^2}{n_{p1}^2} - k_{ix}^2 \left(\frac{1}{n_{p1}^2 n_{p2}^2} - \frac{1}{\gamma^2} \right)$, $\frac{1}{n_{p1}^2} = \frac{\cos^2(\theta)}{n_{to}^2} + \frac{\sin^2(\theta)}{n_{te}^2}$, $\frac{1}{n_{p2}^2} = \frac{\cos^2(\theta)}{n_{te}^2} + \frac{\sin^2(\theta)}{n_{to}^2}$ and $\frac{1}{\gamma} = \cos(\theta) \sin(\theta) \left(\frac{1}{n_{to}^2} - \frac{1}{n_{te}^2} \right)$. With the angle between the extraordinary axis of the prism and e_z : $\theta = 40^\circ$. (We can notice that in this case n_t and k_{tz} are complex). (Demonstration in Appendix B)

It is important to notice that the s-polarization (with the electric field polarization along \mathbf{e}_y) and the p-polarization (with the electric field polarization in the plan $(\mathbf{e}_x, \mathbf{e}_z)$) are a good decomposition for the problem. In the resonator, the extraordinary axis is perpendicular to the wave vector, so the extraordinary beam polarization is along the extraordinary axis (\mathbf{e}_y) and the ordinary beam polarization is in the plane $(\mathbf{e}_x, \mathbf{e}_z)$ perpendicular to the wave vector. Obviously the decomposition is correct in the gap which is isotropic. For the third medium, for the SF11 and the red calcite prism, the same arguments occur, for the green calcite the ordinary beam polarization is orthogonal to the wave vector and to the extraordinary axis, so it is in the direction of \mathbf{e}_y . The extraordinary beam polarization is orthogonal to the

ordinary beam polarization, so also in the plan $(\mathbf{e}_x, \mathbf{e}_z)$. (subsection 2.2.2, and [78])

We can also notice that for the first two cases (SF11 and red calcite), and for the third case for the s-polarization, there is coupling between the prism and the resonator if and only if $n_i \sin(\theta_i) < n_t$, and when there is propagation in the prism, the transmission wave vector \mathbf{k}_t makes an angle θ_t with the direction \mathbf{e}_z given by the expression $n_i \sin(\theta_i) = n_t \sin(\theta_t)$, as if there were no gap between the two media and we were applying Snell's laws. If $n_i \sin(\theta_i) > n_t$, \mathbf{k}_t is purely imaginary.

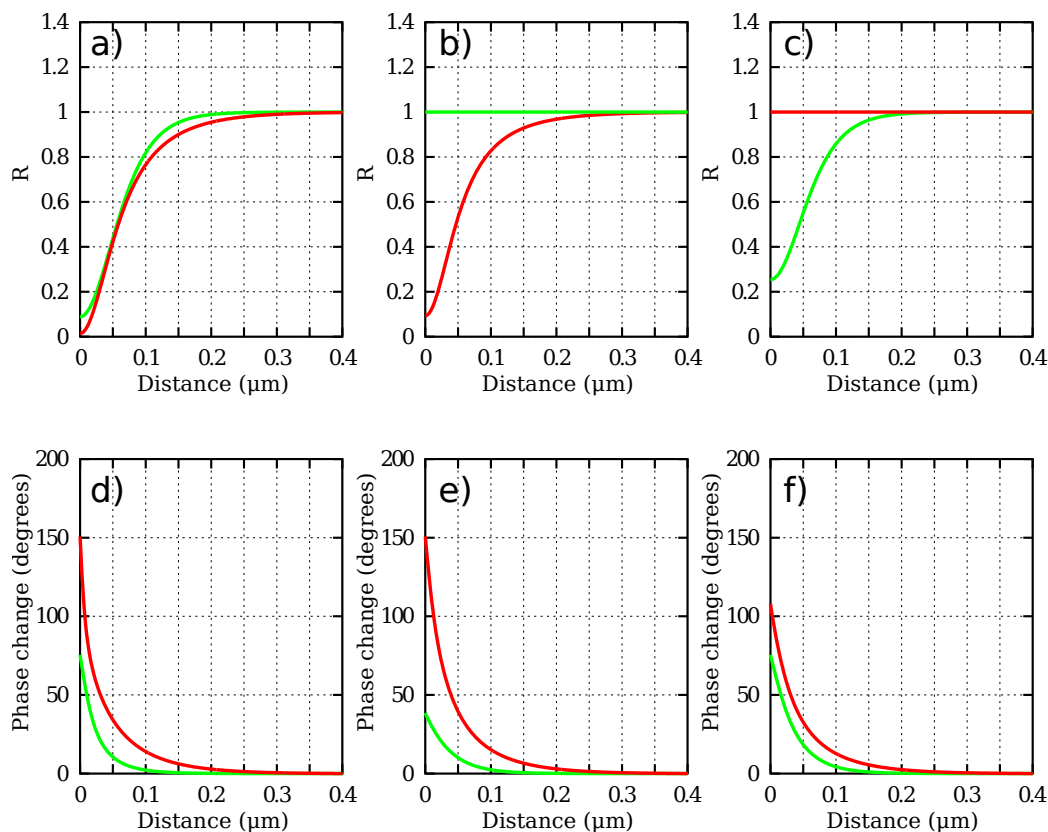


Figure 11.2.: Reflectivity $R = |r|^2$ and dephasing $\Im(r)$ versus distance L between the prism and the resonator for 1064nm (red) and 532nm (green) for the SF11 prism (a,d), for the red calcite prism (b,e) and for the green calcite prism (c,f).

11.1.1. S-Polarization

For the s-polarization case (in practice the green light case), the incident and reflected electric fields \mathbf{E}_i and \mathbf{E}_r , the two electric fields in the gap \mathbf{E}_1 and \mathbf{E}_2 , and the transmitted field \mathbf{E}_t are all along \mathbf{e}_y .

$$\left\{ \begin{array}{l} \mathbf{E}_i = E_0 \mathbf{e}_y \exp[i(k_{ix}x + ik_{iz}z)] \\ \mathbf{E}_r = r_s E_0 \mathbf{e}_y \exp[i(k_{ix}x - ik_{iz}z)] \\ \mathbf{E}_1 = E_{10} \mathbf{e}_y \exp[i(k_{ix}x - \alpha z)] \\ \mathbf{E}_2 = E_{20} \mathbf{e}_y \exp[i(k_{ix}x + \alpha z)] \\ \mathbf{E}_t = t_s E_0 \mathbf{e}_y \exp[i(k_{ix}x + ik_{tz}z)] \end{array} \right. .$$

where r_s and t_s are the reflection and transmission coefficients, E_0 the amplitude of the incident field, and E_{10} and E_{20} the amplitude of the fields in the gap.

The continuity of the transverse electric fields at the two interfaces give the equations:

$$\left\{ \begin{array}{l} E_0(1 + r_s) = E_{10} + E_{20} \\ E_{10} \exp(ik_{1z}L) + E_{20} \exp(-ik_{1z}L) = t_s E_0 \end{array} \right. \quad (11.1)$$

By using the Maxwell-Faraday equation $\nabla \times \mathbf{E} = i\omega \mathbf{B}$ and the fact that the electric fields are only along \mathbf{e}_y . It gives in the \mathbf{e}_x direction: $\frac{\partial E_y}{\partial z} = i\omega B_x$. Knowing that the transversal component of the magnetic field is continuous, we deduce that the field $\frac{\partial E_y}{\partial z}$ is also continuous at the interfaces. We get two more equations:

$$\left\{ \begin{array}{l} k_{iz} E_0(1 - r_s) = k_{1z}(E_{10} - E_{20}) \\ k_{1z}(E_{10} \exp(ik_{1z}L) - E_{20} \exp(-ik_{1z}L)) = k_{tz} t_s E_0 \end{array} \right. . \quad (11.2)$$

Eq. 11.1 and Eq. 11.2 can easily be solved, we obtain:

$$t_s = 2 \left(\frac{1}{i\alpha} [i\alpha \cosh(\alpha L) + k_{tz} \sinh(\alpha L)] + \frac{1}{k_{iz}} [i\alpha \sinh(\alpha L) + k_{tz} \cosh(\alpha L)] \right)^{-1},$$

$$r_s = \frac{\frac{1}{i\alpha} [i\alpha + k_{tz} \tanh(\alpha L)] - \frac{1}{k_{iz}} [i\alpha \tanh(\alpha L) + k_{tz}]}{\frac{1}{i\alpha} [i\alpha + k_{tz} \tanh(\alpha L)] + \frac{1}{k_{iz}} [i\alpha \tanh(\alpha L) + k_{tz}]}.$$

We can check that if the distance L goes to zero, we get the usual coefficients for one surface between the first and the third media and if the distance L goes to infinity the transmission t_s goes to zero and the reflection r_s goes to one in absolute value.

We can notice that if $n_i \sin(\theta_i) < n_t$, which means \mathbf{k}_t is purely imaginary, $|r_s| = 1$, there is still total internal reflection in the resonator whatever the distance L , but the reflected beam acquires a phase $\Im(r_s)$ which depends on L (Figure 11.2).

The coefficients in energy are obtained by calculating the Poynting vectors $\mathbf{\Pi} = \frac{1}{2}\Re(\mathbf{E} \times \mathbf{H}^*)$. The magnetizing field in each medium can be calculated from the electric field with the Maxwell-Faraday equation: $\mathbf{H} = \frac{E_y}{\omega\mu_0}(k_z\mathbf{e}_x - k_x\mathbf{e}_z)$, we obtain the reflection and transmission of the energy:

$$R = \frac{\Pi_{rz}}{\Pi_{iz}} = |r_S|^2$$

$$T = \frac{\Pi_{tz}}{\Pi_{iz}} = |t_S|^2 \frac{\Re(k_{tz})}{k_{iz}}$$

The phase shift and reflectivity experienced by the beam at this double interface are shown in Figure 11.2.

11.1.2. P-Polarization

For the p-polarization case (in practice, the red light case), the incident and reflected magnetizing fields \mathbf{H}_i and \mathbf{H}_r , the two magnetizing fields in the gap \mathbf{H}_1 and \mathbf{H}_2 , and the transmitted field \mathbf{H}_t are all along \mathbf{e}_y .

$$\begin{cases} \mathbf{H}_i &= H_0\mathbf{e}_y \exp[i(k_{ix}x + ik_{iz}z)] \\ \mathbf{H}_r &= r_H H_0\mathbf{e}_y \exp[i(k_{ix}x - ik_{iz}z)] \\ \mathbf{H}_1 &= H_{10}\mathbf{e}_y \exp[i(k_{ix}x - \alpha z)] \\ \mathbf{H}_2 &= H_{20}\mathbf{e}_y \exp[i(k_{ix}x + \alpha z)] \\ \mathbf{H}_t &= t_H H_0\mathbf{e}_y \exp[i(k_{ix}x + ik_{tz}z)] \end{cases} .$$

Where r_H and t_H are the reflection and transmission coefficients of the magnetizing field, H_0 is the amplitude of the incident field, and H_{10} and H_{20} are the amplitudes of the fields in the gap.

In the same way than for the s-polarization, the continuity of the transverse fields at the two interfaces gives the equations:

$$\begin{cases} H_0(1 + r_H) &= H_{10} + H_{20} \\ H_{10} \exp(ik_{1z}L) + H_{20} \exp(-ik_{1z}L) &= t_H H_0 \end{cases} \quad (11.3)$$

For the two other equations we use the Maxwell-Ampère equation $\nabla \times \mathbf{H} = \frac{\partial H_y}{\partial z}\mathbf{e}_x - \frac{\partial H_y}{\partial x}\mathbf{e}_z = -i\omega\mathbf{D} = -i\omega\epsilon_0\epsilon\mathbf{E}$ with ϵ the relative permittivity tensor of the material. The transverse component of the electric field is continuous, so that means that the

field $\left(\boldsymbol{\epsilon}^{-1} \left(\frac{\partial H_y}{\partial z} \mathbf{e}_x - \frac{\partial H_y}{\partial x} \mathbf{e}_z\right)\right)_{\mathbf{e}_x}$ is continuous at both interfaces. For the resonator this corresponds to $iH_0 k_{iz}/n_{io}^2$ for the incident field and $-ir_H H_0 k_{iz}/n_{io}^2$ for the reflected beam. In the evanescent gap, it corresponds to $iH_{10} k_{1z}/n_g^2$ and $-iH_{10} k_{1z}/n_g^2$ with $k_{1z} = i\alpha$ the z coefficient of the wave vector in the gap.

For the case of the isotropic SF11 prism or the red calcite prism, we get $it_H k_{tz}/n_t^2$, and so we obtain

$$\begin{cases} \frac{k_{iz}}{n_{io}^2} H_0 (1 - r_H) & = \frac{k_{1z}}{n_g^2} (H_{10} - H_{20}) \\ \frac{k_{1z}}{n_g^2} (H_{10} \exp(ik_{1z}L) - H_{20} \exp(-ik_{1z}L)) & = \frac{k_{tz}}{n_{to}^2} t_H H_0 \end{cases} \quad (11.4)$$

These four equations Eq. 11.3 and Eq. 11.4 are analogous to the s-polarization case (Eq. 11.1 and Eq. 11.2) with the replacements $\mathbf{E} \rightarrow \mathbf{H}$, $t_s \rightarrow t_H$, $r_s \rightarrow r_H$ and $k_z \rightarrow k_z/n^2$.

$$t_{H_{1,2}} = \frac{2}{\frac{n_g^2}{i\alpha} \left[\frac{i\alpha}{n_g^2} \cosh(\alpha L) + \frac{k_{tz}}{n_t^2} \sinh(\alpha L) \right] + \frac{n_{io}^2}{k_{iz}} \left[\frac{i\alpha}{n_g^2} \sinh(\alpha L) + \frac{k_{tz}}{n_t^2} \cosh(\alpha L) \right]}$$

$$r_{H_{1,2}} = \frac{\frac{n_g^2}{i\alpha} \left[\frac{i\alpha}{n_g^2} + \frac{k_{tz}}{n_t^2} \tanh(\alpha L) \right] - \frac{n_{io}^2}{k_{iz}} \left[\frac{i\alpha}{n_g^2} \tanh(\alpha L) + \frac{k_{tz}}{n_t^2} \right]}{\frac{n_g^2}{i\alpha} \left[\frac{i\alpha}{n_g^2} + \frac{k_{tz}}{n_t^2} \tanh(\alpha L) \right] + \frac{n_{io}^2}{k_{iz}} \left[\frac{i\alpha}{n_g^2} \tanh(\alpha L) + \frac{k_{tz}}{n_t^2} \right]}$$

One more time, we can check that if the distance L goes to zero, we get the usual coefficients for one surface between the first and the third media.

Similarly if $n_i \sin(\theta_i) < n_t$, we also have $|r_{H_{1,2}}| = 1$, there is still total internal reflection in the resonator whatever the distance L , and the phase of the reflected beam acquires a phase $\Im(r_H)$ which depends on L Figure 11.2.

By applying the Maxwell-Faraday equation, we can calculate the electric field in the prism and obtain the energy coefficient. The coefficient of reflection in energy is given by $R = |r_{H_{1,2}}|^2$, and the coefficient of transmission in energy is given by $T = |t_H|^2 \frac{n_{io}^2}{n_{to}^2} \frac{\Re(k_{tz})}{k_{iz}}$.

For the green calcite, we need to apply a rotation θ around \mathbf{e}_y to the inverse of the permittivity tensor of the prism to get its value in the reference frame $(\mathbf{e}_x, \mathbf{e}_y, \mathbf{e}_z)$

$$\boldsymbol{\epsilon}^{-1} = \begin{pmatrix} 1/n_{p1}^2 & 0 & -1/\gamma \\ 0 & 1/n_o^2 & 0 \\ -1/\gamma & 0 & 1/n_{p2}^2 \end{pmatrix}. \quad (11.5)$$

The continuous field in the prism is: $it_H H_0 \left(\frac{k_{tz}}{n_{p1}^2} + \frac{k_{ix}}{\gamma} \right)$. Defining $k_{tp} = \frac{k_{tz}}{n_{p1}^2} + \frac{k_{ix}}{\gamma}$ and noting that k_{tp} is purely imaginary (see Appendix B for the demonstration), we get the equations:

$$\begin{cases} \frac{k_{iz}}{n_{io}^2} H_0 (1 - r_H) & = \frac{k_{1z}}{n_g^2} (H_{10} - H_{20}) \\ \frac{k_{1z}}{n_g^2} (H_{10} \exp(ik_{1z}L) - H_{20} \exp(-ik_{1z}L)) & = k_{tp} t_H H_0 \end{cases} \quad (11.6)$$

Eq. 11.3 and Eq. 11.6 give the solutions:

$$t_{H_3} = \frac{2}{\frac{n_g^2}{i\alpha} \left[\frac{i\alpha}{n_g^2} \cosh(\alpha L) + k_{tp} \sinh(\alpha L) \right] + \frac{n_{io}^2}{k_{iz}} \left[\frac{i\alpha}{n_g^2} \sinh(\alpha L) + k_{tp} \cosh(\alpha L) \right]}$$

$$r_{H_3} = \frac{\frac{n_g^2}{i\alpha} \left[\frac{i\alpha}{n_g^2} + k_{tp} \tanh(\alpha L) \right] - \frac{n_{io}^2}{k_{iz}} \left[\frac{i\alpha}{n_g^2} \tanh(\alpha L) + k_{tp} \right]}{\frac{n_g^2}{i\alpha} \left[\frac{i\alpha}{n_g^2} + k_{tp} \tanh(\alpha L) \right] + \frac{n_{io}^2}{k_{iz}} \left[\frac{i\alpha}{n_g^2} \tanh(\alpha L) + k_{tp} \right]}$$

By applying the Maxwell-Faraday equation and by using the tensor expression Eq. 11.5, we can calculate the electric field in the prism: $\mathbf{E} = \frac{t_H H_0}{\omega} \boldsymbol{\varepsilon}^{-1} (-k_z \mathbf{e}_x + k_x \mathbf{e}_z) = -\frac{t_H H_0}{\omega} \left(k_{tp} \mathbf{e}_x + \left(\frac{k_{tz}}{\gamma} + \frac{k_{ix}}{n_{p2}^2} \right) \mathbf{e}_z \right)$. We deduce the coefficients in energy: in reflection $R = |r_{H_3}|^2 = 1$ and in transmission $T = |t_{H_3}|^2 n_{io}^2 \frac{\Re(k_{tp})}{k_{iz}} = 0$ because k_{tp} is purely imaginary.

The phase shift and reflectivity experienced by the beam at this double interface are shown in Figure 11.2.

11.2. Resonator

As we saw in the previous chapter, the prism can allow a fraction of a light beam in total reflection in the prism to enter the resonator. The amount of light coupling in the resonator controlled by the distance between the prism and the resonator can fluctuate continuously between ~80% to 0% ([92]). If the angle in the resonator is exactly 45°, the light will bounce on every other surface with total internal reflection and come back exactly along the same path. It is a resonant cavity (Figure 11.4) with one tunable coupling mirror and 3 mirrors with transmission $T = 0$, but eventually some losses. The reflected intensity I_r in function of the incident intensity I_i is given by (section 4.2):

$$I_r = \mathcal{F} I_i \left(\frac{\frac{(r_1 - (1 - L_m)(1 - L))^2}{4r_1(1 - L)} + (1 - L_m) \sin^2(kd)}{1 + \mathcal{F} \sin^2(kd)} \right) \quad (11.7)$$

Where L_m is the losses due to the coupling, L is the losses in the cavity during a round trip, k is the wave vector in the resonator, d is the round trip length of the resonator and \mathcal{F} is the coefficient of finesse of the resonator given by $\mathcal{F} = 1/\sin^2(\frac{\pi}{2F})$ where F is the finesse of the cavity. We also sometimes use the linewidth to describe the resonator which is given by: $\Delta\nu = FSR/F$ where FSR is the free spectral range of the cavity (19GHz for our cavity).

The losses in the resonator L come essentially from two sources: the scattering in the mirrors and material absorption. The scattering is due to imperfections in the mirrors. All dust or micro scratches at the interface could make a part of the light experience a different surface angle causing a bit of the light not to be resonant anymore, and even transmitting out. This problem can be solved by carefully polishing the surface of the mirrors to a better quality surface.

The absorption is more of an issue because we can't really do a lot for it. It is just the matter of getting the most quality material possible to avoid unnecessary impurities absorbing more of the light at the frequency that we are using. Lithium Niobate has an absorption loss at 1064nm of $\sim 0.05\%/mm$ and $\sim 0.25\%/mm$ at 532nm. For a resonator of diameter $d=2.3mm$ (total propagation length of $2\sqrt{2}d = 6.5mm$), it corresponds to $\sim 1.5\%$ of losses by round trip for green and $\sim 0.30\%$ for red. (Or a maximum finesse around ~ 400 and a minimum linewidth of $\sim 40MHz$ for green and a maximum finesse of ~ 2000 and a minimum linewidth of $\sim 10MHz$ for red.) The linewidth of the light also depends on how much coupling there is between the prism and the resonator, something that we can tune with the distance between the prism and the resonator (Figure 11.3).

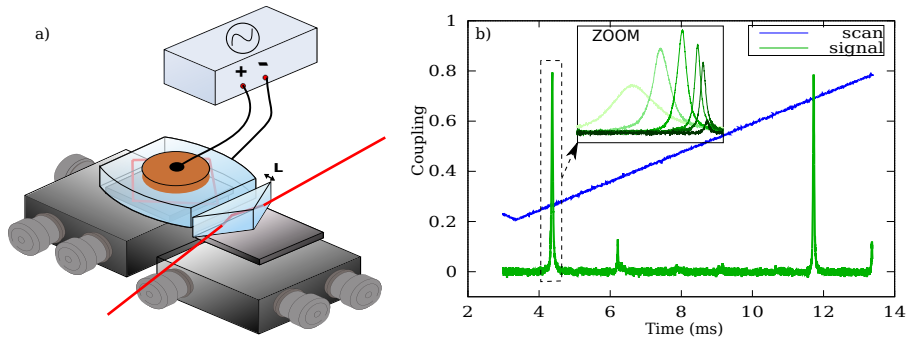


Figure 11.3.: (a) Schematic of the resonator with an electrode for applying voltage and a control of the coupling distance L . (b) Example of scan obtained by varying the applied voltage at the electrode (around 600V for 532nm light (green).) The zoom shows the effect of the movement of the coupling distance L on the resonant peak.

At resonance, the square sine in Eq. 11.7 is zero, and only the term $\frac{(r_1 - (1 - L_m)(1 - L))^2}{4r_1(1 - L)}$ matters. When the prism is far $r_1 > (1 - L_m)(1 - L)$ (under coupling regime (Figure 11.4)), the losses of the resonator are mostly due to the scattering and

the absorption in the resonator, and the finesse is the largest, but the light directly reflected by the resonator is larger than the light coming from the resonator and they can't cancel each other perfectly at resonance, the reflected light doesn't reach zero. When the prism gets closer, eventually, $r_1 = (1 - L_m)(1 - L)$ (critically coupling regime (Figure 11.4)) and the coupling is the highest possible, only limited by the mode matching. If the mode matching is perfect, the light directly reflected by the first mirror is perfectly canceled by the light coming from the resonator at resonance. When the prism continues to get closer, $r_1 < (1 - L_m)(1 - L)$ (over coupling regime (Figure 11.4)) the finesse is the smallest, and the light coming out of the resonator at resonance is larger than the light directly reflected leading to a smaller coupling.

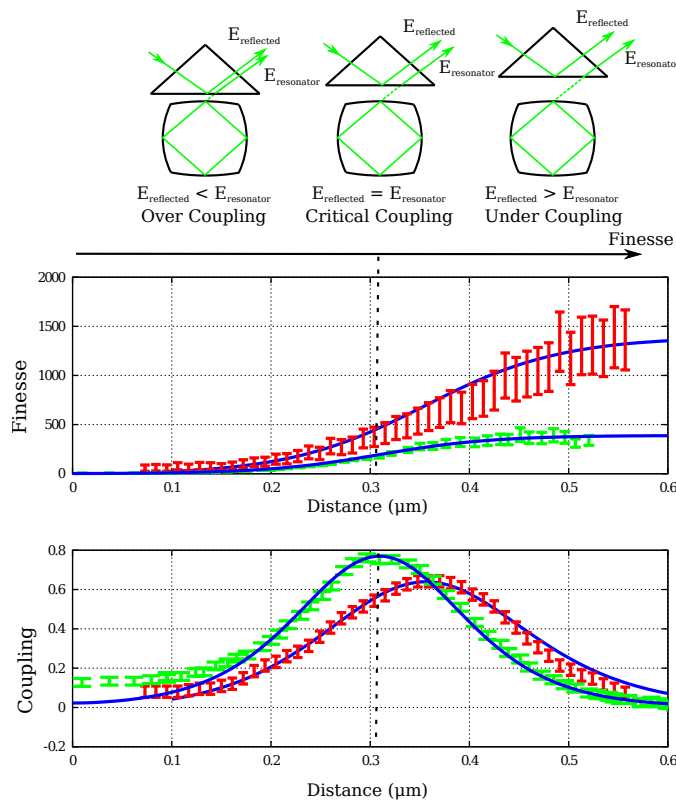


Figure 11.4.: Schematic of the three coupling regimes, over-coupling, critical coupling, and under-coupling, and experimental data of coupling (1- normalised reflection) and finesse for 1064nm (red) and 532nm (green) in function of the distance between the prism (SF11) and the resonator. The coupling doesn't reach one because of mode matching.

The design of the system allows another prism to be added in the other side (Figure 11.5). It means adding another coupler to the detector equivalent to a back cavity mirror for a standard cavity (with a tunable reflectivity from 20% to $\sim 100\%$). The beam exiting can be sent to a detector or used for alignment purpose. It is easy when there is a first beam exiting the prism, to align another one

in a contra propagating way. The light exiting from the back prism can be considered as additional losses for the resonator, and it is possible to a certain extent to always change the position of the input prism to reach the critically coupling regime (Figure 11.5) whatever the distance of the output prism. That means, for a large range of finesses, having all the light going through the cavity and exiting the other side.

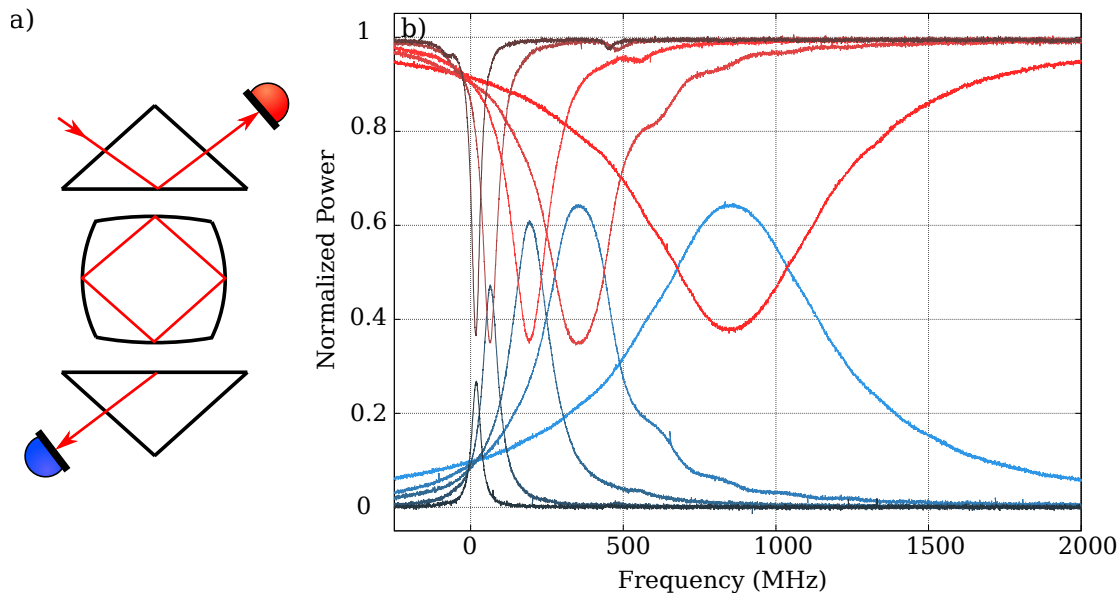


Figure 11.5.: (a) Schematic of the system to achieve impedance matching for different linewidths of the resonator. By scanning the resonator frequency and by tuning the two distances between the resonator and the prism we demonstrate constant impedance matching of the resonator. (b) shows the normalized power in reflection (red) and the transmission power (blue) during the scan of the frequency for different distances between the resonator and the second prism (on the side of the blue detector) for some experimental data for 1064nm.

11.2.0.1. Electro-Optics Tuning

To make the light resonate in the cavity it is possible to change the frequency of the light to match the cavity, but it is not really appropriate when dealing with more than one system. It is much more interesting to be able to directly move the frequency of the resonator. In a standard cavity, we can move the position of the mirrors to change the frequency of the resonator, but this monolithic design doesn't allow it. Fortunately, the refractive index of Lithium Niobate can be tuned with an applied voltage with the Pockel effect ([85][89]). It provides a similar result then moving a mirror in a standard cavity, allowing us to match the frequency of the resonator to the frequency of the laser.

$$\Delta n = \frac{1}{2} r n_0^3 \frac{V}{h}$$

with V the applied voltage, h the length of crystal between the two electrodes, n_0 the index at $V = 0$ and r the electro-optic coefficient. The green light is polarized vertically in the resonator which correspond to the r_{22} electro-optic coefficient of $33\text{pm}/V$. The red light is polarized horizontally and correspond to the r_{33} electro-optic coefficient of $7\text{pm}/V$.

With 600V of HV tuning, it is possible to scan a bit more than an FSR for the green (Figure 11.3) which is useful for alignment purposes. Unfortunately the red coefficient is much smaller so it is not possible to observe one full FSR. The initial alignment is harder, but when the TEM00 peak is identified, a change of temperature of the crystal or frequency of the laser will make the peak in the range of the scan. The monolithic aspect of the resonator makes the system very stable, and almost no drift of the peak is experienced. (The resonator is $200\mu\text{m}$ thick, and allows us to get a tuning of $40\text{MHz}/V$ for green and $6\text{MHz}/V$ for red (FSR = 19GHz)).

Electro Optic tuning also has the advantage to be very fast. It is possible to modulate the cavity frequency at hundredth of MHz directly by adding a modulation in the voltage (Figure 11.6). In Figure Figure 11.6(d) we modulate the voltage at 249MHz and demodulate the signal to create an error signal for the red light without any external EOM on the beam.

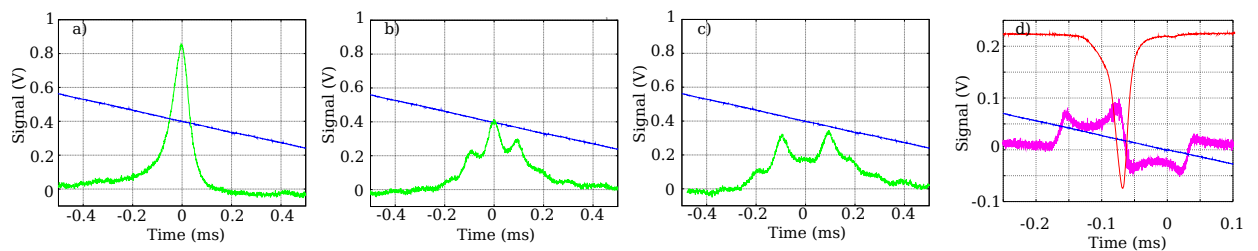


Figure 11.6.: (a-c) A few volts of modulation applied directly to the electrode during the scan of the resonator (with the voltage of this same electrode) with 532nm light (green). ((a) is the reference without modulation.) (d) Error signal obtained by modulating the voltage at the electrode at 249MHz and demodulating the reflected signal (magenta) during the scan of the frequency of the light of the laser at 1064nm (red).

11.3. Phase Control

Even when a prism doesn't couple out some light because the indices doesn't allow for propagation, there is still a very noticeable effect on the phase of the light in the

resonator (Figure 11.7). By moving the green calcite coupler close enough to the resonator, we observe a broadening of the linewidth of the green peak like expected, but also a displacement of the red peak (with the green peak almost unmoving) (Figure 11.7 (c-e)). This displacement can go as far as from double resonant with a peak of the green light to almost double resonant with the next FSR of the green light (Figure 11.7). It is explained by the fact that the applied voltage mostly moves the index of the green light, almost without changing the red light index. So a very small change of phase for the red light will have a huge effect on the coincidence between green and red during the scan of the applied voltage.

The linewidth of the red shouldn't be affected at all by the green calcite prism, but in practice it is. It is explained by the fact that the prism and the resonator axis may not be perfectly in the vertical axis leading to some light still being a bit coupled in the prism, but as long as the distance is large, the coupling should be negligible and there is a possibility to use this control to achieve double resonance in the resonator. We are using this technique to perform squeezing with this resonator.

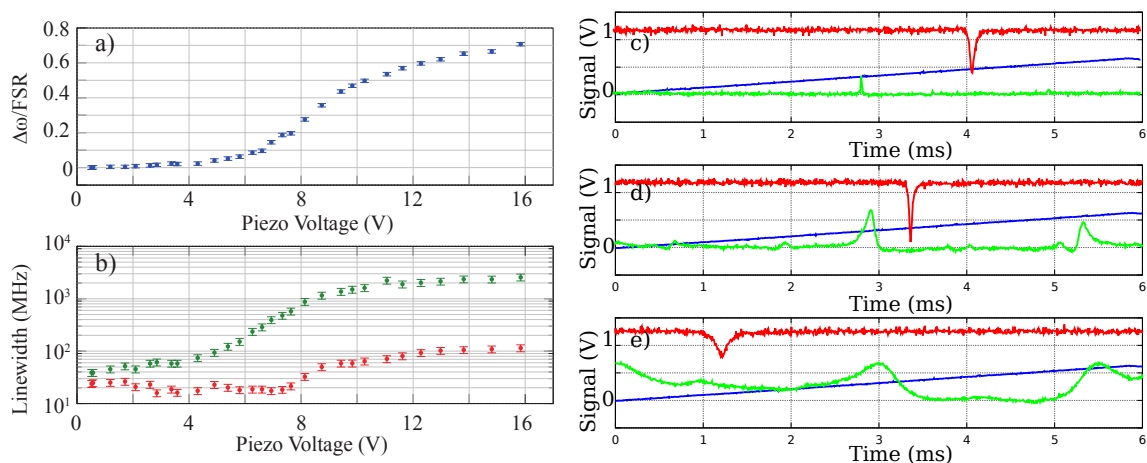


Figure 11.7.: (a) Relative phase between 1064nm light and 532nm light during the scan of the applied voltage in function of the distance between the green calcite prism and the resonator. (b) Linewidth variation of the light for 1064nm (red) and 532nm (green). (c-e) are examples of scans where the distance between the green calcite coupler and the resonator is decreased (from (c) to (e)).

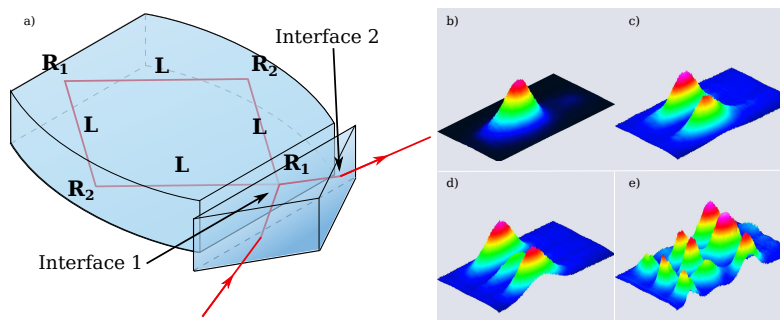


Figure 11.8.: Schematic of the resonator. The resonator is made of four curved mirrors and four times a propagation of $L = d\sqrt{2}$ where d is the diameter of the resonator. For leaving the resonator, the beam goes through the two interfaces that modified its waist. (b-e) are some of the modes of the resonator with light at 1064nm (red) exiting by the SF11.

11.4. TEM Modes

11.5. ABCD Matrix Considerations and Stability of the resonator

A big advantage of this resonator, compared to a Whispering Gallery Mode Resonator (WGMR), is the fact that there are only four reflection surfaces (Figure 11.8). The system is equivalent to a ring cavity with four mirrors and unlike the WGMR ([96]), the finite number of reflections allows the resonant modes to be the familiar Hermite-Gaussian TEM modes of a free space cavity. It is possible to use ABCD matrices (subsection 2.1.4, section 4.3) to know the shape of the modes and the stability of the resonator. The resonator is made of two surfaces in front of each other of curvature R_1 , R_2 and 4 propagation lengths l which are the 4 sides of a square of diagonal $d = 2.3mm$ (Figure 11.8). The matrix of the resonator is given by:

$$T = L * C_{R1} * L * C_{R2} * L * C_{R1} * L * C_{R2}$$

where $L = \begin{pmatrix} 1 & l \\ 0 & 1 \end{pmatrix}$ with $l = d/\sqrt{2}$ and $C_R = \begin{pmatrix} 1 & 0 \\ -2/R_e & 1 \end{pmatrix}$ with $R_e = R \cos(\theta)$ in the horizontal plane, and $R_e = R/\cos(\theta)$ in the vertical plane, and with $R = \{R_1, R_2\}$ and $\theta = 45^\circ$ the angle between the beam and the mirror normal in the horizontal plane. The mirrors have been design to make the beam almost spherical in the resonator. (In the horizontal plane: $R_1 = 13mm$, $R_2 = 17mm$, and in the vertical plane: $R_1 = 55mm$, $R_2 = 5.5mm$.) We deduce that the system is stable and corresponds for the red light to a waist of $w_r = 21\mu m$ in the horizontal plane and $w_r = 25\mu m$ in the vertical plane, and for the green light to a waist of $w_g = 15\mu m$ for

the horizontal plane and $w_g = 18\mu m$ for the vertical plane. The beam has 4 waist positions arranged in a symmetric way very close to the two coupling surfaces.

It is important for the waist not to be too small in the resonator or the instability due to electro-optic effect becomes too pronounced. A few of the systems that we worked with had too-small waists and were completely impossible to work with.

11.5.0.1. Coupling Mode

The beam exiting the resonator has to go through the prism with an angle $\theta_p = \arcsin\left(\frac{n_r}{n_p} \sin(45^\circ)\right)$, and leaves this same prism with an angle α (given in Figure 12.1 for each prism). The interface between the resonator and the prism (Figure 11.8) can be considered in the same way as an interface between two media of indices n_1 and n_2 (without gap) met with an angle of incidence of 45° . (We neglect the curvature of the coupling surface, a more complete resolution can be done using ([88].) It means that for the two surfaces we can use the matrix:

$$M_{n_1, n_2}(\alpha) = \begin{pmatrix} \sqrt{\frac{1 - \left(\frac{n_1}{n_2} \sin(\alpha)\right)^2}{\cos^2(\alpha)}} & 0 \\ 0 & \frac{n_1}{n_2} * \sqrt{\frac{\cos^2(\alpha)}{1 - \left(\frac{n_1}{n_2} \sin(\alpha)\right)^2}} \end{pmatrix} \text{ for } \alpha \in \left[-\frac{\pi}{2}, \frac{\pi}{2}\right]$$

In the vertical direction, there is no angle at any surface, so the beam just propagates through the different materials. For the horizontal direction, the beam is transformed by the matrix: $M = M_{n_1, n_2}(\alpha) * \begin{pmatrix} 1 & l \\ 0 & 1 \end{pmatrix} M_{n_1, n_2}(45^\circ)$ with l the distance traveled by the light in the prism, and α the angle with which the light exits the prism. Unfortunately the mode in the resonator used in this thesis hasn't been corrected for the propagation by the prism. But it has been demonstrated ([73]) that it is possible to design an elliptical beam in the resonator which leaves the prism with a spherical shape by tuning correctly the curvature in the resonator. Such a correction should be considered in a future system. The waists leaving the resonator for the SF11 are: for red $w_r = 17\mu m$ in horizontal direction and $w_r = 36\mu m$ in vertical direction. And for green, $w_g = 13\mu m$ in horizontal direction and $w_g = 25\mu m$ in the vertical direction. Figure 11.8 are some of the modes of the beam going out of the resonator.

12. Experimental Methods

12.1. Creation of Resonators

The Lithium Niobate comes in rods of ~ 5 mm radius and length of a few centimeters. We slice these rods into small cylinders of around 1 mm thick with a high speed blade, and glue them with epoxy on a rod of brass with a screw base made by our mechanical workshop (Figure 12.6). We reduce the thickness of the cylinder with a lathe and glue another small cylinder of brass on top of it to make the top electrode. The top cylinder of brass is made a bit rough with some acid to make sure that the glue holds well; for the bottom brass rod, the rough surface of the crystal cylinder is enough to make the glue hold well. To give the final shape of the resonator we use the lathe to cut the surface of the resonator. The lathe is a very high precision machine, a Moore 250 UPL 4 axis ([98]), which has a very sensitive high speed spindle (10,000 turn/minute maximum around the X axis), two horizontal axes of translation (X and Y axis) and another axis of rotation (around Z), with a precision of a few nm when it is not doing anything and a few tenth of nm when it is cutting). The spindle turns the brass rod around its axis and a diamond tool cuts the crystal on the side. The diamond cut movements are synchronized to the rotation of the spindle to make the square shape, then the diamond tool is slowly translated along the axis of the crystal cylinder to give the shape to all the resonator. This technique allows us to create mirror shapes with a different curvature along the two axis, it can help for shaping the beam to obtain a spherical beam at the end of the prism after coupling. The lathe first roughly reduces the radius of the rod keeping the cylindrical shape then with a small depth, four square faces of $\sim 100\mu m$ width only are cut to avoid large movements of the spindle. For the resonator that I am describing in this thesis, the two coupling faces have the curvature: $R_1 = 13mm$ horizontally, and $R_2 = 17mm$ vertically, and the two other faces have the curvature $R_1 = 55mm$ vertically and $R_2 = 5.5mm$ horizontally. The cut of the resonators with the lathe have been made by Shen Yong and Geoff Campbell ([73]).

12.1.1. Polishing

After the cut with the lathe, the quality of the resonator's faces is not yet good enough for the experiment. The maximum finesse for the light at 1064nm will be a bit less than 100 and the maximum finesse of the green a bit lower again. It is

necessary to polish these faces to a higher quality. After the cut, with some white light interferometry done on the face of the resonator on the lathe, it is possible to see some tiny scratches from the tool during the cut. These imperfections can be removed with some hand polishing. I used some polishing diamond paste ([69]) on a polishing pad or a simple clean lens tissue ([67]) to improve the quality of the surfaces. I usually add water to the diamond paste, it makes the polishing longer, but softer. The polishing paste comes with different particle sizes. I usually start with $1\ \mu\text{m}$ particle to remove the big scratches and slowly decrease to $0.5\ \mu\text{m}$, then $0.25\ \mu\text{m}$ and finally $0.1\ \mu\text{m}$. The $1\ \mu\text{m}$ particle will actually add more scratches visible with the white light, but will help to remove the biggest ones rapidly. $0.5\ \mu\text{m}$ and $0.25\ \mu\text{m}$ will allow me to remove completely any visible scratches with the white light, and $0.1\ \mu\text{m}$ will be the very fine final polishing. The result can only be checked by actually aligning the resonator and measuring the finesse of it. The pad and the particle paste need to be very clean, since if there are any big particles in the mix during the polishing (like dust), it ends up with more scratches and usually it needs to be polished again from the $1\ \mu\text{m}$ particle paste. It is not necessary to polish Lithium Niobate too much, because the material absorption is quite high and will at one point be the main limitation for the losses of the system. For the resonator that I am using in this thesis (a square of side 2.3mm), I got a polishing corresponding to a linewidth of 9MHz which corresponds more or less to the absorption of the bulk material. ([83]).

Too much polishing can be counterproductive. At one point the shape of the surfaces will be affected by the polishing and it can lead to a shape of mode not Gaussian anymore.

12.2. Prisms

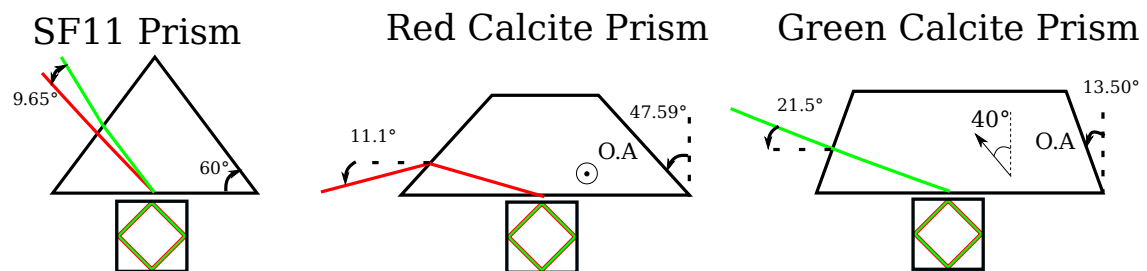


Figure 12.1.: Different prisms used in this thesis with their coupling angles.

Three different prisms have been used for different purposes in the system Figure 12.1. The simplest one is the SF11 prism. It is an equilateral piece of SF11 material of 1cm side length. It is isotropic and allows the red light and the green light to be coupled. An inconvenience is that it is not possible to look at the interface through it directly with the camera, but we can still do it indirectly (with a bit of trouble)

by looking at the reflection of the image from one face of the crystal. The index of the material is $n_t = 1.75$ for red and $n_g = 1.79$ for green.

The second prism is the red calcite. It is made of birefringent material (calcite) with the extraordinary axis in the vertical direction. (For the green: $n_e = 1.4882$ and $n_o = 1.64246$, and for the red: $n_e = 1.4796$ and $n_o = 1.6425$.) It can couple the red light (polarized horizontally), but not the green light (polarized vertically), and can move the phase of the green light in the resonator, but only if it is brought very close to the resonator. The prism is made in a trapezoid form to be able to see the interface through the prism with the camera. And its angle is made to have the beam leaving the resonator with a Bruster angle to limit losses.

The third prism, the green calcite, is also made of calcite but with the extraordinary axis on the horizontal plane making an angle of 40° with the normal of the coupling face. It allows the coupling of the green light, but not the red light. It does, however, still allow us to change the phase of the red light in the resonator Figure 11.7. The prism is also made in a trapezoid shape to facilitate the alignment of the surfaces.

The different combinations of prisms allow us to choose in which regime of linewidth we can tune the system (Figure 12.2).

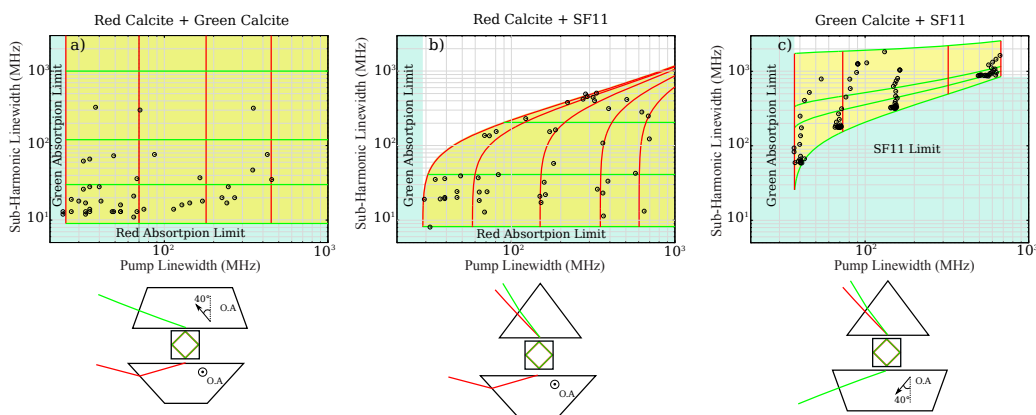


Figure 12.2.: Available linewidths for green and red in the cavity that the system can reach (in yellow) with (a) the two calcite prisms, (b) an SF11 prism and a green calcite prism and (c) a SF11 prism and a red calcite prism. The dots are experimental data.

12.3. Mechanical System

Lasers: We used two different lasers for studying this resonator. The first is the Diablo laser as described in the section on the mini-OPO (subsection 7.2.1). It has the advantage of being powerful and of having the two frequencies that we need for squeezing (1064nm and 532nm). But changing its frequency produces mode hopping

which usually collapses the double resonance. We also used a less powerful laser, the TLB-6721 Velocity diode laser ([65]), which provides only 1064nm light with only 40mW of power. This makes this laser not suitable for generating squeezing, but it has the advantage to be very highly and rapidly tunable in frequency (22GHz of fast tuning and 22nm of slow tuning free from mode hops) The resonator has an FSR of 18GHz, which makes it hard to align with the Diablo laser, but the large scan range of the diode laser is really helpful for alignment purposes.

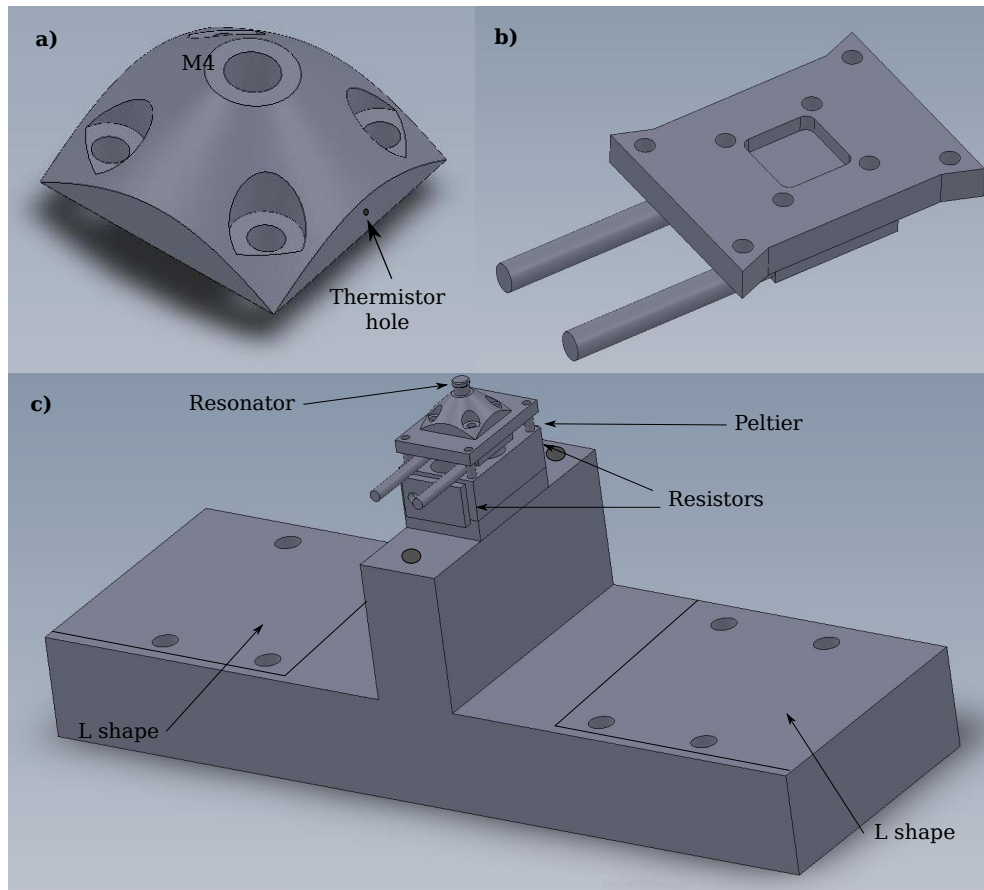


Figure 12.3.: (a) Dome holding the resonator brass holder (Figure 12.6). (b) Piece of copper holding a peltier with a square shape adjusted to the dome to be able to remove the dome and put it back without changing alignment. (c) Schematic of the base holding all the system with two L shapes to place the prism holders and to be able to switch between different prisms without changing alignment.

Dome The resonator brass holder is not really convenient to screw and unscrew. Since it would need realignment all the time, we created a little dome Figure 12.3(a) in copper with a square shape perfectly adjusted to the square hole of the second copper piece Figure 12.3(b). It can be removed and replaced without disturbing too much the alignment, and the curved shape allows easy access to the resonator

with the prism mounts. A similar square hole on a piece of aluminum, which can be attached to the lathe spindle, allows the resonator to go back and forth between the optic table and the lathe for polishing and measuring finesse. A little hole is also made in the dome to be able to add the thermistor to measure the temperature of the system.

Base The second copper piece Figure 12.3 (b) is holding a peltier (TEC3-2.5 ([67])) with four plastic screws to the T base Figure 12.3 (c) to allow control of temperature. The temperature that needs to be reached is around 60°C which is a bit high for fast tuning with the peltier, so we also added some holes on the side of the T base Figure 12.3(c) head for adding resistors on each side to have constant heating of the whole system. If the resistors are used, it is important to use one on each side, or the gradient of temperature can deform too much the total mount making it harder to use. On each side of the top of the T base, there are two M4 holes to fix the clamp that will hold the HV electrode. The two sides of the T base also have an L shape imprint. There are small grooves (1mm) in the shape of an L to be able to remove the prism holders and put them back without changing alignment. It is pretty reliable, I usually don't need to realign the prisms when swapping to another mount already pre-aligned. For moving the prisms, we need precise positioning, but also long range translation for being able to remove one prism without damaging the whole system. We are using a translation stage (M-461 ([65])) with a precision adjustment screw which gives a few centimeters of coarse translation and fine translation. The translation stages are directly screwed onto the base using the L shapes to position them in a repeatable way. It is useful to have three of them at least with a prism mount and a prism on them to be able to switch from one to another without changing any alignment.

Prisms Holder The prism is held at the limit of the platform in aluminum Figure 12.4 (c)). The top surface of the platform has three M4 screw holes to be able to fix a clamp somewhere to be able to hold the prism with the coupling face a bit beyond the limit of the platform. (It makes the contact with the resonator easier.) It is a simple design, but it allows us to hold any kind of prism, and it gives less chance to have something in the path of the beam of one of the prisms, or to be in front of the point that we want to observe with the microscope or the white light interferometer. The three holes that we can see in the schematic Figure 12.4 (c)) are grooves for screws to be able to fix the aluminum piece to the platform of the rotation stage (Figure 12.4 (b)). There are also two holes horizontally which go through the aluminum with a very small quantity of material left (around 1mm for each flexure lines). It allows the platform to bend elastically at those points and allows a small horizontal translation of all the top part of the platform. This movement is done by a piezo (Figure 12.4 (d)) with an M9 screw step on its side, fixed to the rotation stage (Figure 12.4 (b) and pushing the platform. For holding the platform, we used two systems: a Radian Dyes mirror holder (Figure 12.4 (a)) ([66]) with an

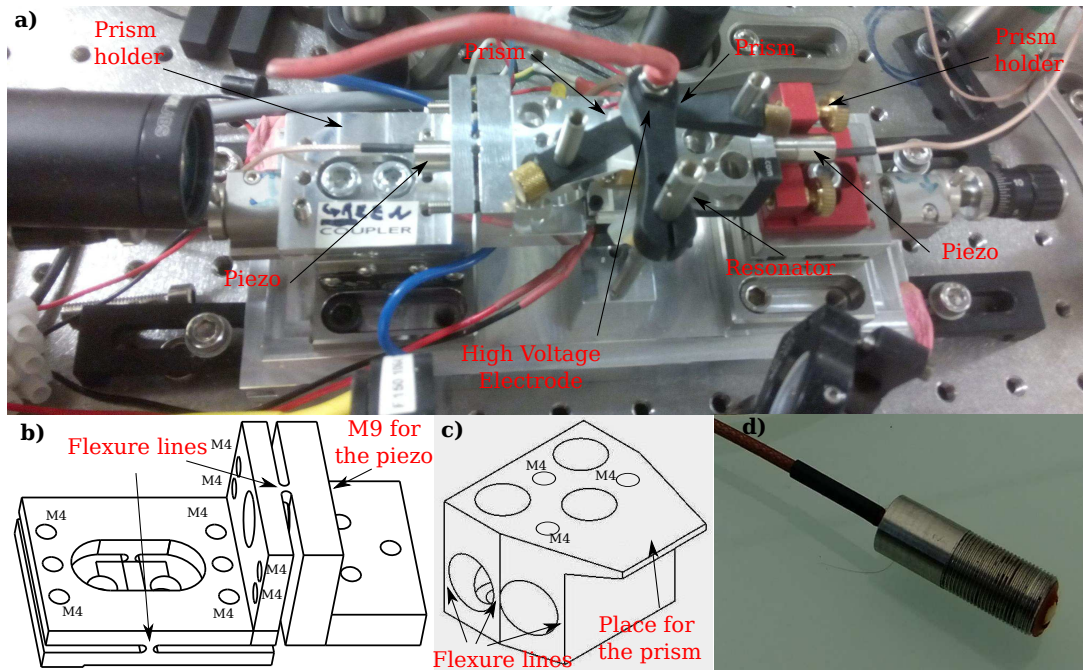


Figure 12.4.: (a) Image of the SqOPO with the two different prism holders. (b) Schematic of the custom prism holder with the two flexure lines. (c) Platform holding the prism with a clamp. (d) Piezo (FPSt 150/4/20 M8 ([70])) used in the experiment.

L platform with three screw holes for fixing the platform and a custom M9 screw hole for holding the piezo. It is a compact system, but the strings of this mount are not really stiff which makes the system less stable. We also used a custom flexure stage (Figure 12.4 (b)) using the same principal as the platform, but with only one flexure line for each rotation and some M4 screws pushing in one direction or the other to control the angle. The prism and the resonator faces need to be very well aligned to allow us to be as close as possible. So by using one screw on each side of a flexure line and by unscrewing a bit one and tightening the other, the rotation stage bends and turns a bit the prism in one direction. With the two flexure lines, we have the two degrees of freedom that we need. The rotation stage is fixed to the translation ((Figure 12.4 (b))) stage by two M6 screws in the middle, and because the two horizontal flat surfaces move and may contact the screw's head, the system needs a big empty area at this level to provide against this problem. Similarly for the piezo, the vertical plane on the right contains a M9 screw hole, and the other plane has a hole big enough to allow movement of the core of the piezo during the rotation of the stage without colliding the piezo. This configuration is stable enough that I don't really need any feedback for the position of the prisms compared to the resonator, we observe a drift in the position (and so, in the coupling) only after several minutes.

12.4. High Voltage

The voltage applied to the resonator should be done only with very low current, but the voltage is high enough (600V) to need to be careful with the electrodes. We used a copper wire and a plastic M4 screw to isolate the positive electrode. We heated the wire with a soldering iron, and melted the middle of the screw with it by passing it through. The wire exceeded the screw at the end with just enough length to go between the two prisms and when the wire cooled down, the plastic stuck to it very well, giving a very good insulation. The wire and the screw are recovered by some heat shrink gain to avoid electrical contact, and I screwed the plastic screw to a clamp (PM3 ([67])) directly fixed to the T base M4 holes. There are two M4 holes on the T base on each side, because the clamp is usually exactly in the way of one of the beams, which can be problematic. I solved this difficulty by gluing a tiny mirror to the rod holding the clamp to get the light in reflection Figure 12.4 (a)).

12.5. Alignment

12.5.1. How to Align Prisms and Resonators

The coupling between the prism and the resonator is done by frustrated internal reflection. It requires both media to be very close to each other (few hundreds of nanometers) at the point where the beam is reflected. The two surfaces are more or less flat, so to be able to make them that close, it is necessary to have them as parallel as possible. Moreover, if the surfaces are not parallel at the reflecting point, one side of the beam will experience a bigger distance than the other one, making the coupling bigger on one side comparing to the other, creating a mode with some TEM01 components.

We first used a microscope (Figure 12.6 (b)) attached to a camera on a flexible arm to be able to look at the surfaces from the side and from the top. It is a good first way to align the prism but it is usually not enough. Moreover when no light is aligned yet in the resonator, there is no real way to know if the prism and the resonator are contacting and starting to damage each other, or if they are still too far from each other to see any coupling. It makes the first alignment of the beam very frustrating. A very good solution is to use white light interferometry and observe newton rings.

Depending on the prisms that are in place and how many of them, the illumination of the surface will be different, but mostly we need to have some light with low coherence sent perpendicularly to the surfaces, and imaging it with a lens. The calcite prisms have a flat back surface, so some light can be sent through it and with a 50 cm lens, we can image the surface to a camera. We can sent the light through the resonator from the other side, or from the same side using a Beam

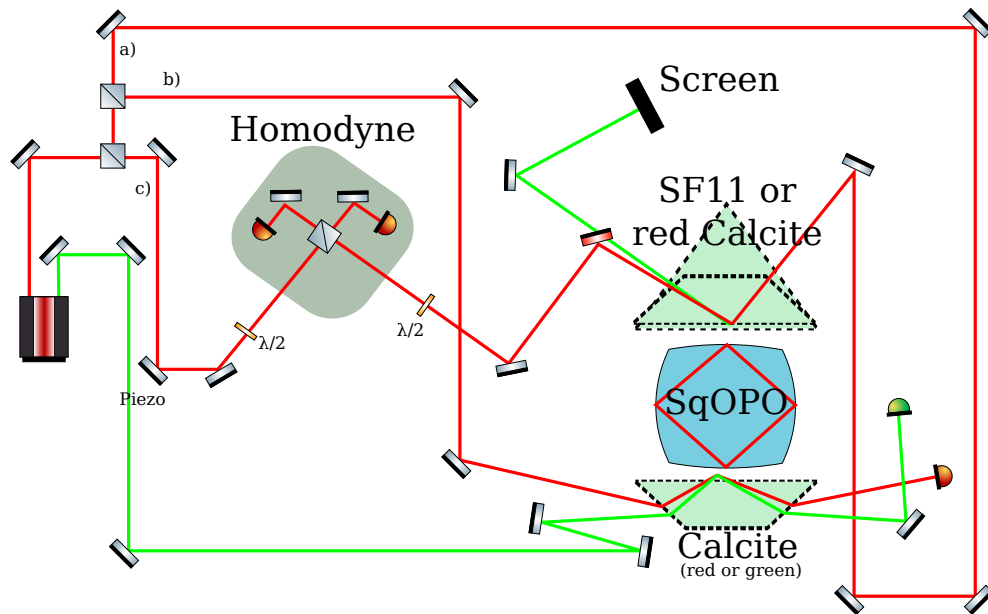


Figure 12.5.: Schematic of the experiment. For both sides of the SqOPO resonator, it is possible to choose which prism to use. The Diablo laser is sending a green beam (the pump at 532nm) to the green calcite prism in the bottom. With a SF11 prism on the top, the green light is coupled out and sent to a screen which allows to observe the mode during locking. The laser also generates some red light (sub-harmonic at 1064nm) that we divide in three. (a) is aligned to the SF11 or the red calcite on top to observe double resonance, (b) is aligned to the red calcite prism in the bottom for alignment of the homodyne with the light going out of the top prism, and (c) is the LO of the local oscillator. The two calcite prisms in the bottom can be switched without disturbing the alignment of the homodyne, but not the top ones.

splitter before the camera. The SF11 prism doesn't have any flat back surface, but it is equilateral, so the light going through one surface with a normal incidence, will be reflected on the next side inside the prism, and go through the last surface with a normal incidence. In this way we can observe the surfaces or illuminate them through the side of the prism. The microscope is just a camera ([67]) connected to a lens tube (SM1L20 [67]) and a 50 cm lens. This system is fixed on a translation stage that allows to mostly image one face of the resonator or the other. In practice, I image both faces at the same time to be able to see how close the prisms are, to make sure that I am not contacting too much which would damage the surfaces. I can also observe how good is the alignment by looking at the interference between the two surfaces. At the beginning of the alignment, I mostly see lines, but by turning the prism rotation stages accordingly, I can align the surfaces to a very good parallelism. The limited factors are the alignment of the illumination and the microscope, that can make you miss where the contour of the resonator surface are,

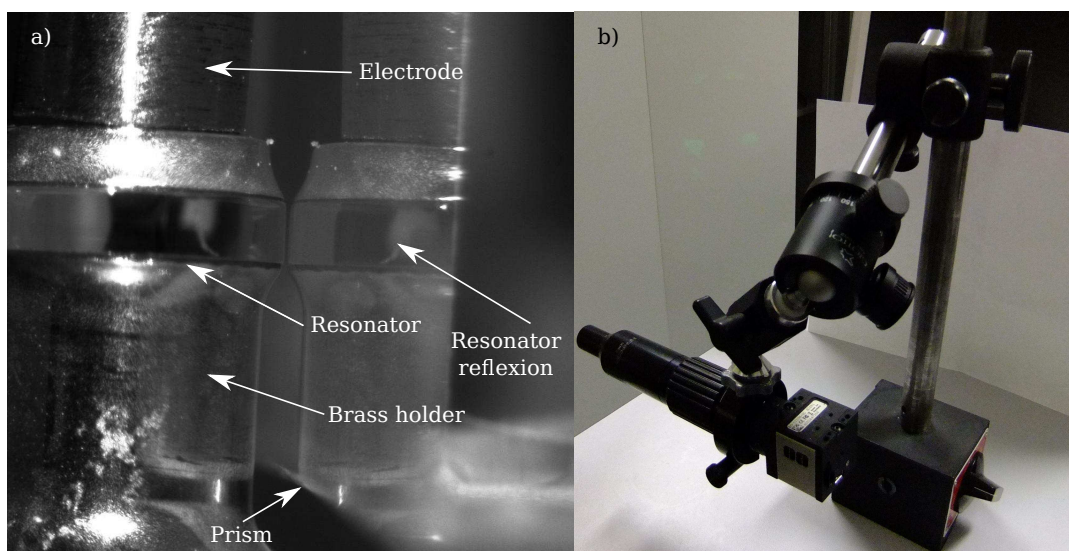


Figure 12.6.: (a) Image of the resonator from the side with the camera on a microscope tube (InfiniProbe ([64])) (b).

and so where is the middle point where the light is reflected. The surface of the resonator is curved, so we can see rings, but it is not completely obvious where should be the center (it should be where the light is reflected). The light that I used is a SLG150T-WT which gives 3 different illumination colors, I use the red color which allows to start to see rings after a few tenth of microns of distance, then I usually switch to green which gives only a few rings visible before contact.

Even after alignment, the white light is always turned on to monitor the distance between the surfaces. When there are no peaks on the oscilloscope, it is important to still have an idea of how close the prism and the resonator are.

12.5.2. How to Align the Beam with Contra-Propagating Beams

When the prisms are aligned, the alignment of the beam can start. For the first alignment of a beam, it helps a lot to have two prisms that can couple the light that we intend to align. Even if the second prism needs to be a prism that doesn't couple this light and is already aligned, it is interesting to swap it against another one. The L shape on the T base allows us to switch between prisms almost without realigning anything, and this will make it easy to return later to another configuration. I used a collimated beam with the correct polarization and the waist corresponding to the lens that I intend to use as coupler, and without the coupling lens, I align the beam as much as possible on the face of the prism with the height at the level of the resonator with the angle that the Fresnel calculation (section 12.2) gives, and I make sure that the beam is as horizontal as possible. I use the camera and the white light to place the prism that I am aligning in contact with the resonator and the other one

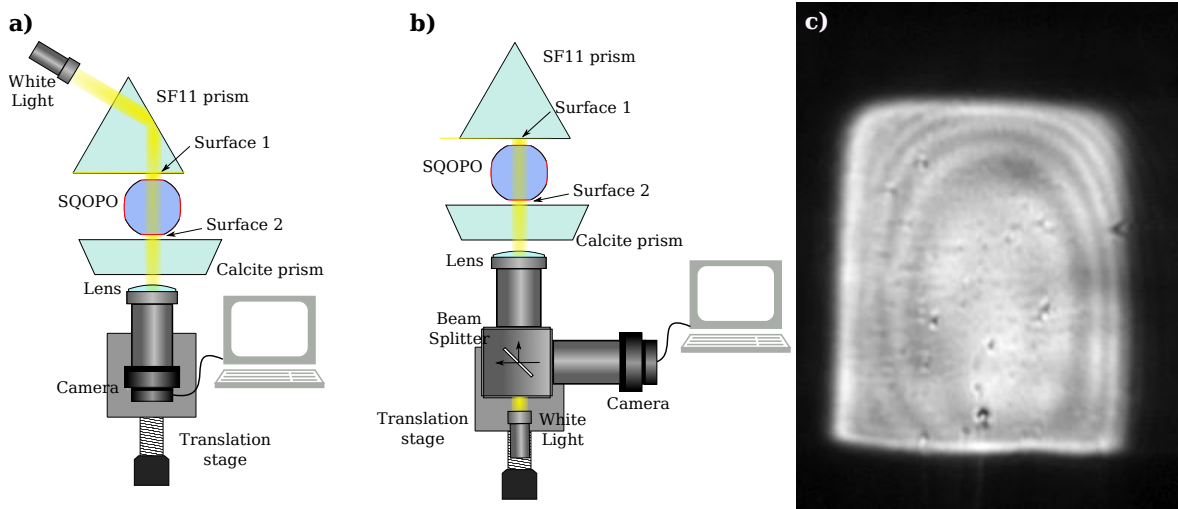


Figure 12.7.: (a-b) Schematic of the white light interferometry to observe the alignment between the prisms and the resonator, (a) with illumination from the SF11, and (b) using a beam splitter for the illumination. (c) Image of the Newton rings with the camera.

far enough not to have any coupling (a few fringes of the white light are enough). I make sure that the high voltage is scanning $\sim 600\text{V}$ at a speed around $\sim 1\text{Hz}$. I put the coupling lens in the path of the beam a bit too far from the resonator to have a spot big enough to simplify the first alignment.

With enough input light, and with the exposure time of the camera (of the white light interferometer) long enough, I should be able to see the beam spot on the camera (the camera can see close infrared (IR)). Then I usually move around the coupling lens by hand to move the light spot point, moving up and down a bit if I need to. When the light spot is close enough to the contact point, all the resonators start to shine with some moving scattering light everywhere. With the IR card, we can observe the reflected beam at the other end of the resonator, it has usually a very strange shape and usually is moving. I send the reflected beam to a detector with a large window with a lens, and observe the signal with an oscilloscope. At this point I may just see some weak oscillations. I can very slightly increase the distance between the prism and the resonator to increase its finesse and play a bit with the lens, bringing it slowly closer to the resonator moving it side to side by hand, still adjusting the position of the prism with the piezo when I need to. At this point I usually can see some small cavity peaks in reflection. Then I get closer with the second prism until I can see some light going out the other way. It will be a compromise between a high finesse cavity with the two prisms far enough but almost no light exiting, or enough light exiting but a shape of the beam hard to interpret. Seeing the output beam makes it easier to align to a more spherical shape and find the TEM₀₀. It is also sometimes a good idea to align rapidly another beam in the other direction (from the other prism) to have the TEM₀₀ going out from the

prism that we want to align, and put all the optics to have the beam nicely in the center, and perfectly collimated to get the best coupling possible.

12.5.3. Temperature Tuning of the Crystal

To control the temperature of the crystal, we have two resistances for the coarse tuning and a peltier for the fine tuning. The two resistances are connected to the same power supply to heat the system close to the temperature expected in a constant way. A thermistor on the dome allows us to read the temperature precisely and send its fluctuation to a PID controller (LFI-3751 ([68])) to feed it back to the peltier. In that way we can obtain a sensibility of a millidegree. To get the optimal temperature for squeezing, we generate second harmonic generation (SHG) with a powerful 1064nm beam in the resonator, and look for the best efficiency temperature. This method has some inconvenience that SHG will vary with the coupling of the prisms, and the distances will change with the change of temperature. The solution was to align a beam on the side of the resonator and generate SHG in single pass through the side. In this way we can get the maximum coupling temperature for the crystal. Another issue for optimal temperature is the fact that the thermistor is still far from the resonator itself, and green light is absorbed significantly in the resonator changing the local temperature in the crystal. So for the same temperature measured by the thermistor, different green light powers in the resonator can change in an important way the real temperature in the crystal.

12.5.4. Homodyne Alignment

To align correctly the homodyne detection, it is necessary to have a beam of light exiting the resonator in the same mode as the expected squeezed mode. It means that we need two prisms able to couple the red light. One will be the out coupler for the squeezing (the SF11 or the red calcite), the other one is a red calcite or a SF11 to couple some red light inside the resonator. After alignment, it is obviously not possible to move the out coupler prism anymore, but the input coupler can be later switched to another prism more ideal for coupling the green light. I usually lock the resonator with the HV using PDH locking system (with the modulation at 12MHz of the Diablo laser) to have some continuous light leaving the resonator. Then, in the same way as the miniOPO in the previous chapter (subsection 7.2.5), the beam is mixed with a strong beam, the Local Oscillator (LO) in a NPBS. A $\lambda/2$ on the path coming from the resonator allows us to make sure that the beam splitter is perfectly 50/50, and another $\lambda/2$ on the LO path allows us to match the two polarizations. The beam coming from the resonator is still slightly elliptical for the SF11 and very elliptical for the red calcite which makes the homodyne harder to align, and repetitive polishing on this specific crystal may have changed the shape of the resonator leading to a beam not necessarily perfectly Gaussian anymore.

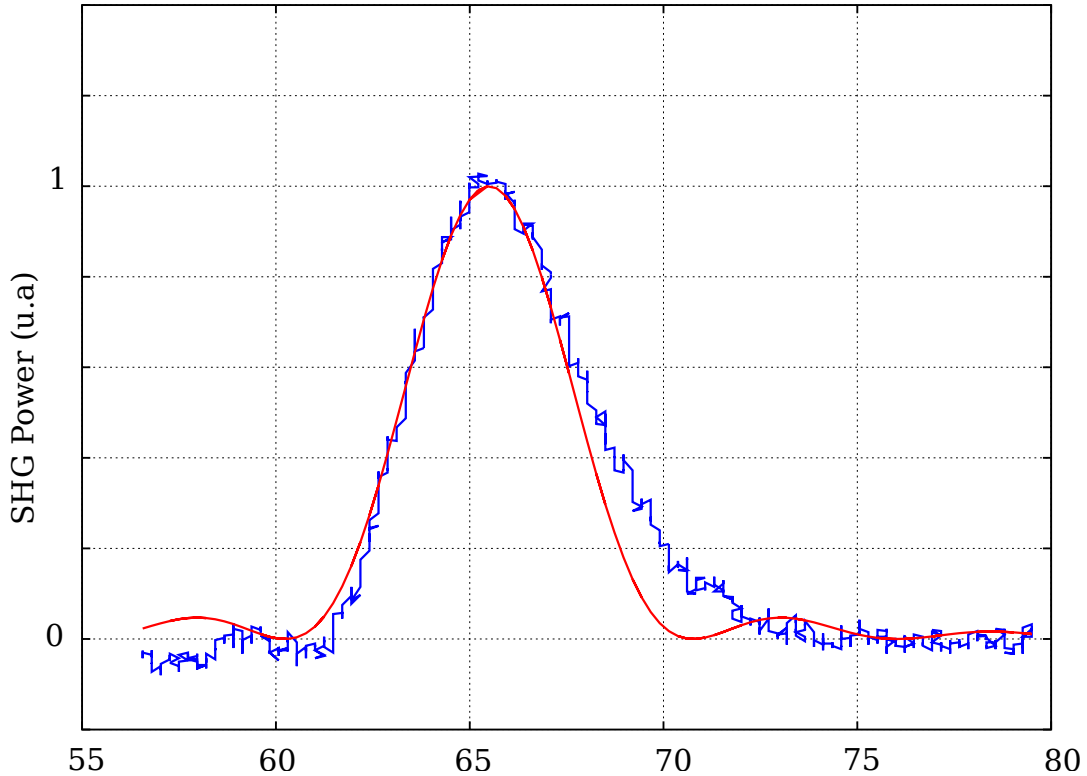


Figure 12.8.: Second harmonic generation with a beam sent through the resonator by the side (there is no cavity involved, the beam just goes through the bulk material) fitted by $\text{sinc}^2(\alpha(T - T_0))$ with $\alpha = 0.19^\circ\text{C}^{-1}$.

Moreover, the SF11 doesn't allow an easy access to the face making the alignment between the prism and the resonator harder. If the two faces are not parallel the beam will experience a different coupling for different positions of the beam leading to a TEM01 component. All these things should explain why we obtain only 84% of visibility in the homodyne for the measurement with the SF11 and 85% for the measurement with the red calcite. But it has been recorded in a similar resonator in Lithium Niobate with a SF11 prism a coupling of 90% ([73]), so it should be possible to design another resonator with a better geometry and using a prism in a trapezoid shape to be able to have perfectly parallel surfaces and a better mode, allowing us to obtain much better visibility in the homodyne.

12.5.5. Prism Switching and alignment for Squeezing

When the homodyne is aligned with the SF11 prism or the red calcite as input coupler prism, it is necessary to switch to a prism that can couple the green light and doesn't perturb the squeezed light. The SF11 could couple the green light, but the characteristic distance to couple the green light is slightly smaller than the one to couple red leading to a finesse too small for the red to have squeezing and some

leaking of the squeezing, so we need to switch it for the green calcite. The green calcite should have been previously aligned properly to facilitate the alignment. The L shape groove on the base (section 12.3) allows us to remove the translation stage with the red calcite and switch it to the one with the green calcite without changing too much the alignment. When the prism is contacted with the resonator (monitored with the white light interferometer), the green beam should already be aligned or very close to it. When the green TEM00 is identified and optimized, it is possible to start the measurement of the squeezing.

12.6. Lock and Self Locking

HV locking: The system can be locked in frequency with a PDH locking ([77]) feedback to the HV electrode. We usually use a phase modulator in the path of the beam (red or green), or we use the modulation already coming from the laser at 12MHz. The light in reflection from the resonator is collected by a detector, and the AC signal from it is demodulated at the same frequency with a mixer and a low pass filter to obtain the error signal. This signal is more or less the derivative of the reflecting power vs the frequency, it allows us to know in real time on which part of the peak the cavity is located and to be able to correct for it. This signal is sent to an FPGA controlled by a Labview program made by Seiji Armstrong (Armstrong [71]) to create the lock. Two signals are generated from the error signal: one is just a rescaling of the first one (proportional gain), and the other one is an integration of the error signal (integral gain). The sum of these two signals are sent back in real time to the HV amplifier, then to the HV electrode of the resonator to correct any little fluctuations from resonance. The Labview controller (NI PXI 1042Q, NI PXI 7833R) allows us to control how much of integral and proportional gain to use to optimize the lock.

This locking system is working well for the red, even with quite high power, as long as there is no SHG generated, and it also works well with green light at low power (few mW). In these regimes, it is even possible to change the position of the prisms relatively far without losing the lock. At high green power, the light is absorbed by the crystal and the temperature is locally increasing making the voltage locking point moves to the limits of the amplifier. It is possible to increase the performance of the lock by sending a copy of the error signal to the temperature of the laser to be able to follow this drift, but it doesn't really help at very high power, the laser eventually meets a mode hop and the resonator loses the lock. Second harmonic generation also usually makes the locking very unstable. The green light generated disturbs the system leading to some oscillatory regimes. Some more studies are needed to be able to get a stable second harmonic generation with such a system.

Self Locking Lithium Niobate has a significant absorption coefficient for green light, moreover, the system has four waists where the light is focused. It induces

strong thermal effects susceptible to affect the behavior of the resonator and makes the locking of the system difficult. But it can also allow us to use self locking ([74]). Self locking was also used in the previous chapter about the miniOPO. I refer the reader to it for a detailed explanation of self locking (subsection 7.5.2). During the scan, thermal absorption will broaden the linewidth in one direction of the scan, and narrow it in the other direction. This effect is enhanced by increasing the power of the field, or by decreasing the scan speed. The power of the beam increases the effect in a continuous way, but decreasing the speed of the scan seems more like a threshold behavior where nothing happens until the scan speed is slowing down enough and the self lock effect appears suddenly. (Figure 12.9) We use this effect to lock the system at high green power (in the condition for squeezing),. We move the frequency of the laser in one direction to push the resonance of the resonator until the power of the green is high enough. We are in self locking condition. This regime is stable enough to change the position of all the prisms and to measure squeezing without perturbing the lock. This lock is only sensitive to low frequency and won't affect high frequencies. It could be imagined to be combined with a high frequency lock made with HV using the DC power with an high pass filter as an error signal, but this amelioration hasn't been implemented yet in the experiment.

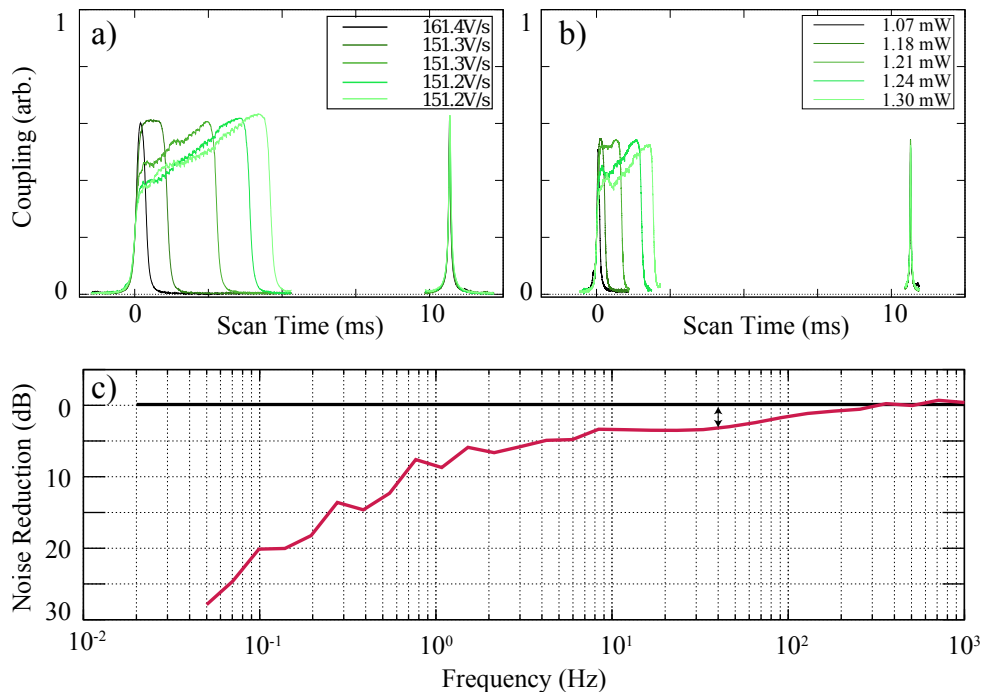


Figure 12.9.: (a) Self locking in function of the speed of the scan (on the left for the positive slope, on the right for the negative slope). (b) Self locking in function of the power of the input beam (renormalized). (c) Frequency noise response measured with a network analyzer by sending noise in the piezo of the laser and by measuring the response of an error signal made with a phase modulation on the beam.

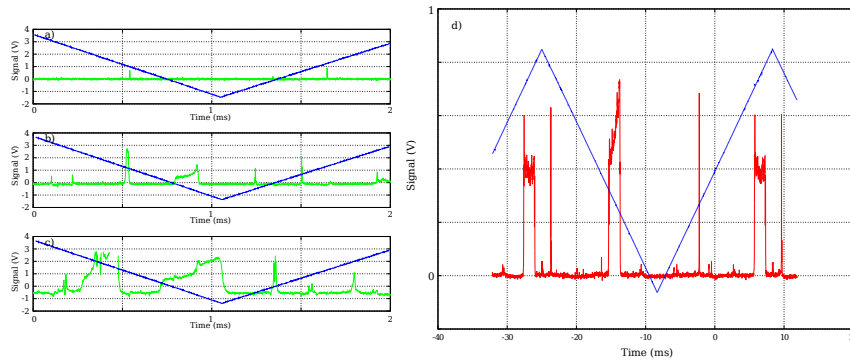


Figure 12.10.: (a-c) Effect of self locking on the peaks during the scan of applied voltage. (a) is with low power and relatively good alignment. By increasing power from (a) to (c), more peaks can be noticed and chaotic behavior starts to appear. (d) Self locking and self anti-locking in the same scan slope during the scan of high voltage meaning that there is a change of sign of the index thermal fluctuation coefficient which may means that the effect is actually not thermal.

Self Locking Limitations An interesting thing is that the self locking behavior with the applied voltage is different at high voltage and low voltage (Figure 12.10(d)). As explained in subsection 7.5.2, if the index thermal fluctuation coefficient is always the same, for one particular scan speed, we should always observe a broadening of the linewidth or a reduction of it, but not both at the same time. In our system, if the scan is large enough to observe two peaks, we observe the two effects happening on the same scan slope (Figure 12.10 (d)). It means that the change of index with the high voltage and the power has a non linear component. It explains certainly the great difficulty to lock the green light with the high voltage with high green power.

Another limitation is about the alignment. The green alignment is made at low power and can easily reach a good visibility (80% of visibility has been obtained with the green light), but when the power is increased, the peak behaviors change completely (Figure 12.10(a-c)), and some secondary modes start to be enhanced. It is really useful to have a prism that out couples the green to be able to see the shape of the mode and to be able to self lock on the TEM00 and not on other things.

Distance lock: Changing the coupling with prism distance is relatively stable, but it still fluctuates in the long term. Moreover, fluctuation of the distance due to acoustic noises could in principle be fed to the resonator, resulting in eventual amplitude and phase noise after the resonator. Far from critical coupling, it is possible to simply use the reflection power as a measure of the distance and feed it back in the control of the distance to enhance the stability, but close to the critically coupling distance, the coupling reaches an extrema, and the reflected power can't be used anymore as an error signal to increase stability. Nevertheless, it is still

possible to create an error signal in distance on the critical coupling point ([75]). For the cavity at resonance, the reflection intensity I_{ref} in function of the reflectivity coefficient r_1 of the first coupler and the incident intensity I_{inc} is given by:

$$I_{ref} = I_{inc} \left(\frac{r_1 - (1 - L_m)(1 - L)}{1 - r_1(1 - L)} \right)^2$$

with L the losses in the resonator and L_m the losses at the input mirror. The important point is that there is a change of sign from $r_1 < (1 - L_m)(1 - L)$ (under coupling) to $r > (1 - L_m)(1 - L)$ (over coupling), so by modulating the input beam in amplitude, and by demodulating the signal from the detector in reflection, it is possible to create an error signal for the distance to the critical coupling point $r = (1 - L_m)(1 - L)$. (Figure 12.11 (a)) We demonstrate (Figure 12.11 (b)) an improvement of the stability by sending some noise to the distance controller, and measuring the response of the resonator in frequency with this error signal feed back to the distance at the critical coupling.

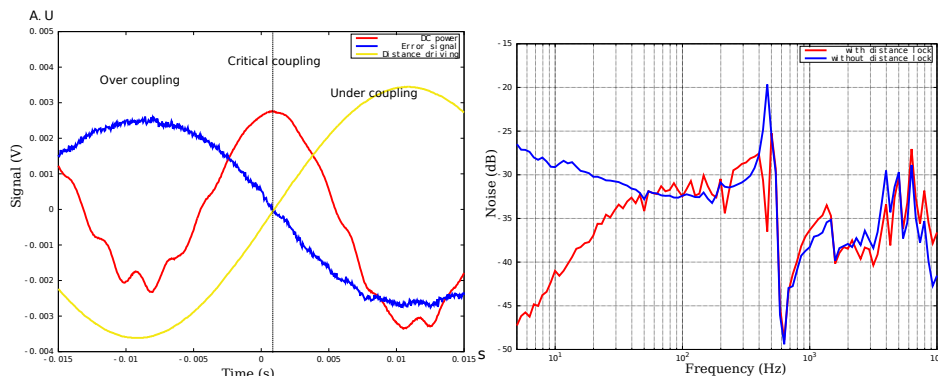


Figure 12.11.: (a) Error signal in distance (blue) during the scan of the prism distance (yellow) with the cavity locked in frequency by a standard PDH locking fed back to the applied voltage. (Red) gives the coupling in the resonator. This error signal is made by sending an amplitude modulation on the beam and by demodulating the signal in reflection.

This method allows us to enhance stability of the system, but in practice the prisms are stable enough for most experiments. This locking system demonstrated here hasn't been used for the measurement of squeezing made later in this thesis.

13. Results

13.1. Non Linearity

13.1.1. SHG and De-amplification

Before generating squeezing, a few different intermediate results can be achieved to characterize the non linearity in the resonator. The first one is to create second harmonic generation. By sending some light at 1064nm in the resonator (a few milliwatts) through the SF11 and by measuring the green light leaving the resonator by the green calcite during the scanning of the applied voltage, I can measure the conversion efficiency of the green light (Figure 13.1). It is theoretically possible to tune the coupling of the prisms to maximize the conversion efficiency for any input power of red ([72]). But in practice the green generation immediately changes the characteristic of the resonator related to electro-optic tuning, making the optimal point very hard to find and moving with time (Figure 12.10). We were able to demonstrate a conversion efficiency of 37% during the scan (Figure 13.1). A better result would necessitate active compensation of the prism distances. It is possible to lock the red light to the resonator with the applied voltage, but the green generation becomes completely chaotic and starts to oscillate. More work would need to be done in this direction to be able to generate reasonable second harmonic with this system.

A second thing that can be observed before doing squeezing is down conversion. The high possible finesse for red and green in this system allows us to reach over-threshold behavior for a green power $\sim 10mW$, so by sending enough green light in the resonator, we can observe red light appearing in the detector (Figure 13.1).

13.1.2. Squeezing

To obtain squeezing, we use an SF11 prism and a calcite prism as output coupler already aligned to the homodyne (subsection 12.5.4) and a green calcite prism to couple the green light (pump). We also align some red light in the output coupler going into the resonator, then into the homodyne detection, to be able to notice the double resonance. This light doesn't need to be perfectly well aligned and will be blocked during the vacuum squeezing measurement.

We scan the applied voltage on the resonator to see the peaks of the sub-harmonic (red) and pump. The temperature of the crystal should be already close to the phase

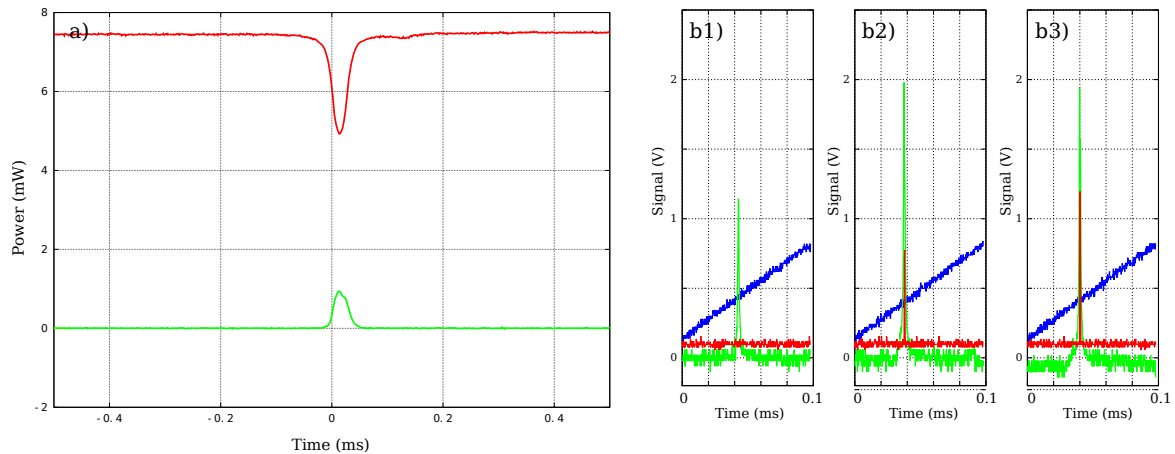


Figure 13.1.: (a)SHG (green) during scan of the applied voltage with 37% of efficiency. Some light at 1064nm (red) is sent to the resonator with the SF11, the green light at 532nm generated is observed with the green calcite prism. (b1-b3) Down conversion by sending some green light (green) and measuring the red light (red) generated for different powers of green during the scan of the applied voltage.

matching temperature (subsection 12.5.3). We tune it a little bit or we change slightly the frequency of the laser (by changing its temperature) to have the two peaks at low applied voltage (during the scan) and very close to each other. Then we stop the applied voltage and change the frequency of the laser in the correct direction to obtain self locking of the pump. It is important to self lock to the correct pump mode (TEM00) because a lot of modes are enhanced by self locking. The SF11 as a output coupler is easier to use because it is possible to see the pump mode leaving from it. When a wrong mode is self locked, I block the beam suddenly, to drop the lock of this particular mode and move a bit more the frequency to reach the next mode.

When the TEM00 mode of the pump is obtained, it is still possible to move slowly up and down the frequency of the laser to reach roughly the resonance of the red light. Then by adjusting the position of the green calcite prism, I can control the phase of the sub-harmonic and place it to resonance.

Then I block the red light coming to the resonator and observe the homodyne signal with a spectrum analyzer when the phase of the LO is scanned (Figure 13.2). I usually observe oscillation of the noise. By blocking the input signal beam coming to the homodyne, I can measure the shot noise level which is usually higher than the minimum of the noise oscillation. The difference between the shot noise and the minimum of the oscillation is the squeezing (Figure 13.2).

With the SF11 as an output coupler, we demonstrated $1.4 \pm 0.1 \text{ dB}$ (2.5 dB corrected) of squeezing at a sideband of 3 Mhz and 4 dB of anti-squeezing. The finesse of the cavity for the sub-harmonic is around 50, and around 10 for the pump, and the

pump power used is around 200mW . The correction of the squeezing takes into account the 84% of visibility of the homodyne detection, 7.4% of losses due to the squeezed beam leaving the SF11 prism through a non coated face, 1.6% of losses due to the various optics and 98% of quantum efficiency of the detectors. No correction is made for the intra cavity losses due to scattering, absorption or leakage through the green calcite prism.

With the red calcite as an output coupler, we demonstrated $2.6 \pm 0.5dB$ (4.7dB corrected) of squeezing and $5dB$ of anti-squeezing. The finesse of the cavity for the sub-harmonic is around 100, and for the pump around 200, and the pump power is around 10mW. The correction of the squeezing takes into account the 85% of visibility of the homodyne detection, 1.6% of losses due to the various optics and 98% of quantum efficiency of the detectors. The squeezing leaves the red calcite prism with a Brewster's angle so no losses are considered due to the second face of the prism.

The small size of the resonator also allows the squeezing to be relatively high bandwidth. The FSR of the system is $19GHz$ and the finesse of the resonator in red during squeezing is around 100, which should correspond to a squeezing bandwidth around $190MHz$. With the SF11 output coupler, we demonstrated $0.28 \pm 0.08dB$ ($0.8dB$ corrected) of vacuum squeezing at $100MHz$ and $0.16 \pm 0.018dB$ ($0.5dB$ corrected) of vacuum squeezing at $150MHz$.

The amount of squeezing observed is still quite modest, but a few known inefficiencies in our system can be redressed. The relatively low visibility of the system can be mostly explained by excessive polishing of this specific resonator, astigmatism of the beam and misalignment of the prism and the resonator. A trapezoid shape for the prism, a better observation system for the white light interferometry and a new geometry allowing round beams to leave the resonator should help a lot to address these points.

With the SF11 output coupler The majority of the losses correspond to some leakage of the squeezed light in the green calcite coupler. To obtain a good escape efficiency, it is necessary to have the squeezing prism coupler (SF11) as close as possible, but it is still also necessary to have enough pump power in the system. The pump is leaking out by the SF11 coupler, so to build enough pump power it is necessary to make the green calcite prism also closer (because the power of the pump is limited by the laser) which makes the losses for the squeezing much larger. The total correction of the losses considering squeezing and anti-squeezing at $3MHz$ is $7.4dB$ of squeezing generated in the cavity with 66% of total losses. By removing the losses already considered, it means that around 47% of losses which should correspond to the absorption of the resonator, the scattering from the faces and the leakage from the green calcite. It is possible to obtain a linewidth of $9MHz$ at $1064nm$ for this resonator which corresponds to 0.30% of losses by round trip and so 3% of losses only for a considered finesse of 100. It means that 45% of losses are due to either GRIIRA effects ([84]), the coupling from the resonator to the SF11 or should appear

because of the losses due to the green calcite being too close.

With the red calcite prism output coupler the total correction of all losses corresponds to a total of $6.7dB$ of squeezing and anti-squeezing generated in the cavity with 42% of total losses. After removing the losses already considered, we get 18% of losses. By removing the 3% of losses due to the absorption we get 15% of losses which are, one more time, due to either GRIIRA effects or the coupling from the resonator to the red calcite prism.

In the two cases the losses in the output coupling prism can also be due to a misalignment of the vertical axis of the resonator and the axis of the extraordinary axis of the crystal.

13.1.3. Conclusion

We investigated in this part of the thesis a very stable, highly tunable and compact system and demonstrated the feasibility of producing quantum states of light with it. We presented the first demonstration of vacuum squeezing from a monolithic resonator using only total internal reflection. The resonator is coating-free, and allows independent tunable coupling rates between the pump and the squeezed beam, and the frequency stability can be assured passively with self locking of the resonator to the pump field.

The amount of squeezing obtained up until now is still quite low, but the technique with this resonator is still young and a lot of improvements can be made. A more careful design in the curvature of the resonator and a better alignment of the couplers should allow a much better mode to be produced making the measurement simpler, and a more careful control of the axis of the crystals should reduce the amount of losses in the resonator. With all these improvements and some more time spent on this system, it should be possible to achieve the same performance as similar systems in free space using bulk crystals ([91]) in a potentially more compact way.

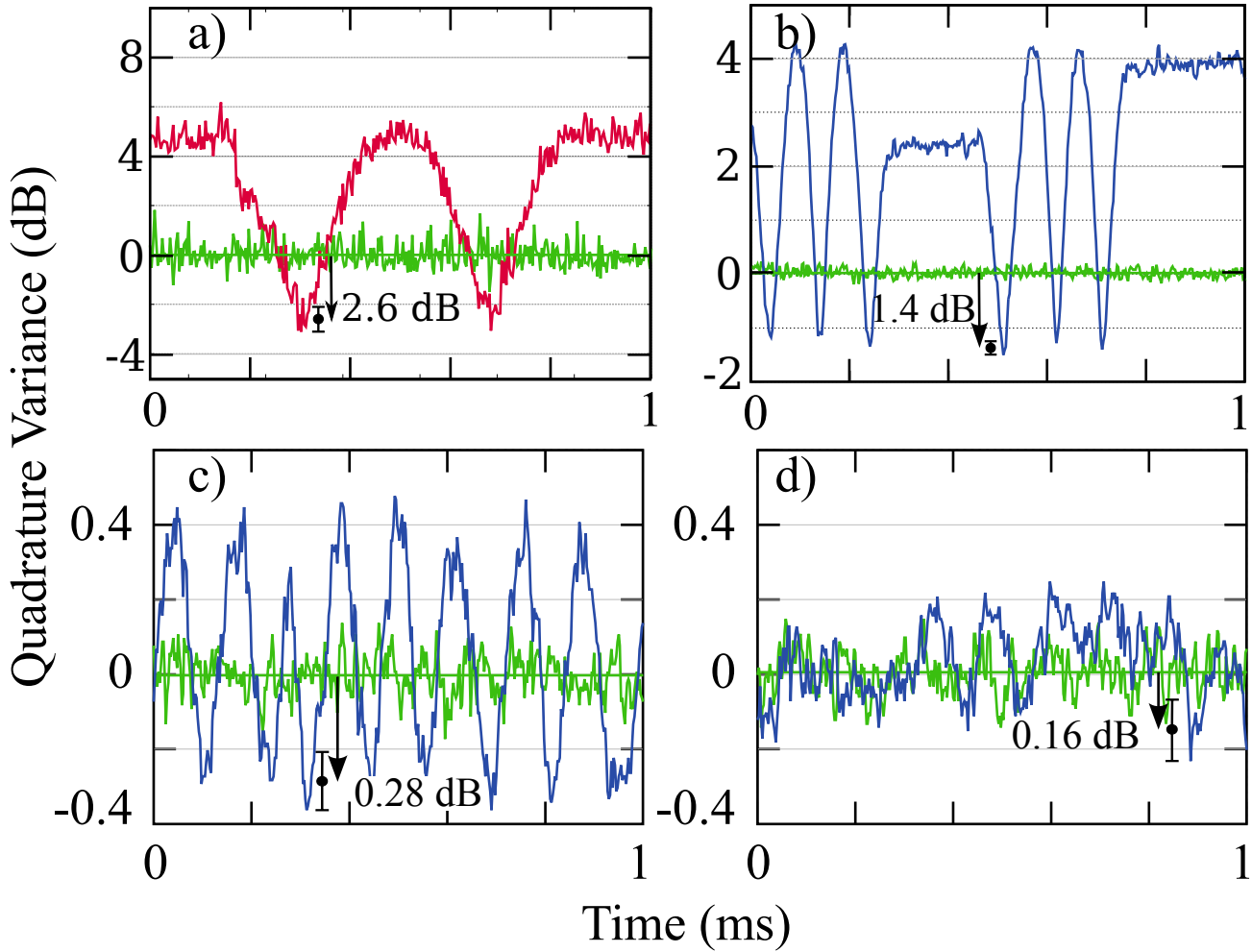


Figure 13.2.: Squeezing and anti-squeezing during scanning of the local oscillator phase at 1 Hz with a red calcite prism as an output coupler (a) and during the scanning at 3Hz with a SF11 prism as an output coupler (b-d). (a) has been taken at sideband frequency of 5MHz and (b) at 3MHz with the same detector with 18 dB of shot-to-dark noise clearance and 50MHz of bandwidth. (b) and (c) are taken respectively at 100MHz and 150MHz of sideband frequencies, with another detector with 4dB of shot-to-dark noise clearance and 3GHz of bandwidth.

Bibliography

- [64] Edmund optics. www.edmundoptics.com.
- [65] Newport. www.newport.com/.
- [66] Radian dyes. www.radiant-dyes.com.
- [67] Thorlabs, inc. www.thorlabs.com/.
- [68] Wavelength electronics. www.teamwavelength.com.
- [69] Allied high tech products. <http://www.alliedhightech.com/>.
- [70] Piezomechanik. www.piezomechanik.com.
- [71] Seiji Armstrong. Experiments in quantum optics: Scalable entangled states and quantum computation with cluster states. Jan 2014.
- [72] Preben Buchhave, Haim Abitan, and Peter Tidemand-Lichtenberg. Non-linear frequency conversion in coupled ring cavities. *Optics Communications*, 200(1-6):359 – 368, 2001. ISSN 0030-4018. doi: [http://dx.doi.org/10.1016/S0030-4018\(01\)01579-6](http://dx.doi.org/10.1016/S0030-4018(01)01579-6). URL <http://www.sciencedirect.com/science/article/pii/S0030401801015796>.
- [73] Geoff Campbell. *Quantum Memories and Monolithic Resonators*. PhD thesis, ANU, 2015.
- [74] Jong H. Chow, Benjamin S. Sheard, David E. McClelland, Malcolm B. Gray, and Ian C. M. Littler. Photothermal effects in passive fiber bragg grating resonators. *Opt. Lett.*, 30(7):708–710, Apr 2005. doi: 10.1364/OL.30.000708. URL <http://ol.osa.org/abstract.cfm?URI=ol-30-7-708>.
- [75] Jong H. Chow, Ian C. Littler, David S. Rabeling, David E. McClelland, and Malcolm B. Gray. Using active resonator impedance matching for shot-noise limited, cavity enhanced amplitude modulated laser absorption spectroscopy. *Opt. Express*, 16(11):7726–7738, May 2008. doi: 10.1364/OE.16.007726. URL <http://www.opticsexpress.org/abstract.cfm?URI=oe-16-11-7726>.
- [76] J. Dai, C. X. Xu, R. Ding, K. Zheng, Z. L. Shi, C. G. Lv, and Y. P. Cui. Combined whispering gallery mode laser from hexagonal zno microcavities. *Applied Physics Letters*, 95(19):191117, 2009. doi: <http://dx.doi.org/10.1063/1.3264080>. URL <http://scitation.aip.org/content/aip/journal/apl/95/19/10.1063/1.3264080>.

- [77] R.W.P. Drever, J.L. Hall, F.V. Kowalski, J. Hough, G.M. Ford, A.J. Munley, and H. Ward. Laser phase and frequency stabilization using an optical resonator. *Applied Physics B*, 31(2):97–105, 1983. ISSN 0946-2171. doi: 10.1007/BF00702605. URL <http://dx.doi.org/10.1007/BF00702605>.
- [78] Salah Hassab Elnaby. Optics of anisotropic media. 2013. URL http://niles.cu.edu.eg/courses/EAL603_FALL_2013/EAL603_2013%20lec2.pdf.
- [79] K Fiedler, S Schiller, R Paschotta, P Kürz, and J Mlynek. Highly efficient frequency doubling with a doubly resonant monolithic total-internal-reflection ring resonator. *Optics letters*, 18(21):1786–1788, 1993.
- [80] Michael Förtsch, Gerhard Schunk, Josef U. Fürst, Dmitry Strekalov, Thomas Gerrits, Martin J. Stevens, Florian Sedlmeir, Harald G. L. Schwefel, Sae Woo Nam, Gerd Leuchs, and Christoph Marquardt. Highly efficient generation of single-mode photon pairs from a crystalline whispering-gallery-mode resonator source. *Phys. Rev. A*, 91:023812, Feb 2015. doi: 10.1103/PhysRevA.91.023812. URL <http://link.aps.org/doi/10.1103/PhysRevA.91.023812>.
- [81] J. U. Fürst, D. V. Strekalov, D. Elser, A. Aiello, U. L. Andersen, Ch. Marquardt, and G. Leuchs. Low-threshold optical parametric oscillations in a whispering gallery mode resonator. *Phys. Rev. Lett.*, 105:263904, Dec 2010. doi: 10.1103/PhysRevLett.105.263904. URL <http://link.aps.org/doi/10.1103/PhysRevLett.105.263904>.
- [82] J. U. Fürst, D. V. Strekalov, D. Elser, A. Aiello, U. L. Andersen, Ch. Marquardt, and G. Leuchs. Quantum light from a whispering-gallery-mode disk resonator. *Phys. Rev. Lett.*, 106:113901, Mar 2011. doi: 10.1103/PhysRevLett.106.113901. URL <http://link.aps.org/doi/10.1103/PhysRevLett.106.113901>.
- [83] JU Fürst, DV Strekalov, Dominique Elser, Mikael Lassen, Ulrik Lund Andersen, Christoph Marquardt, and Gerd Leuchs. Naturally phase-matched second-harmonic generation in a whispering-gallery-mode resonator. *Physical review letters*, 104(15):153901, 2010.
- [84] Y. Furukawa, K. Kitamura, A. Alexandrovski, R. K. Route, M. M. Fejer, and G. Foulon. Green-induced infrared absorption in mgo doped linbo3. *Applied Physics Letters*, 78(14):1970–1972, 2001. doi: <http://dx.doi.org/10.1063/1.1359137>. URL <http://scitation.aip.org/content/aip/journal/apl/78/14/10.1063/1.1359137>.
- [85] A. M. Glass, D. von der Linde, and T. J. Negran. High-voltage bulk photovoltaic effect and the photorefractive process in LiNbO₃. *Applied Physics Letters*, 25: 233, #aug# 1974. doi: 10.1063/1.1655453.
- [86] Vladimir S. Ilchenko, Anatoliy A. Savchenkov, Andrey B. Matsko, and Lute Maleki. Nonlinear optics and crystalline whispering gallery mode cavities. *Phys. Rev. Lett.*, 92:043903, Jan 2004. doi: 10.1103/PhysRevLett.92.043903. URL <http://link.aps.org/doi/10.1103/PhysRevLett.92.043903>.

- [87] Fernando Lahoz, Claudio J. Oton, David López, Jorge Marrero-Alonso, Alicia Boto, and Mario Díaz. Whispering gallery mode laser based on antitumor drug–dye complex gain medium. *Opt. Lett.*, 37(22):4756–4758, Nov 2012. doi: 10.1364/OL.37.004756. URL <http://ol.osa.org/abstract.cfm?URI=ol-37-22-4756>.
- [88] Hongzhan Liu, Liren Liu, Rongwei Xu, and Zhu Luan. Abcd matrix for reflection and refraction of gaussian beams at the surface of a parabola of revolution. *Appl. Opt.*, 44(23):4809–4813, Aug 2005. doi: 10.1364/AO.44.004809. URL <http://ao.osa.org/abstract.cfm?URI=ao-44-23-4809>.
- [89] Sasikanth Manipatruni, Carl B. Poitras, Qianfan Xu, and Michal Lipson. High-speed electro-optic control of the optical quality factor of a silicon microcavity. *Opt. Lett.*, 33(15):1644–1646, Aug 2008. doi: 10.1364/OL.33.001644. URL <http://ol.osa.org/abstract.cfm?URI=ol-33-15-1644>.
- [90] Andrey B Matsko. Practical applications of microresonators in optics and photonics. 2009.
- [91] Moritz Mehmet, Henning Vahlbruch, Nico Lastzka, Karsten Danzmann, and Roman Schnabel. Observation of squeezed states with strong photon-number oscillations. *Phys. Rev. A*, 81:013814, Jan 2010. doi: 10.1103/PhysRevA.81.013814. URL <http://link.aps.org/doi/10.1103/PhysRevA.81.013814>.
- [92] Yong-Le Pan and Richard K. Chang. Highly efficient prism coupling to whispering gallery modes of a square ÎCE cavity. *Applied Physics Letters*, 82(4):487–489, 2003. doi: <http://dx.doi.org/10.1063/1.1540242>. URL <http://scitation.aip.org/content/aip/journal/apl/82/4/10.1063/1.1540242>.
- [93] R. Paschotta, K. Fiedler, P. KÄErz, and J. Mlynek. Nonlinear mode coupling in doubly resonant frequency doublers. *Applied Physics B*, 58(2):117–122, 1994. ISSN 0946-2171. doi: 10.1007/BF01082345. URL <http://dx.doi.org/10.1007/BF01082345>.
- [94] Stephan Schiller and Robert L Byer. Quadruply resonant optical parametric oscillation in a monolithic total-internal-reflection resonator. *JOSA B*, 10(9):1696–1707, 1993.
- [95] Stephan Schiller, II Yu, Martin M Fejer, and Robert L Byer. Fused-silica monolithic total-internal-reflection resonator. *Optics letters*, 17(5):378–380, 1992.
- [96] Gerhard Schunk, Josef U. Fürst, Michael Förtsch, Dmitry V. Strekalov, Ulrich Vogl, Florian Sedlmeir, Harald G. L. Schwefel, Gerd Leuchs, and Christoph Marquardt. Identifying modes of large whispering-gallery mode resonators from the spectrum and emission pattern. *Opt. Express*, 22(25):30795–30806, Dec 2014. doi: 10.1364/OE.22.030795. URL <http://www.opticsexpress.org/abstract.cfm?URI=oe-22-25-30795>.
- [97] S. I. Shopova, G. Farca, A. T. Rosenberger, W. M. S. Wickramanayake, and N. A. Kotov. Microsphere whispering-gallery-mode laser using hgte quantum dots. *Applied Physics Letters*, 85(25):6101–6103, 2004. doi: <http://dx>.

doi.org/10.1063/1.1841459. URL <http://scitation.aip.org/content/aip/journal/apl/85/25/10.1063/1.1841459>.

[98] Moore Nanotechnology Systems. L. nanotech 250upl ultra precision lathe.

A. Fourier Transform of the Polarisation Field versus the Susceptibility

The polarization at the second order is given by:

$$P_i(t) = \underbrace{\epsilon_0 \int \chi_{ij}^1(t - \tau) E_j(\tau) d\tau}_{P^1(t)} + \underbrace{\epsilon_0 \iint \chi_{ijk}^2(t - \tau_1, t - \tau_2) E_j(\tau_1) E_k(\tau_2) d\tau_1 d\tau_2}_{P^2(t)}$$

The first term P^1 doesn't imply any particular difficulty, it is a convolution of two terms we have:

$$P^1(\omega) = \chi_{ij}^1(\omega) E_j(\omega)$$

For the second order, we use the Fourier development of the susceptibility:

$$P^2(t) = \epsilon_0 \iiint \chi_{ijk}^2(\omega_1, \omega_2) \exp(i\omega_1(t - \tau_1)) \exp(i\omega_2(t - \tau_2)) E_j(\tau_1) E_k(\tau_2) d\tau_1 d\tau_2 d\omega_1 d\omega_2,$$

$$P^2(t) = \epsilon_0 \iiint \chi_{ijk}^2(\omega_1, \omega_2) \exp(i(\omega_1 + \omega_2)t) E_j(\tau_1) \exp(-i\omega_1\tau_1) d\tau_1 E_k(\tau_2) \exp(-i\omega_2\tau_2) d\tau_2 d\omega_1 d\omega_2.$$

We recognize the Fourier transform of E_j and E_k :

$$P^2(t) = \epsilon_0 \iint \chi_{ijk}^2(\omega_1, \omega_2) \exp(i(\omega_1 + \omega_2)t) E_j(\omega_1) E_k(\omega_2) d\omega_1 d\omega_2.$$

By using $\omega = \omega_1 + \omega_2$, we get

$$P^2(t) = \epsilon_0 \iint \chi_{ijk}^2(\omega_1, \omega - \omega_1) \exp(i(\omega)t) E_j(\omega_1) E_k(\omega - \omega_1) d\omega_1 d\omega.$$

Which is the Fourier decomposition of $P^2(t)$:

$$P^2(\omega) = \epsilon_0 \int \chi_{ijk}^2(\omega_1, \omega - \omega_1) E_j(\omega_1) E_k(\omega - \omega_1) d\omega_1.$$

The energy density associated to the electric field is given by:

$$U = \frac{1}{2} \langle \mathbf{D} \cdot \mathbf{E} \rangle$$

We can consider independent the energy due to the linear field at the first order U_{p1} and the non linear field at the second order U_{p2} .

For the linear field, the expression of the electric displacement is given by: $D_i(t) = \epsilon_0 \int (\delta_{ij} + \chi_{ij}^1(\omega)) E_j(\omega) e^{i\omega t} d\omega$, which give the energy

$$U_1 = \frac{\epsilon_0}{2} \int E_i^*(\omega) \cdot E_i(\omega) d\omega + \frac{\epsilon_0}{2} \int E_i^*(\omega) \chi_{ij}^1(\omega) E_j(\omega) d\omega.$$

It can be considered as the energy density of the field in the vacuum, plus the energy corresponding to the polarization of the medium.

If we consider only the energy due to the polarization of the medium and we consider independent the energy due to the linear field at the first order U_{p1}

$$U_{p1} = \frac{\epsilon_0}{2} \int E_i^*(\omega) \chi_{ij}^1(\omega) E_j(\omega) d\omega.$$

This value is real so if we subtract it by its conjugate:

$$U_{p1} - U_{p1}^* = 0 = \frac{\epsilon_0}{2} \int \left(E_i^*(\omega) \chi_{ij}^1(\omega) E_j(\omega) - E_i(\omega) \chi_{ij}^{1*}(\omega) E_j^*(\omega) \right) d\omega$$

We can inverse the coefficient i and j in the second expression:

$$\int E_i^*(\omega) E_j(\omega) \left(\chi_{ij}^1(\omega) - \chi_{ji}^{1*}(\omega) \right) d\omega = 0$$

For every value $E(\omega)$ it imply:

$$\chi_{ij}^1(\omega) = \chi_{ji}^{1*}(\omega) \text{ for every } \omega.$$

Because $\chi_{ij}^1(\omega)$ is real,

$$\chi_{ij}^1(\omega) = \chi_{ji}^1(\omega).$$

For the second order, we get:

$$U_{p2} = \frac{\epsilon_0}{2} \iint E_i^*(\omega_1 + \omega_2) \chi_{ijk}^2(\omega_1, \omega_2) E_j(\omega_1) E_k(\omega_2) d\omega_1 d\omega_2.$$

The order of the frequencies and the coefficients of the susceptibility are arbitrary, so we have invariance by permutating them:

$$\chi_{ijk}^2(\omega_1, \omega_2) = \chi_{jik}^2(\omega_1 + \omega_2, -\omega_2) = \chi_{kij}^2(\omega_1 + \omega_2, -\omega_1).$$

B. Index calculation for the green calcite coupler in p-polarization

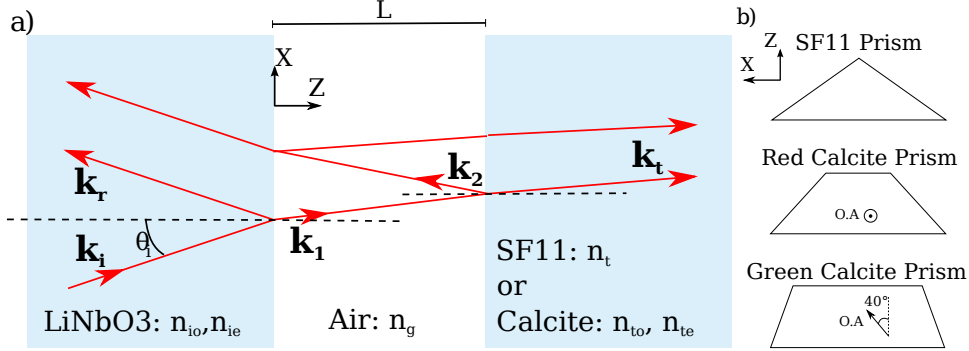


Figure B.1.: (a) Schematic of the coupling media. On the left the resonator, in the middle the gap of air, and on the right one of the prism couplers. (b) The three different prisms that can be used as the third medium. An isotropic prism in SF11, or two anisotropic prisms in calcite with the extraordinary axis allowing us to couple only the red light, or only the green light.

In Chapter (Figure 11.1) we said that the wave vector in the prism is given by:

$$\mathbf{k}_t = \begin{pmatrix} k_{ix} \\ 0 \\ k_{tz} \end{pmatrix}$$

where k_{ix} is the x component of the incident wave vector which is real and known, and $k_{tz} = \left((n_t k_0)^2 - (k_{ix})^2 \right)^{1/2}$ with n_t being the refractive index of the prism and $k_0 = \frac{\omega}{c}$. The prism considered here is the green prism, it has the extraordinary axis in the horizontal plan ($\mathbf{e}_x, \mathbf{e}_z$) making an angle $\theta = 40^\circ$ with the direction \mathbf{e}_z (green calcite prism). We can use the Fresnel anisotropic equation in the axis of the anisotropy of the prism:

$$k_0^2 = \frac{k_{z'}^2}{n_o^2} + \frac{k_{x'}^2}{n_e^2} \quad (\text{B.1})$$

where n_o and n_e are the ordinary and extraordinary indices of the prism, and $(k_{x'}, k_{y'}, k_{z'})$ the coordinates of the wave vector \mathbf{k}_t in the reference frame of the anisotropic axis of the prism. Those coordinates can be transformed to the reference frame of the problem by applying $k_{x'} = k_{tx} \cos(\theta) - k_{tz} \sin(\theta)$, $k_{y'} = k_{ty} = 0$, and $k_{z'} = k_{tz} \cos(\theta) + k_{tx} \sin(\theta)$, with θ being the angle between the extraordinary axis and \mathbf{e}_x . Eq. B.1 becomes:

$$k_0^2 = \frac{(k_{tz} \cos(\theta) + k_{tx} \sin(\theta))^2}{n_o^2} + \frac{(k_{tx} \cos(\theta) - k_{tz} \sin(\theta))^2}{n_e^2}$$

$$k_0^2 = k_{tz}^2 \left(\frac{\cos(\theta)}{n_o^2} + \frac{\sin(\theta)}{n_e^2} \right) + k_{tx}^2 \left(\frac{\cos(\theta)}{n_e^2} + \frac{\sin(\theta)}{n_o^2} \right) + 2k_{tz}k_{tx} \cos(\theta) \sin(\theta) \left(\frac{1}{n_o^2} - \frac{1}{n_e^2} \right)$$

$$k_0^2 = \frac{k_{tz}^2}{n_{p1}^2} + \frac{k_{tx}^2}{n_{p2}^2} + \frac{2k_{tz}k_{tx}}{\gamma}. \quad (\text{B.2})$$

where $\frac{1}{n_{p1}^2} = \frac{\cos(\theta)}{n_o^2} + \frac{\sin(\theta)}{n_e^2}$, $\frac{1}{n_{p2}^2} = \frac{\cos(\theta)}{n_e^2} + \frac{\sin(\theta)}{n_o^2}$ and $\frac{1}{\gamma} = \cos(\theta) \sin(\theta) \left(\frac{1}{n_o^2} - \frac{1}{n_e^2} \right)$. For $\theta = 40^\circ$, and $n_o = 1.64246$ and $n_e = 1.47964$, the values for the light at 1064nm, we obtain: $n_{p1} = 1.5689$, $n_{p2} = 1.5408$ and $\gamma = -23.595$. Eq. B.2 is a second degree equation in k_{tz} .

$$k_{tz} = -\frac{k_{ix}n_{p1}^2}{\gamma} \pm n_{p1}^2 \Delta^{1/2}$$

where $\Delta = \frac{k_0^2}{n_{p1}^2} - k_{ix}^2 \left(\frac{1}{n_{p1}^2 n_{p2}^2} - \frac{1}{\gamma^2} \right)$. For the light at 1064nm $\Delta < 0$, so k_{tz} is complex. The beam is evanescent and decreases in amplitude so the value to consider is the one with a positive imaginary part: $k_{tz} = -\frac{k_{ix}n_{p1}^2}{\gamma} + n_{p1}^2 \Delta^{1/2}$.

It is interesting to note that the value $k_{tp} = \frac{k_{tz}}{n_{p1}^2} + \frac{k_{ix}}{\gamma}$ is purely imaginary.